

**MORPHOLOGY AND PERMEABILITY IN EXTRUDED
POLYPROPYLENE / ETHYLENE VINYL-ALCOHOL COPOLYMER
BLENDS**

by

GÜNTER WERNER LOHFINK

A Thesis Submitted to the Faculty of Graduate Studies and
Research in Partial Fulfillment of the Requirement for the
Degree of Doctor of Philosophy

Department of Chemical Engineering
McGill University
Montreal, Canada

February 1990

Copyright © Gunter Werner Lohfink (1990)

"Everything that is really great and
inspiring is created by the individ-
ual who can labor in freedom."

Albert Einstein

ABSTRACT

Studies of the morphology of extruded polymer blend systems have shown that it is feasible to produce a laminar structure of an ethylene vinyl-alcohol copolymer (EVOH) dispersed phase in a polypropylene (PP) matrix phase. The laminar structure forms in the core of the extrudate when a slit die is incorporated into the extrusion process.

Morphological studies, including a study of morphology development inside the die and studies of the effect of processing conditions on the morphology of the final product, revealed that the laminar structure is a result of die design. Processing conditions influence mainly the shape and dimensions of the laminar core region of the extrudate.

Oxygen permeation tests have shown that the blend exhibits lower oxygen permeability than pure PP, when EVOH is incorporated as a dispersed phase into the system. Oxygen transmission rates obtained with a blend system can be as low as those obtained with a multi-layer coextrusion product, although only at high EVOH concentrations. Comparison of experimental data with theoretical permeation predictions shows that, up to 20wt% EVOH, the reduction in oxygen transmission rate is only minor, and follows the prediction for a homogeneous system. At 25wt%, a considerable decrease in oxygen transmission rate is noticeable, and the trend for higher EVOH contents is towards the behavior of a multi-layer system.

RESUME

Des études sur la morphologie de mélanges de polymères extrudés ont démontré qu'il est possible de produire une structure laminaire d'une phase dispersée de copolymère alcool-covinyl éthylène (EVOH) dans une matrice de poly-propylène (PP). La structure laminaire se forme au coeur du produit extrudé lorsqu'une filière plate est incorporée dans le procédé d'extrusion.

Des études morphologiques, incluant une étude de la formation de la morphologie à l'intérieur de la filière et des études de l'effet des conditions de mise en oeuvre sur la morphologie du produit final, ont révélé que la structure laminaire est fonction de la forme de la filière. Les conditions de mise en oeuvre influencent surtout les formes et dimensions de la région laminaire au coeur du produit extrudé.

Des tests de perméabilité à l'oxygène ont prouvé que le mélange présentait une moins grande perméabilité à l'oxygène que le PP pur lorsque l'EVOH est incorporé en phase dispersée dans le système. Les taux de transmission d'oxygène obtenus à travers un mélange peuvent être aussi bas que ceux à travers un produit d'extrusion en couches multiples, à condition d'avoir des concentrations élevées d'EVOH. Des comparaisons de données expérimentales et de prédictions théoriques de perméabilité montrent que, jusqu'à un taux massique de 20% en EVOH, la réduction du taux de transmission d'oxygène est mineure et suit la prédiction pour un système homogène. A un taux massique de 25%, une baisse considérable du taux de transmission peut être observée et la tendance pour de plus grandes concentrations d'EVOH est celle qui suit le comportement d'un système à couches multiples.

ZUSAMMENFASSUNG

Morphologische Untersuchungen von extrudierten Polymer Blend Systemen haben gezeigt, daß es möglich ist eine dispergierte Ethylen Vinyl-Alkohol Copolymer (EVOH) Phase lamellar in einer Polypropylen (PP) Matrix Phase anzuordnen. Diese laminaire Struktur kann im Extrudatskern erzeugt werden, wenn ein Breit-schlitzwerkzeug in der Verarbeitung eingesetzt wird.

Untersuchungen über die Entwicklung der Morphologie im Werkzeug und über die Auswirkungen der Verarbeitungsbedingungen auf die Extrudatsmorphologie haben deutlich gemacht, daß die Ausbildung der laminaren Struktur von der Gestaltung des Fließkanals im Werkzeug abhängt. Die Verarbeitungsbedingungen beeinflussen hauptsächlich die Form und Dimensionen der laminaren Struktur im Extrudatskern.

Sauerstoffdurchdringlichkeitsmessungen haben gezeigt, daß Extrudate, welche EVOH als dispergierende Phase beinhalten, geringere Sauerstoffdurchlassigkeitswerte aufweisen als reine PP Extrudate. Die mit einem Mehrschichten-Coextrusions Verfahren erzielbaren Sauerstoffdurchlassigkeitswerte können jedoch nur dann mit einem Blend System erzielt werden, wenn größere Mengen von EVOH in das System eingearbeitet werden. Bei einem EVOH Gewichtsanteil bis zu 20% verringert sich dabei der Durchlassigkeitswert nur geringfügig und Meßpunkte stimmen mit den für ein homogenes System errechneten theoretischen Werten überein. Wenn der Gewichtsanteil auf über 25% angehoben wird verringert sich der Durchlassigkeitswert erheblich und die Meßpunkte nähern sich den theoretischen Werten für laminare Mehrschichtensysteme.

ACKNOWLEDGEMENTS

I would like to express my utmost gratitude and appreciation to Professor M.R. Kamal, my research supervisor for his invaluable guidance, inspiration and encouragement throughout this project.

In addition I would like to thank the following :

- Professor G.R. Brown for his helpful discussions and help in providing the permeability measurements.
- Professor G. Menges for his inspiration and encouragement throughout my engineering studies.
- Messrs. C. Dolan, A. Gagnon, and W. Greenland for their helpful discussions in design and construction of the slit die and take-off equipment.
- Messrs. L. Cusmich, J. Dumont, and N. Habib for their patience and assistance on equipment problems.
- Dr. K. Patel for carrying out all permeation tests in the laboratory of Professor G.R. Brown.
- CCL Industries Inc., EVAL® Company of America, and Mitsui Petrochemicals (America) LTD. for the supply of materials used in this work.
- World University Service of Canada (Government of Canada Awards), Natural Sciences and Engineering Research Council of Canada, and Ministère de l'Education of the Government of Quebec for the financial support of this project.
- Dr. T. Mutel, S.-H.&E. Chu, A.&A. Haber, L.&T. Samurkas, C.&A. Kallos, Drs. S.&O. Polat, N.&I. Slobod, P. Bates, T. Broadhead, J. McDermid, M. Weber, G.&M. Krull, and Dr. A. Hof for their helpful discussions and friendship.
- my parents and family for their encouragement from so far away. Their support contributed significantly to the successful completion of this thesis.

TABLE OF CONTENTS

ABSTRACT	i
RESUME	ii
ZUSAMMENFASSUNG	iii
ACKNOWLEDGEMENTS	iv
LIST OF FIGURES	viii
LIST OF TABLES	xiv
NOMENCLATURE	xv

Chapter

1 INTRODUCTION	1
2 LITERATURE REVIEW	6
2.1 Emulsions	6
2.1.1 Theory	6
2.1.2 Experimental	15
2.1.2.1 Newtonian Dispersed Phase	15
a) Couette Flow	15
b) Pressure-driven Flow	21
2.1.2.2 Non-Newtonian Dispersed Phase	24
a) Couette Flow	24
b) Pressure-driven Flow	26
2.2 Polymer Blends	31
2.2.1 Theory	34
2.2.2 Morphology	36
2.2.2.1 Effect of Flow Field	36
a) Rotating Parallel or Cone-and- Plate Geometry	36
b) Capillary Flow	39
c) Annular and Slit Flow	47
d) Mixing Devices	49
2.2.2.2 Effect of Interfacial Properties and Compatibilizers	55
a) Mixing Devices	56
b) Slit Flow	60
2.3 Conclusions	60

3	EXPERIMENTAL	63
3.1	Materials	63
3.1.1	Resin Characterization	64
3.1.1.1	Steady Shear Viscosity	64
3.1.1.2	Shear Storage Modulus	64
3.1.1.3	Determination of Functionalized Groups in Adhesive Polymers	67
	(a) Fourier Transform Infrared (FT-IR) Spectroscopy	69
	(b) Titration	73
3.2	Processing Equipment	76
3.2.1	Extruder	77
3.2.2	Extrusion Die	78
3.2.3	Take-off Equipment and Cooling	80
3.3	Processing Conditions	80
3.4	Flow Analysis in Slit Die Extrusion	85
3.5	Morphology Studies	88
3.5.1	Sample Preparation and Analysis Procedure	89
3.6	High Speed Impact Testing	92
3.7	Oxygen Permeability Tests	95
4	RESULTS AND DISCUSSION	97
4.1	Morphology Development in the Adapter and Slit Die	97
4.1.1	Metering Screw	97
4.1.2	Mixing Screw	105
4.1.3	Analysis of Flow Kinematics	112
4.2	Morphology of Extruded Ribbons	125
4.2.1	Morphology of Pure Resins	125
4.2.2	Morphology of Extruded Blends	127
4.2.2.1	PP/EVOH Blends	128
	(a) Variation across Ribbon Thickness	128
	(b) Effect of EVOH Content	132
4.2.2.2	PP/MAPP/EVOH Blends	132
	(a) Variation across Ribbon Thickness	132

(b) Effect of Screw Design	135
(c) Effect of Die Exit Gap Size	137
(d) Effect of Screw Speed	139
(e) Internal Structure	141
(f) Adhesion	143
4.2.2.3 MAPP2/EVOH Blends	145
(a) Variation across Ribbon Thickness	147
(b) Effect of Temperature and Screw Speed	147
(c) Adhesion	151
4.2.3 Summary of Morphological Observations	156
4.3 Impact Properties	157
4.3.1 Pure Resins	157
4.3.2 PP/EVOH and PP/MAPP/EVOH Blends	157
4.3.3 MAPP2/EVOH Blends	164
4.4 Specific Extruder Energy	168
4.4.1 PP/EVOH and PP/MAPP/EVOH Blends	169
4.4.2 MAPP2/EVOH Blends	171
4.5 Oxygen Permeability	176
4.5.1 Evaluation of Barrier Performance	179
5 CONCLUSIONS AND RECOMMENDATIONS	185
5.1 Conclusions	185
5.2 Recommendations for Future Work	188
5.3 Original Contributions to Knowledge	190
REFERENCES	192
APPENDIX A	A1
APPENDIX B	A6
APPENDIX C	A12
APPENDIX D	A23

LIST OF FIGURES

FIGURE

2.1	Schematic of droplet deformation: a) uniform shear flow field; b) plane hyperbolic flow field.	8
2.2	Behavior of Drops in Shear Flow up to Burst : Class A ($\lambda < 0.2$); Class B ₁ and B ₂ ($0.03 \leq \lambda \leq 2.2$); Class C ($\lambda > 3.8$). It was reported that the three classes were related to λ but that there were no sharp boundaries between them [12].	17
2.3	Deformed Fluid Drop in an Emulsion undergoing Poiseuille Flow. a) Coordinates b) Forces acting on Drop . . .	22
2.4	Schematic of the Droplet Deformation Process that would occur in the entrance and fully developed regions for a viscoelastic drop suspended in a viscoelastic fluid [21].	27
2.5	Schematic Layout of the Experimental Apparatus [8].	29
2.6	Comparison of the theoretically predicted droplet shape with the experimentally observed one [8]: a) $\lambda = 0.037$, $We = 0.067$, $\gamma_E = 0.0042 \text{sec}^{-1}$ b) $\lambda = 0.055$, $We = 0.19$, $\gamma_E = 0.024 \text{sec}^{-1}$	30
2.7	Schematic of Processing-Morphology-Property Interactions in Dispersed Multi-Phase Polymeric Systems.	33
2.8	Representation of the Fibrillation Process in the entrance zone and in the duct [32].	42
2.9	Empirical model representation of Molten Two- Phase Dispersed Polymer Blend flowing through a Capillary [37].	44
2.10	The schematic view of longitudinal phase morphologies at various viscosity ratios $\lambda = \eta_d / \eta_m$ for a HDPE/PS blend [39]. a) $\lambda < 0.7$ b) $0.7 < \lambda < 1.7$ c) $\lambda > 2.2$	46
2.11	Hydrocarbon permeability in laminar walled PE/nylon barrier bottles [41].	50
2.12	Volume average diameter versus torque ratio from TR of 0.078 to 12.8 [45].	52

2.13	Dimensionless master curve of We vs. λ for the melt extrusion using a co-rotating twin screw extruder [46].	54
3.1	Steady Shear Viscosity vs. Shear Rate for PP, MAPP1, MAPP2 and EVOH, $T=200^{\circ}C, 230^{\circ}C$	66
3.2	Shear Storage Modulus G' vs. Frequency for PP, MAPP1, MAPP2 and EVOH, $T=200^{\circ}C, 230^{\circ}C$	68
3.3	Infrared Spectrum for Maleic Anhydride [68].	70
3.4	Infrared Absorbance Spectrum for MAPP1.	71
3.5	Infrared Absorbance Spectrum for MAPP2.	72
3.6	Infrared Subtraction Spectrum for MAPP1.	74
3.7	Infrared Subtraction Spectrum for MAPP2.	75
3.8	Schematic of Slit Die Unit Design.	79
3.9	Sample Locations for OM Analysis.	87
3.10	Fracture Sample Locations for SEM Analysis (parallel and perpendicular to flow).	90
3.11	Fracture Sample Locations for SEM Analysis (45° to flow).	91
3.12	Idealized deformation stages and transitions for puncture testing of flat-plate specimens by a hemispherical probe [84].	94
4.1	OM Micrographs of Morphology Development in <u>Adapter</u> for Samples using a Metering Screw.	98
4.2	OM Micrographs of Morphology Development in <u>Adapter</u> for Samples using a Metering Screw.	99
4.3	OM Micrographs of Morphology Development in <u>Slit Die</u> for Samples using a Metering Screw.	101
4.4	OM Micrographs of Morphology Development in <u>Slit Die</u> for Samples using a Metering Screw.	102
4.5	OM Micrographs of Morphology Development in <u>Slit Die</u> for Samples using a Metering Screw.	104
4.6	OM Micrographs of Morphology Development in <u>Adapter</u> for Samples using a Mixing Screw.	106
4.7	OM Micrographs of Morphology Development in <u>Adapter</u> for Samples using a Mixing Screw.	107

4.8	OM Micrographs of Morphology Development in <u>Slit Die</u> for Samples using a Mixing Screw.	109
4.9	OM Micrographs of Morphology Development in <u>Slit Die</u> for Samples using a Mixing Screw.	110
4.10	OM Micrographs of Morphology Development in <u>Slit Die</u> for Samples using a Mixing Screw.	111
4.11	Finite element mesh for a 30° adapter and slit die design.	113
4.12	Finite element mesh for a 70° adapter and slit die design.	114
4.13	Deformation behavior of four particles for a 30° adapter and slit die design.	116
4.14	Deformation behavior of four particles for a 70° adapter and slit die design.	117
4.15	Deformation behavior of three particles in a 30° adapter.	118
4.16	Deformation behavior of three particles in a 70° adapter.	119
4.17	Deformation behavior of two particles in the diverging section of the slit die (30° adapter angle).	121
4.18	Deformation behavior of two particles in the diverging section of the slit die (70° adapter angle).	122
4.19	Deformation of three particles. Front view (y-axis) of area A (see Figure 4.11).	123
4.20	Deformation of three particles. Front view (y-axis) of area A (see Figure 4.12).	124
4.21	SEM micrographs for the Pure Resins.	126
4.22	SEM micrographs showing Flow Lines for different Compositions and Processing Conditions.	129
4.23	SEM micrographs for a PP/EVOH blend systems showing Morphology Variations across Ribbon Thickness for a 80/20wt% composition ratio as a Function of Die Temperature (Metering Screw, 30rpm, h=1.0mm).	130

4.24	SEM micrographs for a PP/EVOH blend system showing the Influence of Composition and Die Temperature on Laminar Structure Development in the Core Region (Metering Screw, 60rpm, h=1.0mm).	133
4.25	SEM micrographs for a PP/MAPP1/EVOH blend system showing Morphology Variations across Ribbon Thickness for a 67.8/15.3/16.9wt% composition ratio as a Function of Die Temperature (Metering Screw, 30rpm, h=1.0mm)	134
4.26	SEM micrographs for a PP/MAPP2/EVOH blend system showing the Effect of Screw Design on Laminar Structure Development in the Core Region for a 71.4/10.7/17.9wt% composition ratio ($T_{Die}=230^{\circ}C$, 60rpm, h=0.5mm).	136
4.27	SEM micrographs for a PP/MAPP2/EVOH blend system showing Morphology Variations across Ribbon Thickness as a Function of Screw Design for a 71.4/10.7/17.9wt% composition ratio ($T_{Die}=230^{\circ}C$, 60rpm, h=0.5mm).	138
4.28	SEM micrographs for a PP/MAPP1/EVOH blend system showing the Effect of Exit Gap Size on Laminar Structure Development in the Core Region as a Function of Screw Design for a 71.4/10.7/17.9wt% composition ratio ($T_{Die}=230^{\circ}C$, 60rpm).	140
4.29	SEM micrographs for a PP/MAPP1/EVOH blend system showing the Effect of Screw Speed on Laminar Structure Development in the Core Region as a Function of Exit Gap Size for a 67.8/15.3/16.9wt% composition ratio (Metering Screw, $T_{Die}=230^{\circ}C$).	142
4.30	SEM micrographs for a PP/MAPP1/EVOH blend system showing Internal Structures for a 64.2/8.3/27.5 wt% composition ratio (Metering Screw, $T_{Die}=230^{\circ}C$ 30 rpm, h=1.0mm).	144
4.31	SEM micrographs for a PP/MAPP/EVOH blend system showing Adhesion for two Screw Designs, and two Compatibilizers, for a 67.8/15.3,16.9wt% composition ratio ($T_{Die}=230^{\circ}C$, 60rpm, h=0.5mm).	146
4.32	SEM micrographs for a MAPP2/EVOH blend system showing Morphology Variations across Ribbon Thickness as a Function of Screw Design for a 80/20wt% composition ratio ($T_{Die}=230^{\circ}C$, 30rpm, h=0.5mm).	148

4.33	SEM micrographs for a MAPP2/EVOH blend system showing the Effect of Composition on Laminar Structure Development in the Core Region (Metering Screw, $T_{Die}=230^{\circ}\text{C}$, 30rpm, $h=0.5\text{mm}$). . .	149
4.34	SEM micrographs for a MAPP2/EVOH blend system showing the Effect of Composition on Laminar Structure Development in the Core Region (Metering Screw, $T_{Die}=215^{\circ}\text{C}$, 60rpm, $h=0.5\text{mm}$). . .	150
4.35	SEM micrographs for a MAPP2/EVOH blend system showing the Effect of Composition on Laminar Structure Development in the Core Region (Mixing Screw, $T_{Die}=230^{\circ}\text{C}$, 30rpm, $h=0.5\text{mm}$). . .	152
4.36	SEM micrographs for a MAPP2/EVOH blend system showing the Effect of Composition on Laminar Structure Development in the Core Region (Mixing Screw, $T_{Die}=215^{\circ}\text{C}$, 60rpm, $h=0.5\text{mm}$). . .	153
4.37	SEM micrographs for a MAPP2/EVOH blend system showing Adhesion for two Composition Ratios (Metering Screw, $T_{Die}=230^{\circ}\text{C}$, 30rpm, $h=0.5\text{mm}$). . .	154
4.38	SEM micrographs for a MAPP2/EVOH blend system showing Adhesion for two Composition Ratios (Mixing Screw, $T_{Die}=230^{\circ}\text{C}$, 30rpm, $h=0.5\text{mm}$). . .	155
4.39	Schematic of typical Impact Traces for EVOH and PP.	158
4.40	Impact Ultimate Force for PP/EVOH and PP/MAPP1/EVOH blend systems as a Function of Composition and Die Temperature.	160
4.41	Impact Slope for PP/EVOH and PP/MAPP1/EVOH blend systems as a Function of Composition and Die Temperature.	161
4.42	Impact Ultimate Force and Slope for a PP/MAPP/EVOH blend system as a Function of Composition and Screw Design.	163
4.43	Impact Ultimate Force for a MAPP2/EVOH blend system as a Function of Composition and Processing Conditions.	165
4.44	Impact Slope for a MAPP2/EVOH blend system as a Function of Composition and Processing Conditions.	167
4.45	Specific Extruder Energy for PP/EVOH and PP/MAPP1/EVOH blend systems as a Function of Composition and Die Temperature ($h=1.0\text{mm}$). . . .	170

4.46	Specific Extruder Energy for a PP/MAPP1/EVOH blend system as a Function of Adapter Angle, Exit Gap Size and Screw Design (60 rpm).	172
4.47	Specific Extruder Energy for a PP/MAPP1/EVOH blend system as a Function of Screw Speed and Exit Gap Size.	173
4.48	Specific Extruder Energy for a MAPP2/EVOH blend system as a Function of Composition and Processing Conditions (h=0.5mm).	174
4.49	Oxygen Permeability for a PP/EVOH blend system as a Function of Composition and Die Temperature.	178
4.50	Oxygen Permeability for a PP/MAPP2/EVOH blend system as a Function of Screw Design and Speed.	180
4.51	Oxygen Permeability for a MAPP2/EVOH blend system as a Function of Composition and Processing Conditions.	181
4.52	Comparison of Measured Oxygen Transmission Rates with Model Predictions for a MAPP2/EVOH blend system.	183
A1	Metering Screw Design (C.W.Brabender Instruments, Inc.).	A2
A2	Mixing Screw Design (Brampton Engineering, Inc.).	A3
A3	Extruder-Endflange Assembly Details (C.W.Brabender Instruments, Inc.).	A4
A4	Heating/Cooling Collar Design Arrangements (C.W.Brabender Instruments, Inc.).	A5
B1	Adapter Design (C.W.Brabender Instruments, Inc.).	A7
B2	Slit Die - Top Part (Interior View).	A8
B3	Slit Die - Top Part (Exterior View).	A9
B4	Slit Die - Bottom Part.	A10
B5	Slit Die - Adjustable Die Land.	A11
D1	RVIST Load-Deflection Curves for PP	A24
D2	RVIST Load-Deflection Curves for EVOH	A25

LIST OF TABLES

TABLE

2.1	Breakup of Droplets [13].	19
2.2	Droplet Deformation and Breakup Behavior for a Newtonian Dispersed Phase as a Function of Flow Field and Matrix Phase Fluid.	25
2.3	Droplet Deformation and Breakup Behavior for a Non-Newtonian Dispersed Phase as a Function of Flow Field and Matrix Phase Fluid.	32
2.4	Dispersed Phase Morphology of different Polymer Blend Systems for Rotating Parallel or Cone-and-Plate Geometry.	38
2.5	Dispersed Phase Morphology of different Polymer Blend Systems for Capillary Flow.	48
2.6	Permeability, Loss (g.) [*] , in 4 oz. Blowmolded Containers [41].	51
3.1	Resin Properties [63,64,65,66].	65
3.2	Slit Die and Extruder Barrel Temperature Setpoints.	81
3.3	Weight and Volume Fractions for different Blending Ratios for a Two-Component Blend System of PP-EVOH or MAPP2-EVOH.	83
3.4	Weight and Volume Fractions for different Blending Ratios for a Three-Component Blend System of PP/MAPP/EVOH.	84
4.1	Oxygen Transmission Rates.	177

NOMENCLATURE

a	droplet radius
b_i	principle radius of curvature
d_v	volume average diameter
D	steady state deformation
D'	time-dependent deformation
\bar{e}	specific extruder energy
ΔF	net free energy
F_{rr}	net radial force
G'	storage modulus
L/d	length to diameter ratio of single-screw extruder
\dot{m}	mass flow rate
M	extruder torque
n	rpm (rounds per minute)
N_{1i}	first normal stress difference of phase i
p	pressure
P	extruder power
P_i	permeability of phase i
P_c	permeability of composite
PO_2	oxygen permeability , oxygen transmission rate
P_n	Legendre polynomial of degree n
Q	volumetric flow rate
r	nondimensionalized sphere radius
R	tube diameter (Poiseuille flow)
R_1, R_2	inner and outer radius of Couette apparatus
t	time
T	temperature , relaxation time
T_0	oscillation period
TR	torque ratio
\underline{v}	velocity field
vol%	volume percentage
We	Weber number ($\equiv (\eta_m \cdot \gamma \cdot a) / \sigma$)
wt%	weight percentage
Zi	extruder zone i
x, y, z	rectangular coordinates

r, θ, z	cylindrical coordinates
α	orientation angle with respect to flow direction
α'	time-dependent orientation angle
β	material constant (fluid elasticity)
α, β	phase description
γ	shear rate
γ_b	critical shear rate at droplet burst
γ_E	rate of strain (elongation rate)
ϵ	perturbation parameter
η	viscosity
η_d	dispersed phase viscosity
η_m	matrix phase viscosity
λ	viscosity ratio ($\equiv \eta_d/\eta_m$) , wavelength in FT-IR
ν	wavenumber in FT-IR
ρ	density
σ	interfacial tension
$\sigma_{\alpha\beta}$	interfacial tension between phases α and β
$\sigma_{\alpha\beta}^0$	interfacial tension in absence of flow
$\underline{\tau}$	stress tensor
τ	tortuosity (permeation studies)
ϕ_i	volume fraction of phase i
ω	rotational speed

ABBREVIATIONS

ASTM	American Society for Testing and Materials
CPA	copolyamide
CEVAC	ethylene vinyl-acetate copolymer
DMF	dimethylformamide
EP	ethylene-propylene rubber
EVA	ethylene vinyl-acetate
EVOH	ethylene vinyl-alcohol copolymer
FDA	Food and Drug Administration
FT-IR	Fourier Transform Infrared
HDPE	high density polyethylene

HCl	hydrochloric acid
HPB-b-PS	hydrogenated butadiene-b-styrene diblock copolymer
KOH	potassium hydroxide
LDPE	low density polyethylene
MA	maleic acid
MAA	methacrylic acid
MAH	maleic anhydride
MAH-PP	maleic anhydride grafted polypropylene
MAPP	maleic anhydride grafted polypropylene
N6	nylon 6
N66	nylon 66
OM	optical microscope
PC	polycarbonate , personal computer
PE	polyethylene
PET	polyethyleneterephthalate
PMMA	polymethylmethacrylate
POM	polyoxymethylene
PP	polypropylene
PS	polystyrene
PVDF	polyvinylidene fluoride
RVSIT	Rheometrics variable speed impact tester
SEM	scanning electron microscope
TEM	transmission electron microscope
St-MAA	styrene-methacrylic acid

CHAPTER 1

INTRODUCTION

Exact applications for industrial materials are appearing continually. The need for enhancement of product properties and processing behavior, and for meeting government regulations have motivated the development of materials with improved performance. Polymers and their products have provided solutions to material related problems in many situations, with both economic and technical advantages. While synthesis of new polymers has been the major focus of research in the past, the trend is now shifting in another direction. The development of polymer systems, obtained by combining thin layers of polymers, by mixing two or more polymers, or by introducing additives, often offers a more efficient method of obtaining new materials than the synthesis of new polymers.

In recent years, the use of polymers in the packaging industry has increased steadily. Polymers offer advantages over other packaging materials, such as their low cost, relative ease of processing, flexibility, good physical properties, and light weight. An important obstacle in the use of polymers in the packaging industry, however, relates to the high permeability of various gases and solvents through a single polymer layer. With excellent barrier properties to moisture, solvents, oxygen and odorous substances, glass and metal containers have maintained a substantial share of food packaging.

As a result of innovations in materials and process technology, and in package design, plastics are no longer intended primarily as replacements for metal, glass or paper in food container packaging applications. Plastics are used increasingly in new products where their unique qualities, combined with esthetic considerations, are serving to reinterpret and

upgrade the utility of packages. Moreover, cost-effective, new barrier resins with improved performance and processing characteristics, for use as rigid and flexible containers, have given barrier-resin technology new tools in manufacturing containers for the food packaging market.

Much of the success of plastics in the packaging industry stems from the growing use of barrier plastics which, when incorporated into food packaging, protect the contents from spoilage. Barrier resins provide the increased shelf life for foods, beverages, and pharmaceuticals, while imparting light weight, breakage resistance, and esthetic appeal, which are characteristic of plastics packaging. The improved barrier properties have been made possible by co-processing, which employs combinations of plastics to obtain optimized products, combining the best properties of different polymers.

One of the fastest growing food packaging product lines involves high-gas-barrier, coextruded bottles. A key polymer used in these bottles is ethylene vinyl-alcohol copolymer (EVOH), which is approved by the Food and Drug Administration (FDA) for food-contact applications. EVOH is resistant to permeation of oxygen, carbon dioxide, other gases, and hydrocarbons. The main shortcomings of EVOH are its moisture sensitivity, and its reduced oxygen permeation resistance with increasing relative humidity. Thus, during manufacture, a layer of EVOH is sandwiched between layers of one or more common polymers, such as polyethylene (PE), or polypropylene (PP). PE and PP have excellent water barrier properties, but low oxygen permeation resistance. The combination of EVOH with PE or PP, in a multi-layer coextrusion or co-blow molding operation, with the incorporation of adhesive tie-layers between EVOH and the polyolefins, results in structures which exhibit mechanical strength, light weight and excellent barrier properties.

The available multi-layer processing techniques require multi-layer extrusion dies, additional extruders, and appropriate adhesive tie-layers. Although multi-layer extrusion products satisfy many of the needs of packaging applications, they still involve heavy commitments in capital investment, require difficult process optimization and process control, and have limited utility in the blow-molding process.

One alternative to multi-layer extrusion could be based on the use of polymer blend systems to achieve desirable product properties. Blends have been used extensively by the plastics industry to meet some stringent requirements of performance and cost.

Polymer blend systems usually incorporate two or more polymer compositions, mixed physically together. Compatible (soluble) blends yield polymer alloys, whereas most of the commercial blends are incompatible (insoluble), representing a dispersion of one polymer in the other. The ultimate behavior of a polymer blend product will depend, to a large extent, on the microstructure of the blend, reflecting the size and configuration of the dispersed phase, and the nature of the interface between the two phases.

Research regarding the processing of polymer blends in the past has concentrated primarily on the injection-molding process and capillary extrusion. In injection-molding, the main interest has focused on improving the impact properties, determining the effect of processing conditions on weldline development, etc. In capillary extrusion, as encountered in the spinning process, the focus has been to achieve orientation of the dispersed phase in the longitudinal direction, in order to improve fiber strength in the spinning direction. The studies in capillary extrusion suggest the formation of a variety of morphologies (droplets, fibers, telescopic tubular structures, etc.), depending on the balance of composi-

tional, rheological, and processing factors.

In many instances, commercial applications of blend systems involve the extrusion of the material through more complex die geometries than encountered in capillary extrusion. Of particular commercial interest, as indicated above, are packaging and barrier applications associated with sheet extrusion and blow molding.

In light of the above, the present work has dealt with the study of the morphology and related properties of extruded sheets, based on polypropylene and ethylene vinyl-alcohol copolymer. Many of the observations associated with sheet extrusion are also of relevance for blow molding applications.

In comparison to the multi-layer coextrusion process, blending can be achieved in simple processing equipment. It removes the need for an adhesive tie-layer, although a compatibilizing agent may be required to control the quality of the interface between the dispersed and the matrix phase materials. The processing of the materials and process control are much simpler in the case of blending. Another important consideration relates to the recycling of regrind and the ultimate recyclability of the product, which are not feasible in the case of multi-layer products.

The present study is part of a larger effort to develop techniques for the evaluation and control of the morphology of polymer blend systems through processing, with emphasis on gaining a better understanding of the development of morphology during processing. This will enable the process engineer to specifically tailor the blend morphology to meet application requirements.

The main objective of this work was to evaluate the feasibility of producing a laminar structure in PP/EVOH polymer blend

systems, in which a minor amount of the EVOH high-barrier dispersed phase resin forms layers in the plane of flow. This structure would act as an effective barrier against permeant molecules, possibly comparable to the barrier obtained with the more complicated multi-layer coextrusion process.

A slit extrusion die was chosen to study the effect of processing conditions and equipment design on morphology and morphology development. The role of interfacial agents in influencing morphology and coalescence is evaluated. The influences of morphology, obtained with different compositions and processing conditions, on mechanical and processing properties, and on the permeation barrier properties are also studied and evaluated.

The thesis continues, in Chapter 2, with a general review of available emulsion theories, and significant experimental observations in dilute emulsions and polymer blend systems. Chapter 3 describes the experimental setup and morphology analysis methods employed in this study. Chapter 4 contains the results and discussion of the experimental observations, for three different PP/EVOH blend systems, with emphasis on the relationship between processing conditions and extrudate morphology. Mechanical, processing, and oxygen permeation properties are evaluated in light of the extrudate morphology. The thesis concludes with a summary of the conclusions and recommendations for future work.

CHAPTER 2

LITERATURE REVIEW

The understanding of the phenomena of deformation of droplets of one phase suspended in a continuous second phase is of great importance to the control of various polymer processing operations dealing with mixtures of immiscible fluids subjected to flow.

2.1 Emulsions

2.1.1 Theory

The flow of the dispersed phase in a matrix phase relates to the motion of viscous, incompressible liquids of small particle Reynolds numbers. The term $\rho \underline{v} \cdot \nabla \underline{v}$ in the momentum equation can be neglected, leaving the equation

$$\rho \frac{\partial \underline{v}}{\partial t} = -\nabla p + \nabla \cdot \underline{\underline{\tau}} \quad (1)$$

with the continuity equation for incompressible fluids

$$\nabla \cdot \underline{v} = 0 \quad (2)$$

where p is the viscous pressure, and \underline{v} the velocity field. For a generalized Newtonian fluid, the stress tensor, $\underline{\underline{\tau}}$, is given by

$$\underline{\underline{\tau}} = \eta (\nabla \underline{v} + \nabla \underline{v}^T) \quad (3)$$

where η is the fluid viscosity. Equation (1), however, contains the local acceleration term $\rho (\partial \underline{v} / \partial t)$, which also either vanishes (for steady-state) or is of the same order of small-

ness as $\rho \underline{v} \cdot \nabla \underline{v}$ (quasi-static motion). If this term is neglected, then

$$\nabla p = \nabla \cdot \underline{\underline{\tau}} \quad (4)$$

Equations (2) and (4) are known as the creeping-flow equations and their validity is assumed throughout the following presented theoretical approaches.

The theories discussed below are concerned with the calculation of the deformation of suspended liquid droplets. The theories are limited to plane hyperbolic, laminar shear, Poiseuille, and converging cone (extensional) flows.

When a suspension of fluid droplets is subjected to flow, the fluid stresses arising in the suspension medium tend to deform and orient the droplet. These fluid stresses may be resolved into tangential and normal components acting at the surface of a dispersed droplet. In the case of a liquid droplet, where the interface is not contaminated by impurities, the tangential stresses are continuous at the interface, so that a system of velocity gradients is established inside the droplet by internal circulation. The normal stresses, on the other hand, are discontinuous at the interface and generate a pressure difference across it given by the Laplace equation

$$\Delta p = \sigma \cdot (b_1^{-1} + b_2^{-1}) \quad (5)$$

where b_1 and b_2 are the principal radii of curvature and σ is the interfacial tension. The drop is deformed in such a way that the stresses generated by the flow are balanced by the interfacial tension.

Taylor [1,2] considered the deformation of a Newtonian droplet suspended in a Newtonian medium in uniform shear and plane hyperbolic flow (Figure 2.1). He used the general solution of the Stoke's equation of creeping motion given by Lamb [3] in

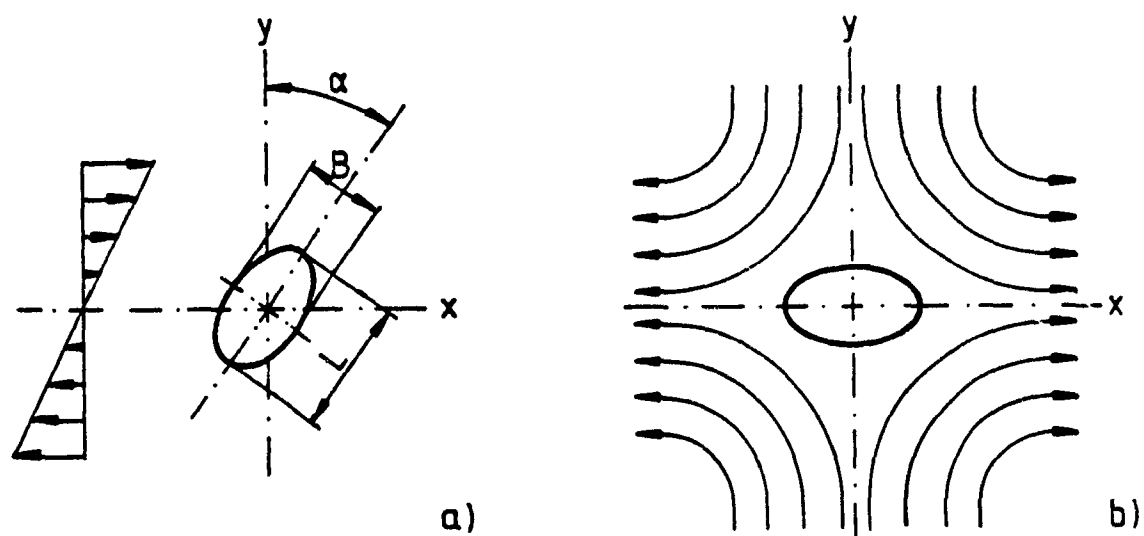


Figure 2.1 Schematic of droplet deformation:
a) uniform shear flow field; b) plane hyperbolic
flow field.

order to determine the velocity and pressure fields inside and outside the droplet. His basic assumptions were :

- 1) The drops are so small that they remain nearly spherical when deformed.
- 2) There is no slippage at the interface of the drop (tangential component of the velocity vector is continuous).
- 3) The stress tangential to the surface is continuous at the surface of the drop, so that any film which may exist between the two liquids merely transmits tangential stress from one fluid to the other. The normal stresses, on the other hand, are discontinuous at the drop interface and generate a pressure difference across the interface.

By calculating the velocities inside and outside a fluid droplet, Taylor derived the following equation for the pressure difference across an interface due to deformation in a simple shear field :

$$\Delta p_D = 4 \cdot \dot{\gamma} \cdot \eta_m \left[\frac{19\lambda + 16}{16\lambda + 16} \right] \sin(2\alpha) \quad , \quad \lambda = \frac{\eta_d}{\eta_m} \quad (6)$$

where $\dot{\gamma}$ is the shear rate, η_m the viscosity of the suspension medium, η_d the viscosity of the suspended fluid, and α the orientation angle with respect to the direction of flow. The magnitude of Δp_D changes sign in each quadrant, the droplet being subjected to alternate tensile and compressive stresses. This pressure difference generated by the flow is balanced by the interfacial tension. Thus, the drop will undergo a change in curvature to satisfy the Laplace equation, in the form

$$\sigma(b_1^{-1} + b_2^{-1}) = \Delta p_D + \text{constant} \quad (7)$$

This system of pressure differences for small deformations can be accommodated if the cross section of the equatorial plane of the droplet assumes an elliptical form, described by the polar equation

$$r = a(1 + D \cdot \sin 2\alpha) \quad (8)$$

where a is the radius of the undeformed droplet. D is the deformation in the equatorial plane defined by Taylor as (Figure 2.1)

$$D = \frac{L-B}{L+B} \quad (9)$$

In his study of deformation, D , Taylor showed that, in steady uniform shear flow, the droplet deforms into a spheroid, and the shape of the droplet depends on the viscosity ratio of the droplet phase to matrix phase, λ , and the Weber number, We , which is the ratio of the product of the local shear stress and the droplet radius to the interfacial tension. Taylor distinguished between two cases :

- a) when the interfacial tension effect dominates the viscous effect (i.e. $\lambda=O(1)$, $We \ll 1$), the droplet deformation D and the orientation angle α in the flow field are expressed as

$$D = We \left[\frac{19\lambda + 16}{16\lambda + 16} \right] \quad (10a) \quad \alpha = \frac{1}{4}\pi \quad (10b)$$

$$\text{where } We = \frac{\eta_m \cdot \dot{\gamma} \cdot a}{\sigma}, \quad \lambda = \frac{\eta_d}{\eta_m}.$$

From Equation (10a), it can be seen that over the entire range of λ from zero to infinity, $(19\lambda+16/16\lambda+16)$ varies from 1.0 to 1.187, so that D is nearly equal to We .

- b) when the viscous effect dominates the interfacial effect (i.e. $We=O(1)$, $\lambda \gg 1$), the analysis yields

$$D = \frac{5}{4\lambda} \quad (11a) \quad \alpha = \frac{1}{2}\pi \quad (11b)$$

Taylor observed experimentally that, at low rates of deformation, the experimental observation of droplet deformation agreed with his theory, in both uniform shear (parallel band apparatus) and plane hyperbolic flow (four-roller apparatus).

Chaffey and Brenner [4] tried to improve Taylor's theory and obtained second-order solutions in terms of the deformation parameter D (Equation (10)). They found in their studies that this second-order solution allowed a more refined prediction of drop behavior than does the first-order theory. In particular, in Couette flow, the angle of maximum extension, α , was always found to exceed $\pi/4$, approaching $\pi/2$ for highly viscous drops at larger deformation D . For the case that interfacial tension effects were dominant over viscous effects ($\lambda=O(1)$ and $We \ll 1$), they found that α increased with D according to

$$\alpha = \frac{\pi}{4} + \left[\frac{3}{5} + \frac{2\lambda}{5} \right] \cdot D \quad (12)$$

Cox [5] developed a first-order theory for the deformation of a droplet in a general time-dependent shearing flow field. By making a series expansion of the velocity field in terms of a perturbation parameter, thus not placing any restriction upon λ and We other than those which may be implied by the assumption that the deformation is small, he obtained theoretical expressions for the shape and orientation angle of a droplet. In his theory, Cox showed that a spherical drop, initially placed in a fluid at rest (time $t=0$) and which at $t=0$ is suddenly subjected to a constant shear rate $\dot{\gamma}$, would become spheroidal with a time-dependent deformation D' , which is always taken to be positive, and an orientation angle, α' , given by :

$$D' = D[1 - 2e^{-x}\cos(\dot{\gamma}t) + e^{-2x}]^{1/2} \quad (13)$$

$$\alpha' = \frac{\pi}{4} - \frac{1}{2} \tan^{-1} \left[\frac{19\lambda [e^{-x} \cos(\gamma t) - 1] + 20We^{-1} e^{-x} \sin(\gamma t)}{-20We^{-1} [e^{-x} \cos(\gamma t) - 1] + 19\lambda e^{-x} \sin(\gamma t)} \right] \quad (14)$$

$$\text{where } x = \frac{20\dot{\gamma}t}{19\lambda We}$$

After a long time ($t \rightarrow \infty$), the drop assumes a steady shape with a deformation and orientation angle given by

$$D = \frac{5(19\lambda + 16)}{4(\lambda + 1) [(20/We)^2 + (19\lambda)^2]^{1/2}} \quad (15)$$

$$\alpha = \frac{1}{4}\pi + \frac{1}{2} \tan^{-1} \left[\frac{19\lambda We}{20} \right] \quad (16)$$

Cox's theory reduces to Taylor's results in the limiting cases mentioned above.

When the interfacial tension, σ , is zero, the We number is infinity and the deformation is given by

$$D \approx \frac{5}{2} \frac{1}{\lambda} \sin\left(\frac{1}{2}t\right), \quad \alpha = \frac{1}{4}(\pi + t) \quad (17)$$

which represents an undamped periodic oscillation of the drop. Thus, for this case, the drop never actually attains an equilibrium deformation.

Using the method of series expansion proposed by Cox, Frankel and Acrivos [6] obtained a second-order solution in terms of a perturbation parameter for the shape of a droplet in a time-dependent shearing flow field and developed a constitutive equation for dilute emulsions based on this calculation. Their predicted droplet shape during deformation is in qualitative agreement with the first-order perturbation theory (Cox). The

numerical procedure failed to predict the droplet shape for We numbers close to those given by Taylor's approximate empirical criterion for droplet breakup.

Turner and Chaffey [7] based their droplet shape calculation on the second-order theory of Chaffey and Brenner [4], and extended the theory to hyperbolic-radial flow. Comparison with experimental data showed that although the second-order theory predicts observed deformations only qualitatively, it could be used to predict the orientation angle of the droplet. They concluded that the domain of validity of the second-order theory is where the first-order approximation is quite close to the observed deformation D.

The extensional deformation of a viscoelastic droplet suspended in a viscoelastic medium was investigated by Chin and Han [8], both theoretically and experimentally.

A theoretical analysis was carried out on the deformation of a droplet suspended in a steady extensional flow field, where both fluids may be represented by the Coleman-Noll second-order fluid model defined by

$$\underline{\underline{\tau}} = \eta_0 \underline{\underline{A}}^{(1)} + \beta (\underline{\underline{A}}^{(1)})^2 + \nu \underline{\underline{A}}^{(2)} \quad (18)$$

where η_0 , β , ν are material constants, and $\underline{\underline{A}}^{(1)}$ and $\underline{\underline{A}}^{(2)}$ are the first and second-order Rivlin-Ericksen tensors, respectively. The study took into account the effects of the elasticity, viscosity, and interfacial tension of the fluids concerned. Using a perturbation technique, they obtained a first-order solution, and thereby the following expression for predicting the droplet shape :

$$\begin{aligned} r = 1 + We \cdot Z_0 \cdot P_2(\mu) + We^2 \cdot Z_0 \cdot [Z_{01} \cdot P_2(\mu) + Z_{02} \cdot P_4(\mu)] \\ + \epsilon \cdot We \cdot [Z_1 \cdot P_2(\mu) + Z_2 \cdot P_4(\mu)] \end{aligned} \quad (19)$$

in which

$$Z_0 = \frac{2(19\lambda+16)}{16\lambda+16}, \quad Z_{01} = \frac{9\lambda^2-8\lambda+12}{28(\lambda+1)^2}, \quad Z_{02} = \frac{111\lambda+96}{126(\lambda+1)} \quad (20)$$

$r=1$ represents a sphere, and $\mu=\cos\theta$, where θ is a spherical coordinate. $P_n(\mu)$ is the Legendre polynomial of degree n , We is defined by Equation (10a), Z_1 and Z_2 are complicated functions of system parameters and ϵ is the perturbation parameter defined by

$$\epsilon = \frac{\beta \cdot \gamma_E}{\eta_0} \quad (21)$$

where γ_E is the rate of strain (elongation rate). Theoretically predicted droplet shapes at different values of Weber number, We , show that droplet deformation increases with We . The calculation of streamlines inside and outside the deformed droplet predicts an internal circulation inside the droplet, which results from the use of the boundary condition that the tangential stress is continuous at the surface of the droplet. The computational results show that the Weber number has a much greater influence on the droplet deformation than the viscosity ratio, λ , and elasticity parameter, ϵ . The authors conclude from their theoretical observations that, in steady extensional flow, the medium viscosity plays a much more important role in determining the droplet deformation than the medium elasticity and the droplet phase viscosity.

The above theoretical studies of droplet deformation are all based on the assumption of dilute emulsions. Choi and Schowalter [9] extended Cox's theory to describe the deformation of Newtonian droplets in a moderately concentrated emulsion of Newtonian liquids. To describe the complex particle interactions, the calculations were based on a cell model

approach. They obtained the deformation, D , and the orientation angle, α , of droplets in steady uniform shear flow as follows :

1) $We \ll 1$ and $\lambda = O(1)$:

$$D = We \frac{19\lambda + 16}{16\lambda + 16} \left[1 + \phi \frac{5(5\lambda + 2)}{4(\lambda + 1)} \right] \quad (22)$$

$$\alpha = \frac{\pi}{4} + We \frac{(19\lambda + 16)(2\lambda + 3)}{80(\lambda + 1)} \left[1 + \phi \frac{5(19\lambda + 16)}{4(\lambda + 1)(2\lambda + 3)} \right] \quad (23)$$

2) $We = O(1)$ and $\lambda \gg 1$:

$$D = \frac{5}{4\lambda} \left[1 + \phi \frac{25}{4} \right] \quad (24)$$

$$\alpha = \frac{\pi}{4} + \frac{1}{2} \tan^{-1} \left[\frac{19\lambda We}{20} \right] \quad (25)$$

3) $We \ll 1$ and $\lambda \gg 1$:

$$D = \frac{5(19\lambda + 16)}{4(\lambda + 1) [(20/We)^2 + (19\lambda)^2]^{1/2}} \left[1 + \phi \frac{5(5\lambda + 2)}{4(\lambda + 1)} \right] \quad (26)$$

$$\alpha = \frac{\pi}{4} + \frac{1}{2} \tan^{-1} \left[\frac{19\lambda We}{20} \right] \rightarrow 0 \quad (27)$$

where ϕ is the volume fraction of the droplets in emulsion. This theory reduces to Cox's results as the value of ϕ approaches zero.

2.1.2 Experimental

2.1.2.1 Newtonian Dispersed Phase

a) Couette Flow

Bartok and Mason [10] studied shear induced circulation and rotation of liquid droplets dispersed in a Newtonian medium and determined that the deformation of droplets agreed with Taylor's theory. Their experiments did not show any internal

circulation for perfectly spherical drops. Internal circulation was observed in larger drops ($>200\mu\text{m}$ diameter), which became visibly deformed into prolate spheroids at gradients as low as 0.1 s^{-1} . A number of experiments showed an increase in eccentricity and in the angle of orientation with increasing shear rate. As the shear rate was increased even further, the drops deviated markedly from the ellipsoidal shape and could not be described by Taylor's theory.

Bartok and Mason [11] also studied two-body interactions and explained the coalescence phenomena in uniform shear flow with a three-step mechanism. Initially, the flow must bring a pair of particles into close proximity. This "collision pair" rotates together in the shear field, remaining separated by a thin film of the continuous phase fluid. During this rotation, drainage of the intervening film by viscous flow can reduce the film thickness. If the film is reduced to a sufficiently small size so that rupture occurs before the pair of particles rotate into the next quadrants and are pulled apart by the flow field, then actual coalescence of the drops into a single particle can result. At shear rates less than 0.1 s^{-1} , a considerable fraction of the collisions result in coalescence, but, at increased shear rates, the drops separate after collision. This suggests that sufficient time of contact is required to drain the intervening film of continuous medium to such a thickness that the interaction forces could cause coalescence.

Rumscheidt and Mason [12] studied the droplet deformation and breakup over a wide range of viscosity ratios and interfacial tension values in a suspending Newtonian medium. At low gradients, a drop was deformed into a prolate spheroid initially aligned at $\alpha = \pi/4$, with both D and α increasing with γ . As the deformation increased, four distinct modes of deformation behavior were observed which depended mainly on the viscosity ratio (Figure 2.2).

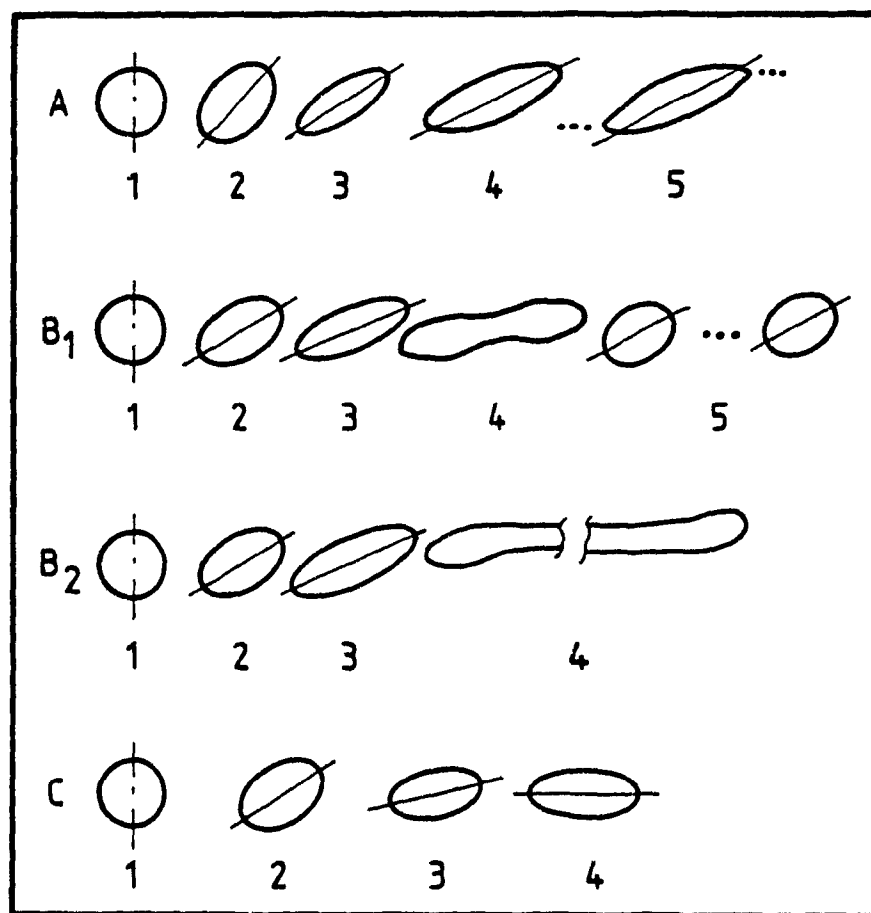


Figure 2.2 Behavior of Drops in Shear Flow up to Burst :
 Class A ($\lambda < 0.2$); Class B₁ and B₂ ($0.03 \leq \lambda \leq 2.2$);
 Class C ($\lambda > 3.8$). It was reported that the three
 classes were related to λ but that there were no
 sharp boundaries between them: [12].

Karam and Bellinger [13] investigated the influence of the viscosity ratio on droplet deformation and breakup in a suspending Newtonian medium. Their experiments showed the following results:

- i) Breakup always occurred for a viscosity range of 0.2 to 1.0.
- ii) A minimum and maximum viscosity ratio existed outside which a droplet did not burst. Irrespective of the systems studied, those limits were $4.0 < \lambda < 0.005$.
- iii) For a given drop size, breakup occurred at the lowest shear rate, in the system having the lowest interfacial tension.
- iv) The higher the was viscosity of the continuous phase, the greater was the ease of breakup of the liquid drop.
- v) The ease of breakup for any given component combination was a function of drop radius; the smaller was the drop, the higher was the shear rate needed to break it up.

In comparing their experimental results with the theory developed by Taylor, they found that the deformation D varied linearly with the shear rate even for larger deformations than expected and concluded from their results that other forces acting on a highly deformed liquid droplet linearize the theory over a greater deformation range. Table 2.1 gives a summary of breakup phenomena observed by Karam and Bellinger.

Torza, Cox and Mason [14] experimentally measured droplet deformations, D , in a Newtonian medium and found that their results agreed fairly well with Equation (15). Deformation data were in good agreement with Equation (10a) for small λ , and with Equation (11a) for large λ . This suggested that Equation (15), which contains Equations (10a) and (11a) as limiting cases, describes D more completely than Taylor's equations, especially for systems with intermediate values of the viscosity ratio λ . They also observed that droplet breakup occurred most readily when the viscosity ratio was in the range




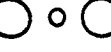







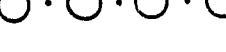


Karam and Bellinger [13] investigated the influence of the viscosity ratio on droplet deformation and breakup in a suspending Newtonian medium. Their experiments showed the following results:

- i) Breakup always occurred for a viscosity range of 0.2 to 1.0.
- ii) A minimum and maximum viscosity ratio existed outside which a droplet did not burst. Irrespective of the systems studied, those limits were $4.0 < \lambda < 0.005$.
- iii) For a given drop size, breakup occurred at the lowest shear rate, in the system having the lowest interfacial tension.
- iv) The higher was the viscosity of the continuous phase, the greater was the ease of breakup of the liquid drop.
- v) The ease of breakup for any given component combination was a function of drop radius; the smaller was the drop, the higher was the shear rate needed to break it up.

In comparing their experimental results with the theory developed by Taylor, they found that the deformation D varied linearly with the shear rate even for larger deformations than expected and concluded from their results that other forces acting on a highly deformed liquid droplet linearize the theory over a greater deformation range. Table 2.1 gives a summary of breakup phenomena observed by Karam and Bellinger.

Torza, Cox and Mason [14] experimentally measured droplet deformations, D , in a Newtonian medium and found that their results agreed fairly well with Equation (15). Deformation data were in good agreement with Equation (10a) for small λ , and with Equation (11a) for large λ . This suggested that Equation (15), which contains Equations (10a) and (11a) as limiting cases, describes D more completely than Taylor's equations, especially for systems with intermediate values of the viscosity ratio λ . They also observed that droplet breakup occurred most readily when the viscosity ratio was in the range

Table 2.1 Breakup of Droplets [13].

Deformation Prior To Break-Up	Deformation After Break-Up	Viscosity Ratio λ	Deformation Prior To Break-Up
		.03 - .3	.60 - .83
		.3 - 4.0	.70 - .93
		.005 - 3.0	.90 - .97
			
			
			
			
			
			
	No Break-Up	> 4.0	.10 - .36
	No Break-Up	< .005	

of 0.3-0.9, and that it did not occur at all when the ratio was greater than 3.0. Thus, they concluded that their results confirmed the theory of transient and steady deformation developed by Cox. This theory has the advantage that no limitations are imposed on λ and We other than those implied by $D' \rightarrow 0$.

Gauthier, Goldsmith and Mason [15] studied deformable droplet motions in non-Newtonian media. They found that, for drops in a pseudoplastic liquid, the linear relationship between D and $\dot{\gamma}$ does not hold. They explained this behavior by the dependence of the matrix viscosity on shear rate, which results in a higher viscosity ratio λ and, hence, deformation D for increasing shear rate.

Migration studies for both viscoelastic and pseudoplastic liquids revealed that fluid drops migrated away from the cylinder walls towards an equilibrium position. The position of equilibrium itself was dependent on $\dot{\gamma}$ and $a/(R_2 - R_1)$, where R_1 and R_2 are the inner and outer radii of the Couette apparatus, respectively. The equilibrium position is closer to the inner cylinder for drops suspended in a pseudoplastic liquid and closer to the outer cylinder for drops in a viscoelastic medium.

In an attempt to clarify the influence of normal stresses on droplet behavior, Elmendorp and Maalcke [16] studied non-Newtonian systems. Throughout the study, care was taken to use only systems with equal interfacial tension. A matrix exhibiting viscoelastic behavior caused droplet deformation to increase less at higher rates than at lower ones, due to a decreasing viscosity with increasing shear rate. The experiments showed that normal stresses exhibited by the matrix tended to increase the deformation by destabilizing the droplets.

b) Pressure-driven Flow:

The behavior of deformable particles in non-uniform shear flow, Poiseuille flow for example, differs from that in uniform shear flow. The velocity gradient varies with radial distance in Poiseuille flow, while it is constant in uniform shear flow. As a result of this velocity gradient, it is expected that droplet deformation will vary depending on the location of the droplet in the plane of shear. In polymer processing, droplet deformation in Poiseuille flow and/or extensional flow fields is of greater importance than in uniform shear flow.

Goldsmith and Mason [17] found that deformable droplets, suspended in a Newtonian medium, migrated towards the tube axis during flow, the rate of migration increasing with increasing drop radius, flow rate, and radial distance. Apart from this migration across the planes of shear, the behavior of the droplets was similar in all respects to that observed in Couette flow.

Goldsmith and Mason explained the mechanism of axial migration of deformable drops by calculating the net radial force acting on a particle as a result of variation of $\dot{\gamma}$ across the drop. The drop, shown in Figure 2.3, experiences compressive and tensile forces normal to its surface, and the calculation of the net force acting upon the drop yields

$$F_{rr} = - \frac{5 \pi^2 k a^3 \eta_m D}{2(\lambda+1)} \left[\left(1 + \frac{2\lambda}{5}\right) \left(\lambda + \frac{3}{5}\right) - \frac{1}{4} \left(\lambda + \frac{6}{5}\right) \right] \quad (28)$$

where k is a function of the volumetric flow rate \dot{Q} .

$$k = \frac{4 \dot{Q}}{\pi R^4} \quad (29)$$

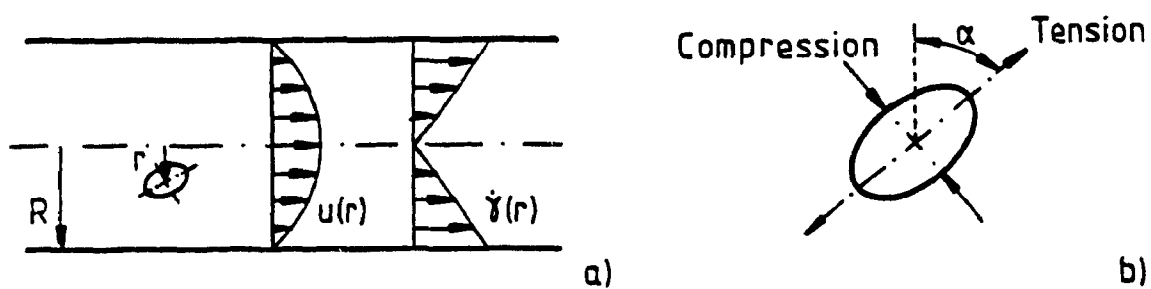


Figure 2.3 Deformed Fluid Drop in an Emulsion undergoing Poiseuille Flow.
 a) Coordinates b) Forces acting on Drop

This net force pushes the drop to a region of lower gradient. When $D = 0$, as in the case of a rigid sphere, $F_{rr} = 0$, thus accounting for the observed difference in behavior between rigid and deformable particles. Likewise, $F_{rr} = 0$ when $k = 0$, as in Couette flow, and hence there is no tendency to migrate across the planes of shear.

For Poiseuille flow, Gauthier, Goldsmith and Mason [18] reported that drops suspended in a pseudoplastic liquid underwent a two-way migration. Drops initially close to the tube axis migrated towards the wall, and those initially close to the wall migrated towards the axis. The migration rates in both directions decreased with time until an equilibrium position was reached, which at a given drop radius, a , depended on the flow rate, \dot{Q} , and, at a given \dot{Q} , depended on a . In viscoelastic fluids, only migration towards the tube axis occurred, the equilibrium position being at $R=0$. The rates of migration increased with increasing particle size and flow rate.

The authors concluded qualitatively that the migration of liquid drops in pseudoplastic and viscoelastic emulsions could be accounted for by assuming that there is a superposition of the particle radial velocities due to the non-Newtonian properties of the suspending fluids on those due to wall interactions of the deformable drops.

V.d.Reijden-Stolk and Sara [19] studied droplet deformations in a converging cone. In such a system, the elongational rate is not constant, but increases along the direction of flow. The experimental results showed that Cox's theory [5], applied for a simplified, linearized flow field in the converging cone, predicted the drop deformation quite well, even for higher deformations. For $D > 0.2$, the predicted shape was not ellipsoidal anymore, while the measured deformed droplets always had an ellipsoidal shape. Comparison of the experimental results with the theoretical calculations from the second-

order theory, given by Frankel and Acrivos [6], seemed to indicate that deformation in elongational flow could be described better by a first-order theory.

Table 2.2 summarizes the experimental results for the Newtonian dispersed phase. The results by Karam et al. [13] for droplet breakup in a Newtonian matrix agree with those of Mason and co-workers [14]. The droplet deformation behavior in a Newtonian matrix in Poiseuille flow is similar to that encountered in Couette flow. In a non-Newtonian matrix, the deformation behavior is influenced by the normal stresses of the matrix phase.

2.1.2.2 Non-Newtonian Dispersed Phase

a) Couette Flow

Gauthier, Goldsmith and Mason [15] observed that the deformation of pseudoplastic drops in a Newtonian liquid followed Equation (10), and the angles of orientation followed Equation (12). The measured deformation of viscoelastic drops, while still a function of $\dot{\gamma}a$, was lower than predicted by Cox's theory [5], which was developed for a Newtonian drop suspended in a Newtonian medium. The authors speculated that this behavior may be due to the existence of normal stresses and/or elastic recovery of the liquid inside the drops, which act to decrease the deformation.

Bartram, Goldsmith and Mason [20] studied the transient deformation and burst of drops in a viscoelastic medium in the absence of interfacial tension. For viscoelastic drops with $\lambda > 1$, the initially spherical drop became extended vertically into a cylindrical shape. As the longitudinal deformation continued, the thread buckled, which resulted in the formation of thin threads which finally broke up into discrete daughter drops. Although the time to burst in a given system decreased with increasing shear rate, the mode of extension of the drop

Table 2.2 Droplet Deformation and Breakup Behavior for a Newtonian Dispersed Phase as a Function of Flow Field and Matrix Phase Fluid.

Author	Flow Field	Matrix Phase	Droplet Behavior
Mason [10]	Couette	Newtonian	spheroid; $f(\dot{\gamma})$
Mason [12]	Couette	Newtonian	low $\dot{\gamma}$: spheroid high $\dot{\gamma}$: four modes of breakup - $f(\lambda)$
Karam [13]	Couette	Newtonian	breakup: $0.2 < \lambda < 1.0$ no breakup: $4.0 < \lambda < 0.005$
Mason [14]	Couette	Newtonian	breakup: $0.3 < \lambda < 0.9$ no breakup: $\lambda > 3.0$
Mason [15]	Couette	pseudo-plastic	migration towards center (equil.: near inner cyl.)
		visco-elastic	migration towards center (equil.: near outer cyl.)
Maalcke [16]	Couette	visco-elastic	normal stresses destabilize droplet
Mason [17]	Poiseuille	Newtonian	migration towards tube axis
Mason [18]	Poiseuille	pseudo-plastic	two-way migration (equil.: middle axis/wall)
		visco-elastic	migration towards equil. at tube axis
Sara [19]	converging cone	Newtonian	ellipsoid

and final burst were identical. This was the first detailed observation that a viscoelastic droplet was not deformed into an ellipsoid in the plane defined by the flow and velocity gradient direction, as predicted by all previous theories. For $\lambda < 1$, the measured deformation, D' , and orientation angle, α' , were greater than the values predicted by theory [5]. For pseudoplastic drops the deformation and burst of the drops was found to be independent of the viscosity ratio. When suddenly sheared, the initially spherical drop deformed into an ellipsoid from which continuous threads of liquid were withdrawn from the pointed ends. Thus, the drop, while retaining its ellipsoidal shape, gradually diminished in size with time.

For viscoelastic droplets in Newtonian matrices, Elmendorp and Maalcke [16] found that, although the viscosities of a pair were equal, the solution having the higher normal stresses exhibited the smaller deformation. In addition, breakup shear rate data showed that droplets exhibiting the higher normal stresses were the most stable.

b) Pressure-driven Flow

Han and Funatsu [21] studied the deformation and breakup phenomena of single viscoelastic droplets suspended in a viscoelastic medium (viscosity ratio $\lambda < 1$) in flows through converging and uniform channels. The experiments showed that the droplets were drawn out in the entrance region into long threadlike cylinders at high shear rates (Figure 2.4). While single droplets were elongated in the converging section, they subsequently recoiled and yielded less elongated droplets. The recoil might be attributed to either the relaxation of the stresses built up in the entrance region or interfacial tension effects or both. Concerning the droplet breakup phenomena the authors drew the following conclusions: i) viscoelastic droplets may be considered to be hydrodynamically more stable than Newtonian droplets; ii) the critical shear rate for drop-

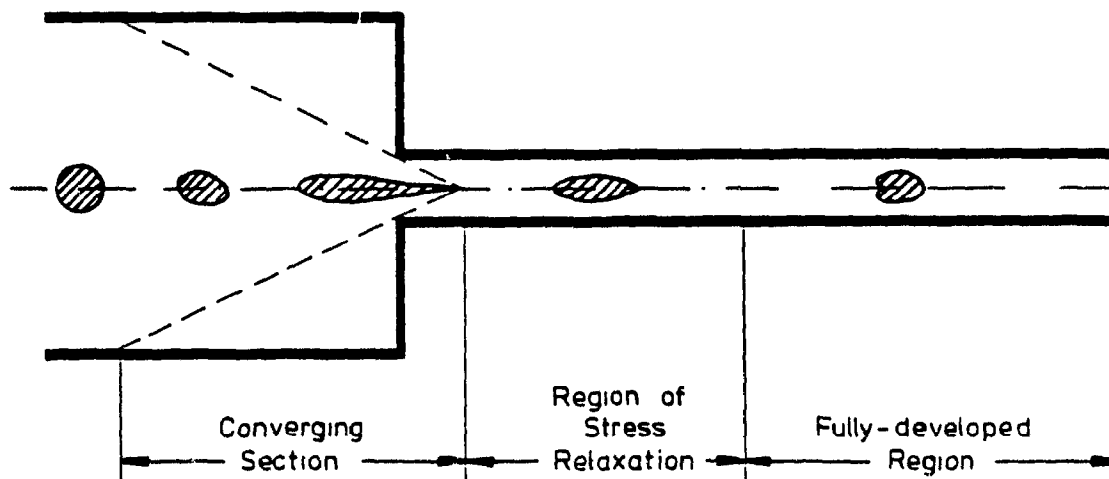


Figure 2.4 Schematic of the Droplet Deformation Process that would occur in the entrance and fully developed regions for a viscoelastic drop suspended in a viscoelastic fluid [21].

let breakup will be lower with a high viscosity suspending medium than with a low viscosity suspending medium; and iii) droplet breakup occurs while the droplet, elongated into a thread-like form in the entrance region, recoils in the region of stress relaxation.

Chin and Han [8] designed a flow channel consisting of a reservoir section, a conical section, and a straight cylindrical tube section (Figure 2.5). This flow channel provided extensional flow along the centerline in the conical section, and Poiseuille flow in the tube section. For a viscoelastic droplet suspended in a viscoelastic medium ($\lambda < 1$), their experiments showed that larger droplets gave rise to a greater deformation than smaller droplets. The higher the shear rate, the greater was the droplet deformation. The high viscosity medium yielded a greater deformation of the droplet than the low viscosity medium. The theoretically predicted deformation (Equation (19)) was in good agreement with the experimental observations only at low values of We , and deviated considerably at larger values of We . As We increased, the theoretically predicted droplet developed a pinch at the center along the major axis, thus resembling a dumbbell. However, no such dumbbell shape was observed during the experiments (Figure 2.6).

Chin and Han [22] attempted to determine the role of fluid elasticity on droplet breakup. Their observations seemed to indicate that droplet breakup depended very much on the medium viscosity. Breakup always occurred after the long, thread-like liquid cylinder passed through the entrance section of the cylindrical tube and started to recoil. The authors attributed the breakup of the extended long liquid cylinder to the change of fluid velocity in the entrance region, namely, from the time-dependent (i.e., accelerative) extensional flow to the Poiseuille non-uniform shear flow. From their experiments, the authors concluded that the greater the interfacial tension, the less likely the occurrence of breakup. The greater the

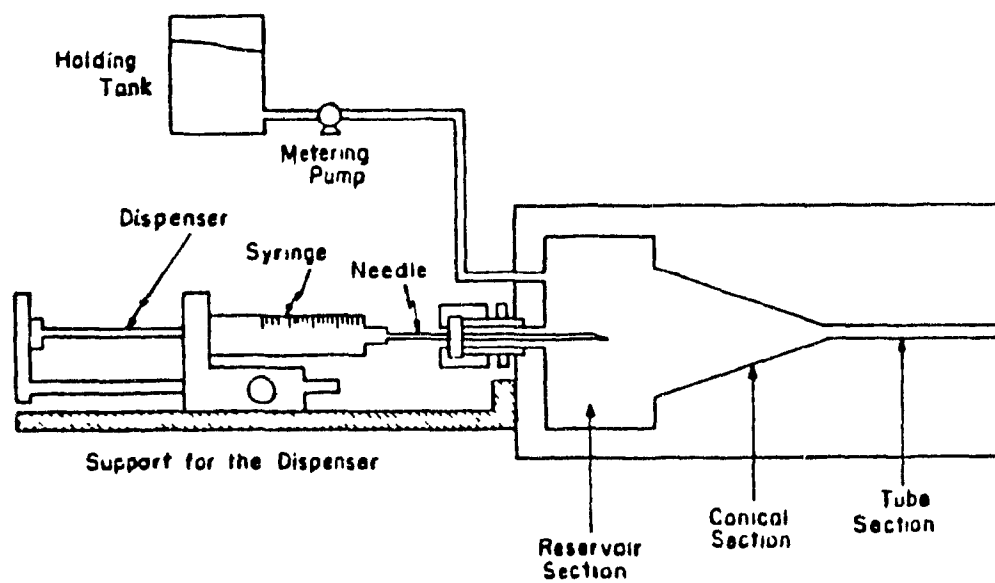


Figure 2.5 Schematic Layout of the Experimental Apparatus [8].

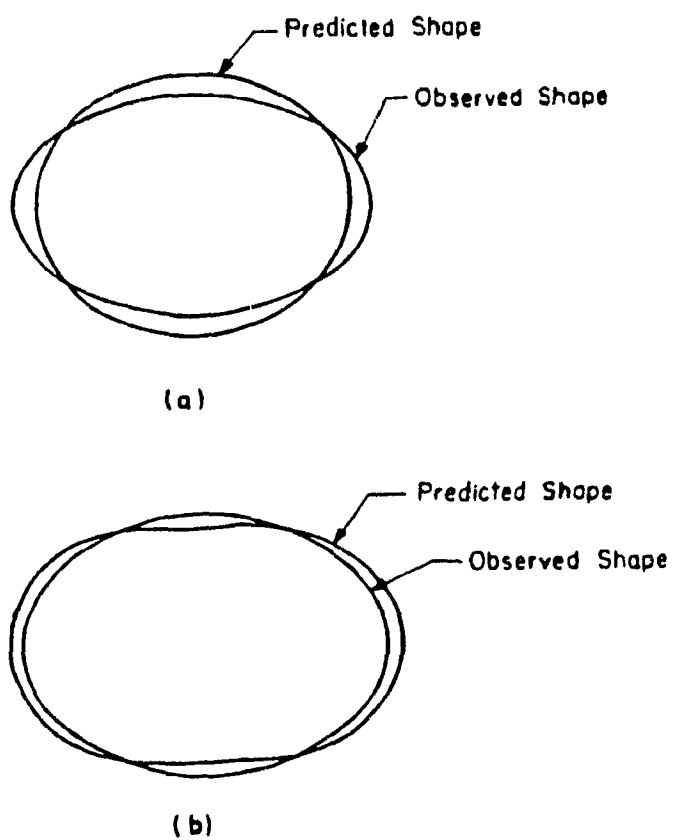


Figure 2.6 Comparison of the theoretically predicted droplet shape with the experimentally observed one [8]:
a) $\lambda=0.037$, $We=0.067$, $\dot{\gamma}_E=0.0042\text{sec}^{-1}$
b) $\lambda=0.055$, $We=0.19$, $\dot{\gamma}_E=0.024\text{sec}^{-1}$

elasticity of the droplet phase, the less likely was the occurrence of breakup, because the droplet phase elasticity had the same effect as the interfacial force, i.e. to resist deformation and hence breakup.

Table 2.3 presents a summary of the experimental results for the non-Newtonian dispersed phase. The results show that, even under uniform shear conditions, a viscoelastic droplet, suspended in a viscoelastic medium, can be deformed into a long, thin fiber.

2.2 Polymer Blends

Blend morphology (or sometimes microstructure) is understood as the spatial arrangement of the blend component phases. Three different morphologies may be identified : disperse, stratified (lamellar, sandwich), and co-continuous phases (interlocked). The morphology in a molten polymer blend is the result of the viscosity ratio (size) and elasticity ratio (shape) of the phases, which depend on the stress (or shear rate) level, as well as on the initial size of the components (melt mixing process). The rheological properties of the bulk of a two-phase system depend partly on size, size distribution, and the shape of the discrete phase droplets dispersed in the continuous matrix phase. The stability of the morphology is influenced by thermodynamics and interface dynamics. In multiphase polymeric systems, many variables interact to control the ultimate mechanical / physical properties of the finished product (Figure 2.7).

In the following sections, an attempt is made to summarize theoretical and experimental results regarding the factors influencing the morphology of polymer blends.

Table 2.3 Droplet Deformation and Breakup Behavior for a Non-Newtonian Dispersed Phase as a Function of Flow Field and Matrix Phase Fluid.

Author	Flow Field	Dispersed/ Matrix Phase	Droplet Behavior
Mason [20]	Couette	viscoel./ viscoel.	$\lambda > 1$: long cylinder (thin threads) $\lambda < 1$: spheroid
Maalcke [16]	Couette	pseudopl./ viscoel.	deformation and burst $\neq f(\lambda)$
Han [8,21]	converging cone and cylindrical tube	viscoel./ viscoel. ($\lambda < 1$)	elongation into cylinder in converging cone and recoil with breakup in cylindrical tube

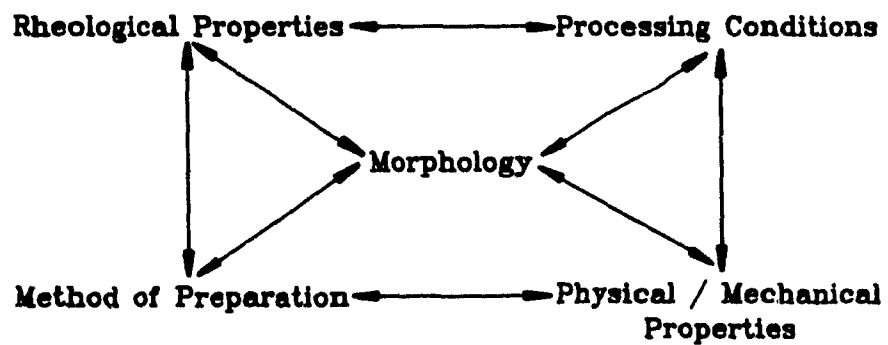


Figure 2.7 Schematic of Processing-Morphology-Property Interactions in Dispersed Multi-Phase Polymeric Systems.

2.2.1 Theory

In order to understand the type of dispersion achieved in flow when both phases are viscoelastic fluids, such as polymer melts, VanOene [23] developed a rheo-thermodynamic theory. VanOene attempted to characterize the dispersion in terms of droplet size, interfacial tension, and differences in the viscoelastic properties of the two components. He based his theoretical approach on the concept of "elastic free energy". In general, the recoverable free energy of deformation is a function of the state of flow; when the state of flow of a fluid element changes, its free energy of deformation will change accordingly. In binary mixtures, or heterogeneous viscoelastic fluids, a change in the state of deformation of the composite fluid can be brought about by a certain mode of dispersion during flow.

In his approach, VanOene argues that in a two-phase system, however, a possible mode of relaxation of the free energy of deformation is conversion into interfacial free energy. If the contribution to the free energy of deformation by internal circulation is neglected, the deformation of a droplet of a fluid α , with a larger first normal stress difference than the matrix liquid β , should result in a free energy decrease of

$$\Delta F = \frac{1}{2} [N_{1\alpha} - N_{1\beta}] \quad (30)$$

where $N_{1\alpha}$ and $N_{1\beta}$ are the first normal stress differences in fluids α and β , respectively. If this decrease in free energy is recovered by formation of interfacial free energy, one obtains for the formation of n droplets of radius 'a'

$$n 4\pi a^2 \sigma_{\alpha\beta} = n \frac{1}{2} [N_{1\alpha} - N_{1\beta}] \frac{4}{3} \pi a^3 \quad (31)$$

which formally can be regarded as the viscoelastic contribution to the interfacial tension $\sigma_{\alpha\beta}$. Taking the equilibrium interfacial tension in the absence of flow, $\sigma_{\alpha\beta}^0$, into account, the complete expression for the interfacial tension in flow is therefore

$$\sigma_{\alpha\beta} = \sigma_{\alpha\beta}^0 + \frac{1}{6} a [N_{1\alpha} - N_{1\beta}] \quad (32)$$

The interfacial tension is a positive quantity, hence Equation (32) is only satisfied when i) $[N_{1\alpha} - N_{1\beta}]$ is positive or ii) $\sigma_{\alpha\beta}^0 > 1/6 \cdot a \cdot [N_{1\alpha} - N_{1\beta}]$. When these conditions are satisfied, a droplet of phase α may be formed in phase β . The interfacial tension for a droplet of phase β in phase α can be expressed as

$$\sigma_{\beta\alpha} = \sigma_{\alpha\beta}^0 - \frac{1}{6} a [N_{1\alpha} - N_{1\beta}] \quad (33)$$

Hence, for a certain droplet size, $\sigma_{\beta\alpha}$ must be zero. Only droplets smaller than this critical size are stable.

VanOene points out that a number of definite predictions follow from his analysis :

- i) If it is observed that phase β stratifies (i.e., does not form droplets) in phase α , then phase α will form droplets in phase β .
- ii) If a particular morphology is observed, it should not be influenced by the magnitude of the shear rate or by raising the temperature of extrusion, except for effects which can be attributed to the hydrodynamic stability of a particular mode of dispersion.
- iii) Changes in the molecular weight and the molecular weight distribution of the components can be used to verify the predictions that the phase with largest normal stress functions will form droplets.

The theory of Cox [5] has shown that the relevant parameters governing the deformation of fluid drops are the viscosity ratio λ , and the parameter We , which is the ratio of the shear stress and the interfacial tension. Since the viscosity is independent of the elastic properties of the material, the elastic properties can only have a direct influence through the parameter We . VanOene's analysis of the free energy changes in droplet formation provides a criterion for the process of formation itself, but not for the precise state of deformation of such droplets in flow.

2.2.2 Morphology

2.2.2.1 Effect of Flow Field

a) Rotating Parallel or Cone-and-Plate Geometry

Starita [24] studied blend systems of atactic polystyrene and linear polyethylene to establish a basis for predicting the microstructure of a blend from the knowledge of the mixing history and the rheological properties of the constituents. Mixing was achieved in a normal stress extruder, where the flow was due to torsional shear between parallel plates and material is transported radially across the flow field. Four different composition ratios (20, 40, 60, and 80wt%) were used. Starita structured his results, based on the rheological properties of the minor component, into three main groups. When the viscosity and elasticity of the minor component are: a) greater than those of the major component, the minor component is coarsely dispersed; b) smaller than those of the major component, the minor component is finely dispersed; and c) the same as the major component, the minor component is finely dispersed, no matter which component is the minor phase.

A PMMA/PS blend system was mixed, by Chuang and Han [25], using a twin-screw compounding machine. Subsequently, samples

were compression molded into disks for rheological investigations with a cone-and-plate rheometer. For this blend system, the viscosities cross over as shear rate increases. The viscosity ratio varied between 0.5 and 2.0 over the range of shear rates investigated. On the basis of studies employing transmission electron microscopy, Chuang and Han made the following observations: i) the blend composition determines the state of dispersion; ii) for the PS/PMMA 10/90 blend, considerable breakage of the PS droplets occurs while the specimen is subjected to a steady shearing motion; iii) the state of dispersion of the PS/PMMA 50/50 blend becomes very complex; both PS and PMMA phases form continuous phases, and in each continuous phase one component is dispersed into the other; and iv) for the PS/PMMA 70/30 and 90/10 blends, the dispersed PMMA phase gives rise to elongated droplets.

Dreval et al. [26] have studied the deformation of melts of mixtures of linear low density polyethylene (LDPE) and PS. The polymers had different viscosities, but similar elasticity moduli. The results indicate that fibril formation in melts of mixtures of incompatible polymers in a uniform shear field takes place upon reaching a certain shear stress. A lower ratio between the viscosities of the fibril-forming polymer and the matrix component is associated with a lower shear stress. For pronounced fibril formation to take place in a uniform shear field, the melt has to be deformed, in some cases over a long period of time, to attain steady flow. The authors conclude that a decisive role is played by the ratio of viscosities rather than elasticities of the components, since the viscosities of polymers are high and may vary by several orders of magnitude, while elasticities vary only within one order of magnitude.

The results for the rotating parallel or cone-and-plate geometry are summarized in Table 2.4. The results of Han et al. [25] and Dreval et al. [26] are in agreement with observations

Table 2.4 Dispersed Phase Morphology of different Polymer Blend Systems for Rotating Parallel or Cone-and-Plate Geometry.

Author	Blend	Viscosity Ratio	Dispersed Phase Morphology
Starita [24]	PE/PS	$\lambda > 1$ $\lambda < 1$ $\lambda = 1$	coarse distribution fine distribution fine distribution
Han [25]	PS/PMMA	$0.5 < \lambda < 2.0$	dependent on composition PS : droplet breakup PMMA : elongated droplets
Dreval [26]	PE/PS	$\lambda < 1$ $\lambda > 1$	long PE fibers long PE fibers

for dilute emulsions (Mason et al. [20]), and show that a uniform shear field can be effective in orienting the dispersed phase in the matrix phase.

b) Capillary Flow

To verify his theoretical conclusions, VanOene [23] studied PS/PE blends, in four mixing ratios (10,30,70, and 90wt%), in a capillary rheometer equipped with a static mixer. Since neither shear rate, residence time in the capillary, nor temperature had a marked influence on the morphology of the extrudate, VanOene argued that the various structures must arise from parameters that depend on the radial position in the capillary, but are independent of the length.

Han and Yu [27,28] investigated the flow behavior and morphology of blends of high density polyethylene (HDPE) and polystyrene (PS) (ratios 10,20,50,80, and 90wt%). Photomicrographs of the extrudate cross section showed a vortex at the center position. The material forming the vortex was determined by the melt viscosities. A finer dispersion appeared to occur near the center rather than near the wall. Photomicrographs, for a system with a viscosity ratio $\lambda < 1$, in the longitudinal direction showed that the discrete phase formed long fibers or droplets in the continuous phase. Han and Yu concluded from their results that mixtures of two polymers, known to be incompatible in the molten state, exhibit a dispersed phase flow when fed to circular tubes or ducts of any arbitrary cross section. It seemed unlikely to the authors, therefore, that two incompatible polymers, when fed as a blend, would ever result in stratified flow.

Han, Kim and Chen [29] studied the effect of mixing on the modes of dispersion of a PS/PP blend system in three blending ratios (25,50,75wt%). A static mixer, downstream from a single screw extruder, and a twin-screw compounding machine were used

as mixing devices. When only a single screw extruder was used, the micrographs showed that the PS phase (25 and 50wt% , $\lambda = (\eta_{PS}/\eta_{PP}) > 1$) formed long fibrils in the longitudinal direction, and droplets, fibers, or agglomerates in the cross section located in the continuous PP phase. When a static mixer, together with the single screw extruder, was used, the PS phase (for all three blending ratios) formed particles of well defined shape in both sections. The authors attributed the improvement in mixing to the breakup of long fibrils of the dispersed phase, as the molten polymer passed through the stationary mixing elements. Photomicrographs of samples obtained with the twin-screw compounding machine showed that the dispersion in this case was more coarse, closer to an interpenetrating network than that obtained with a single screw extruder plus static mixer.

Danesi and Porter [30] used a single screw extruder with a static mixer to prepare blends of isotactic polypropylene (PP) and ethylene-propylene rubbers (EP), where the viscosity of each rubbery component was larger or equal to the viscosity of the polypropylene component, i.e. $\lambda = \eta_{EP}/\eta_{PP} < 1$ or $= 1$. Their results showed that the dispersion characteristics of the phases were influenced by the difference between the melt viscosity of the components. Blends with a greater disparity in the melt viscosity of the constituents showed a greater variation of the microstructure with composition. For the same processing history, a melt viscosity of the minor component lower than, or equal to, that of the major component brought about a finer and more uniform dispersion than for a minor component with a higher melt viscosity. Fully developed laminar flow and low swelling facilitated the development of highly oriented structures in the extrusion direction. Orientation was higher when the minor component had a melt viscosity lower than, or equal to, that of the major component. High values of shear stress and swelling brought about telescopic or composite structures of the dispersed phase, depending on the

type of flow experienced by the blend during extrusion.

Vinogradov, Tsebrenko et al. [31,32,33] have used mixtures of polyoxymethylene (POM) and copolyamide (CPA) as model systems for studying the formation of ultrathin fibers, tubular membranes, and films during flow. In general, the viscosity ratio $\lambda = \eta_{\text{POM}} / \eta_{\text{CPA}}$ is < 1 or ≈ 1 , for the systems under study. The results show that the fibrillation takes place by stretching of POM particles in the direction of the stream. Coalescence is the necessary prerequisite for producing long uniform continuous fibers. Rapidly freezing the whole capillary shows that fibrillation takes place in the entrance zone (Figure 2.8, A), and is due to the effect of elongational stresses which extend and coalesce the POM particles in the direction of the streamlines. In the zone adjacent to the entrance to the capillary, the streamlines form concentric, cone-like funnels in which the fibrillation is very pronounced. The stream narrows sharply (Figure 2.8, B), and at a definite distance from the entrance (Figure 2.8, C) the influence of the walls becomes manifest, leading to the intensive development of shear and retardation of the stream. This results in shrinkage (enlargement of diameters) of the fibrils and loss of parallelism. In the zone of shear flow, the fibrils become parallel once again (Figure 2.8, D).

In the above work, the formation of ultra-thin fibers was most pronounced when very short capillaries were used. With large diameter capillaries (i.e., with small reservoir to capillary diameter ratio), fibers might not be obtained at all. The microstructure of the extrudates was greatly affected by the shear stress. With increasing τ , the mean diameter of POM fibers decreased. Layers of POM fibers were observed, and these layers were found in regions close to the capillary walls. When the stream was cooled, bundles of continuous fibers enclosed in a thin fibrous film were observed in the axial direction. Intensive swelling enhanced the formation of concentrically arranged tubular membranes. At high values of

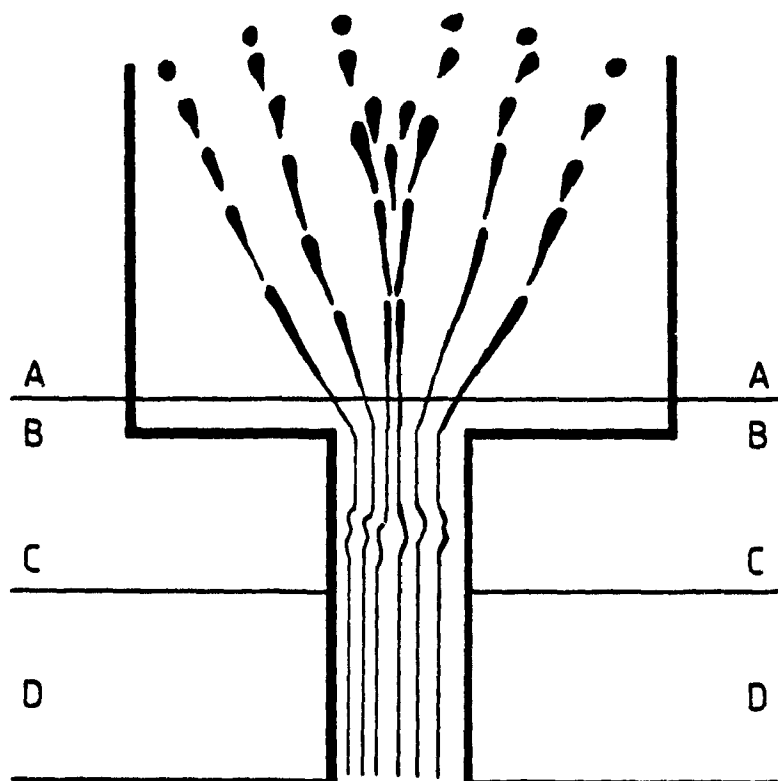


Figure 2.8 Representation of the Fibrillation Process in the entrance zone and in the duct [32].

shear stress, telescopic structure was observed.

Krasnikova et al. [34] investigated a PP and PS mixture (33/67vol%), in which the viscosities of PP and PS were close to each other. Morphological analysis revealed that the formation of samples under conditions providing fewer possibilities of relaxation, such as low ambient temperature at the capillary outlet, decrease in the capillary length, or increase in the shear strain, gave rise to thinner PP fibrils arranged in layers in the PS matrix.

Tsebrenko et al. [35] studied the microstructure of polymer blends of POM and ethylene vinyl-acetate copolymer (CEVAc) (20/80wt%). When the viscosity ratio, $\lambda = \eta_{\text{POM}} / \eta_{\text{CEVAc}}$, was 1.32 and 1.05, continuous POM microfibers (of unlimited length) were the only structure in the blend extrudates; fiber formation was manifested most distinctly at a ratio of 1.32. Blends containing more viscous POM melts revealed that defective fibers were formed consisting of a large number of POM particles. The content of such fibers reached 50 percent if the viscosity ratio was 4.3. If the viscosity ratio was near unity, a slight decrease in the shear stress led to an increase in the average diameter of fibers, the formation of films, and a decrease in the total number of fibers.

Alle and Lyngaae-Jorgensen [36,37,38] used blends of isotactic polypropylene (PP) and high density polyethylene (HDPE), prepared and pelletized in three mixing ratios (25/75, 50/50, and 75/25wt%) in a single screw extruder. Melt flow properties and the influence of flow behavior on morphology were determined using a capillary rheometer. Based on the analysis made by Han and Funatsu [21], and Vinogradov et al. [32], the authors analyzed two possible cases (Figure 2.9). In two-phase flow through a capillary, the average velocity of the high viscosity polymer phase is smaller than that of the low viscosity polymer phase. Thus, the high viscosity phase experiences less

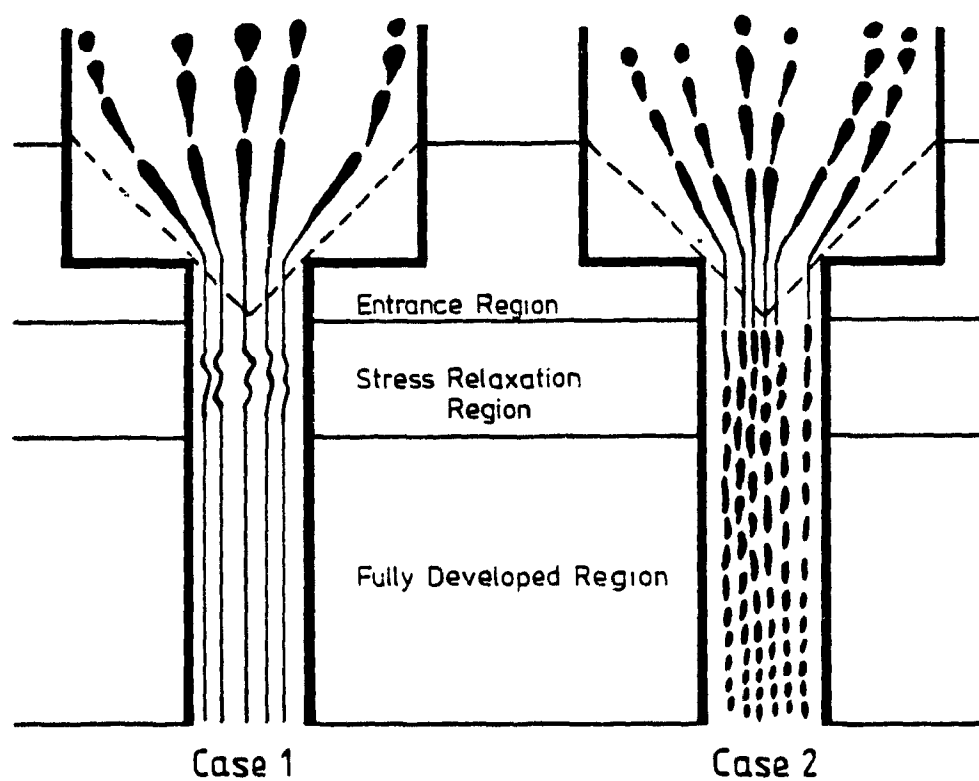


Figure 2.9 Empirical model representation of Molten Two-Phase Dispersed Polymer Blend flowing through a Capillary [37].

elongational deformation at the entrance region, and consequently, retracts less than the low viscosity phase in the capillary. The opposite will occur for the low viscosity phase. This phase experiences larger elongational deformations at the entrance and contracts more in the capillary. Therefore, the dispersed droplets of a high viscosity minor component survive in the surrounding low viscosity medium (Case 1), and flow as stable threads or fibers in the fully developed laminar flow region. In contrast, the dispersed droplets of a less viscous minor component are bound to breakup into smaller droplets in the surrounding high viscosity medium (Case 2). These smaller droplets would break up further, with a possible tendency to migrate towards the tube axis in the fully developed flow region.

White and co-workers [39] studied the development of phase morphology of polymer blends in mixing and extrusion. They investigated three different blend systems: HDPE/PS, HDPE/PC, and HDPE/N6, in five mixing ratios (90/10, 70/30, 50/50, 30/70, and 10/90wt%). The polymers were blended and pelletized using a single screw extruder with static mixer, followed by extrusion through a capillary. Morphological investigations of samples from the static mixer showed the degree of coarseness of HDPE in continuous and dispersed matrices to be in the order N6>PC>PS. This was attributed to different interfacial tension levels of the three blends but no data were presented. In the HDPE/PS blend system, increasing shear stress caused the dispersed phase to become finer in the outer layers of the extrudate, but it remained coarser near the centerline. This was most likely due to the fact that the high stress would occur only in the outer regions of the capillary. Morphology strongly depended on the viscosity ratio, λ ($=\eta_d/\eta_m$): $\lambda < 0.7$ uniform filamentous morphology; $0.7 < \lambda < 1.7$ undulant fibers or rods; $\lambda > 2.2$ undeformed droplets (Figure 2.10).

White and co-workers did not see any direct evidence of VanOene's [23] argument that incompatible blend morphology is

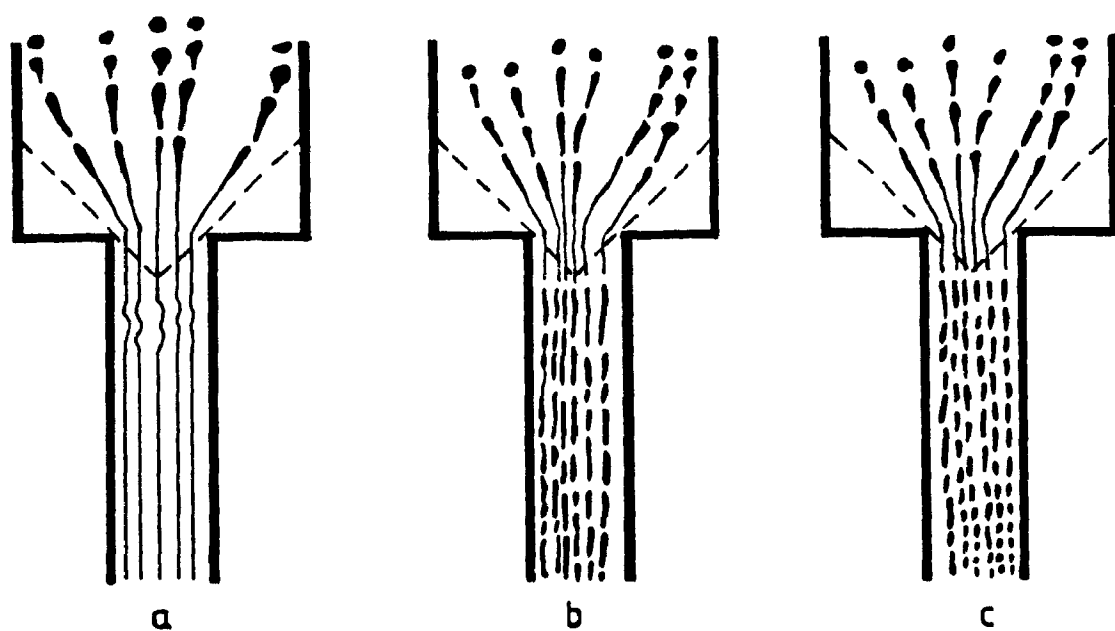


Figure 2.10 The schematic view of longitudinal phase morphologies at various viscosity ratios $\lambda = \eta_d / \eta_m$ for a HDPE/PS blend [39].
a) $\lambda < 0.7$ b) $0.7 < \lambda < 1.7$ c) $\lambda > 2.2$

determined by viscoelasticity, specifically first normal stress characteristics as the interfacial tension is influenced by the elastic energy in the two phases. They observed, however, that the values of interfacial tension required for HDPE/N6 and HDPE/PC might be larger than would be expected. These larger values could be the result of first normal stress differences in addition to quiescent interfacial tension.

A 80/20wt% PP/EVOH blend system was studied by Lepoutre [40], with a viscosity ratio $\lambda = \eta_{\text{EVOH}}/\eta_{\text{PP}} > 1$. The EVOH dispersed phase appeared as long cylinders embedded in the PP matrix. The cylinders were oriented in the direction of flow.

Table 2.5 summarizes observations regarding dispersed phase morphology development in capillary flow as a function of viscosity ratio. It is observed that viscosity ratio alone is not suitable for classifying polymer blend morphology. Depending on the blend system, for a viscosity ratio above or below unity, it is possible to obtain the dispersed phase as long, continuous, uniform fibers in the direction of flow.

c) Annular and Slit Flow

Subramanian [41,42] investigated different possibilities for the development of new morphologies in polymer blends and a method to impart permeability barriers to low cost polyolefins using small amounts of a barrier polymer by melt processing. The results showed that a blend of linear HDPE and 20% modified nylon, the barrier polymer, when subjected to normal processing under good mixing conditions, resulted in a homogeneous, very tough product with good physical properties. Hydrocarbon permeability, however, only improved by 20% compared to HDPE alone. Morphological studies of the size and shape of the nylon particles showed that the same blend, when processed in an extruder under controlled conditions (not clearly specified), where the melted nylon particles were prevented from

Table 2.5 Dispersed Phase Morphology of different Polymer Blend Systems for Capillary Flow.

Author	Blend	Viscosity Ratio	Dispersed Phase Morphology
Han [27,28]	PE/PS	$\lambda < 1$	PE fibers
Han [29]	PS/PP	$\lambda > 1, \approx 1$	PS fibers
Danesi [30]	PP/EP	$\lambda < 1, \approx 1$	PP fibers length = f(shear stress)
Vinogradov [31-33]	POM/CPA	$\lambda < 1, \approx 1$	POM fibers shape = f(shear stress)
Krasnikova [34]	PP/PS	$\lambda \approx 1$	PP fibers length = f(relaxation)
Tsebrenko [35]	POM/CEVAC	$\lambda \approx 1$ $\lambda = 1.32$ $\lambda = 4.3$	POM films & fibers POM microfibers defect fibers, POM particles
Lyngaae-Jorgensen [36-38]	PE/PP	$\lambda > 1$ $\lambda < 1$	continuous fibers breakup, small droplets
White [39]	HDPE/PS	$\lambda < 0.7$ $0.7 < \lambda < 1.7$ $\lambda > 2.2$	uniform fibers undulant fibers & rods undeformed droplets
Lepoutre [40]	EVOH/PP	$\lambda > 1$	EVOH fibers

forming tiny droplets, possessed outstanding permeability properties (Figure 2.11, Table 2.6). Micrographs of samples produced under controlled processing conditions (blow-molded container and extruded sheet) showed that the nylon material was not distributed as a homogeneous, uniform blend, but rather as multiple layers, or platelets, along the wall thickness. Optimum permeability barrier properties were obtained at 18% nylon, and modest to good properties at concentrations of 5 to 10%. The controlled processing conditions [43] were based on a low shear screw and blend system design. The nylon dispersed phase was transported as solid phase within the HDPE through the feeding and compression zones, thus inhibiting breakup and mixing. In the metering zone, the nylon particles were melted, oriented in the direction of flow, and transported as well defined layers, or platelets, through the extrudate-forming devices. Coalescence was inhibited and, thus, the final size of the dispersed phase in the laminar structure was strongly dependent on the feed pellet size.

d) Mixing Devices

Favis and Chalifoux [44,45] investigated the morphology of PC and PP blends by melt blending the materials in a Brabender mixing chamber with roller blade attachment. They found that: i) these blend systems exhibited a wide polydispersity, especially at high concentrations and, ii) the polydispersity decreased with decreasing concentration. Favis and Chalifoux assumed that the torque was directly related to viscosity and, therefore, used the torque ratio to indicate the viscosity ratio. They examined the size distribution of the minor phase in PP/PC blends, after melt mixing, as a function of the viscosity ratio, λ , and the torque ratio, TR (Figure 2.12).

a) phase size/viscosity ratio dependence for $\lambda > 1$:

The torque ratio value for the dispersed phase size tended to be somewhat less than the viscosity ratio, but the shape of the curves and the correlation were very similar. The viscosi-

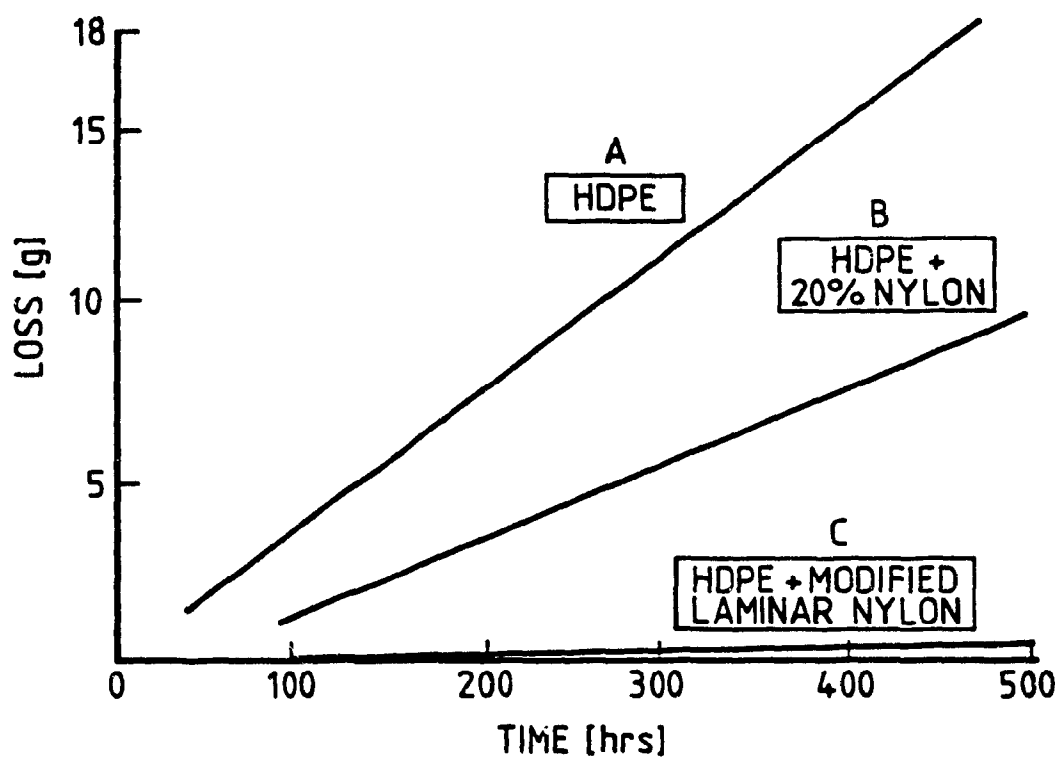


Figure 2.11 Hydrocarbon permeability in laminar walled PE/nylon barrier bottles [41].

Table 2.6 Permeability, Loss (g.)*, in 4 oz. Blowmolded Containers [41].

Solvent	HDPE	HDPE-Nylon Laminar Container	Permeability Factor
Toluene	5.5	0.04	138
Heptane	3.0	0.07	43
Hexane	4.4	0.10	44
Naphtha	2.0	0.07	29
O-Dichlorobenzene	1.6	0.02	80
Trichloroethane	0.56	0.02	28
Tetrachloroethane	12.1	0.10	121
Methylene Chloride	7.6	3.6	2
'Freon' F-113	0.05	0.03	2
Ethyl Acetate	0.30	0.03	10
Methyl Ethyl Ketone	0.15	0.03	5
Acetone	0.10	0.04	2
Methanol	0.03	0.07	2

- *
 • Filled containers
 • 23°C
 • 21 days duration

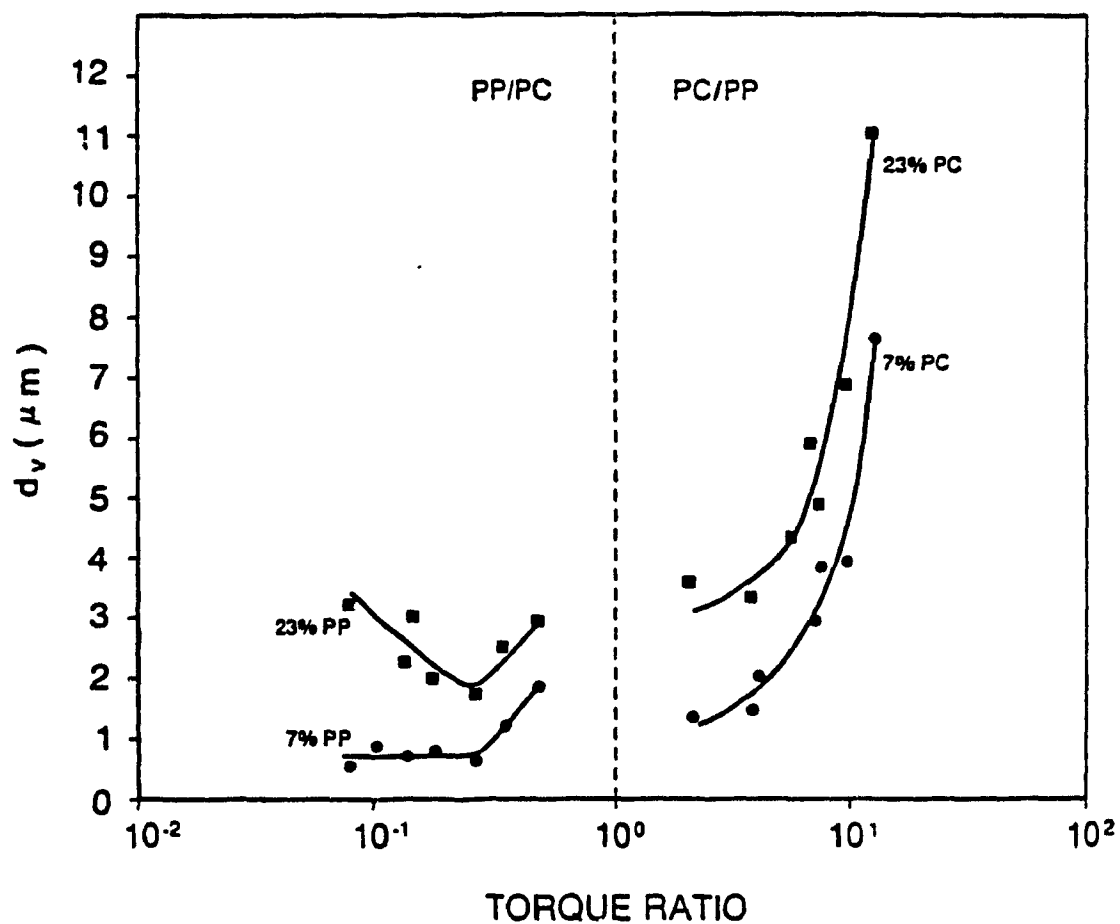


Figure 2.12 Volume average diameter versus torque ratio from TR of 0.078 to 12.8 [45].

ty had a significant effect on the minor phase size. At 30% PC, the volume average diameter, d_v , varied from $1.5\mu\text{m}$ at $\lambda=4.5$ to $12\mu\text{m}$ at $\lambda=17.3$. Even at $\lambda=17.3$, significant particle disruption occurred, unlike Newtonian systems in a shear flow field which do not disrupt above $\lambda=4$.

b) phase size/viscosity ratio dependence for $\lambda < 1$:

A minimum particle size was achieved at $\lambda=0.15$. For low concentrations, particle size increased above this value, whereas below this value, a plateau was maintained. At higher concentrations, no minimum plateau could be found. Rather, a very sharp minimum was observed and the curve had a V-shape appearance with significant increase in particle size observed above and below $\lambda=0.15$.

Wu [46] investigated the formation of dispersed phase in blends during melt extrusion with a co-rotating twin screw extruder, using nylon (N66) or polyester (PET) as the matrix, and ethylene-propylene rubbers (EP) as the dispersed phase. All blends contained 15wt% rubber and 85wt% polymer. A plot of the Weber number ($We=(\eta_m \cdot \dot{\gamma} \cdot a)/\sigma$) versus the viscosity ratio ($\lambda=\eta_d/\eta_m$) showed that all data points for the various blends fall on a single master curve (Figure 2.13). The Weber number appeared to have the lowest value at $\lambda \approx 1$. The portion of the curve for $\lambda > 1$ could be expressed for these blend systems as a straight line, given by $We = 4 \cdot \lambda^{0.84}$. The shape of the curve for $\lambda < 1$ was uncertain due to insufficient data points. However, it could be seen that as the viscosity ratio moved away from unity, the dispersed particles became larger. Wu compared blends having approximately the same viscosity ratio ($\lambda \approx 1$), but an interfacial tension ratio of approximately 40, and found particle sizes with a ratio of 52, confirming that particle size is directly proportional to interfacial tension. Blends having the same interfacial tension, but very different viscosities ($\lambda \approx 4.4$), resulted in very different particle sizes, having a ratio of $(4.4)^{0.84} \approx 3.5$, confirming that particle size was proportional to $\lambda^{0.84}$. Therefore, varying the

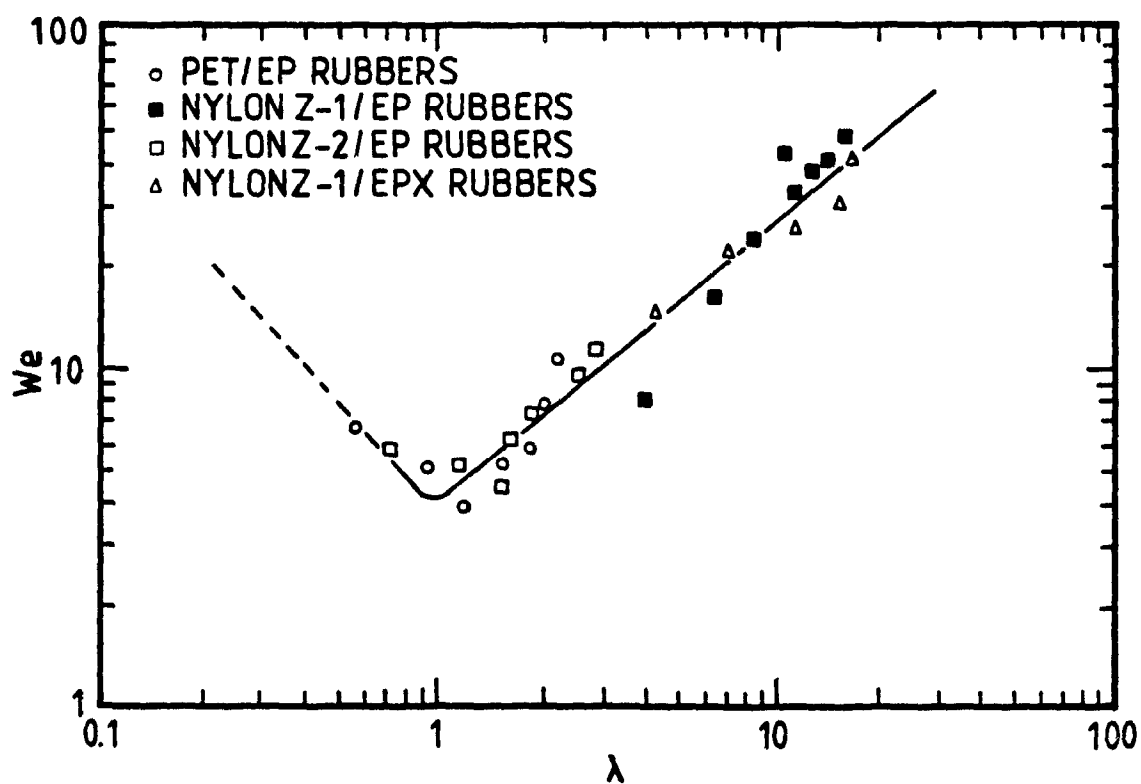


Figure 2.13 Dimensionless master curve of We vs. λ for the melt extrusion using a co-rotating twin screw extruder [46].

interfacial tension was much more effective in controlling the particle size than viscosity ratio variations.

Lepoutre [40] investigated the morphology of PP/EVOH blends by melt blending the components, in two composition ratios (80/20 and 90/10wt%), in a Brabender mixing chamber with roller blade attachment. SEM analysis of samples taken directly from the mixing chamber showed spherical domains of the minor component in a matrix of the major component. The average diameter of the domains in the 10% EVOH blend was approximately 1.5 microns, whereas in the 20% EVOH blend it was approximately 4.0 microns. The increase in the concentration of the minor component, therefore, led to a significant increase in the average domain diameter. Compression molding of the samples prior to morphology analysis increased the average domain size of the dispersed EVOH phase. Under the influence of thermal and flow fields experienced in compression molding, coalescence takes place. Coalescence produced dispersed EVOH particles as large as 20 microns in diameter. Thus, compression molding changes the blend morphology, and care should be taken to differentiate between the morphology induced by compression molding from that achieved in the mixing chamber.

2.2.2.2 Effect of Interfacial Properties and Compatibilizers

Polymers are usually immiscible, and their mixtures form multi-phase structures with stable interfaces. Dispersion, morphology, and adhesion of the component phases are largely affected by interfacial energies, which play an important role in determining the mechanical properties of a multi-phase polymer blend.

Adhesion refers to a molecular force, compelling bodies of unlike substances to stick together. An adhesion bond is formed in the first stage through forming interfacial contact by wetting and, in the second stage, by interdiffusion and/or

chemical bonding. Interfacial tension between two polymer phases stems mainly from the effects of a mismatch in the nature of intermolecular forces and from the polymer conformational restriction on the interfacial contact.

It seems that the adhesion, as well as the barrier and mechanical properties, of mechanically blended polymer mixtures might be enhanced if better solubility or interfacial interactions could be obtained between the various polymers involved. A suitable "interfacial agent" (compatibilizer) that is soluble in each component of the polymer blend could be the key to this objective.

a) Mixing Devices

Ide and Hasegawa [47] investigated nylon6 (N6) and polypropylene (PP) blend systems, using maleic anhydride grafted PP (MAH-PP) [48] as the inter-polymer. Micrographs for a N6/PP (20/80wt%) blend system showed that the N6 phase of only mechanically blended polymers was easily discernible, having a diameter of about $10\mu\text{m}$. On the other hand, in the presence of MAH-PP graft copolymer, the N6 phase was hardly distinguishable from PP, as the result of interactions at the interface. The physical properties, especially mechanical properties of N6/PP blends, were markedly improved with an increase of MAH-PP added to the polymer blend.

The stabilization of polymer blend morphology was studied by Heikens and Barentsen [49,50] for a blend of low density polyethylene (LDPE) and polystyrene (PS). The blends were prepared in a Brabender blender, and subsequently compression molded. The results obtained showed that a higher viscosity of the matrix polymer facilitated the formation of a fine dispersion. In order to stabilize the morphology, Heikens and Barentsen studied the effect of addition of surface active compounds during the blending operation. If a real interlayer of a certain thickness around the dispersed particles was formed, the

process of coalescence due to local differences in shearing rate might be hampered. The experimental results of Heikens and Barentsen with a specially designed graft copolymer compatibilizing agent supported the results of Ide and Hasegawa [47]. However, they did not present any evidence that the addition of graft copolymers hindered the coalescence of the dispersed phase in strong flow fields, which are common in the polymer processing industry.

Chuang and Han studied blends of nylon6 with a chemically modified polyolefin (CXA3095) [51,52]. The melts were blended in four composition ratios (20,40,60, and 80wt%) using a twin-screw compounding machine; the compounded pellets were compression molded into disks or injection molded. The morphological investigation showed that the domain structure strongly depended on the amount of the dispersed phase present in the blend, and the blend ratio also determined which of the components formed the discrete phase. In both the N6-rich or CXA-rich blends, the discrete phase was tightly bound to the continuous phase.

In another study [53,54], three different blend systems were prepared : N6/CXA3101 (an ethylene-based multifunctional polymer), N6/Plexar3 (an chemically modified polyolefin) and N6/EVA (ethylene vinyl-acetate). For the N6/CXA3101 and N6/Plexar3 blends, the domain size of the discrete phase was small and uniformly dispersed in the continuous phase. Fracture surfaces for these two blend systems indicated very good contact between the dispersed and continuous phases. On the other hand, micrographs of the fractured surfaces of N6/EVA blends showed large sized, dispersed particles, sharp edges, and particles were pulled off clean from the continuous phase upon fracture, showing no evidence of strong adhesion between the two phases. The thickness of the interphase was in the following order : N6/CXA3101 > N6/Plexar3 > N6/EVA. The smaller interphase thickness of Plexar3 compared to CXA3101 was attributed to a smaller amount of reactive groups in Plexar3.

Accordingly, an interfacial agent would reduce the energy needed for breaking large, dispersed particles during melt blending. This gives rise to smaller domains of the discrete phase strongly adherent to the continuous phase.

Fayt, Jerome and Teyssie [55-59] undertook an elaborate study on the emulsifying effect of specifically designed copolymers in polyolefin-polystyrene blends. The polyolefins included low density, linear low density, and high density polyethylenes. The specifically designed copolymer was hydrogenated butadiene-*b*-styrene diblock copolymer (HPB-*b*-PS). The blends were prepared on a two-roll mill, then compression molded. The block copolymer was always mixed first with the minor component before the addition of the major component.

In general, it was found that whereas unmodified PE/PS blends exhibited rather large domain structures, the addition of moderate to small amounts of block copolymer reduced strongly the particle size at every composition. This morphology was practically unmodified by subsequent compression molding as far as block copolymer was added. A pronounced coalescence of the minor component was however observed in unmodified blends. A tapered diblock and a pure diblock copolymer, having the same composition and total molecular weight, were compared [57]. All results suggested that the emulsifying ability of diblock copolymers in polymer blends depends more on their molecular structure than on their block length. SEM micrographs of fractured bars revealed that the tapered diblock copolymer provided stronger adhesion than did the pure diblock.

Transmission electron micrographs (TEM) showed that the block copolymer formed a continuous layer around the dispersed particles of either PS or PE [58]. Its thickness was rather regular, and was in the mean range of about 100Å. In contrast to graft copolymers, the diblock copolymer was not observed as discrete droplets on the surface of the particles, as compared to results of Heikens and Barentsen [49,50]. Apparently, the

sequences are firmly anchored into the domains, which they penetrate. When the block copolymer percentage increases, the morphology of the blends may be so deeply modified that it is impossible to identify the individual phases. The authors suggest that a graft copolymer, and also a triblock copolymer, adsorb mainly onto the phases because of conformational constraints, whereas each sequence of a diblock structure has the opportunity to penetrate its homopolymer phase and provides important entanglements.

The molecular design of multicomponent polymer systems by Fayt, Jerome and Teyssie was extended to poly(vinylidene fluoride)-polyolefin blends, with the addition of a poly(hydrogenated diene-b-methylmethacrylate) diblock copolymer [60], and to low density polyethylene - acrylonitrile-butadiene-styrene blends emulsified by a poly(hydrogenated butadiene-b-methylmethacrylate) diblock copolymer [61]. The results of these experiments again support strongly the efficiency of specifically designed diblock copolymers as emulsifiers in immiscible polymer blends.

In addition to the studies on pure PP/EVOH blends, Lepoutre [40] investigated the influence of a compatibilizing agent on dispersed phase domain size, and adhesion between the PP and EVOH phases. A maleic anhydride modified polyolefine (MAPPI) was chosen as the compatibilizing agent. The PP/EVOH/MAPPI system was studied in two composition ratios (90/9/1 and 80/18/2wt%). Comparison of the pure and modified blend systems did not reveal any changes in the average dispersed phase diameter. In addition, SEM micrographs of fracture surfaces suggested that the addition of MAPPI had no visible effect on the adhesion of the two phases. The particles of EVOH, as well as the holes left by removal of the spheres, were as smooth and clean with MAPPI as they were without it. The author concluded that the concentration of MAPPI was too low, and that the processing conditions employed in the study might be unsatisfactory for achieving compatibilization. During the mix-

ing stages, all three components were fed together to the mixing chamber. On the other hand, studies have shown, Fayt et al. [55-61] and Willis et al. [62], that the mixing order of the components had a pronounced effect on blend structure and mechanical properties.

b) Slit Flow

Subramanian [41,42] showed that a blend of linear HDPE and 20% nylon, when subjected to normal processing under good mixing conditions without any compatibilizers and additives, resulted in extrudates that showed gross incompatibility and broke easily. A similar nylon, modified for compatibility and processed as a blow-molded container or extruded sheet under controlled conditions, showed that the nylon material was distributed as multiple layers, or platelets, along the extrudate thickness. Under a hot-stage microscope, the laminar dispersion of nylon showed that upon heating, the laminar structure disappeared at the temperature when the nylon was molten ($T_{m,nylon} > T_{m,HDPE}$). On cooling, the platelet structure was retained. The nylon was dispersed as large, sheet-like structures, suggesting that, during processing, a chemical modification of the HDPE-nylon interface had occurred.

2.3 Conclusions

The literature review has revealed that it is possible to orient a dispersed phase in the direction of flow, when both the dispersed and matrix phases are viscoelastic fluids. Comparison between Table 2.3, containing results for dilute emulsions, and Table 2.4, containing the results for three polymer blend systems shows, that a uniform shear field can be effective in orienting a dispersed phase.

The majority of studies on dispersed phase morphology development for polymer blend systems has been carried out for capil-

lary flow. Table 2.5 shows that the fibrillation process cannot be explained solely on the basis of viscosity ratio. Interfacial tension and elasticity effects have to be considered. On the other hand, Table 2.5 shows that there exists an upper bound for the viscosity ratio, above which the dispersed phase cannot be deformed and flows as a stable discrete phase in the matrix phase. No lower bound has been established for polymer blends, whereas for a Newtonian/Newtonian system, such a lower bound has been reported (Table 2.2).

Theoretical analysis of the deformation behavior of droplets, suspended in a fluid, has concentrated on Newtonian systems. These theoretical predictions are in the majority only valid for very small deformations and simple flow fields. The influence of coalescence and complex flow fields, as encountered in the commercial processing of polymer blend systems, has not been taken into account. The rheo-thermodynamic theory, developed by VanOene [23] to characterize the dispersed phase morphology of two-component blend systems, is based on a change of interfacial tension in flow. This change in interfacial tension is, according to VanOene, due to a net decrease in free energy of deformation which arises from the difference in the first normal stress function between dispersed and matrix phase. As far as could be established to date, it is not possible to measure the interfacial tension in flow, nor the first normal stress difference at processing shear rates.

Achieving engineering mechanical properties in blend products requires the incorporation of compatibilizers as a third phase into the, commonly, immiscible blend system. Specifically tailored compatibilizers can considerably improve the adhesion between blend component phases, and, thus, help to achieve mechanical properties comparable to those of homopolymers. Explanations for the improvement in mechanical properties, based on fracture theories, have so far dealt only with a homogeneous distribution of the dispersed phase in the matrix phase.

Analysis of laminar structures, as achieved by Subramanian [41,42], is not available. Nevertheless, it is important to evaluate the mechanical behavior of polymer blend products and the influence of composition and processing conditions on fracture behavior.

Permeability studies on laminar blend structures are only available in the work of Subramanian [41,42]. His results have shown that a specifically designed arrangement of the dispersed phase in the matrix phase can provide barrier properties comparable to those achieved in multi-layer products.

CHAPTER 3

EXPERIMENTAL

3.1 Materials

Four different resins were used for all studies in this work. For the continuous phase (matrix phase), a blow molding grade polypropylene, NPP7200-AF, designated as PP in this study, was chosen. This polypropylene resin is a gas phase random homopolymer, manufactured by Quantum Chemical Corporation. It meets FDA requirements for food packaging.

For the dispersed phase, an ethylene vinyl-alcohol copolymer (EVOH), EP-F101A, was chosen. This EVOH is a high barrier resin used in multi-layer barrier structures, manufactured by EVAL[®] Company of America. It has a 32mol% ethylene content, and meets FDA requirements for food packaging. Its excellent gas, solvent, odor, and aroma barrier properties make this resin an excellent candidate for barrier packaging applications.

Due to their non-polar character, it is difficult for polyolefins (e.g. PP) to adhere to other materials (e.g. EVOH). As outlined in Chapter 2.2.2.2, interfacial agents play an important role in overcoming this difficulty, and in determining the mechanical properties of a multi-phase polymer blend. In order to evaluate the influence of interfacial agents (compatibilizers) on the morphology of a PP/EVOH polymer blend, two extrudable adhesive resins have been chosen. Both adhesive resins are basically modified polyolefins, obtained by grafting maleic anhydride and incorporating other special adhesive property improving materials :

- a) MODIC P-300F, designated as MAPP1 in this study, is manufactured by Mitsubishi Petrochemicals Co., Ltd.

b) ADMER QF500A, designated as MAPP2, is manufactured by Mitsui Petrochemical Industries, Ltd.

All of the above four resins are commercially available, and are currently used in the coextrusion blow molding process. A summary of some of the properties of these resins is given in Table 3.1.

3.1.1 Resin Characterization

3.1.1.1 Steady Shear Viscosity

The review of relevant literature in Chapter 2 has shown the importance of the viscosity ratio, based on the analysis starting with Taylor [1,2], and the confusing and opposing results and explanations of morphology development in capillary extrusion experiments.

The viscosity measurements were carried out using an Instron Capillary Rheometer, Model TT-CM. The melt viscosity calculation procedure was described in detail in a related study [40]. The measurements were carried out at 200°C and 230°C, which span the range of extrusion temperatures used in this study.

Figure 3.1 shows the viscosity as a function of shear rate for all four homopolymers and both temperatures. For both temperatures, the dispersed phase material, EVOH, exhibits a higher viscosity than the polypropylene resins, over the whole shear rate range. As a result, in the extrusion experiments conducted in this study, the viscosity ratio of the dispersed phase to the matrix phase is above one ($\lambda > 1$). The shear viscosities for the three polypropylene resins are very similar.

3.1.1.2 Shear Storage Modulus

The studies of Chin and Han [8,22] pointed out the influence

Table 3.1 Resin Properties [63,64,65,66].

Property	Resin			
	NPP7200-AF	P-300F	QF500A	EP-F101A
Melt Flow Rate [g/10min]	2.0 (D1238)	1.3 (D1238)	3.0 (D1238)	1.3 (D1238)
Density [g/cm ³]	0.90 (D692)	0.89 (D1505)	0.90 (D1505)	1.19 (D1505)
T _m [°C]	150-155	168	160	181

Values in parentheses are ASTM methods.

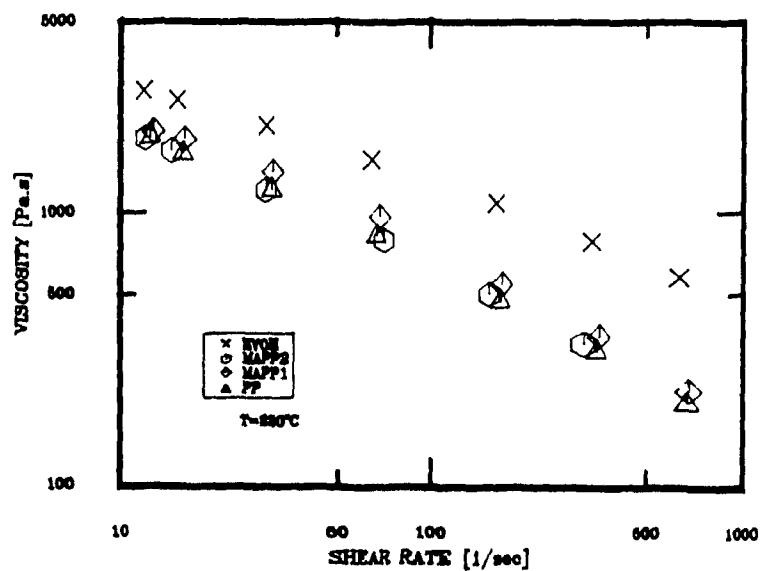
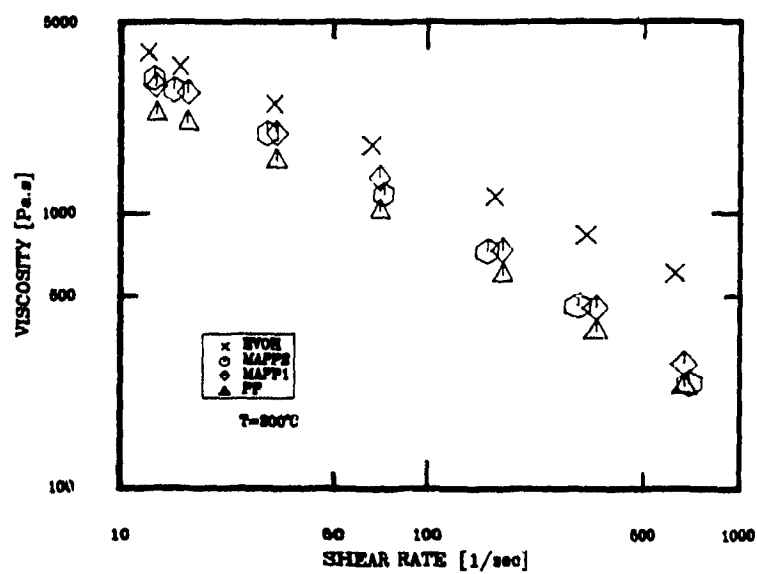


Figure 3.1 Steady Shear Viscosity vs. Shear Rate for PP, MAPP1, MAPP2 and EVOH, $T=200^{\circ}\text{C}, 230^{\circ}\text{C}$.

of the elastic properties of the dispersed and matrix phase in capillary flow.

A Rheometrics Mechanical Spectrometer with rotational parallel plate fixtures was used to measure the shear storage modulus, G' , for PP, MAPP1, and MAPP2. Test samples were prepared by compression molding at 215°C and 5kPa. The parallel plates had a radius of 25 mm, and the gap between the two plates was set to 1 mm. All experiments were conducted under a nitrogen gas blanket to prevent degradation. All three resins showed no measurable degradation effects after 70 minutes at 230°C during a dynamic time sweep experiment. Linear viscoelasticity data for EVOH were supplied by the resin manufacturer [67]. Some difficulties were encountered when attempting to prepare specimens of this material for rheological testing in our laboratory.

Tests were carried out at 200°C and 230°C. Figure 3.2 shows the shear storage modulus, G' , as a function of frequency for all four resins and both temperatures. For both temperatures, the three polypropylene resins exhibit very similar elastic behavior, as measured by G' , over the frequency range tested. The EVOH shows a different elastic behavior. For both temperatures tested, the EVOH is less elastic at lower frequencies, but G' increases with increasing frequency and a cross over with the polypropylene data occurs. At 200°C, the cross over point can be marked at around 10 rad/sec, and for 230°C at around 50 rad/sec. These measurements of G' suggest that, at higher frequencies, the EVOH is more elastic than the three polypropylenes tested.

3.1.1.3 Determination of Functionalized Groups in Adhesive Polymers

Both adhesive resins MAPP1 and MAPP2 are modified polypropylenes, which have maleic anhydride (MAH) and other adhesive

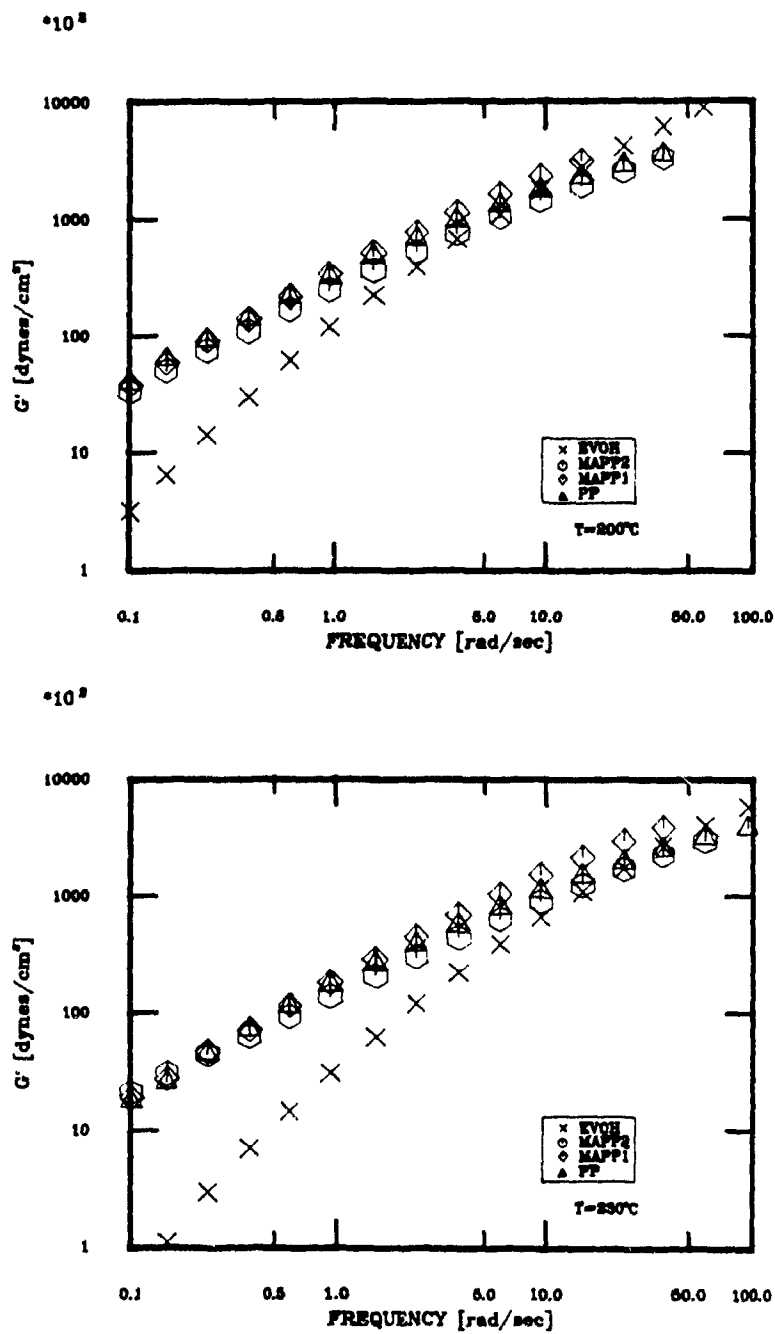


Figure 3.2 Shear Storage Modulus G' vs. Frequency for PP, MAPP1, MAPP2 and EVOH, $T=200^\circ\text{C}, 230^\circ\text{C}$.

property improving materials grafted to the backbone [64]. Due to insufficient information, and the unwillingness, of the two manufacturers of the adhesive polymers to make the recipe ingredients available for research purposes, a study was undertaken to determine the amount of functionalized groups (maleic anhydride) present in the adhesive polymers.

(a) Fourier Transform Infrared (FT-IR) Spectroscopy

Infrared spectroscopy is a simple spectroscopic technique that requires only very small amounts of sample. In this study, a BOMEM Michelson Series™ 100 spectrometer was used. This spectrometer belongs in the class of medium IR and works in a scanning wavelength range of $\lambda = 2.0$ to $25\mu\text{m}$ (corresponding to wavenumbers $\nu = 5000$ to 400cm^{-1}).

Specimens with a thickness of $25\mu\text{m}$ were microtomed from pellets, as delivered by the manufacturers, fixed onto a specimen holder and positioned in the laser beam path. The spectrometer was used in the absorbance mode and 1000 scans were performed for each sample.

An IR spectrum of MAH is shown in Figure 3.3 [68]. The most characteristic anhydride bands in the absorption mode are at 1840cm^{-1} , 1780cm^{-1} , 1050cm^{-1} , and 885cm^{-1} [69], and the exact position of each band is slightly dependent on the nature of the sample. The 1780cm^{-1} band is very strong, and can be conveniently used to estimate the amount of MAH in a mixture by quantitative IR ($\pm 1\%$) [70].

Figures 3.4 and 3.5 present representative spectra for MAPP1 and MAPP2 specimens for the wavenumber range 600 to 2000cm^{-1} , where all characteristic MAH peaks should appear. It can be seen that even the very characteristic peak at around 1780cm^{-1} cannot be established. Close-ups and enlargements of certain sections did not reveal any significant MAH peaks.

Figure 3.4 Infrared Absorbance Spectrum for MAPP1.

BOMEM
MICHELSON-100

MAPP1.ABSORBANCE

Res : 4.00 cm-1

#Scans 1000

Date April 20, 1989

Time 11hr-51min-30sec

Description: pellet as delivered from manufacturer, scan of small additives (25micron)

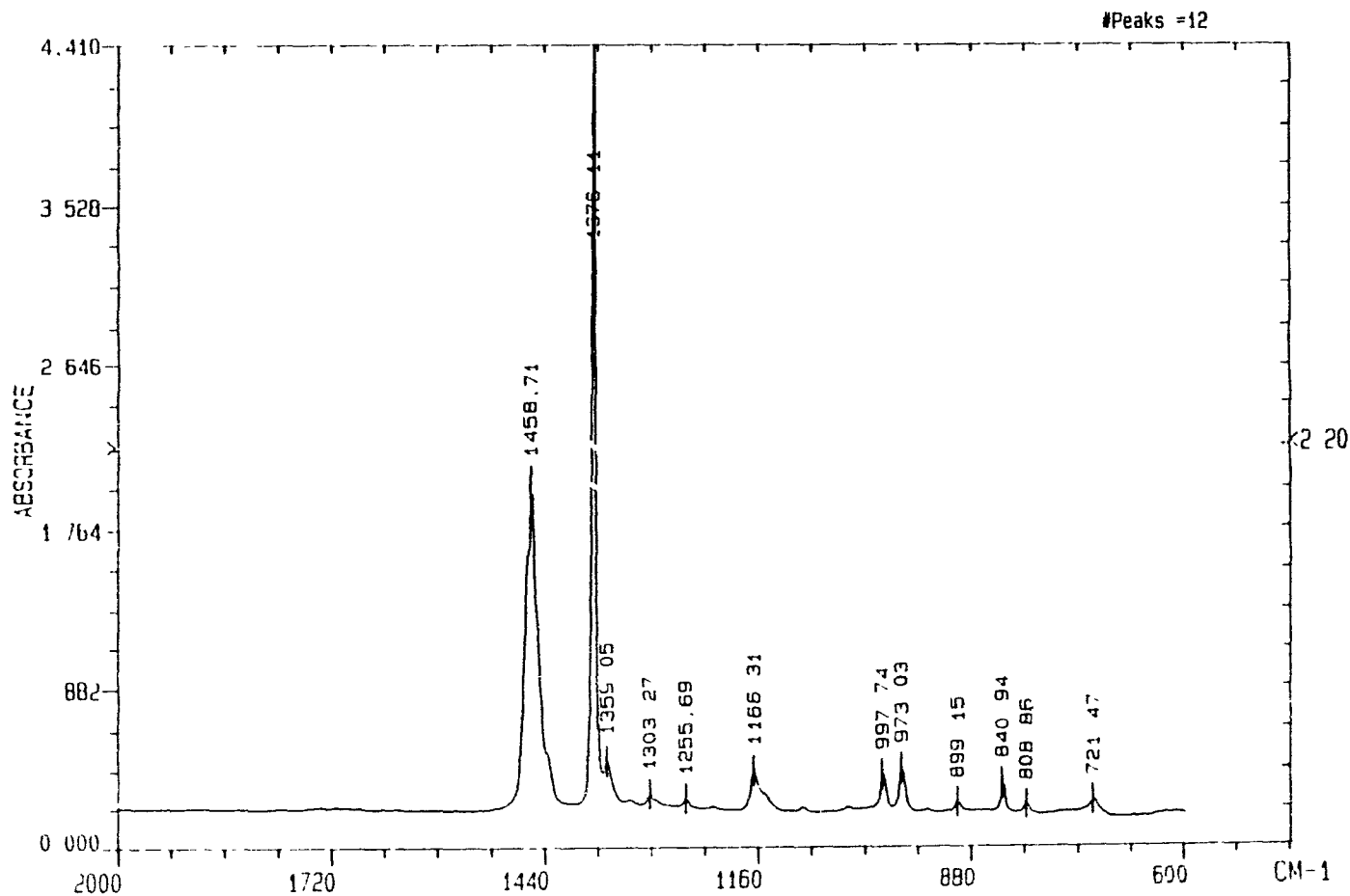
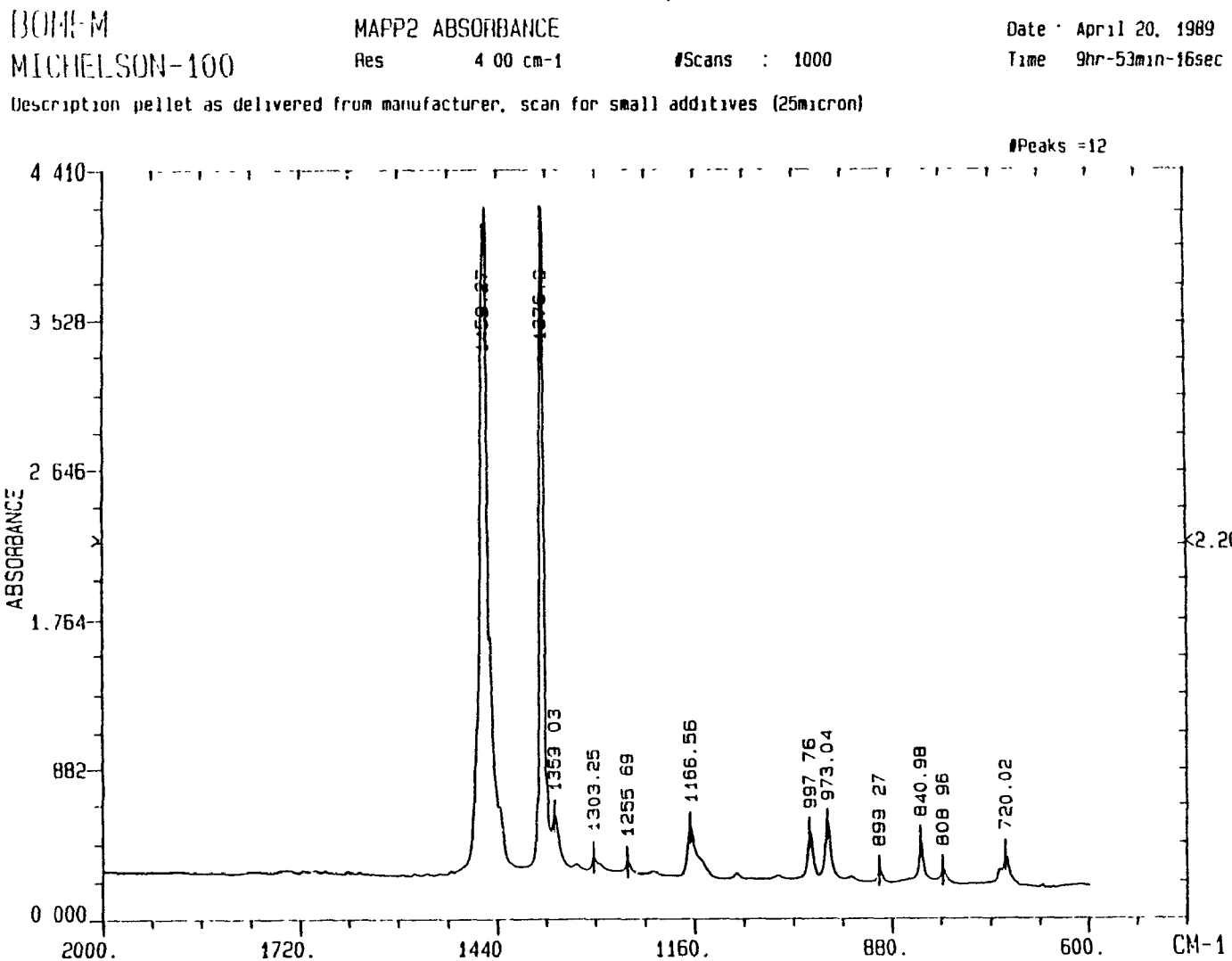


Figure 3.5 Infrared Absorbance Spectrum for MAPP2.



As explained above, the adhesive polymers are graft polymers of maleic anhydride onto polypropylene, so that all characteristic IR bands of PP are also measured in the spectra for MAPP1 and MAPP2. To minimize the overlapping of PP and MAH peaks, a pure PP specimen was prepared and the IR spectra obtained. The PP IR spectra were then subtracted from the MAPP spectra. Figures 3.6 and 3.7 show the modified spectra for the wavenumber range 600 to 2000 cm^{-1} , for both adhesive polymers. Again, no distinct MAH peaks are detectable. The enlargement of representative areas did not reveal any new information.

As a conclusion, it appears that the amount of MAH grafted to the polypropylene, in the two adhesive polymers used in this study, is less than 1%. In these small quantities, MAH cannot be identified by IR measurements.

(b) Titration

Another method to determine small amounts of MAH in complex mixtures is based on titration [70,71]. Maleic anhydride, like most other anhydrides, can be hydrolyzed to the corresponding acid, maleic acid. The maleic acid is a dicarboxylic acid with two different ionization constants in water at 25°C

$$\begin{aligned} \text{p}K_1 &= 1.81 & K_1 &= 1.42 \cdot 10^{-2} \\ \text{p}K_2 &= 6.07 & K_2 &= 8.57 \cdot 10^{-7} \end{aligned}$$

Maleic acid produced in hydrolysis is titrated against KOH to the two end points at pH=3.7 and pH=9.5 [70].

The MAH content of modified PP is determined by titration of a hot water-saturated xylene solution of the polymer with alcoholic base. One gram of the polymer is heated for approximately one hour in 150ml of refluxing water-saturated xylene. The solution is well stirred to assure the homogeneity of polymer concentration. The hot solution is titrated with 0.05 N ethanolic KOH, using 3-4 drops of 1% Trymol blue in DMF as

As explained above, the adhesive polymers are graft polymers of maleic anhydride onto polypropylene, so that all characteristic IR bands of PP are also measured in the spectra for MAPP1 and MAPP2. To minimize the overlapping of PP and MAH peaks, a pure PP specimen was prepared and the IR spectra obtained. The PP IR spectra were then subtracted from the MAPP spectra. Figures 3.6 and 3.7 show the modified spectra for the wavenumber range 600 to 2000cm^{-1} , for both adhesive polymers. Again, no distinct MAH peaks are detectable. The enlargement of representative areas did not reveal any new information.

As a conclusion, it appears that the amount of MAH grafted to the polypropylene, in the two adhesive polymers used in this study, is less than 1%. In these small quantities, MAH cannot be identified by IR measurements.

(b) Titration

Another method to determine small amounts of MAH in complex mixtures is based on titration [70,71]. Maleic anhydride, like most other anhydrides, can be hydrolyzed to the corresponding acid, maleic acid. The maleic acid is a dicarboxylic acid with two different ionization constants in water at 25°C

$$\text{p}K_1 = 1.81 \quad K_1 = 1.55 * 10^{-2}$$

$$\text{p}K_2 = 6.07 \quad K_2 = 8.57 * 10^{-7}$$

Maleic acid produced in hydrolysis is titrated against KOH to the two end points at $\text{pH}=3.7$ and $\text{pH}=9.5$ [70].

The MAH content of modified PP is determined by titration of a hot water-saturated xylene solution of the polymer with alcoholic base. One gram of the polymer is heated for approximately one hour in 150ml of refluxing water-saturated xylene. The solution is well stirred to assure the homogeneity of polymer concentration. The hot solution is titrated with 0.05 N ethanolic KOH, using 3-4 drops of 1% Thymol blue in DMF as

Figure 3.6 Infrared Subtraction Spectrum for MAPP1.

BOMEM
MICHELSON-100

MAPP1.SUBTRACTION[3]

Res : 4.00 cm-1

#Scans : 1000

Date : April 20, 1989

Time : 11hr-51min-30sec

Description: PP subtraction from MAPP1, NF=0.580

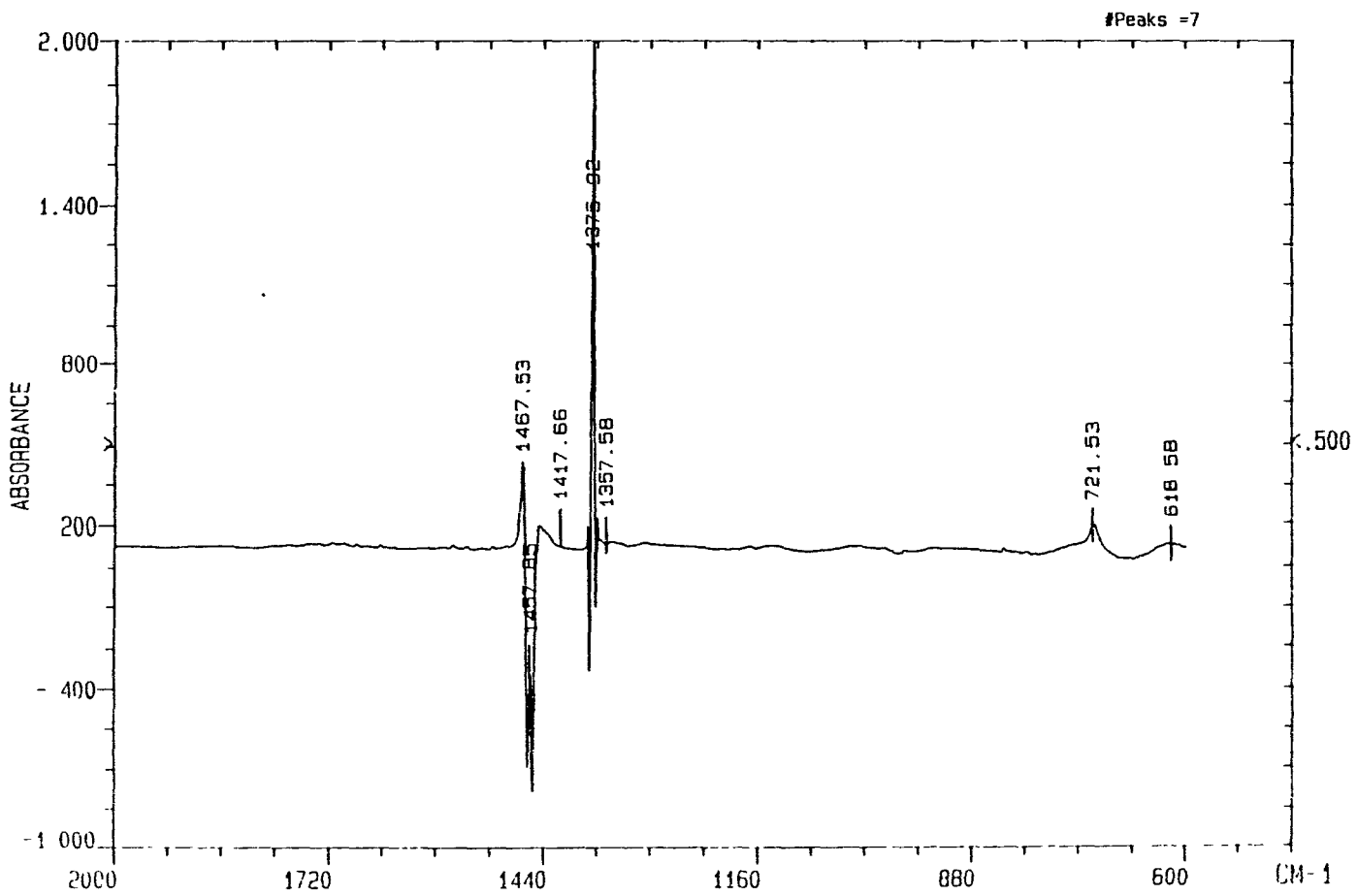
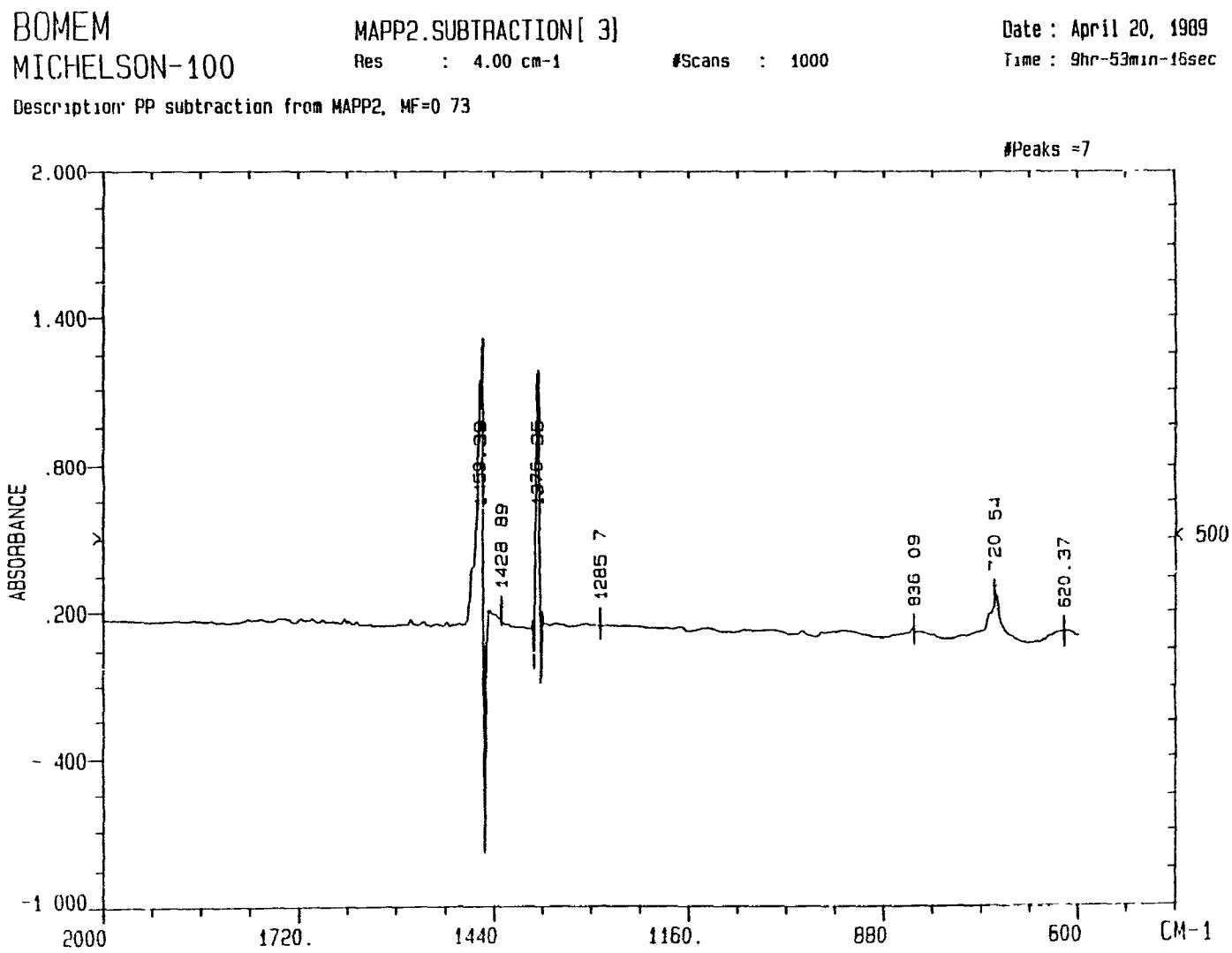


Figure 3.7 Infrared Subtraction Spectrum for MAPP2.



indicator. The end point is indicated by the change of solution color to blue. A 0.5-1 ml excess of KOH is added, and the deep blue color is back-titrated to a yellow end point by the addition of 0.05 N isopropanolic HCl to the hot solution.

In order to determine the amount of MAH, the following calculation is performed at the end points:



- No. moles of MAH = $\frac{1}{2} N_2 V_2$
where N_2 = normality of KOH, and V_2 = volume of titrants.
- gram of MAH = $\frac{1}{2} N_2 V_2 * MW$
where MW = molecular weight of MAH = 99.06 gr/mol.
- amount of MAH present in the mixture
wt% of MAH = $(\frac{1}{2} N_2 V_2 * MW) / \text{gr}_{\text{sample}}$

For each adhesive polymer, five titrations were performed, and the following results, with a reproducibility of $\pm 20\%$, were obtained [72]:

MAPP1 : wt% of MAH = 0.29

MAPP2 : wt% of MAH = 0.25

These amounts of MAH are very small. Furthermore, they are diluted if MAPP1 or MAPP2 is mixed with pure PP.

3.2 Processing Equipment

The processing equipment consists of an extruder, a slit die, a cooling and take-off device, and a data acquisition system for continuous data collection. During the extrusion experiments, the following processing parameters were recorded:

- Temperature : extruder zone 4, two locations in the die
- Pressure : two locations in the die
- Extruder drive : rpm, armature voltage, and armature current

3.2.1 Extruder

A Brabender Prep-Center drive was equipped with a 31.75mm (1 $\frac{1}{4}$ ") and a 25:1 length/diameter ratio single-screw extruder. The barrel had a water cooling channel for the feeding zone, where the hopper attaches to the barrel, and four heater/cooler collars along the barrel length. The temperatures of the extruder zones were controlled by digital temperature controllers which followed heating or cooling set points.

Torque measurement in a mixing device is a helpful tool [44, 45], because the complex flow fields make it difficult to obtain an exact calculation of the shear rates or stresses in such devices. By measuring the drive armature voltage, armature current, and rpm, the torque can be recorded during each experiment. The rpm during an experiment was kept constant using tachometer feedback, keeping speed variations within less than 0.5%, regardless of motor temperature or load. Thus, energy differences associated with changes from one composition ratio to another under otherwise constant processing conditions are reflected by either the extruder power or torque measurements. Since power and torque measurement devices are easy to install in commercial equipment, this parameter can be a useful tool in achieving process and product quality control during the blending process.

Two screw designs were used in the extrusion studies. It is suggested in the literature [8,22,23,29] that a three-stage metering screw should adequately achieve a proper degree of mechanical mixing, considering that a certain droplet size is necessary to obtain a fibrilled or laminar microstructure. On the other hand, when a compatibilizer is used in the blend system, it might be necessary to employ a mixing screw to ensure sufficient wetting of the dispersed EVOH phase with the incorporated interfacial agent. Mixing screws in single screw extruders can be effective, as long as the material is contin-

uously reoriented as it travels downstream along the screw [73-77]. The metering and mixing screws employed in this study were designed to obtain the same extrusion characteristics. They differed only in the design of the metering section, where the mixing screw had a second screw channel with a higher pitch, in addition to the standard metering screw channels. The second channel covered five flights of the screw [Appendix A].

3.2.2 Extrusion Die

As shown in Chapter 2, most of the reported work regarding extrusion of polymer blends was carried out in capillary dies. Thus, the studies dealt mainly with the development of fibrillar structures in the longitudinal (flow) direction. In many instances, commercial applications of blends involve the extrusion of the material through more complex dies. Of particular interest are applications associated with sheet extrusion and blow molding.

A slit die was chosen to study the possibilities of manipulating microstructure in sheet or strip extrusion. Figure 3.8 gives a schematic of the slit die design. The unit consisted of an adapter (sections A and B), and the slit die (sections C to F). The adapter connected the slit die to the extruder. In sections A and C, the flow field is dominated by converging extensional flow; in section D (in the x-y direction), shear flow is dominant, while in the x-z direction, diverging extensional flow prevails. In section E, converging extensional flow becomes dominant again, while in section F shear flow prevails [Appendix B].

The flow field in the slit die can be changed in sections E and F via an adjustable die land gap thickness. This allowed for manipulation of the converging ratio from the constant channel depth in section D to the variable depth in section

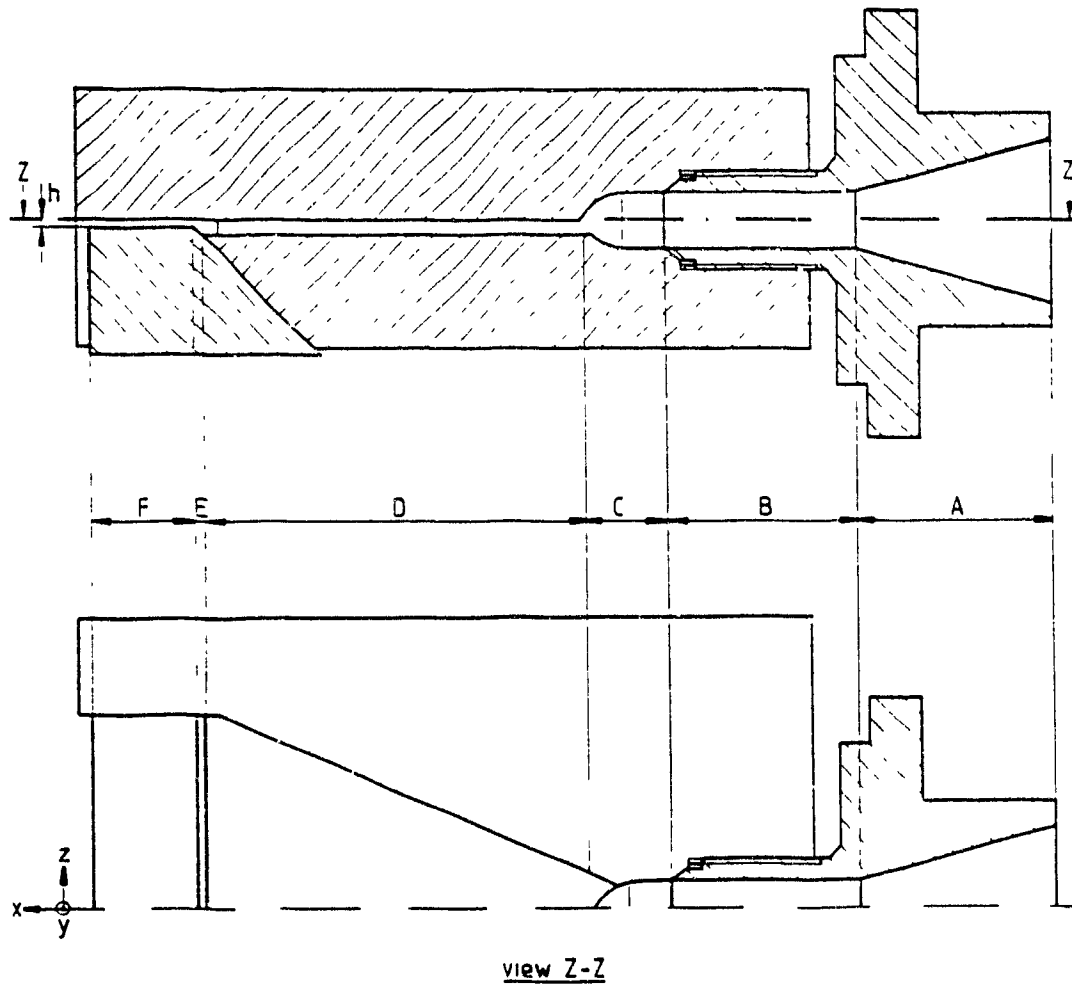


Figure 3.8 Schematic of Slit Die Unit Design.

F. Another possibility for influencing the flow field is by changing the adapter design. A change in the converging angle in section A modifies the flow path length in the tubular section B. The above changes in the flow path between the extruder exit and slit die outlet are expected to influence the microstructure.

The slit die was heated by a band heater box. Die temperature was controlled with the aid of a computer program [Appendix C]. The die was equipped with two pressure transducers (Dynisco TPT432A, 0-3000psi) located along the center line, one in the middle of section D, and one in the middle of section F.

3.2.3 Take-off Equipment and Cooling

Due to the hygroscopic behavior of EVOH, water cooling could not be used. Instead, a variable speed flat belt conveyer was used in conjunction with an air cooling rack to obtain the same cooling conditions in all experiments. The take-off speed was adjusted so that it was equal to the linear speed at the die exit, thus avoiding axial stretching in the cooling section.

3.3 Processing Conditions

The processing conditions were varied in order to evaluate the effects of extrusion temperature, flow geometry, screw speed, screw design, and blend composition on the morphology of the extruded ribbon.

The respective resin manufacturers recommended extruder melt temperatures in the range of 200°C - 240°C for EVOH, and 190°C - 230°C for PP. Accordingly, the range from 200°C to 230°C was chosen for extrusion experiments in this work. Table 3.2 lists three die temperature set points and the corresponding temperature profile settings along the extruder barrel.

Table 3.2 Slit Die and Extruder Barrel Temperature Setpoints.

	Temperature [°C]		
Die	200	215	230
Extruder			
Z1	170	180	180
Z2	185	200	205
Z3	195	205	215
Z4	205	220	235

To study the influence of flow rate, three screw speeds were chosen: 30, 60, and 90 rpm. By changing the extruder speed, the residence time in the extruder and die is affected. This, in turn, influences the contact and/or reaction times available to effect the adhesion between the dispersed and matrix phase. The technical information available on MAPP1 specifically points out the importance of contact time in the molten state on adhesive strength between two adjoining layers [64].

The influence of the flow geometry on the morphology was evaluated by changing the adapter angle. Two angles, 30° and 70°, were chosen. Moreover, two different exit gap thicknesses were used. An exit gap thickness of 1.0mm resulted in a converging ratio of 3.75. The ratio for a thickness of 0.5mm was 7.5. Die gap is a very important parameter in the extrusion blow molding process, where parison thickness programming is employed to control the dimensions of blow molded containers.

As indicated in Section 2.2, the composition ratio plays a major role in determining the morphology of polymer blends and their products. Since the goal of this study was to achieve a layered dispersed phase structure with minor amounts of the dispersed phase EVOH, the maximum amount of EVOH used in the blend system has been limited to 30wt%.

The amount of compatibilizer used strongly influences the number of functionalized groups available at the interface. To study the effect of the amount of compatibilizer present in the blend system, concentrations between 5 and 20 wt% of adhesive polymer were added to the PP/EVOH blend system. In one set of experiments, the matrix PP was replaced by pure adhesive polymer resin MAPP2, in order to ensure constant availability of functionalized polymer at the interface. Tables 3.3 and 3.4 show the weight and volume percentages for two-component or three-component blend systems chosen in this study.

Table 3.3 Weight and Volume Fractions for different Blending Ratios for a Two-Component Blend System of PP-EVOH or MAPP2-EVOH.

Blending Ratio	wt%	vol%
70-30	70-30	75.5-24.5
80-20	80-20	84.9-15.9
90-10	90-10	92.2- 7.8

Table 3.4 Weight and Volume Fractions for different Blending Ratios for a Three-Component Blend System of PP/MAPP/EVOH.

Blending Ratio PP-EVOH(MAPP)	wt%	vol%
	PP-MAPP-EVOH	PP-MAPP-EVOH
70-30(60)	59.3-15.3-25.4	64.1-15.4-20.5
70-30(90)	55.1-21.3-23.6	59.6-21.5-18.9
80-20(60)	71.4-10.7-17.9	75.0-10.8-14.2
80-20(90)	67.8-15.3-16.9	71.3-15.4-13.3
90-10(60)	84.9- 5.7- 9.4	86.9- 5.8- 7.3
90-10(90)	82.5- 8.3- 9.2	84.5- 8.4- 7.1
50-50(200)	25.0-50.0-25.0	26.7-53.3-20.0

In the three-component blends, the weight percent column shows that, for each mixing ratio, the fraction of EVOH is always higher than the fraction of compatibilizing agent. The volume percentage column, on the other hand, shows that for a weight ratio of MAPP/EVOH equal to 0.90, the volume fraction of compatibilizing agent is higher than the volume fraction of EVOH. It would be interesting to examine the effect of this transition of volumetric concentration of compatibilizer on the morphology and mechanical properties of the blend.

The following standard operating procedure was employed during all extrusion experiments:

- a) The extruder and die were heated. When all temperatures reached their respective set points, the system was given 40 minutes to stabilize.
- b) The blend system was extruded for 15 minutes to allow for pressure stabilization before experimental data were collected.
- c) For each experiment, eight ribbons were collected. The 25 cm long ribbons were sealed with a desiccant in plastic bags under vacuum, and stored in a freezer to minimize microstructural changes with time.

Due to its hygroscopic behavior, the EVOH was dried for 24 hours at 75°C, and stored in sealed glass containers prior to the experiments [78]. The components of the blend, in pellet form, were tumbled mechanically prior to extrusion. No other mixing was employed.

3.4 Flow Analysis in Slit Die Extrusion

As indicated in Chapter 2, deformation studies of droplets have only been undertaken for model systems in very dilute

emulsions. Moreover, morphological studies of polymer blends have concentrated almost entirely on capillary dies. In order to understand and explain the final morphology of an extruded product, it is important to study the morphology development in the die itself. For this purpose, a set of experiments was carried out to study morphology development under the following conditions :

Blend composition : 67.8/15.3/16.9 wt% PP/MAPP/EVOH
Die temperature : 230°C
Screw speed : 60 rpm
Screw type : metering and mixing
Adapter design : two entrance angles (30° and 70°)

Due to mechanical restrictions, it was not possible to quench the whole die unit. Instead, the following procedure was used. After stable extrusion conditions were established, the extruder was shut off. The die insulation and the band heater box were immediately removed, and the complete die unit was separated from the extruder. The adapter was removed from the slit die, and both pieces were placed on a cooling rack with cooling fans. It was possible to cool the adapter from processing temperature to handling temperature in about 30 minutes, and the slit die in about 45 minutes. The solidified samples from the adapter and slit die were collected, vacuum sealed with a desiccant, and stored in a freezer to prevent morphological changes with time.

Figure 3.9 presents a schematic of the slit die and the chosen locations for the study of the morphology. The respective locations were selected to allow for views parallel and perpendicular to the flow direction, and also to detect changes over the slit channel width (z-coordinate in Figure 3.8). The sections were cut out of the solidified flow geometries and then microtomed into 10 μ m thin slices using a sliding Reichert

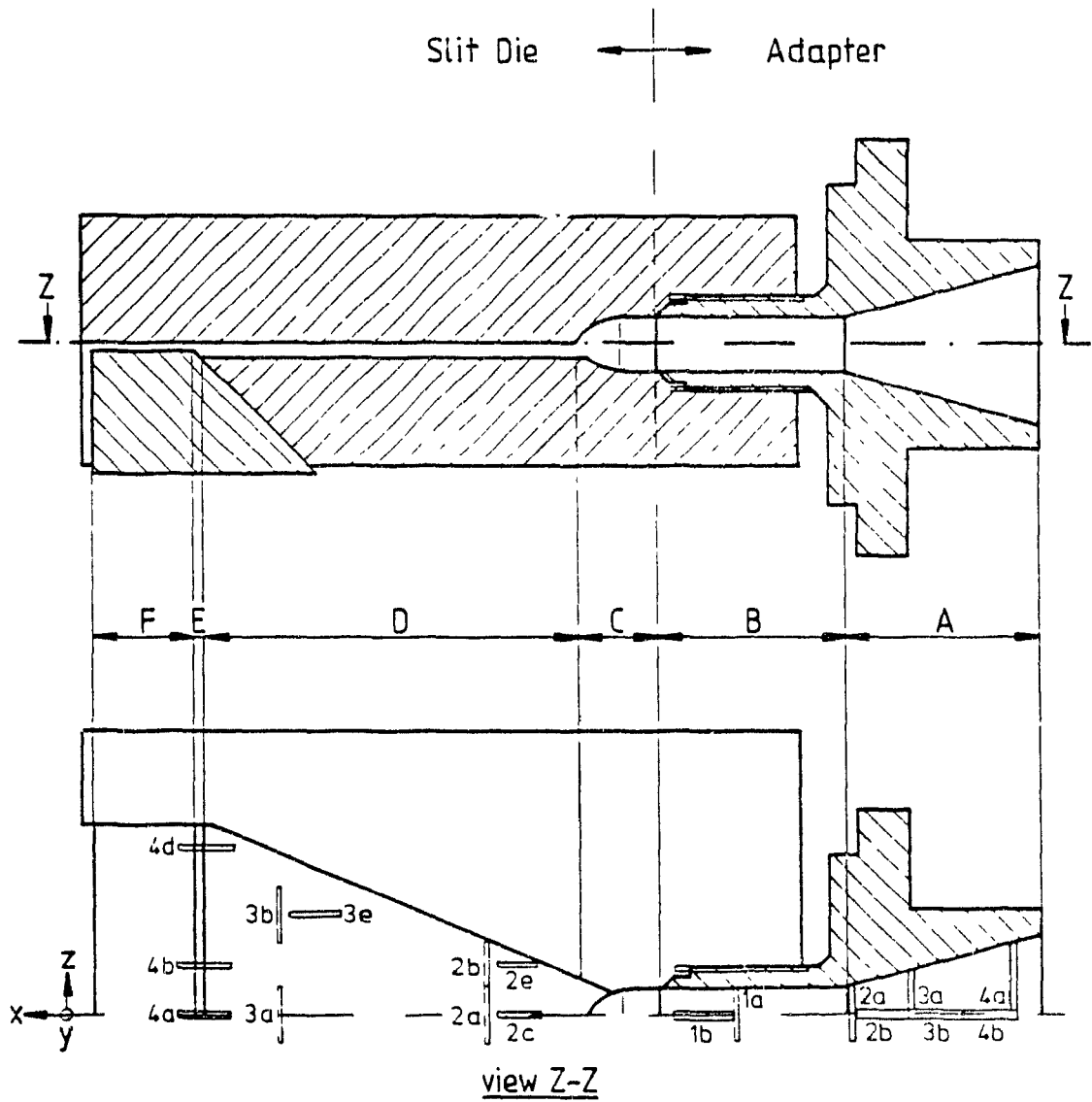


Figure 3.9 Sample Locations for OM Analysis.

microtome, Model OmE, equipped with a Lipshaw surgical steel blade. Optical studies were done using a Leitz Laborlux S optical microscope (OM), under a magnification of 25.

Preliminary evaluation showed that the contrast between the two phases was insufficient, so several different staining agents were tried in an attempt to enhance the contrast. A solution of Toluidine Blue O in ethyl alcohol resulted in the best contrast between the dispersed EVOH phase and PP matrix phase. This solution was used throughout the optical microscopy studies. Microtomed slices were immersed in the staining solution for 24 hours at room temperature, and subsequently placed in immersion oil between two glass slides.

The morphology was studied with a new image analysis system [79] developed in the Department of Chemical Engineering. The glass slide is placed under the objective and focused. The eye-piece for the human eye is replaced by a video camera, which is connected to a personal computer (PC) equipped with a frame grabber and high resolution color monitor. The OM image was produced on the monitor and, due to the insufficient resolution of the human eye for different grey levels, pseudo-colors were used instead of the original grey level image to enhance the contrast. This allowed a more precise analysis of the dispersed phase. After establishing the best contrast between the two phases, an image file was created on the PC which subsequently could be plotted as a hard copy.

In the figures shown for the morphology in the die unit, the dispersed EVOH phase appears black in a white PP matrix phase.

3.5 Morphology Studies

Several key processing parameters were evaluated with regard to their effect on the morphology of the final EVOH/PP blend

product. These parameters were : composition ratio, die temperature, extruder speed, die exit gap thickness, and screw design. The main consideration in these studies related to the feasibility of producing a layered EVOH dispersed phase in the PP matrix phase.

3.5.1 Sample Preparation and Analysis Procedure

Figures 3.10 and 3.11 show the sample locations chosen for the morphological study of extruded ribbon. Sample locations A1 and A4 (Figure 3.10) are fractures parallel to the flow direction, while locations A2 and A3 are in the perpendicular direction. Locations A1 and A2 evaluate morphology at the center of the ribbon, and locations A3 and A4 evaluate morphological variations across the ribbon width. Two additional locations, B1 and B2 (Figure 3.11), both at an angle of 45° to the direction of flow, have been included. The six sample locations provide a detailed overview of the morphology over the width and thickness of the ribbon.

The above locations were marked on the sample of interest. The sample was then frozen in liquid nitrogen for three minutes, and fractured at the marked locations. The fracture surfaces were fixed onto a sample holder using colloidal graphite, and placed in a desiccator to dry for 24 hours. The sample holder was then placed in an Anatech Ltd. Hummer VI Sputtering System, where the sample was coated with a gold/palladium mixture under vacuum. Finally, the sample was inserted into the microscope chamber.

The morphology was examined using a scanning electron microscope (SEM), type JEOL JSM-T300. Tests with several polymers showed that an accelerating voltage of 15kV produced the best image. Thus, this voltage was used throughout the study. Photographs were taken, with a 35mm camera, of representative parts of the fractured surfaces at several magnifications.

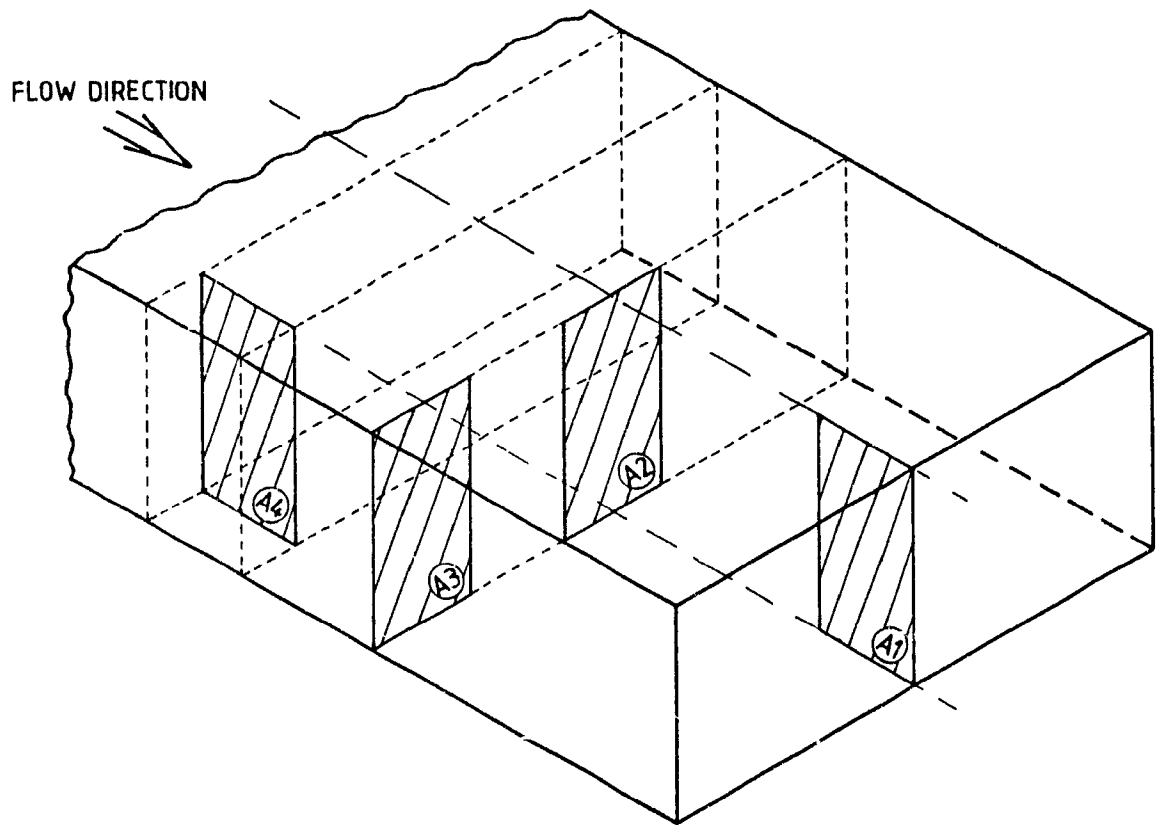


Figure 3.10 Fracture Sample Locations for SEM Analysis (parallel and perpendicular to flow).

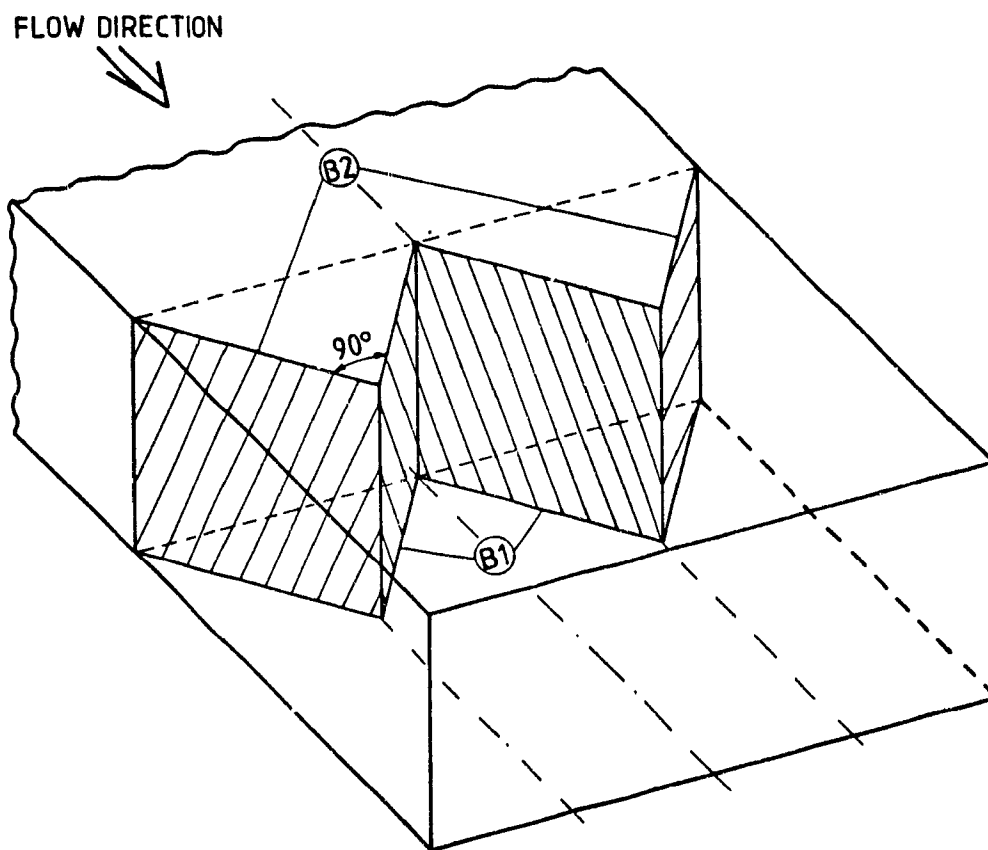


Figure 3.11 Fracture Sample Locations for SEM Analysis (45° to flow).

Each SEM micrograph has, in the lower right corner, a combination of numbers for identification. The first two digits, with a bar on top, specify the scale of the micrograph in μm . The next two digits indicate the acceleration voltage, and the last six digits the individual experiment.

3.6 High Speed Impact Testing

Polymeric materials and their composites and blends are widely used for structural applications. In each instance, the success of the material in the application requires knowledge of its mechanical and chemical property profile. In many applications, ranging from packaging to automotive parts, impact performance is of critical importance.

An instrumented Rheometrics variable-speed impact tester (RVSIT), available in the Department of Chemical Engineering, was used for impact testing. The RVSIT is built around a linear-displacement, velocity-controlled, hydraulically driven mechanism. The system drives a penetrating rod, the shape and size of which may be varied, to impact, short of or up to puncturing, a flat specimen or a formed part. The tester is instrumented and fitted with a data acquisition system, which presents the information on the impact event in the form of load-deflection signals. A detailed description of the RVSIT can be found elsewhere [80-82].

The instrumented impact test is, potentially, a very useful tool for evaluating the dynamic response of materials subjected to a specific set of geometric loading conditions. The biaxial loading imposed by a hemispherical dart on a flat plate specimen rigidly supported over a circular annulus is a typical loading condition. The problem with the use of this kind of test and machine is associated with the lack of standard testing conditions. Work is in progress by ASTM Committee D20 on plastics to develop a practical test method for instru-

mented dart impact testing [83].

According to the procedure employed in this study, the flat specimen was clamped in a 31.5mm diameter ring. A hemispherical probe (12.6mm in diameter) was driven at 0.432 m/s (1000 inch/min) velocity and penetrated through the specimen. All tests were conducted at room temperature.

The relative shape of the load-deflection record is indicative of the deformation and fracture history of the specimen. The load record can be subdivided into deformation stages and characteristic transition points. For any test, the load-deflection record will consist of all, or portions of, the idealized stages indicated in Figure 3.12, and outlined below [84].

Stage A - dynamic offset. Perturbations are generally small and insignificant.

Transition A - start of the linear load-deflection deformation.

Stage B - linear load-deflection deformation.

Transition B - yield. This implies the onset of plastic or permanent deformation, and is not necessarily an indication of cracking.

Stage C - first major permanent deformation. The damage is generally distributed over a relatively large volume, so that a decrease in the load is not observed. For fiber filled or two-phase materials, this can be associated with the development of extensive microcracking or interlaminar shearing of the matrix.

Transition C - maximum load. This is defined as the onset of deformation which does not result in an increase in load. This point has also been identified as the "ultimate" or "peak" load. This transition is usually associated with the first appearance of visible cracks on the tension surface of the specimen.

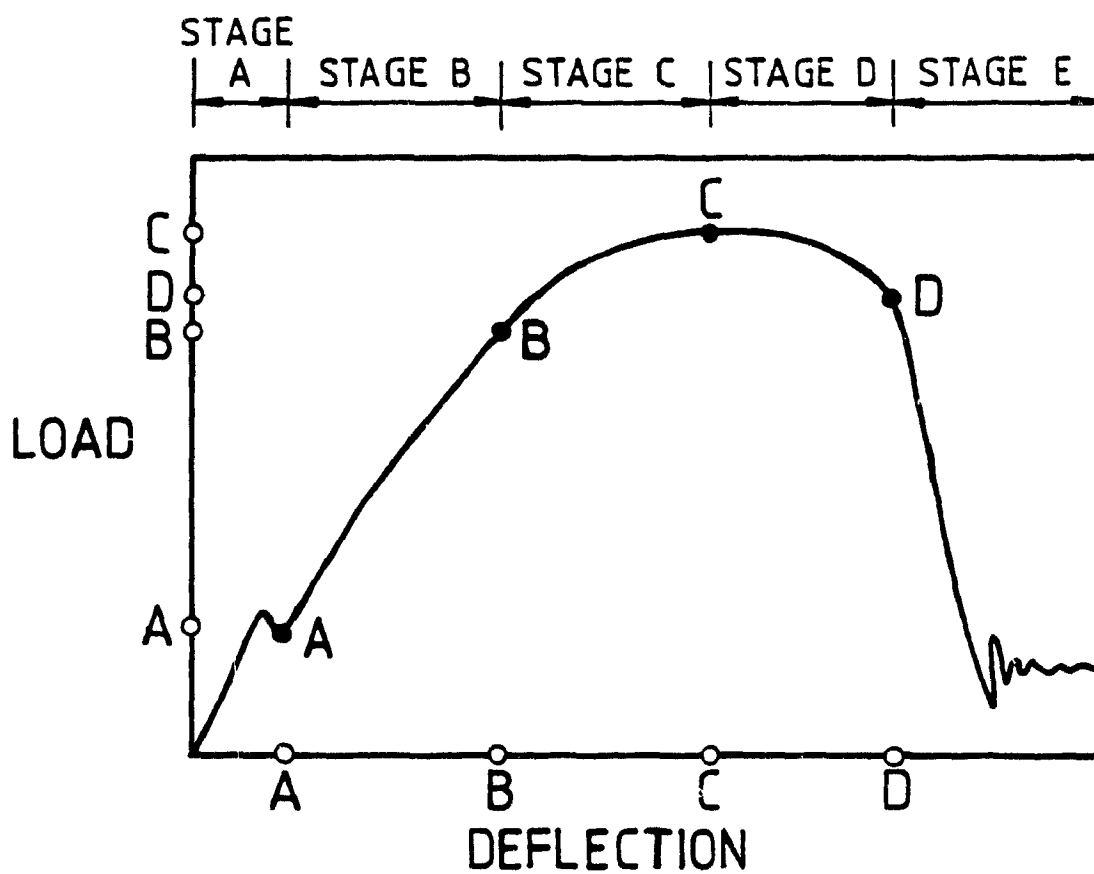


Figure 3.12 Idealized deformation stages and transitions for puncture testing of flat-plate specimens by a hemispherical probe [84].

Stage D - stable or slow-rate deformation after Transition C.
Transition D - end of the test, onset of unstable macro-cracking or fracture, for which the specimen does not have structural integrity.

Stage E - a non descriptive portion of the load-deflection record, essentially showing the probe sliding through the puncture.

Some of the important material characteristics that may be obtained from the test are :

- a) stiffness, which is the slope of the linear elastic load-deflection portion (stage B) of the curve, and
- b) load and deflection values at the following transition points :
 - 1) Transition B, yield (end of linear elastic region), and
 - 2) Transition C, ultimate point (when the curve reaches a significant maximum load for the first time).

The evaluation and discussion of experimental results in this study will be based on data for the slope and ultimate load (force). Due to considerable difficulties in establishing the position of transition B, this value will not be considered in the discussion and evaluation. The values presented here are averaged over 12 specimens, with a reproducibility of $\pm 10\%$.

3.7 Oxygen Permeability Tests

The permeabilities of the four resins and their blends were determined using a Mocon coulometric oxygen detector, in a device similar to the Ox-Tran Model 100 [85]. This device consists of a cell, which is separated into two chambers by the sample ribbon. One side of the sample is flushed with oxygen,

and the other side with a dry nitrogen carrier gas containing 3% hydrogen. Any oxygen molecules diffusing through the film are carried, by the carrier gas, to the sensor, which reacts electrochemically to produce a current that is monitored by a data acquisition system. This current is directly proportional to the mass flow rate of oxygen entering the sensor. Both the oxygen and carrier gas vent directly to the atmosphere, and, when the mass flow rates are identical, there is no differential pressure across the flow. All samples were conditioned for a minimum of 12 hours in the apparatus, with dry nitrogen passing on both sides of the ribbon. The temperature was set at $25.0 \pm 0.1^\circ\text{C}$ with a circulating water bath.

CHAPTER 4

RESULTS AND DISCUSSION

4.1 Morphology Development in the Adapter and Slit Die

4.1.1 Metering Screw

The adapter angle chosen for studies with the metering screw was 30° , because it was thought that the dispersed phase in the blend melt leaving the screw would be coarsely distributed [86,87]. A small, streamlined flow angle would be sufficient to cause coalescence and produce layered structures in the adapter.

Figures 4.1 and 4.2 present OM micrographs parallel and perpendicular to the direction of flow inside the adapter. Micrographs of samples 4a and 4b at position 4 (Figure 4.1) represent the morphological structure of melt leaving the screw. They clearly show that the dispersed phase is coarsely distributed. Sample 4a shows a circular/helical configuration of the EVOH phase, which appears to be similar to the reported circulation patterns in the melt pool between two screw flights in the metering zone [86]. Sample 4b shows oriented EVOH agglomerates in the flow direction, still very coarse, but the onset of a laminar structure is evident.

Further downstream in the conical section of the adapter, in samples 3a and 3b, orientation of the dispersed phase can be seen more clearly. Sample 3a shows a migration of the dispersed phase towards the adapter axis, as was observed for dilute emulsions in the experiments of Mason and co-workers [18]. In sample 3b, the arrangement of the dispersed phase in a laminar structure can be recognized. This effect has been predicted for dilute emulsions [8,20,21]. Surprisingly, the short flow distance from location 4a to 3a is sufficient to

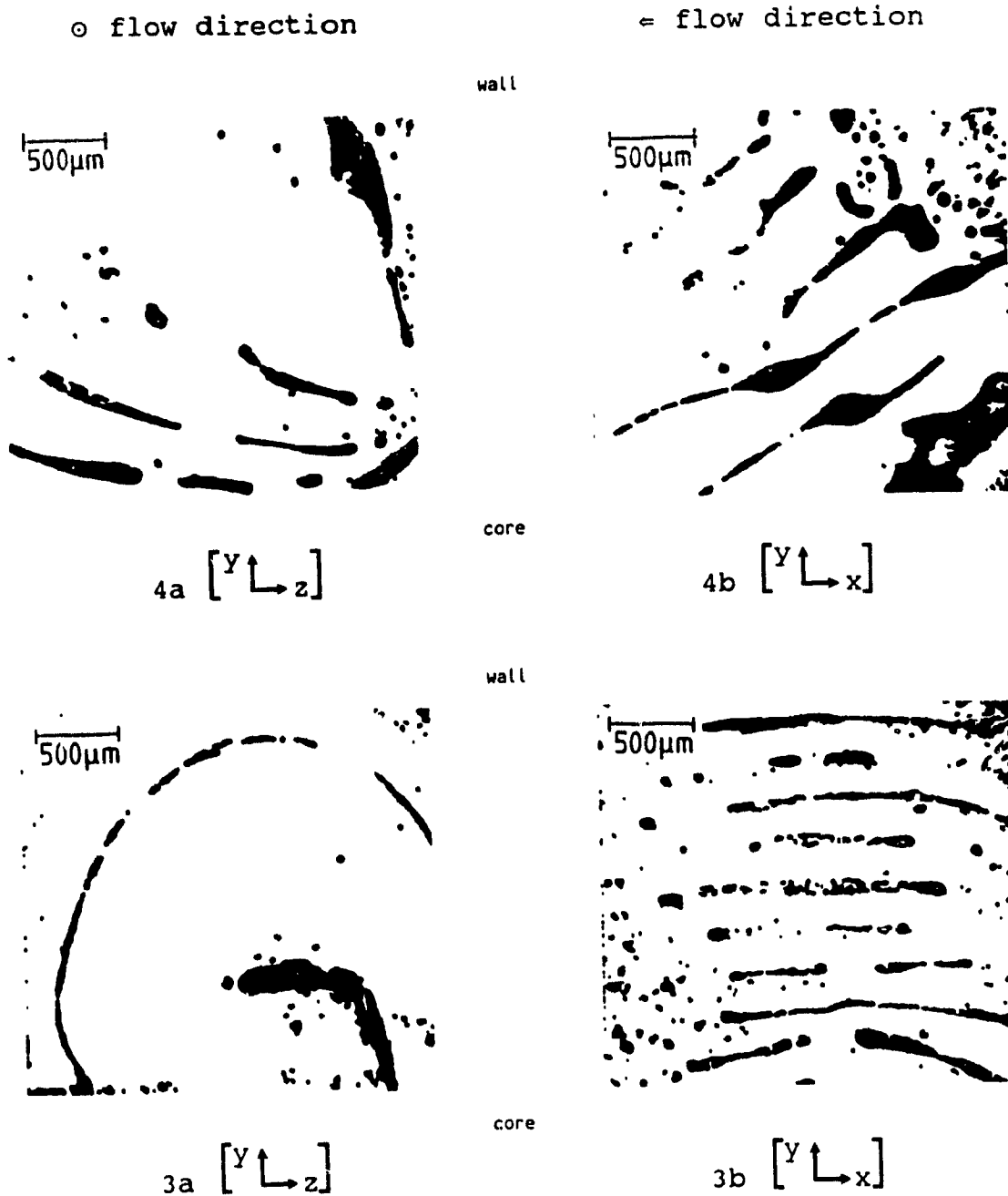


Figure 4.1 OM Micrographs of Morphology Development in Adapter for Samples using a Metering Screw.

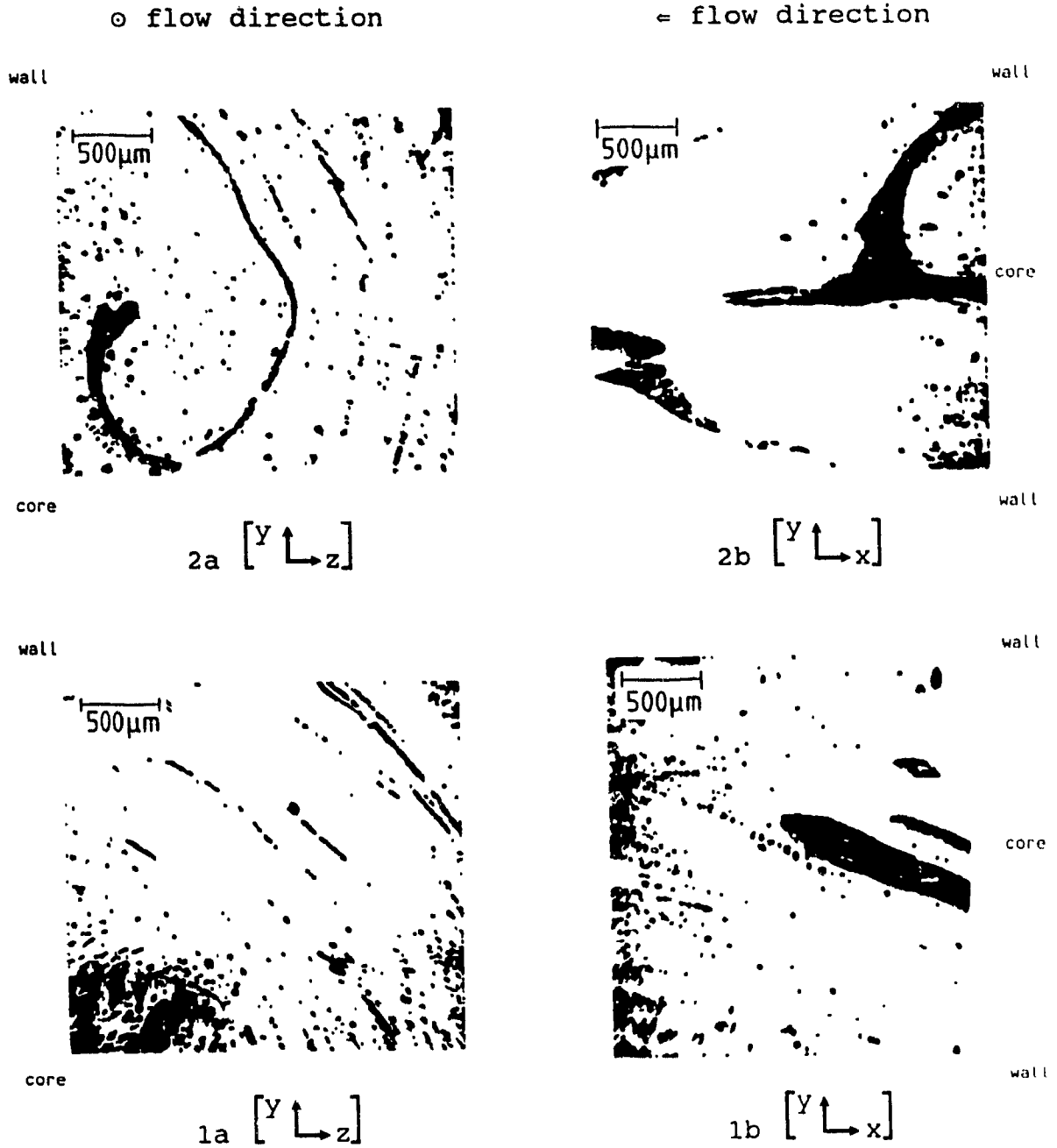


Figure 4.2 OM Micrographs of Morphology Development in Adapter for Samples using a Metering Screw.

create a strong laminar order in the direction of flow.

Subsequently, the melt, having the structure indicated above, enters the tubular section of the adapter (samples 2a and 2b, Figure 4.2), and exits from the tubular section into the slit die (samples 1a and 1b, Figure 4.2). Locations 2a and 1a both show a continuation of dispersed phase migration towards the adapter axis. In 1a, at the end of the tubular section, a large concentration of dispersed phase EVOH can be observed at the center. On the other hand, thin circular laminar arrangements are formed near the channel wall.

Of particular interest in Figure 4.2 is location 2b, where the strong converging flow creates large, fish tail-shaped arrangements in the center axis, which are due to increased migration, coalescence, and extension of the dispersed phase. During the flow through the tubular section of the adapter, migration towards the center is dominant, which results in an agglomeration of the dispersed phase around the center axis, leading to large, cylindrical-shaped dispersed phase arrangements entering into the slit die (location 1b).

Figures 4.3, 4.4, and 4.5 present OM micrographs of the morphological arrangements inside the slit die.

The flow from the adapter into the slit section results in a transformation of the cylindrical-shaped dispersed phase into a thick layer, surrounded by many small platelets, as can be seen in cuts parallel and perpendicular to the direction of flow (Figure 4.3, samples 2a and 2c). In the region near the side walls for location 2, it can be seen that the laminar structure is present in the complete width of the slit flow channel. Very large, thin layers/platelets are present (Figure 4.3, location 2b and 2e).

This laminar structure continues to exist further downstream, as presented in Figure 4.4. Sample 3a shows the dominant layer

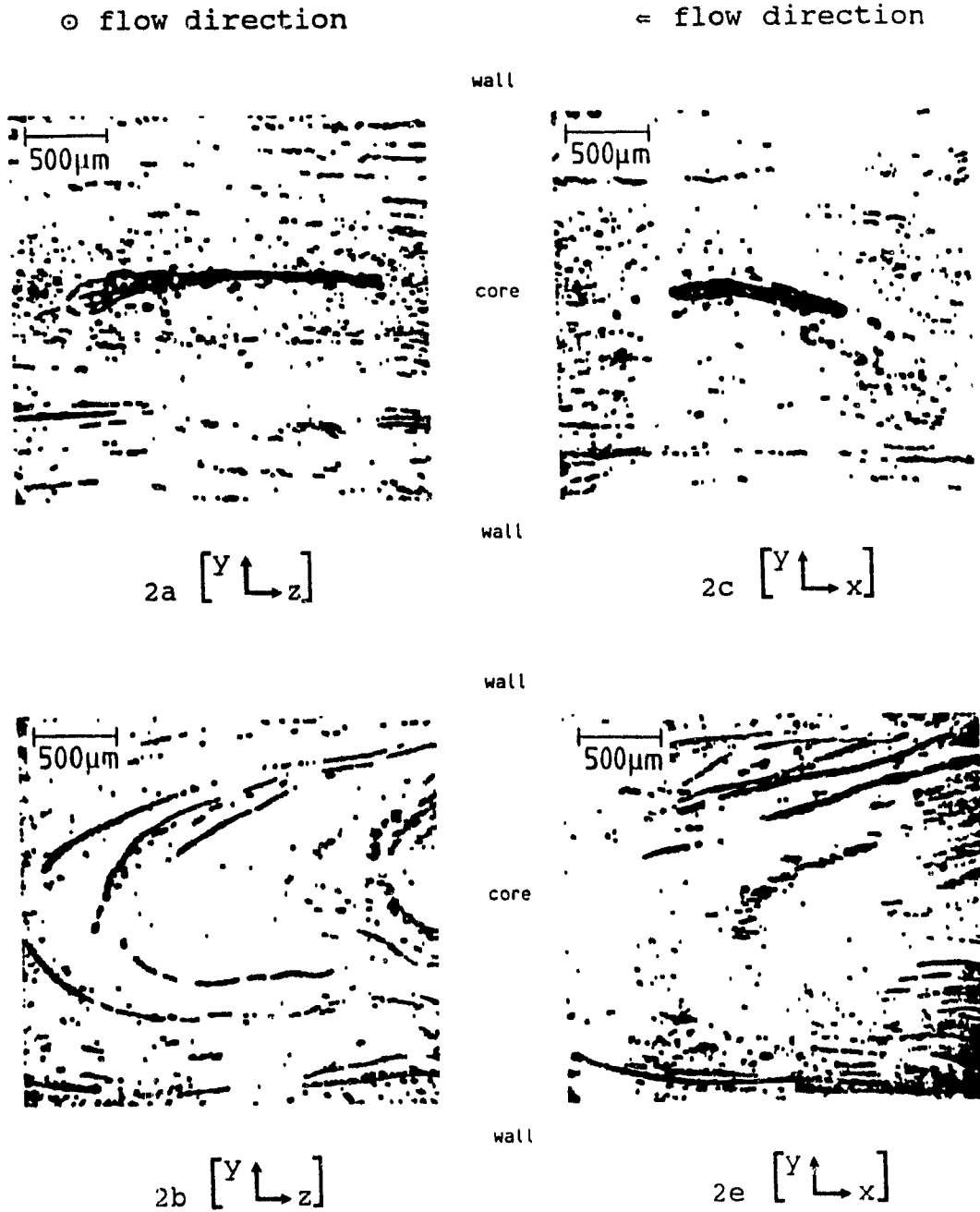


Figure 4.3 OM Micrographs of Morphology Development in Slit Die for Samples using a Metering Screw.

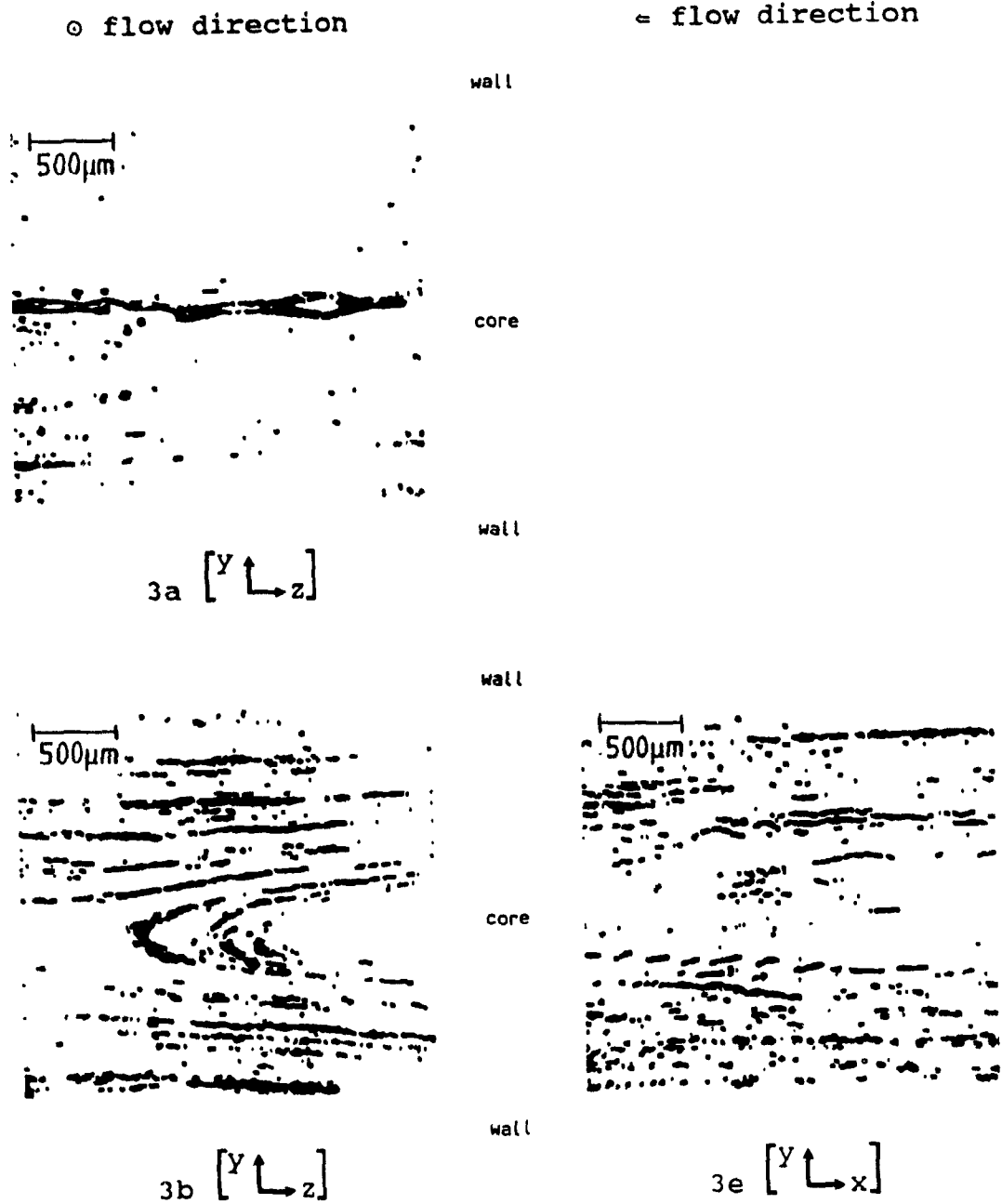


Figure 4.4 OM Micrographs of Morphology Development in Slit Die for Samples using a Metering Screw.

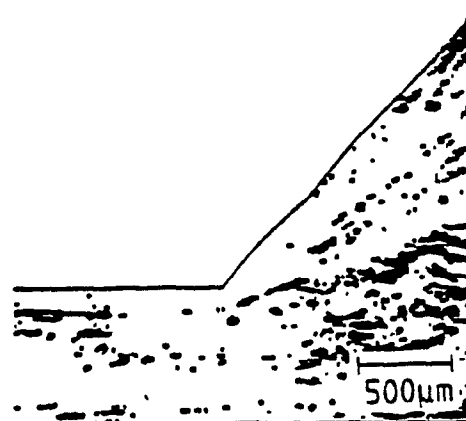
of the center portion of the flow field, which is extended over the whole sample width, surrounded by smaller platelets towards both wall boundaries. In addition, samples 3b and 3e show, that the laminar structure continues to exist over the complete flow channel width in the diverging section (Figure 3.9, x-z plane) of the slit flow geometry.

Sample 2b (Figure 4.3) and location 3b (Figure 4.4), both cut perpendicular to flow, show, in addition to the existence of the laminar structure over the channel width, the influence of the walls on the development of the morphology. The presence of the walls results in a U-shaped morphology close to the walls throughout the die. The retention of the circular laminar structure (sample 1a, Figure 4.2) from the tubular adapter section (\varnothing 9.525mm) into the slit die with a constant height (3.175mm), shows a remarkable flow stability of the laminar structure, even for large dimensional changes of the flow geometry.

Figure 4.5 shows the morphology for the contraction zone, from section D to section F in the slit die (Figure 3.9). Comparing all three locations (4a, 4b, and 4d), it can be seen that the flow behavior is the same over the channel width. In section E, the dispersed phase is streamlined in the contraction section, coalescence is occurring, and the dispersed laminar structure is stretched into exit gap section F. It can also be noticed that the highest dispersed phase concentration (thickest layers) are located in the center. The three micrographs of Figure 4.5 clearly show that the laminar structure persists throughout the contraction.

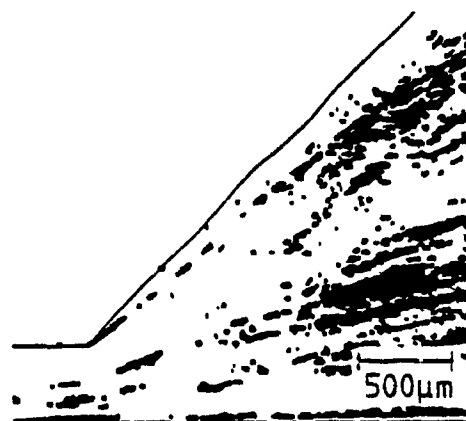
The morphological development along the slit shows that the general features of the blend morphology, consisting of large concentrations of the dispersed phase at the center and finely distributed laminar/layered arrangements near the surfaces, are established in the adapter. In the slit die, only a trans-

← flow direction



wall

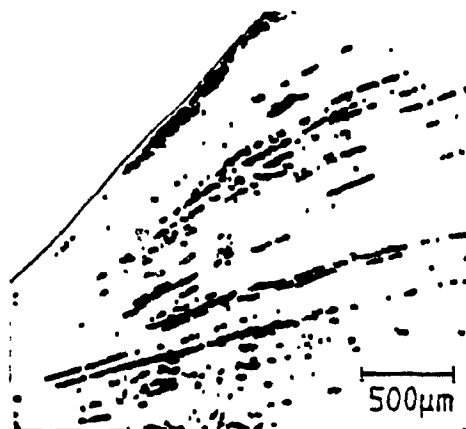
4a [y ↑ x →]



wall

wall

4b [y ↑ x →]



wall

wall

4d [y ↑ x →]

wall

Figure 4.5 OM Micrographs of Morphology Development in Slit Die for Samples using a Metering Screw.

formation from a tubular flow geometry to a diverging slit geometry takes place without major changes in the blend structure. This transformation results in a thick, two-dimensional layer/platelet formation in the center portion of the x-z plane in the diverging slit section, and a continuation of the finely distributed laminar/layered arrangement near the walls.

4.1.2 Mixing Screw

For the mixing screw analysis, an adapter angle of 70° was chosen to enhance converging flow and coalescence in section A of the adapter. The mixing screw employed in a single screw extruder can produce a fine, uniformly distributed dispersed phase in the matrix phase [73-77]. The resulting morphology cannot be transformed into a layered/laminar product morphology [41,42]. It was thought that if the mixing screw employed in this work was efficient in breaking the dispersed phase agglomerates into fine droplets, a large adapter entrance angle should be of help to produce larger agglomerates via coalescence [32]. The agglomerates could then be transformed into a laminar structure along the remaining flow path.

Figures 4.6 and 4.7 present micrographs for the adapter. Compared to the experiments with the metering screw (Figure 4.1), the dispersed EVOH phase is finely distributed around a small, concentrated EVOH phase core (sample 4a, Figure 4.6). The large entrance angle results in extensive coalescence in the short converging section of the adapter, creating large, extended, dispersed phase agglomerates along the axis (samples 3a and 3b, Figure 4.6). In the tubular section of the adapter, these dispersed phase agglomerates continue to flow as cylindrical shaped deformable particles towards the entrance of the slit die (Figure 4.7).

Even though a mixing screw was used to extrude the polymer blend, Figures 4.8, 4.9, and 4.10 convincingly show the lami-

formation from a tubular flow geometry to a diverging slit geometry takes place without major changes in the blend structure. This transformation results in a thick, two-dimensional layer/platelet formation in the center portion of the x-z plane in the diverging slit section, and a continuation of the finely distributed laminar/layered arrangement near the walls.

4.1.2 Mixing Screw

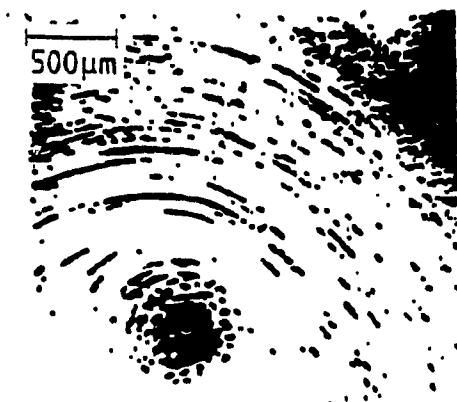
For the mixing screw analysis, an adapter angle of 70° was chosen to enhance converging flow and coalescence in section A of the adapter. The mixing screw employed in a single screw extruder can produce a fine, uniformly distributed dispersed phase in the matrix phase [73-77]. The resulting morphology cannot be transformed into a layered/laminar product morphology [41,42]. It was thought that if the mixing screw employed in this work was efficient in breaking the dispersed phase agglomerates into fine droplets, a large adapter entrance angle should be of help to produce larger agglomerates via coalescence [32]. The agglomerates could then be transformed into a laminar structure along the remaining flow path.

Figures 4.6 and 4.7 present micrographs for the adapter. Compared to the experiments with the metering screw (Figure 4.1), the dispersed EVOH phase is finely distributed around a small, concentrated EVOH phase core (sample 4a, Figure 4.6). The large entrance angle results in extensive coalescence in the short converging section of the adapter, creating large, extended, dispersed phase agglomerates along the axis (samples 3a and 3b, Figure 4.6). In the tubular section of the adapter, these dispersed phase agglomerates continue to flow as cylindrically shaped deformable particles towards the entrance of the slit die (Figure 4.7).

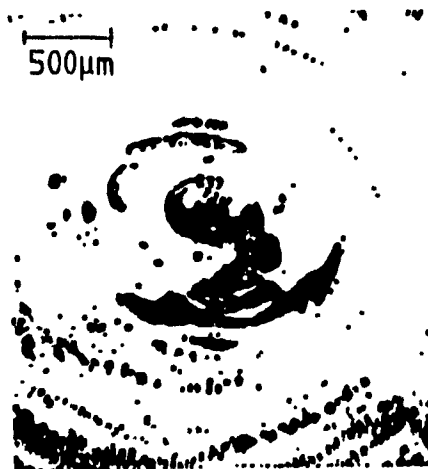
Even though a mixing screw was used to extrude the polymer blend, Figures 4.8, 4.9, and 4.10 convincingly show the lami-

⊙ flow direction

= flow direction



4a [y ↑ z]



3a [y ↑ z]

wall

core

wall

core

wall



3b [y ↑ x]

Figure 4.6 OM Micrographs of Morphology Development in Adapter for Samples using a Mixing Screw.

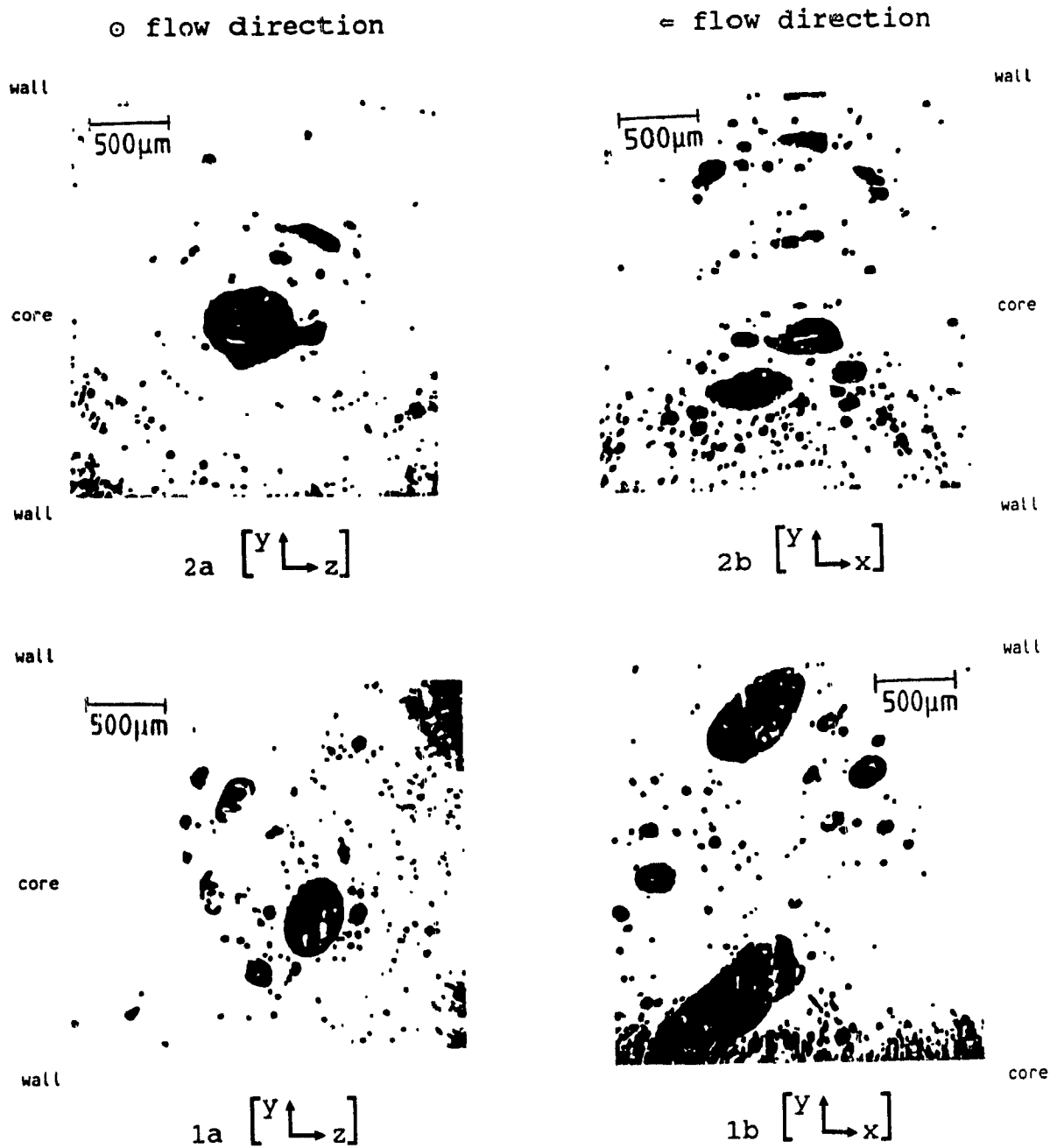


Figure 4.7 OM Micrographs of Morphology Development in Adapter for Samples using a Mixing Screw.

nar arrangement of the dispersed EVOH phase throughout the slit die.

As previously seen in the micrographs for the experiments with the metering screw, the morphology of the center region of the slit die consists of large EVOH layers. The U-shaped morphology near the side walls is also present (Figures 4.8 and 4.9).

Figure 4.10 shows the morphology in section E of the slit die. The coalescence of the fine layer/platelet structure is evident. The laminar structure is not destroyed in the highly extensional flow field, confirming the results of Mason and co-workers [20] for dilute emulsions, which showed that viscoelastic, deformable particles can be highly extended before breakage occurs. Sample 4d shows that the dispersed phase continues to flow in laminar arrangements through the exit gap.

The above morphological analysis has shown that it is possible to achieve a laminar arrangement of the dispersed phase in the matrix phase, even when a mixing screw is used to extrude the polymer blend system. The large entrance angle in section A of the adapter (Figure 3.9) enhances coalescence in this section, resulting in larger dispersed phase agglomerates which exhibit a laminar/layered structure throughout the downstream sections of the die unit.

Subramanian [41,42] showed that a HDPE/modified nylon blend, when subjected to normal processing under good mixing conditions, resulted in a product where the nylon was homogeneously dispersed within the HDPE matrix phase. Subramanian concluded that a laminar structure could be achieved only when the dispersed phase was prevented from forming tiny droplets, thus indicating that good mixing conditions would not be suitable to produce laminar arrangements of the dispersed phase in the matrix phase.

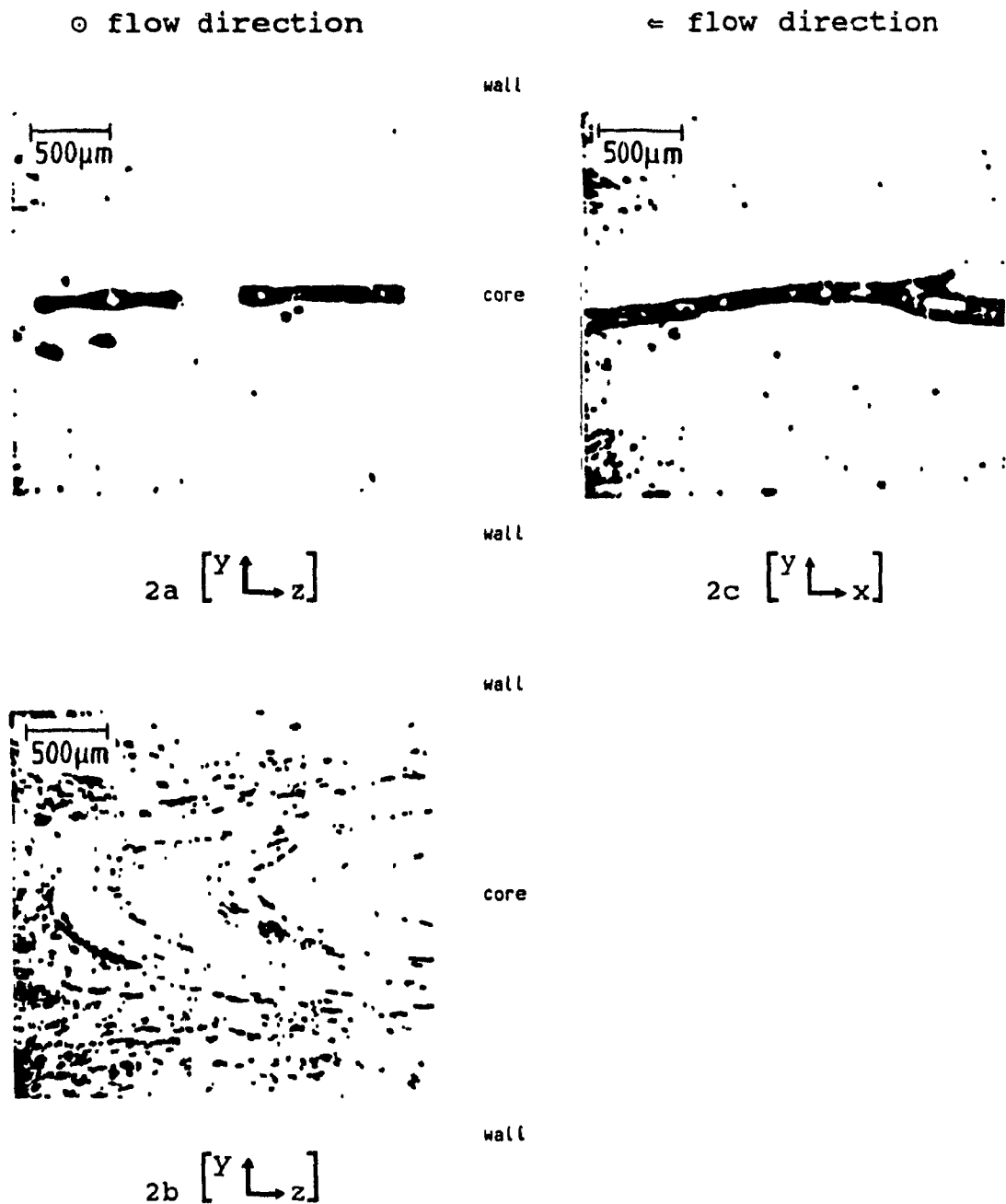
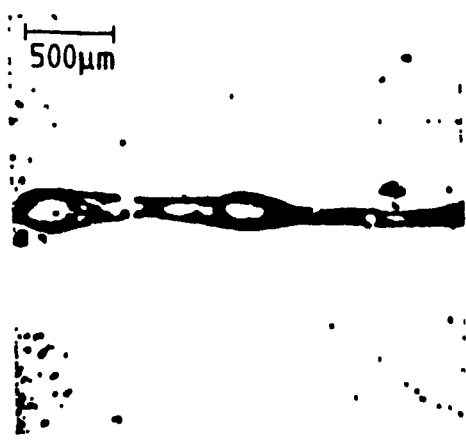


Figure 4.8 OM Micrographs of Morphology Development in Slit Die for Samples using a Mixing Screw.

⊙ flow direction

← flow direction

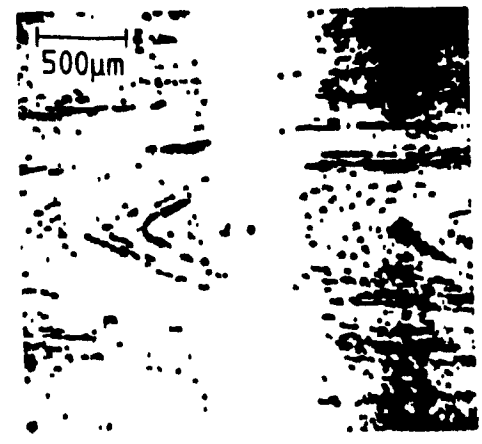


3a [y ↑ z →]

wall

core

wall

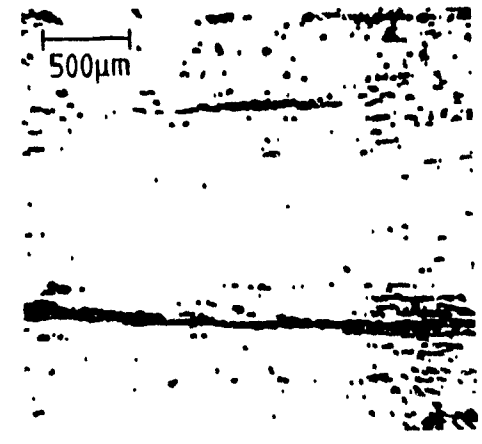


3b [y ↑ z →]

wall

core

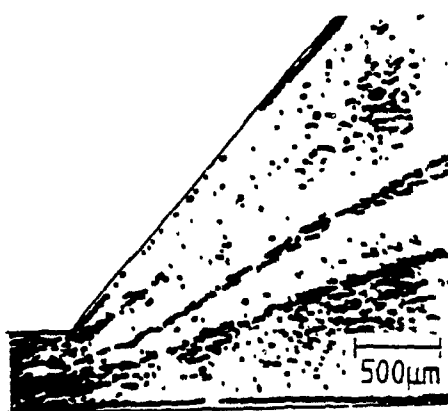
wall



3e [y ↑ x →]

Figure 4.9 OM Micrographs of Morphology Development in Slit Die for Samples using a Mixing Screw.

= flow direction

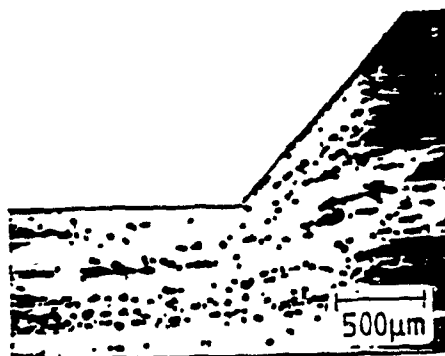


wall

4a [y ↑ x →]

wall

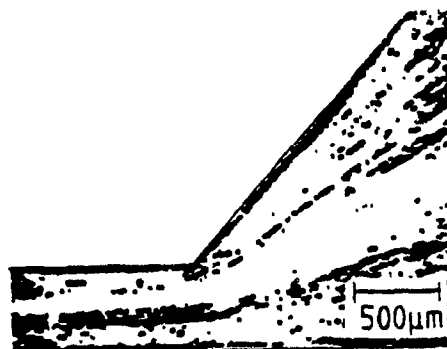
wall



4b [y ↑ x →]

wall

wall



4d [y ↑ x →]

wall

Figure 4.10 OM Micrographs of Morphology Development in Slit Die for Samples using a Mixing Screw.

4.1.3 Analysis of Flow Kinematics

The analysis of the flow field in the slit die unit was performed jointly with Dr. K.T. Nguyen, using a commercial package, FIDAP, from Fluid Dynamics International, Inc. FIDAP is a general purpose finite element program which can simulate many classes of incompressible fluid flows by solving the conservation equations (mass, momentum and energy).

The influence of different adapter angles, 30° and 70° , on the flow field was considered (Figures 4.11 and 4.12). The velocity field was obtained under the following assumptions:

- i) the flow is isothermal and steady,
- ii) inertia is negligible,
- iii) no slip at the die walls,
- iv) the material is considered as a single fluid, i.e., the effect of surface tension is neglected and the viscosity of the dispersed phase is assumed to be the same as the matrix phase,
- v) the viscosity is described by a Power Law model.

As a result of assumption (iv), the deformation of the dispersed phase is simply the deformation of material lines and surfaces.

The literature review has shown that theoretical deformation predictions are only valid for very small deformations and simple flow fields. A detailed analysis of the general deformation solution of Cox [5] showed that this solution cannot be used in the complex flow field encountered in the adapter and in the diverging and converging sections of the slit die. The analysis of the morphology development in Chapters 4.1.1 and 4.1.2 has shown that the dispersed phase is oriented in lamellar arrangements in the matrix phase, thus indicating that the surface tension effect of the EVOH phase on the deforma-

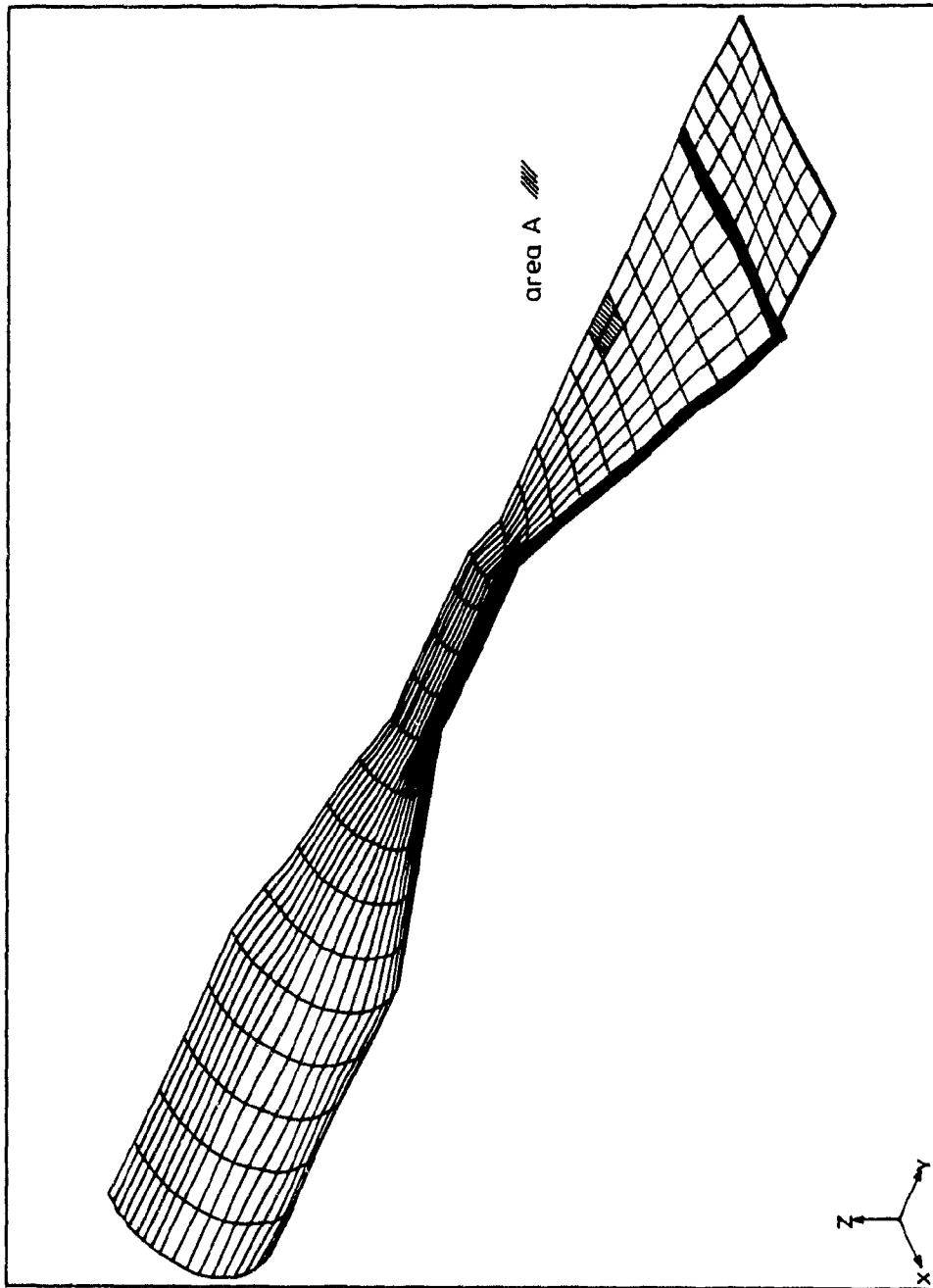


Figure 4.11 Finite element mesh for a 30° adapter and slit die design.

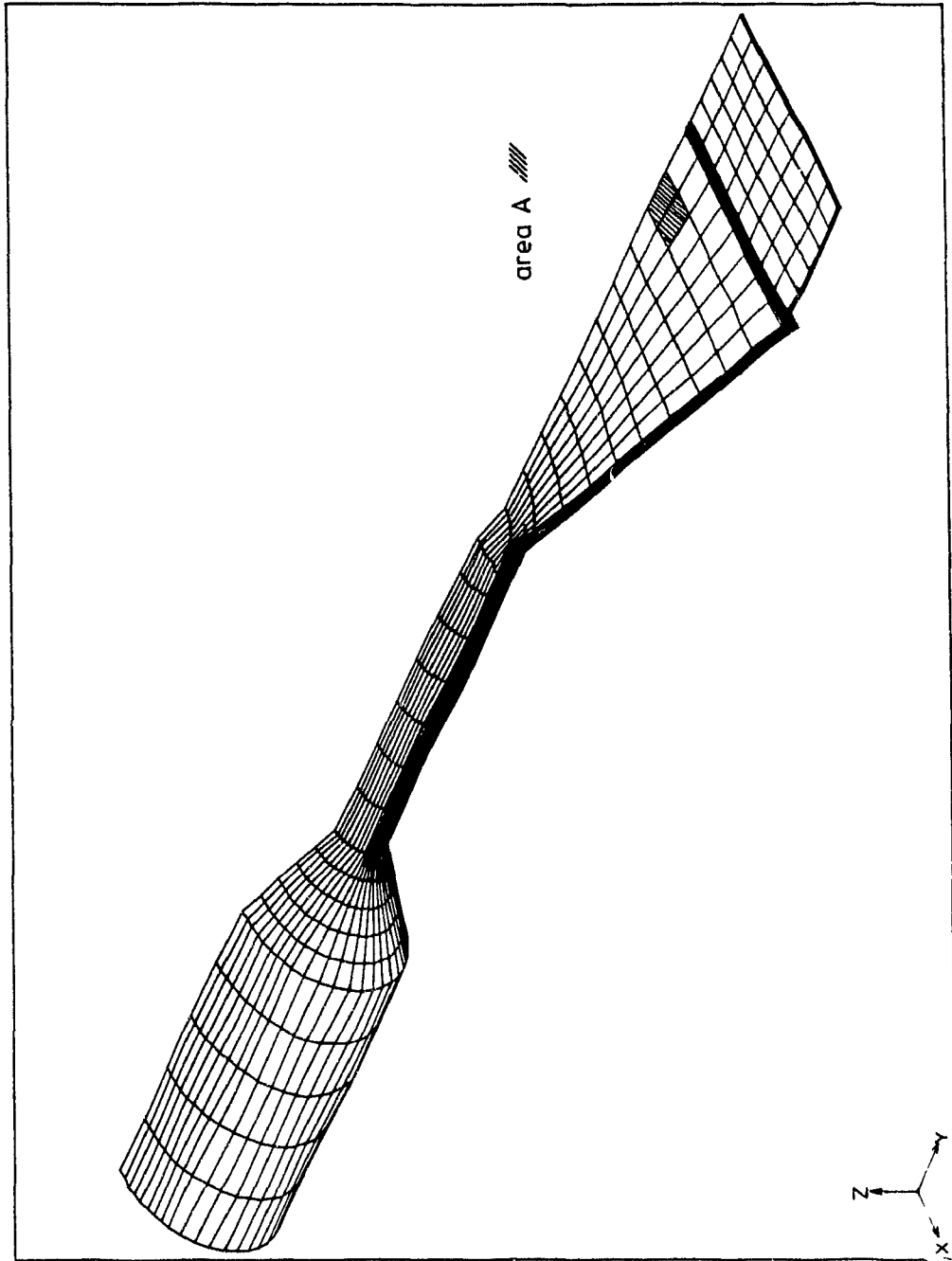


Figure 4.12 Finite element mesh for a 70° adapter and slit die design.

tion is minor compared to the effect of viscosity. On the other hand, Lepoutre [40] calculated that the viscosity ratio, η_{EVOH}/η_{PP} , varied, depending on the shear rate, from 1.1 to 1.7 for a temperature range from 200°C to 240°C. The small surface tension, and the viscosity ratio near unity for the PP/EVOH blend system, indicate that deformation studies with a single fluid model would yield results which could help to improve the understanding of the deformation behavior inside the adapter and slit die, at least qualitatively.

Four cubic particles were introduced at the entrance of the flow geometry and their individual material particle paths were calculated along the adapter and slit die.

Figures 4.13 and 4.14 show the particle deformation behavior for 30° and 70° adapter angles, respectively. The rate of deformation in the conical section is larger for the 70° adapter, due to a sharp decrease in flow area over a shorter distance. Both figures show that the predominant, uni-directional deformation in the y-direction inside the adapter is transformed into a two-dimensional deformation in the x-y direction in the slit die. This two-dimensional deformation occurs shortly after entering the diverging section of the slit die, and has been shown to exist under real processing conditions (Figure 4.3). The analysis shows, for both adapter angles, that this two-dimensional deformation is maintained throughout the diverging section, especially in the core. This also has been shown in the optical microscopy analysis (Figures 4.4 and 4.5).

Figures 4.15 and 4.16 show a close-up of the adapter section for both cone angles. Both figures show that, even though the velocity at the center is highest, the center particle stretches less than the two particles closer to the wall. The deformation behavior of the particles closer to the wall is strongly influenced by the no-slip boundary condition. In real

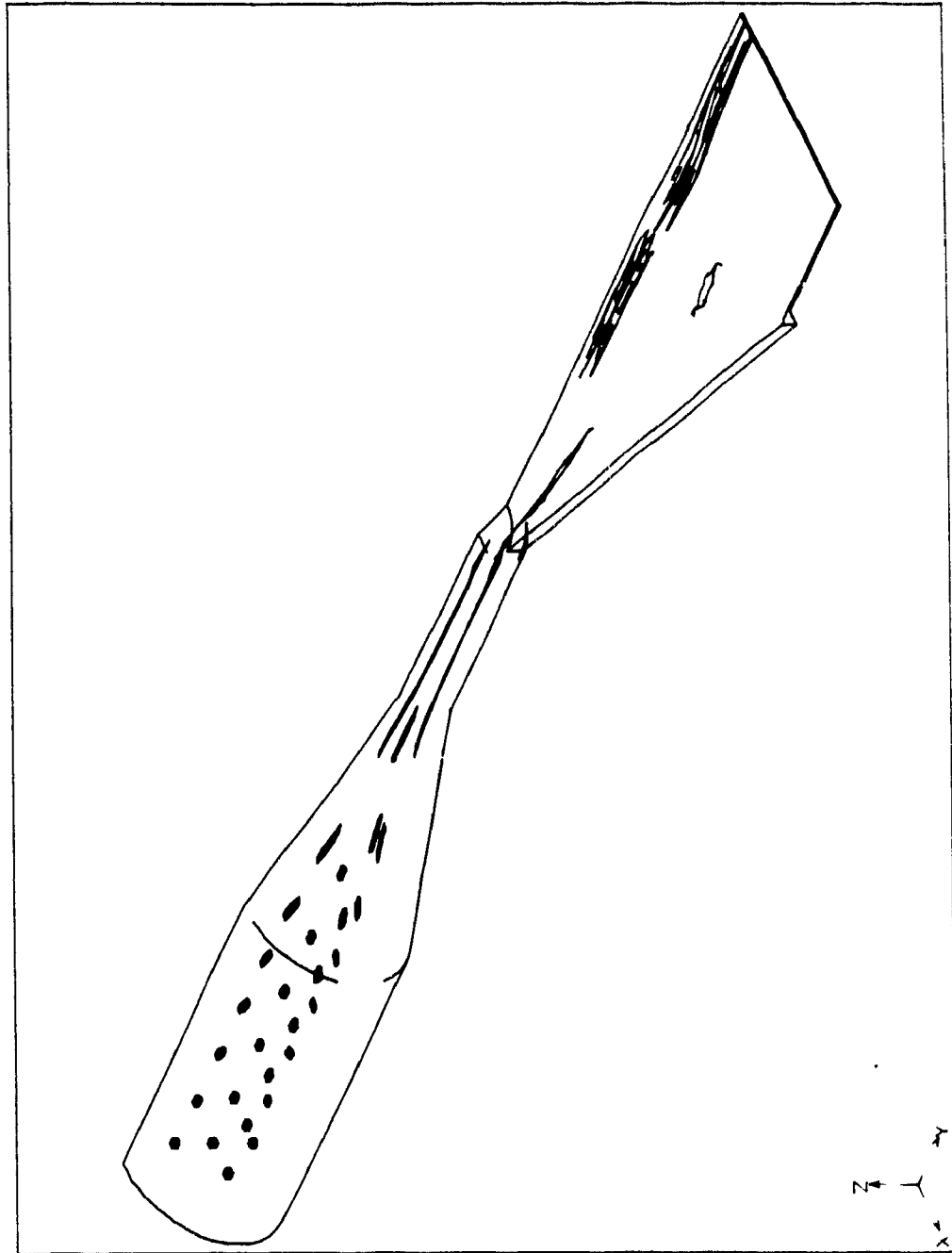


Figure 4.13 Deformation behavior of four particles for a 30° adapter and slit die design.

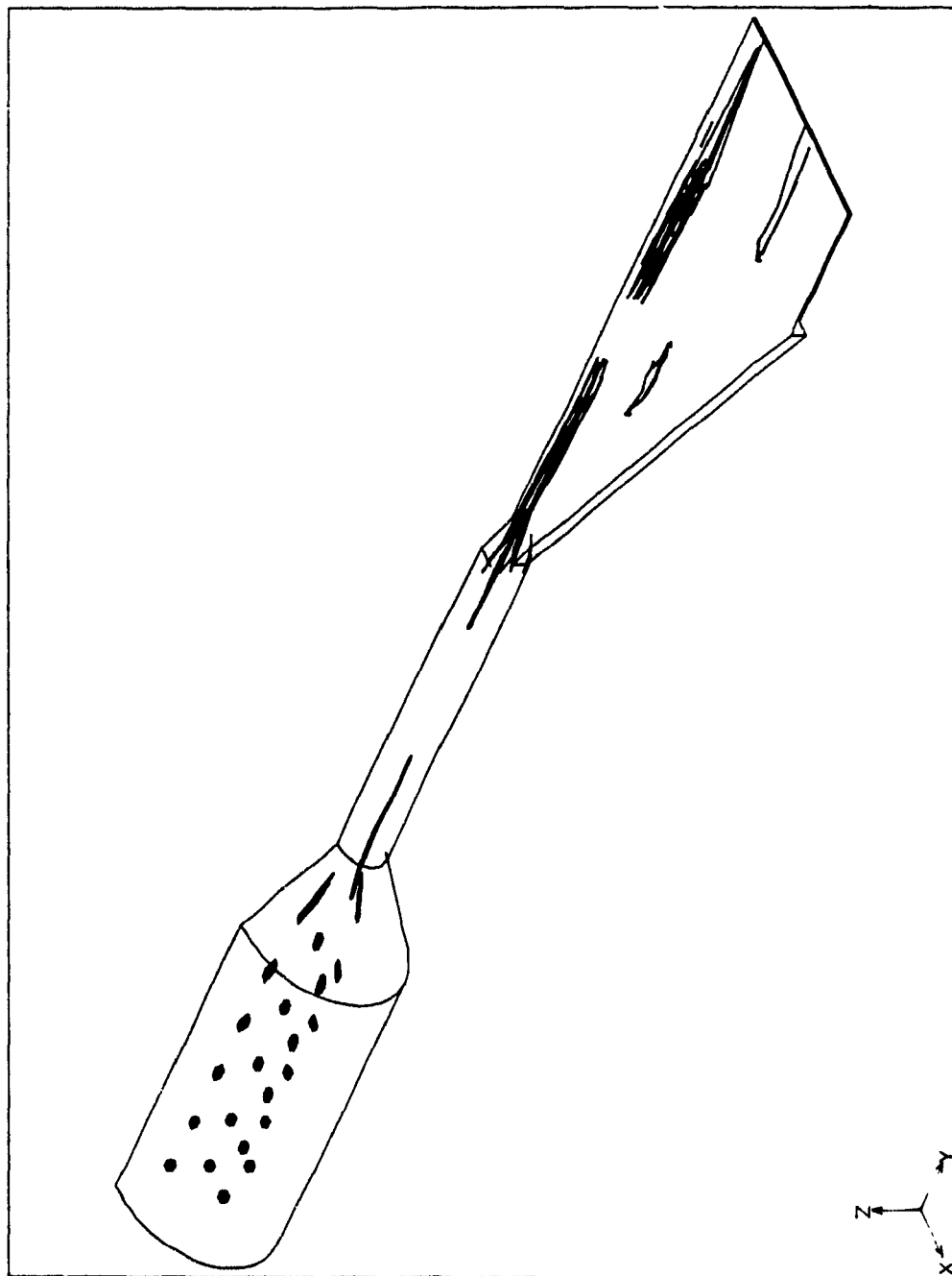


Figure 4.14 Deformation behavior of four particles for a 70° adapter and slit die design.

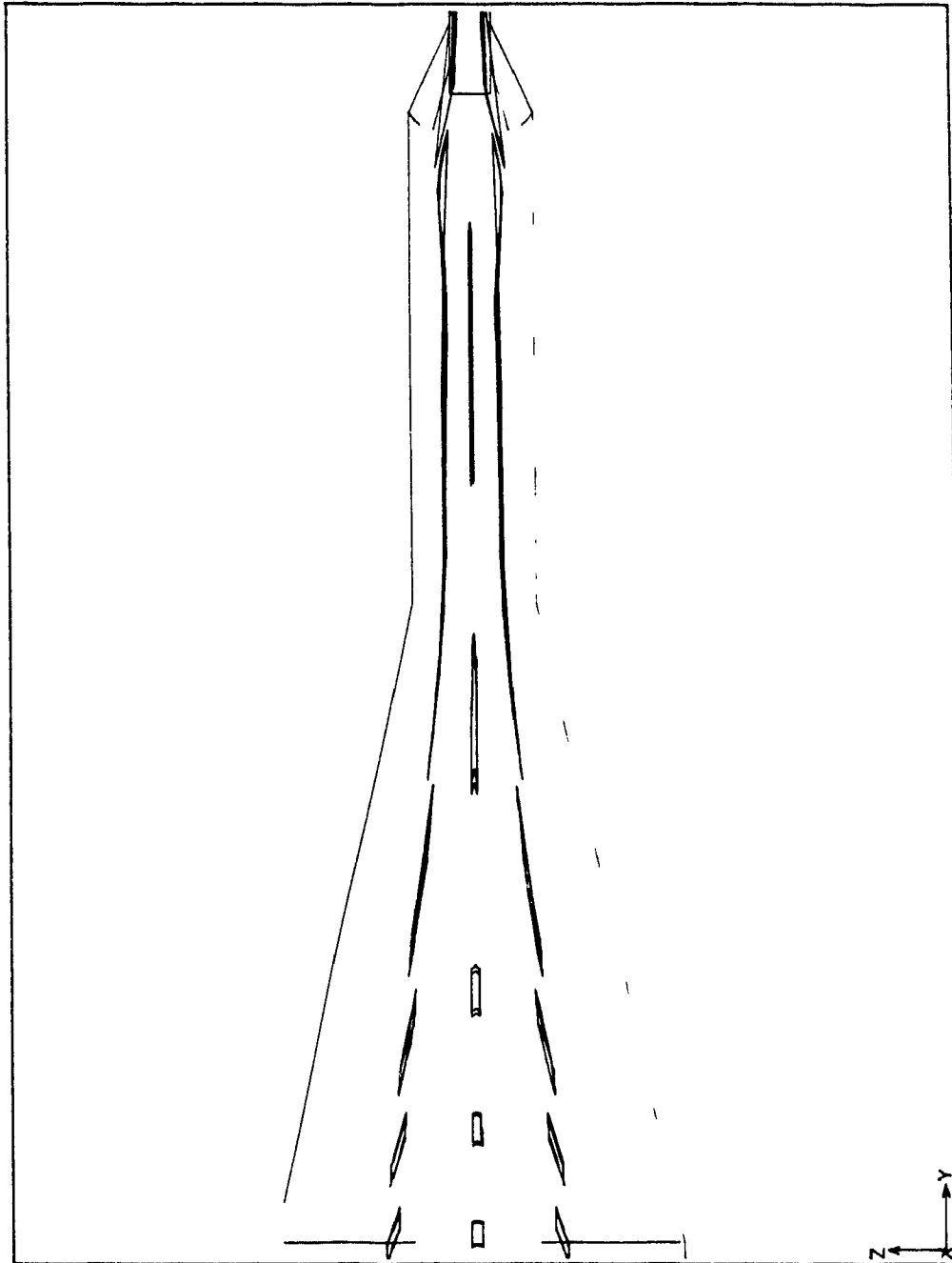


Figure 4.15 Deformation behavior of three particles in a 30° adapter.

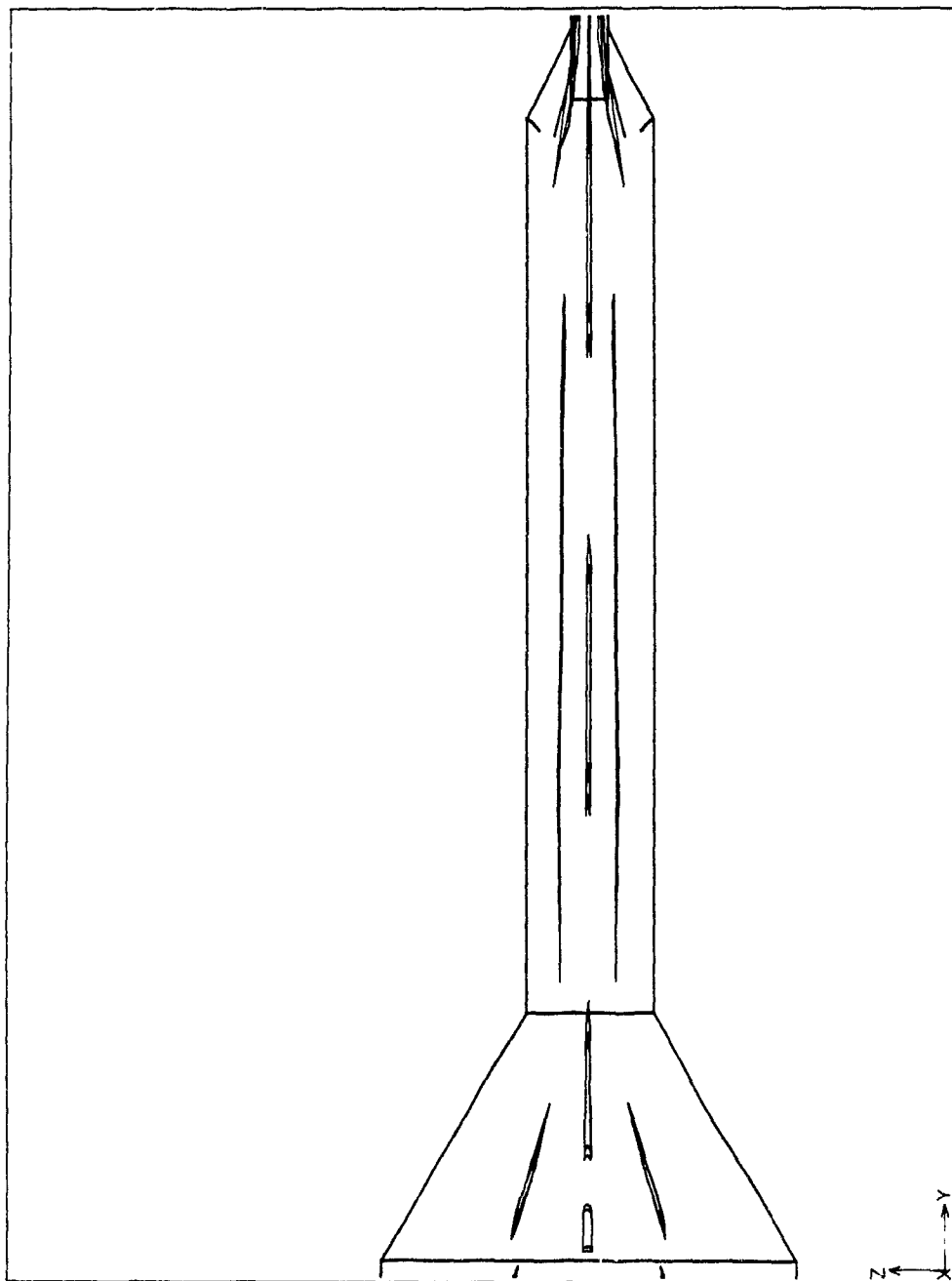


Figure 4.16 Deformation behavior of three particles in a 70° adapter.

processing conditions, such a stretching ratio of the dispersed phase cannot be accomplished, and the particle breaks up into smaller particles. This explains the more homogeneous distribution of the dispersed EVOH phase in the PP matrix phase towards the wall (Figure 4.2), whereas in the core, a cylindrical EVOH distribution can be found.

Figures 4.17 and 4.18 show the deformation of two center particles in the diverging section of the slit die. For both cone angles, the deformation along the center axis of the die is undisturbed and results in a two-dimensional layer formation (x-y plane). The layers in the diverging section of the 70° adapter/slit die unit are longer compared to deformations for the 30° adapter/slit die unit. For both angles, particles located closer to the wall of the slit die exhibit complicated deformations, due to combined shear and extensional flows. Under real processing conditions, this would result in breakup of layers into smaller platelets. Figure 4.3 demonstrates this for the EVOH/PP blend system.

Figures 4.19 and 4.20 present a front view (y-axis) of area A (see Figures 4.11 and 4.12), and show the deformation of three particles. Again, it can be recognized that the deformation in the core results in a thin laminar arrangement. Towards the walls, the deformation of the particles is irregular and complicated. Under processing conditions, this results in a laminar arrangement of the dispersed phase in the core and a homogeneous arrangement towards the walls. This has been shown in the optical microscopy studies, as presented in Figures 4.4 and 4.5.

The analysis of flow kinematics has shown that the deformation behavior of a droplet, calculated for a single fluid model, can give qualitative information regarding the influence of die design on the morphology. The deformation of a particle element along the center axis results in a well defined lami-

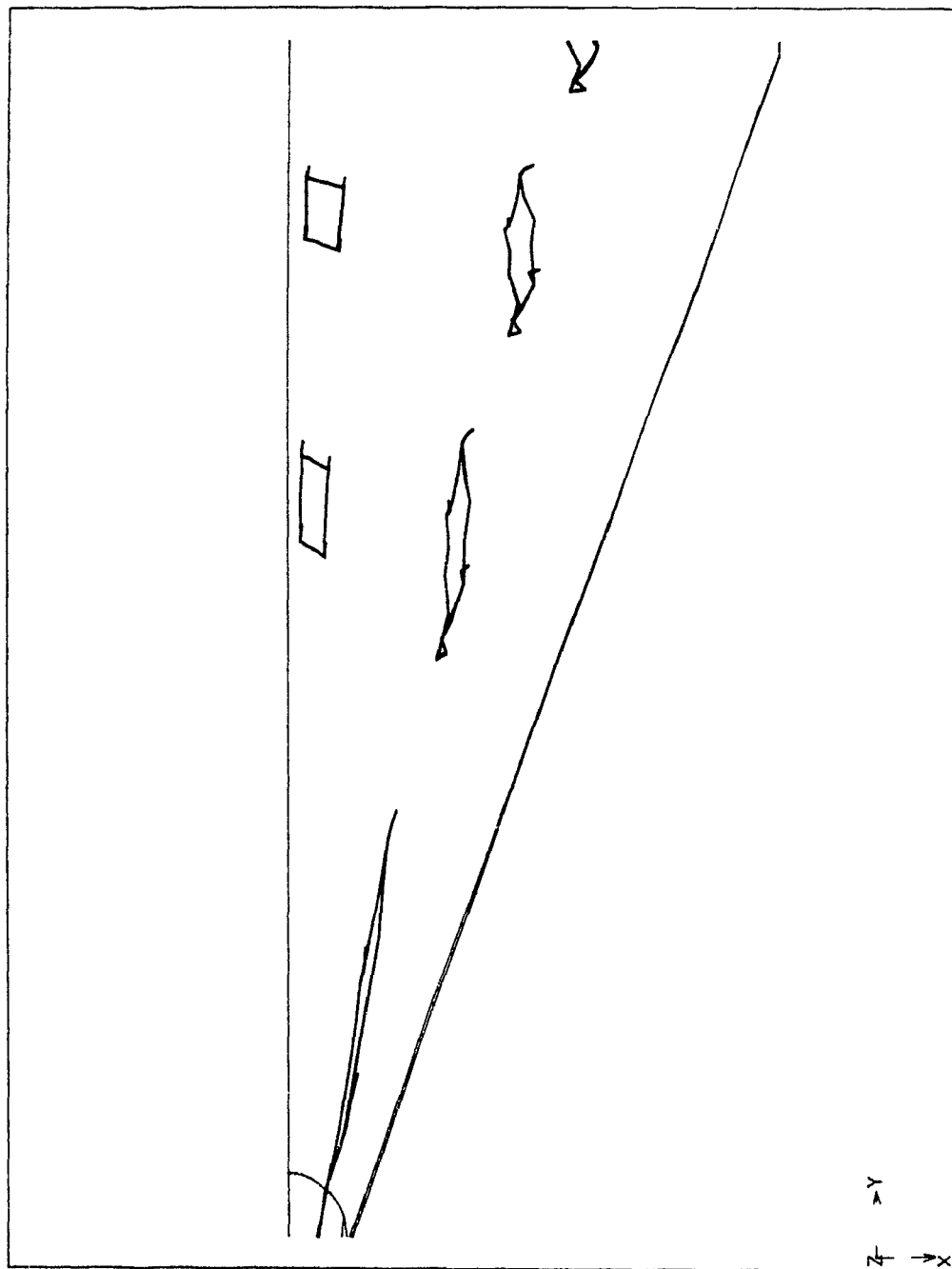


Figure 4.17 Deformation behavior of two particles in the diverging section of the slit die (30° adapter angle).

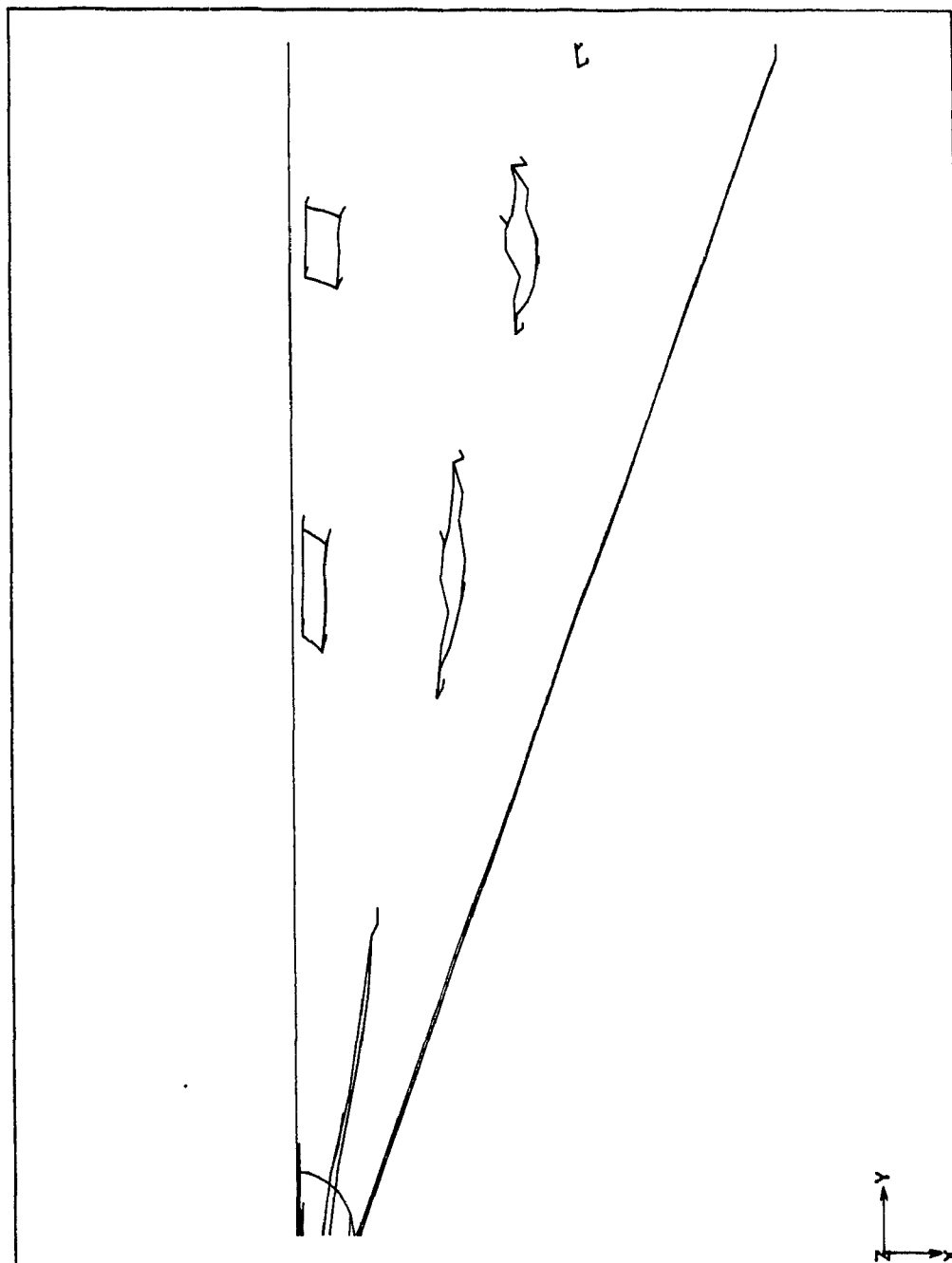


Figure 4.18 Deformation behavior of two particles in the diverging section of the slit die (70° adapter angle).

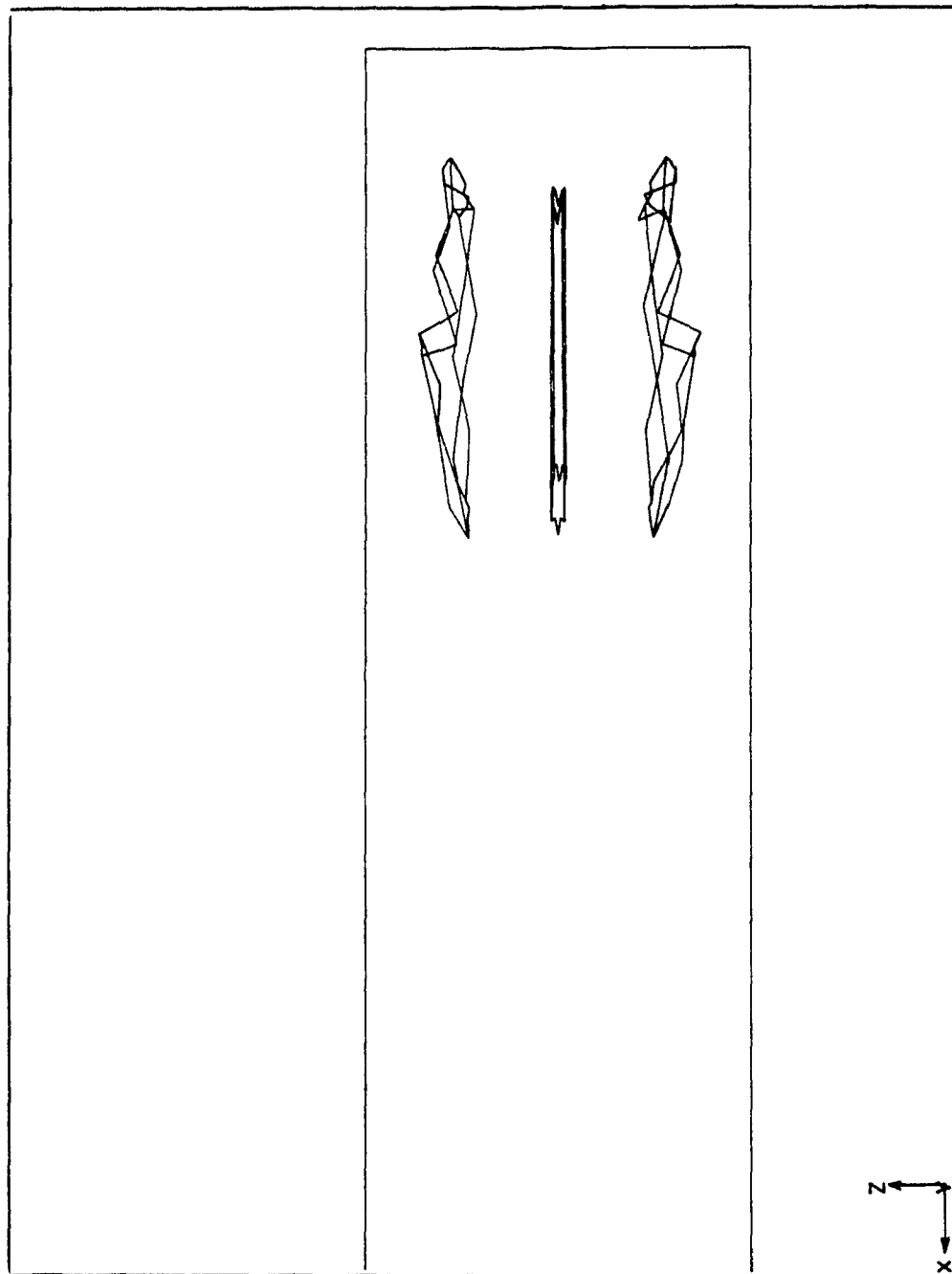


Figure 4.19 Deformation of three particles.
Front view (y-axis) of area A (see Figure 4.11).

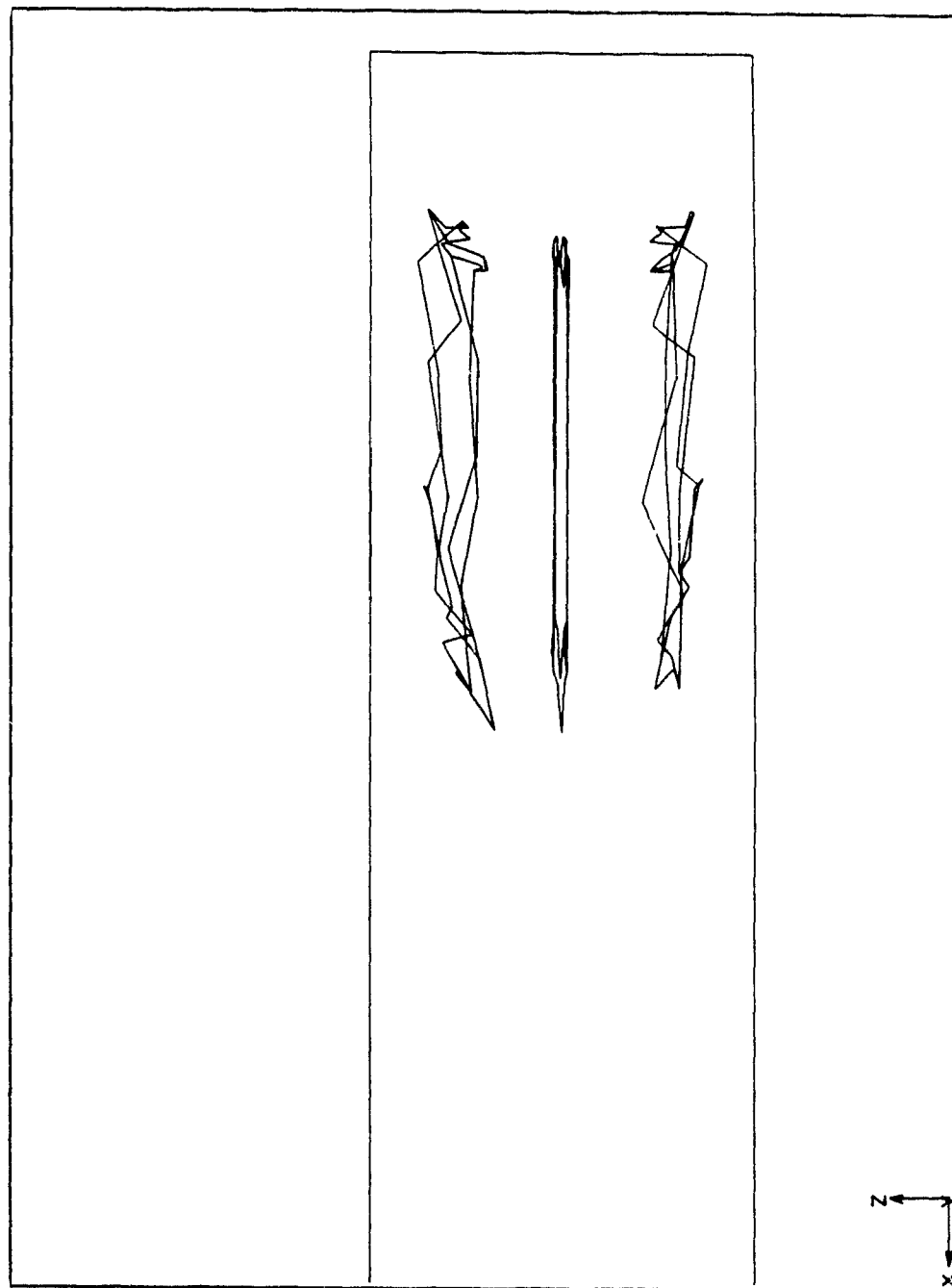


Figure 4.20 Deformation of three particles.
Front view (y-axis) of area A (see Figure 4.12).

nar structure, whereas wall effects disfigure the particle and make characterization impossible. In real processing conditions, this may lead to breakup of the dispersed phase and a morphology containing small platelets, fibers, and spheres.

4.2 Morphology of Extruded Ribbons

4.2.1 Morphology of Pure Resins

The morphology of ribbons extruded from each of the four individual resins was evaluated under the SEM to differentiate between the "virgin" morphology, characteristic to each individual resin, and the morphology introduced due to different composition ratios and processing conditions.

The following processing conditions were employed :

Die Temperature	:	215°C
Screw type	:	metering
Screw speed	:	60 rpm
Exit gap	:	0.5 mm

The die temperature was restricted to 215°C, due to the processing behavior of EVOH. As a single phase, EVOH could only be extruded at 215°C [66], using available processing equipment. Below this temperature, the extruder seized, and it was not possible to melt and transport the EVOH along the screw channel. Above 215°C, the viscosity of the extrudate was very low, and the cooling and take-off equipment could not handle the material.

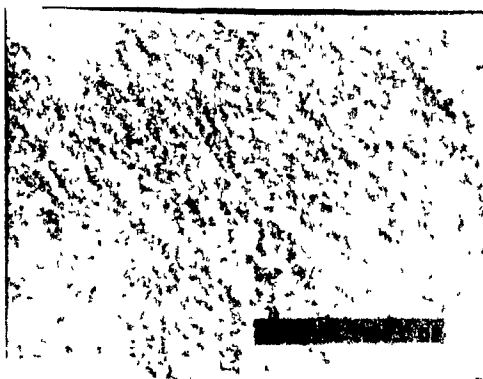
Figure 4.21 shows micrographs of the morphology of three resins incorporated in this study. The morphologies of MAPP1 and MAPP2 are identical, so only one micrograph is presented. As can be seen, the fractured surfaces are smooth and uniform, and no distinct morphology is detectable.



PP



EVOH



MAPP1

Figure 4.21 SEM micrographs for the Pure Resins.

The MAPP1 (and also the MAPP2) micrograph shows evenly distributed, very small, white, spherical inclusions. These inclusions could not be identified. Moreover, the two manufacturers of the resins were not willing to supply this information. In view of the findings to be discussed later, it does not appear that the nature of the inclusions is a critical factor in determining the morphology of the extruded ribbons.

4.2.2 Morphology of Extruded Blends

Three different types of blends were evaluated :

- 1) Blends of PP and EVOH without any compatibilizing agent.
- 2) Blends of PP and EVOH with addition of MAPP adhesive polymers.
- 3) Blends of MAPP2 adhesive polymer and EVOH.

The analysis of the morphology development in the die unit in Chapter 4.1 has revealed that the dispersed phase has a laminar arrangement in the matrix phase. The morphology analysis of the extruded ribbon will show that this laminar structure can be divided into layers and platelets.

All three blend types exhibit morphological variations across the ribbon thickness. These variations, from the extrudate core to the surface, may vary, depending on the blend type and processing conditions used. In general, however, the morphology may be divided into three distinct zones:

core : layered structure over complete sample width; layer thickness and overall dimensions depend on processing conditions.

intermediate : dispersed phase agglomerates in different sizes and shapes; platelets, fibers, and spheres.

surface : dispersed phase mainly in the form of spheres or short fibers.

Depending on composition ratio and processing conditions, a clear distinction between these three zones was not always immediately evident, and it was necessary to study micrographs for all six sample locations (Figures 3.10 and 3.11), in order to distinguish between the various zones. In the following discussion, the morphological variations across the ribbon thickness will be presented for a 80/20wt% (PP+MAPP)/EVOH composition ratio, for all three blend types.

As pointed out in section 4.1.1, the slit die side walls produce a U-shaped morphology close to the wall. This U-shaped morphology ("Flow Lines") is maintained as the extrudate exits the die, and can be seen in the extrudate at locations close to the edge of the ribbon - fracture locations A3 (Figure 3.10) and B2 (Figure 3.11). Figure 4.22 presents "Flow Line" micrographs for all three blend types studied. In this particular region, layers, platelets, and fibers are oriented in a semi-circular (U-shaped) pattern.

It should be pointed out that this "Flow Lines" effect will not be present when a tubular die is used, as in the case of blow molding, due to the symmetrical flow field in this type of die.

4.2.2.1 PP/EVOH Blends

The analysis of PP/EVOH blends was undertaken to study the morphology of two incompatible polymers with no compatibilizing agent present. Thus, bonding or adhesion has no influence on the coalescence and dispersed phase deformation behavior [49,50,55-61].

(a) Variation across Ribbon Thickness

Figure 4.23 shows the morphological changes from the core to the surface at two different temperatures. Differences due to

80/20wt%
PP/EVOH



METERING SCREW
 $T_{Die}=230^{\circ}\text{C}$, 60rpm
 $h=1.0\text{mm}$

67.8/15.3/16.9wt%
PP/MAPP1/EVOH



METERING SCREW
 $T_{Die}=230^{\circ}\text{C}$, 60rpm
 $h=1.0\text{mm}$

80/20wt%
MAPP2/EVOH



MIXING SCREW
 $T_{Die}=215^{\circ}\text{C}$, 60rpm
 $h=0.5\text{mm}$

Figure 4.22 SEM micrographs showing Flow Lines for different Compositions and Processing Conditions.

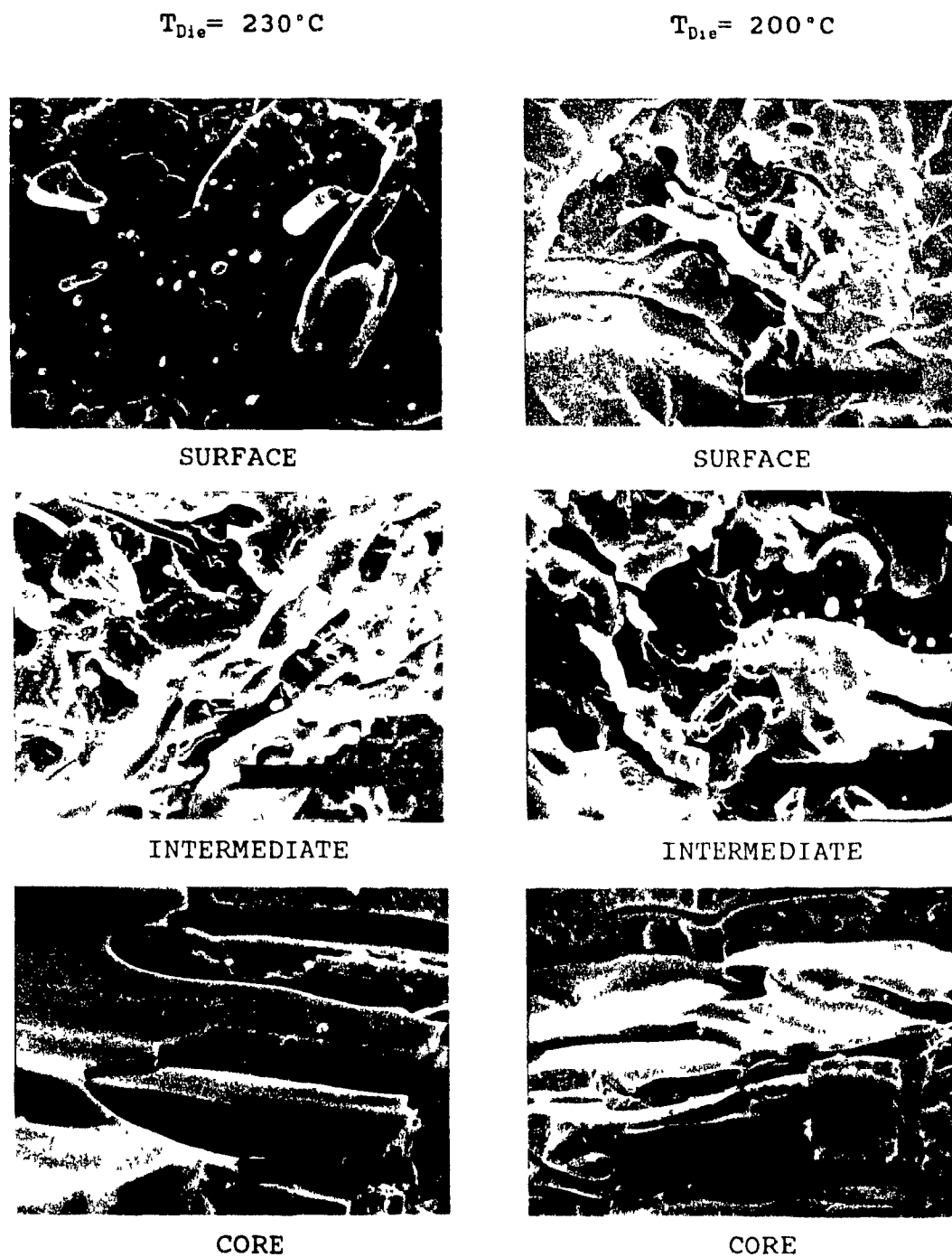


Figure 4.23 SEM micrographs for a PP/EVOH blend system showing Morphology Variations across Ribbon Thickness for a 80/20wt% composition ratio as a Function of Die Temperature (Metering Screw, 30rpm, $h=1.0\text{mm}$).

temperature change can be observed in all three regions. The higher temperature results in a more pronounced layered structure in the core region. The layers are thinner and continuous over the sample width. Decreasing temperature changes the morphology in the core region to a platelet type structure, and differentiation between the core and intermediate regions becomes difficult. Small temperature effects are found in the intermediate region. The higher temperature produces a dispersed structure consisting of agglomerates of different sizes and shapes, while platelet structure is still dominant at the lower temperature. The dispersed phase in the surface region, obtained at the higher temperature, appears in spherical form or as short fibers, except for some larger agglomerates which are partially oriented in the flow direction. For the lower temperature, platelets and long fibers are the main features.

The above observations may be explained by noting the differences in flow behavior for the blend system at the two temperatures. As has been shown in section 4.1, the main features of the morphology are produced in the adapter, and the overall morphology is preserved as the material exits the die unit. At the lower temperature, coalescence and migration towards the adapter axis are inhibited due to the higher viscosities of both phases. This produces an overall coarse distribution of the dispersed phase in the matrix phase. As a result, platelets are formed from large, dispersed phase agglomerates in the core and intermediate regions, whereas long, continuous fibers form in the surface region, due to the extensional flow fields in the adapter and slit die.

A general characteristic is a depletion of EVOH near the surface and a concentration in the core region, in agreement with the discussion in section 4.1.

(b) Effect of EVOH Content

Figure 4.24 presents micrographs showing the effect of composition ratio and temperature on the layered structure in the core region. Generally, it can be observed that increasing the amount of EVOH results, for both temperatures, in a thicker core region with pronounced layered features. Decreasing the amount of EVOH results in a change from a layered form to a more dominant platelet structure. This change appears, for the higher temperature, at an EVOH content between 10 and 20wt% and, for the lower temperature, at approximately 20wt%. Decreasing the temperature produces thicker layers with more pronounced internal structure in the core region.

With the appropriate processing temperature, it is possible to produce large continuous layers in the core region of the extrudate. This display of stretching and spreading the dispersed phase in the matrix can be compared to continuous layers produced by multi-layer coextrusion.

The SEM micrographs show the smooth surfaces at the interfaces of the two phases, indicating poor or no bonding between EVOH and PP, as expected for this group of incompatible polymers.

4.2.2.2 PP/MAPP/EVOH Blends

(a) Variation across Ribbon Thickness

The incorporation of compatibilizing agents does not change the generally observed morphological patterns across the ribbon thickness.

Figure 4.25 shows the variation of the morphology with thickness, at two temperatures, for a 67.8/15.3/16.9wt% PP/MAPP1/EVOH system. In the core region, the laminar structure consists of thin layers stacked on top of each other at the higher temperature, whereas, at the lower temperature, thick

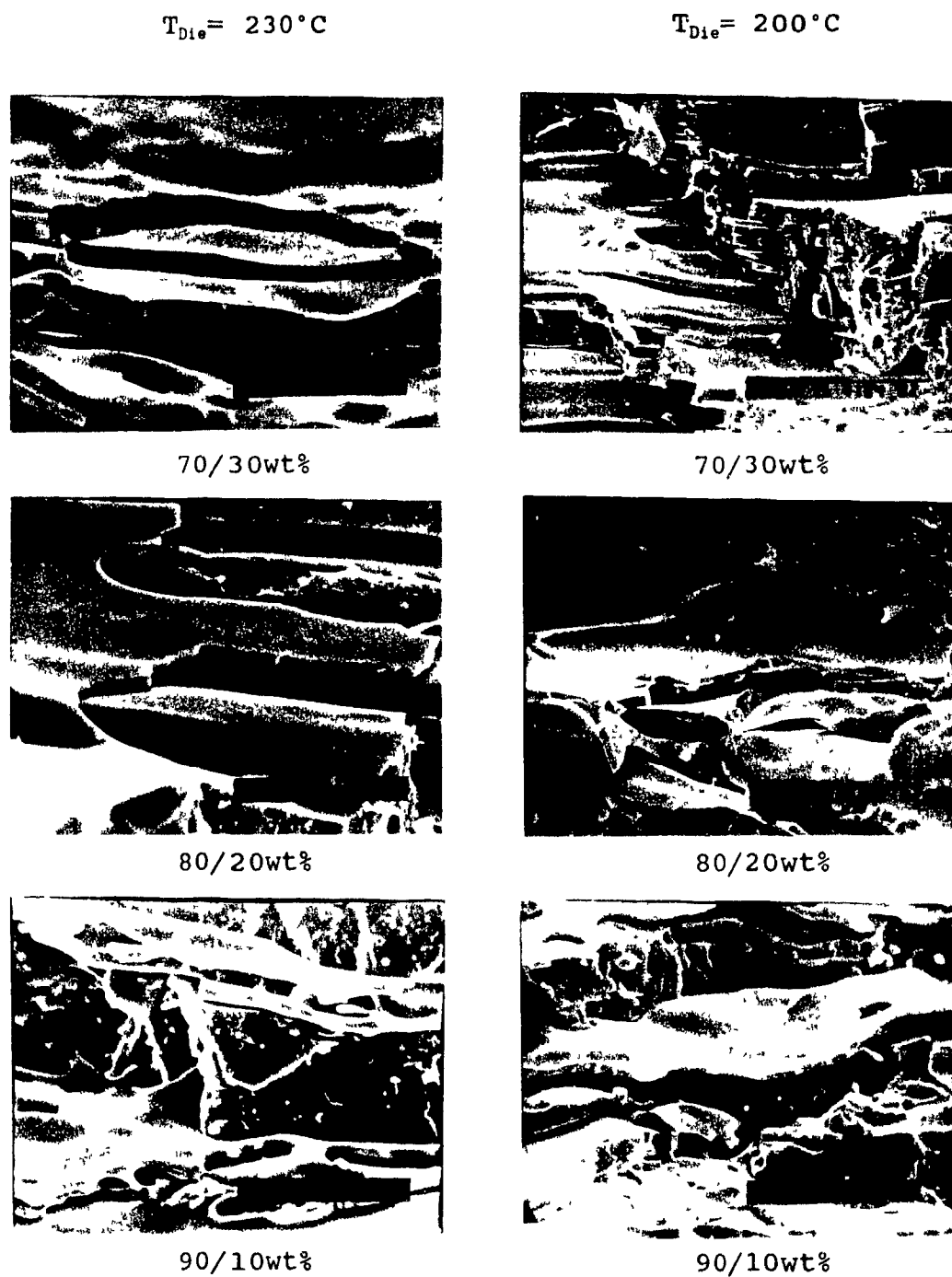


Figure 4.24 SEM micrographs for a PP/EVOH blend system showing the Influence of Composition and Die Temperature on Laminar Structure Development in the Core Region (Metering Screw, 60rpm, $h=1.0\text{mm}$).

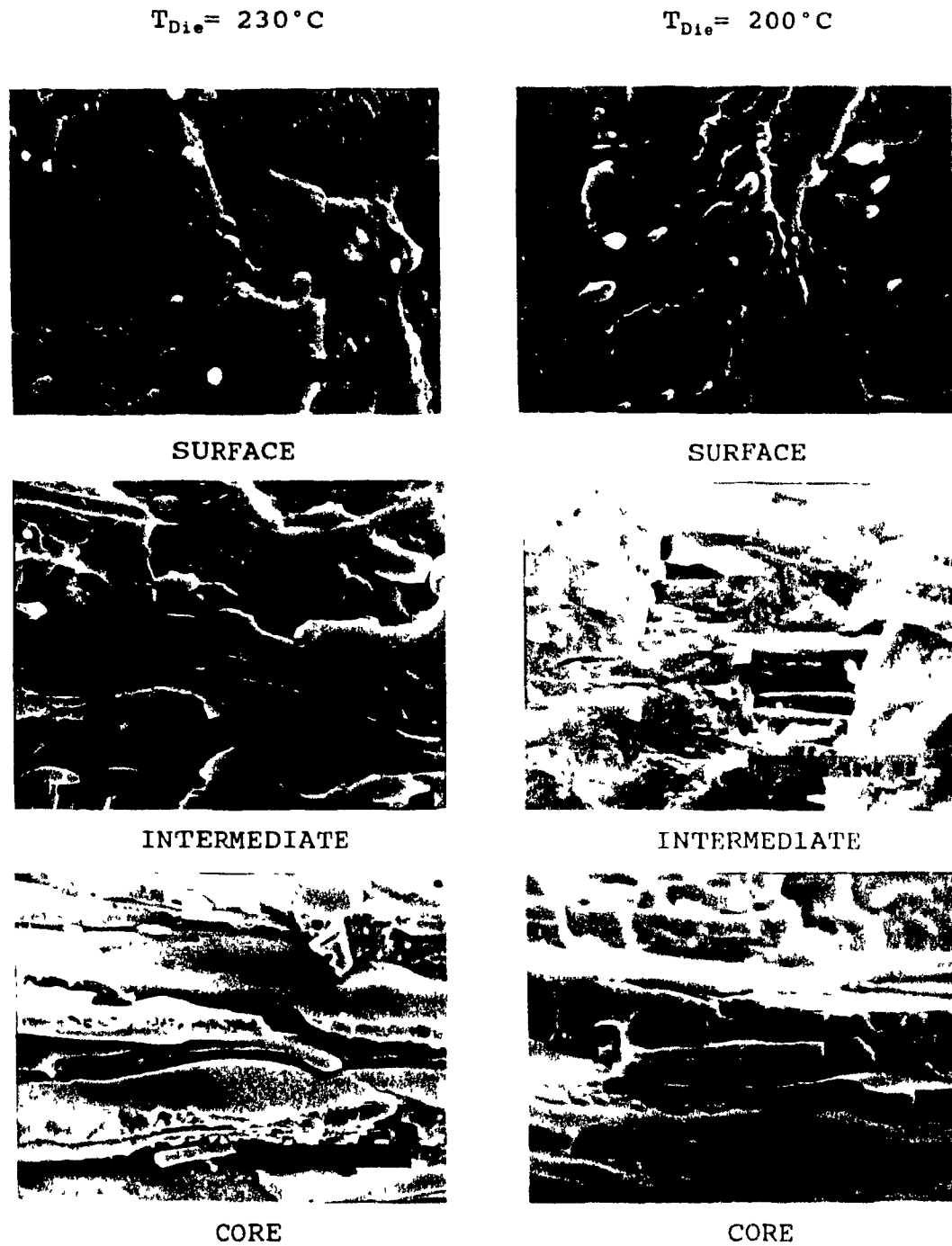


Figure 4.25 SEM micrographs for a PP/MAPP1/EVOH blend system showing Morphology Variations across Ribbon Thickness for a 67.8/15.3/16.9wt% composition ratio as a Function of Die Temperature (Metering Screw, 30rpm, $h=1.0mm$).

layers are dominant. The intermediate regions for both temperatures consist of long fibers and cylindrical-shaped dispersed phase. In addition, larger agglomerates and spheres are present. The surface regions again show depletion of EVOH, which is partially oriented in the direction of flow as short fibers.

Of particular interest is micrograph 5342-03, which depicts a section perpendicular to the flow direction (sample A2, Figure 3.10). It shows the dispersed phase taking on a cylindrical form, perpendicular to the flow direction. These cylinders are probably formed in the diverging section of the slit die unit. As it enters the adapter, the dispersed phase agglomerate is stretched due to the extensional flow field in the converging part of the adapter. In the diverging section of the slit die, the velocity of the tail of the dispersed phase cylinder is higher than that of the nose. Thus, the cylinder is rotated perpendicular to the flow direction. In the exit die gap section, which has constant width and thickness, the velocity gradient between nose and tale is nullified, and the cylinder maintains its orientation.

(b) Effect of Screw Design

It was pointed out in section 4.1 that it was possible to obtain a laminar structure of the dispersed phase in the matrix phase, even when using a mixing screw. This has been attributed to coalescence and migration of the dispersed phase towards the adapter axis. Thus, it would be of interest to compare the morphological patterns obtained with the mixing screw to those obtained with the metering screw.

Figure 4.26 compares the patterns obtained with metering and mixing screws for identical processing conditions. For both screws, the core region shows a layer/platelet arrangement of the dispersed phase. Results obtained with several composition



METERING SCREW



MIXING SCREW

Figure 4.26 SEM micrographs for a PP/MAPP2/EVOH blend system showing the Effect of Screw Design on Laminar Structure Development in the Core Region for a 71.4/10.7/17.9wt% composition ratio ($T_{D_{1e}}=230^{\circ}\text{C}$, 60rpm, $h=0.5\text{mm}$).

ratios suggest that the mixing screw produces more, and thinner, layers, stacked on top of each other (Figure 4.27). The morphology of ribbon extrudates with the mixing screw, using an entrance angle of 30° (the system in section 4.1 was evaluated for an angle of 70°), shows that even with a streamlined transition from the extruder to the slit die, it is possible to obtain laminar structures in the core portion of the extrudate.

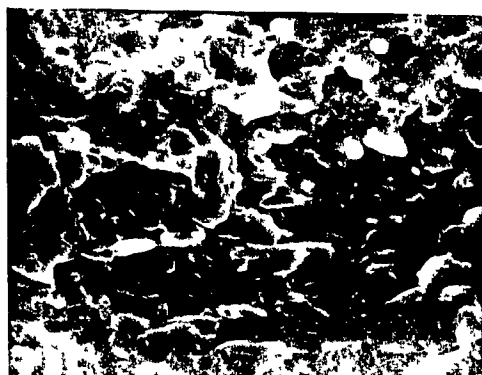
The intermediate and surface regions for both screws show considerable differences, which can be attributed to the mixing effectiveness of the mixing screw employed in this study. The amount of EVOH present in the intermediate and surface regions is higher with the mixing screw than with the metering screw. As a result, it is possible to obtain platelets in the intermediate zone, and long, thin fibers in the surface region, when a mixing screw is used.

Another contribution of the improved mixing effectiveness of the mixing screw is that the EVOH is more uniformly distributed in the product. In the metering screw, however, the EVOH has a high concentration in the core region, which decreases towards the surfaces of the extrudate.

(c) Effect of Die Exit Gap Size

The knowledge of morphological changes which occur due to changes in the die exit gap size is of great importance for the blow molding process, where parison thickness programming is standard procedure during production. Parison programming allows for thickness changes along the parison length to accommodate special design features of the blow molded article [88]. Thus, it has to be established how these changes of the thickness influence the morphological features of an extruded polymer blend.

METERING SCREW



SURFACE



INTERMEDIATE



CORE

MIXING SCREW



SURFACE



INTERMEDIATE



CORE

Figure 4.27 SEM micrographs for a PP/MAPP2/EVOH blend system showing Morphology Variations across Ribbon Thickness as a Function of Screw Design for a 71.4/10.7/17.9wt% composition ratio ($T_{D,e}=230^{\circ}\text{C}$, 60rpm, $h=0.5\text{mm}$).

The effect of an exit gap size change on morphology was evaluated for both screws. Typical results are shown in Figure 4.28. Micrographs for both screws show a change in morphology associated with a change in exit gap size. An increase in gap size yields fewer, but thicker, layers, which show a variety of internal structures. A thinner gap size results in an increasing number of stacked thin layers which are of more uniform thickness. The internal structure is greatly diminished, and the layers are extended over a larger area.

An explanation for the above morphological effects can be found with reference to Figure 3.9. A change in exit gap size from 1.0mm to 0.5mm results in a change of the contraction ratio from 3.75 to 7.5, from section D to section F. This higher contraction ratio influences the extensional flow field significantly. The higher extensional strain rate between section D and section F causes the dispersed phase material to elongate more, thus resulting in thinner and larger layers. Although the morphological differences due to a change in exit gap size are quite large, it should be noted that, for both thicknesses, the laminar structure is dominant in the core region. Thickness variations in parison programming are usually smaller than those seen in the present case. Thus, it is expected that smaller variations in morphology of the core region of the extrudate would be encountered.

(d) Effect of Screw Speed

One of the most important economic variables in commercial extrusion lines is production rate, which depends mainly on screw speed and design, as well as cooling and take-off rates. The screw speed (or extruder rpm) is limited by screw design, which influences the balance between pumping, melting, and solid conveying rates. The extrusion and take-off speeds must be optimized, to ensure that the extrudate product does not undergo undesirable changes and damage after the material

METERING SCREW

 $h = 1.0\text{mm}$

MIXING SCREW

 $h = 1.0\text{mm}$  $h = 0.5\text{mm}$  $h = 0.5\text{mm}$

Figure 4.28 SEM micrographs for a PP/MAPP1/EVOH blend system showing the Effect of Exit Gap Size on Laminar Structure Development in the Core Region as a Function of Screw Design for a 71.4/10.7/17.9wt% composition ratio ($T_{D1.0} = 230^\circ\text{C}$, 60rpm).

leaves the die section.

In the present experimental studies, the screw speed was limited to 90 rpm due to limitations on the melting capacity of the extruder used. Higher screw speeds, e.g. 120 rpm, resulted in an extrudate which contained unmelted EVOH particles for both die temperatures (200°C and 230°C).

Figure 4.29 shows four micrographs for two composition ratios and three rpm settings. It appears that a higher screw rpm produces a more pronounced laminar structure. The core region contains a larger number of thinner layers when the rpm is increased. For the same exit gap size, a higher mass flow rate results in a higher extensional rate, creating longer, extended, and thinner structures of the dispersed phase in the matrix phase. A higher mass flow rate also results in strong coalescence and migration behavior of the dispersed phase, during flow in the adapter. This suggests that the development of laminar structure in the core region of the extrudate is enhanced at higher extruder speed, thus not posing an obstacle on commercial production, in relation to morphological development.

The effect of increased extruder speed on residence time or contact time between the dispersed and matrix phases, which could influence the development of adequate bonding between the two phases, will be discussed later.

(e) Internal Structure

A closer examination of micrographs discussed so far reveals that the layers, produced in the core region of the extrudate, very often exhibit internal structure consisting of fibers and spheres. This structure is more obvious at lower die temperature, larger exit gap thickness, lower extruder rpm, and when a mixing screw is used.

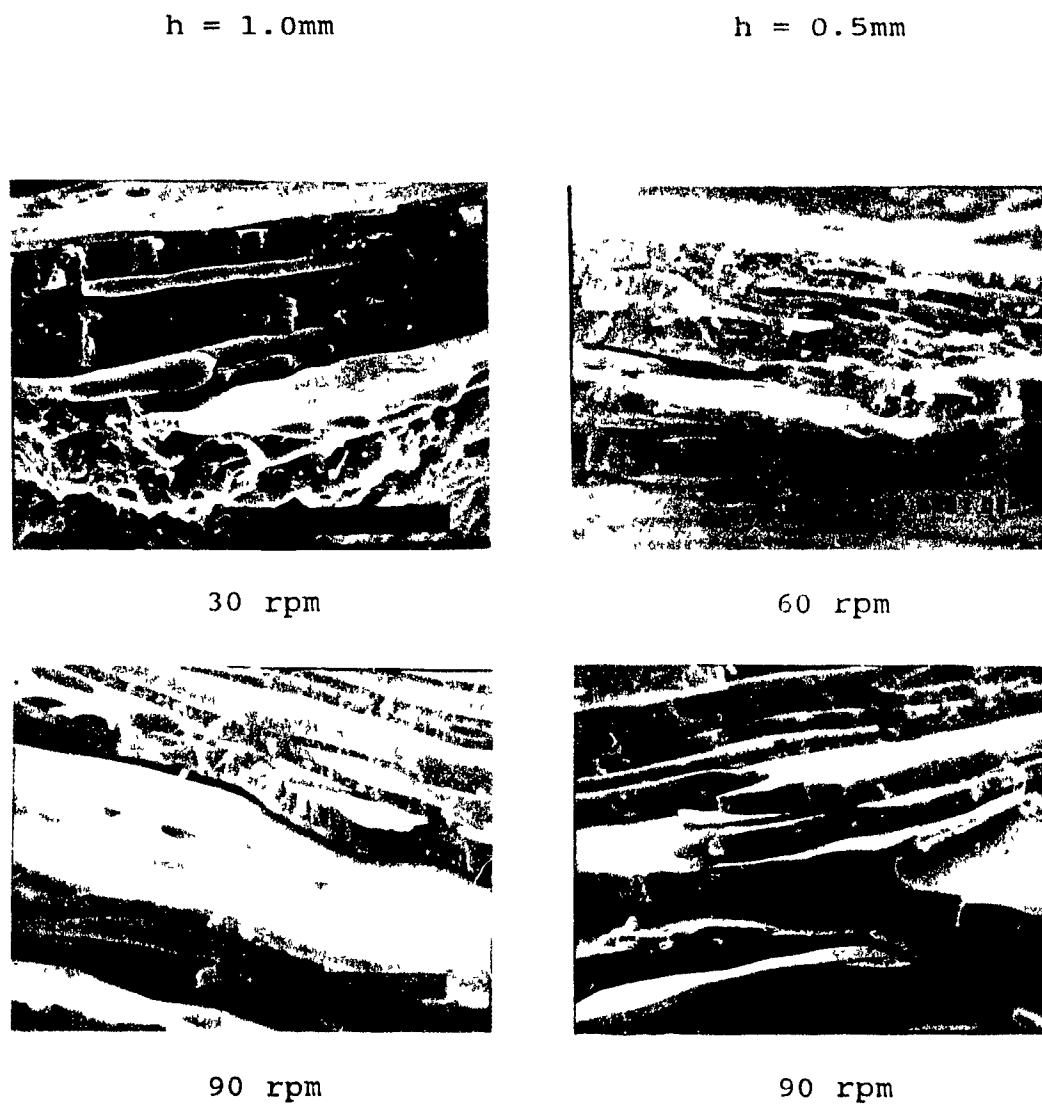


Figure 4.29 SEM micrographs for a PP/MAPP1/EVOH blend system showing the Effect of Screw Speed on Laminar Structure Development in the Core Region as a Function of Exit Gap Size for a 67.8/15.3/16.9wt% composition ratio (Metering Screw, $T_{D,10} = 230^{\circ}\text{C}$).

Figure 4.30 presents a close-up for one processing condition, showing fibers and spheres. The origin of the internal structure is related to the development of the laminar structure. Coalescence and migration in the adapter are prerequisites for the production of a well established, laminar structure in the core region. During coalescence and migration, the dispersed phase is directed towards the adapter axis, becoming highly concentrated in this region. In the process, the dispersed phase incorporates small amounts of the matrix phase, which subsequently show up as internal structure in the final extrudate morphology.

Internal structures have also been observed by Favis et al. [44] in a mixing study of a 60/40wt% PC/PP blend in an internal mixer. The type of structure consisted of a matrix phase, a dispersed phase, and dispersed phase droplets within the dispersed phase. No explanation was given for this composite droplet structure.

(f) Adhesion

Compatibilizing agents (MAPP adhesive polymers) were used to obtain bonding between the two immiscible phases of EVOH and PP, in order to improve both barrier and mechanical properties of the extruded blend product.

Comparison between the morphologies of extrudates manufactured with and without compatibilizer did not show significant differences in the laminar structure. The layer surfaces were smooth in both cases. There did not seem to be any improvement in adhesion between the two phases.

A careful study of samples with a large amount of compatibilizer suggested perhaps minor improvements in adhesion in SEM micrographs. Adhesion "spots", where the usually smooth layer surface became very rough, were observed, indicating that some



FIBERS



SPHERES

Figure 4.30 SEM micrographs for a PP/MAPP1/EVOH blend system showing Internal Structures for a 64.2/8.3/27.5 wt% composition ratio (Metering Screw, $T_{Die}=230^{\circ}C$, 30 rpm, $h=1.0mm$).

parts were torn off during the fracture process. Figure 4.31 presents two micrographs showing different amounts of adhesion. The use of the mixing screw did not appear to improve adhesion.

The reason for the above behavior is not fully understood, but two points have to be considered. In this study, the dry blend was mixed mechanically, and then fed to the extruder. Thus, it could not be ascertained whether the functionalized groups of the compatibilizing agent were concentrated at the interface towards the EVOH phase, rather than being diluted by the pure PP phase. Furthermore, the residence time in the extruder and die was rather short, thus not assuring the diffusion of the maleic anhydride towards the interface, where it could interact with the EVOH.

In order to overcome some of the above obstacles to adhesion, a new set of experiments was carried out, as described below.

4.2.2.3 MAPP2/EVOH Blends

Available technical information [64,89] suggested that higher extrusion temperatures should improve adhesion quality. Moreover, the adhesive strength is affected by contact time in the molten state. To achieve good bonding strength, it is desirable to maximize both temperature and contact time in the molten state. As discussed earlier, the use of high temperatures is limited by material stability and operational considerations. Thus, in order to maximize the possibilities of contact between the functionalized polypropylene and EVOH, the PP portion in the blend was replaced by an adhesive resin (MAPP2).

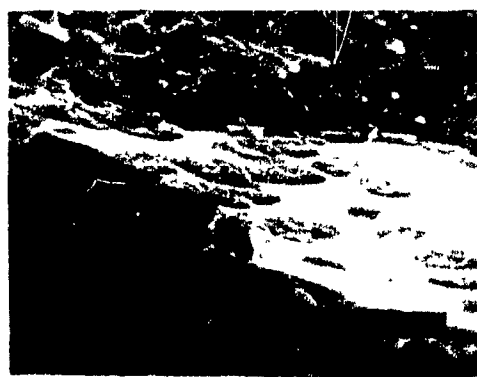
A set of experiments was designed to obtain more favorable conditions for adhesion. Four different blend ratios were extruded at a die temperature of 230°C, with a screw speed of 30 rpm. In another set, less favorable conditions were em-

MIXING SCREW



MAPP1

METERING SCREW



MAPP2

Figure 4.31 SEM micrographs for a PP/MAPP/EVOH blend system showing Adhesion for two Screw Designs, and two Compatibilizers, for a 67.8/15.3,16.9wt% composition ratio ($T_{Die}=230^{\circ}\text{C}$, 60rpm, $h=0.5\text{mm}$).

ployed. The blends were extruded at a die temperature of 215°C, with a screw speed of 60 rpm. Both the metering and mixing screws were used with each set of experiments.

(a) Variation across Ribbon Thickness

Micrographs for the metering and mixing screws are given in Figure 4.32. The dispersed phase is considerably better incorporated into the overall blend. Specifically, in the intermediate and surface regions, it is difficult to distinguish between the two phases (compare to Figures 4.23 and 4.25).

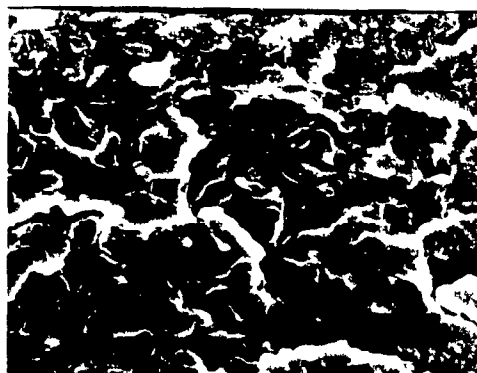
For both screw types, the core region shows a laminar layer/platelet structure which seems to exhibit good adhesion. As before, the amount of EVOH decreases near the surface. There seem to be only minor differences in the morphological structures produced by both screw types.

(b) Effect of Temperature and Screw Speed

Figures 4.33 and 4.34 compare the laminar structures obtained with both processing conditions at different composition ratios, using the metering screw. The comparison shows that the higher temperature, in combination with a lower speed, favors bonding, which causes difficulties in distinguishing the layered structure in the core region, especially when the concentration of EVOH is low. Figure 4.33 shows that the 90/10wt% MAPP2/EVOH ratio does not exhibit a well developed laminar structure. This seems to indicate that, at low concentrations of the dispersed phase, the coalescence and migration towards the adapter axis can be inhibited if enough functionalized groups are present at the interface. Results for composition ratios 80/20wt% and 70/30wt% (Figure 4.33) show a laminar structure, where the number of layers has decreased. The layers are well incorporated into the overall morphology. In comparison, the micrographs for the lower temperature and

METERING SCREW

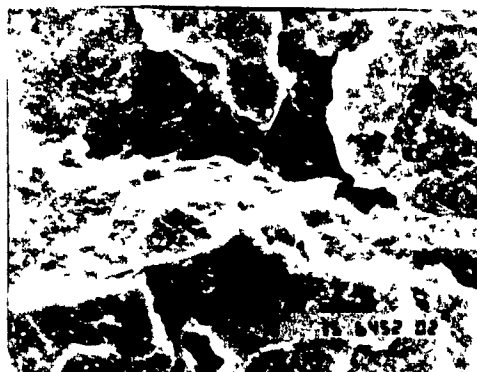
MIXING SCREW



SURFACE



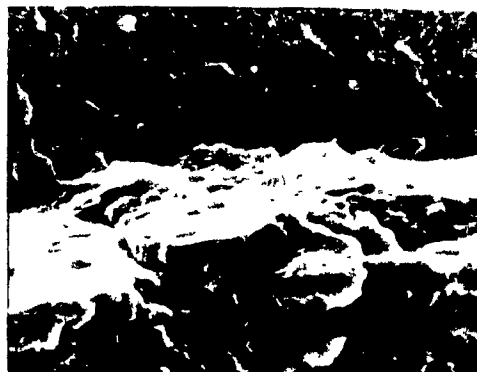
SURFACE



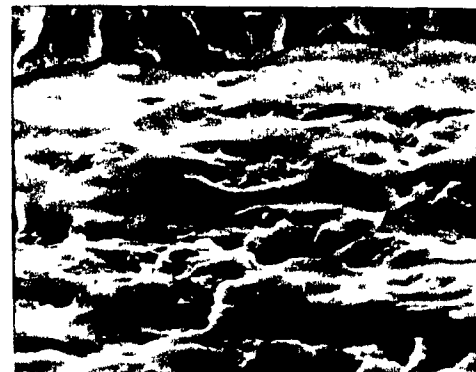
INTERMEDIATE



INTERMEDIATE



CORE



CORE

Figure 4.32 SEM micrographs for a MAPP2/EVOH blend system showing Morphology Variations across Ribbon Thickness as a Function of Screw Design for a 80/20wt% composition ratio ($T_{d1e}=230^{\circ}\text{C}$, 30rpm, $h=0.5\text{mm}$).



90/10 wt%



70/30 wt%



80/20 wt%



50/25/25 wt%

Figure 4.33 SEM micrographs for a MAPP2/EVOH blend system showing the Effect of Composition on Laminar Structure Development in the Core Region (Metering Screw, $T_{D1e}=230^{\circ}\text{C}$, 30rpm, $h=0.5\text{mm}$).

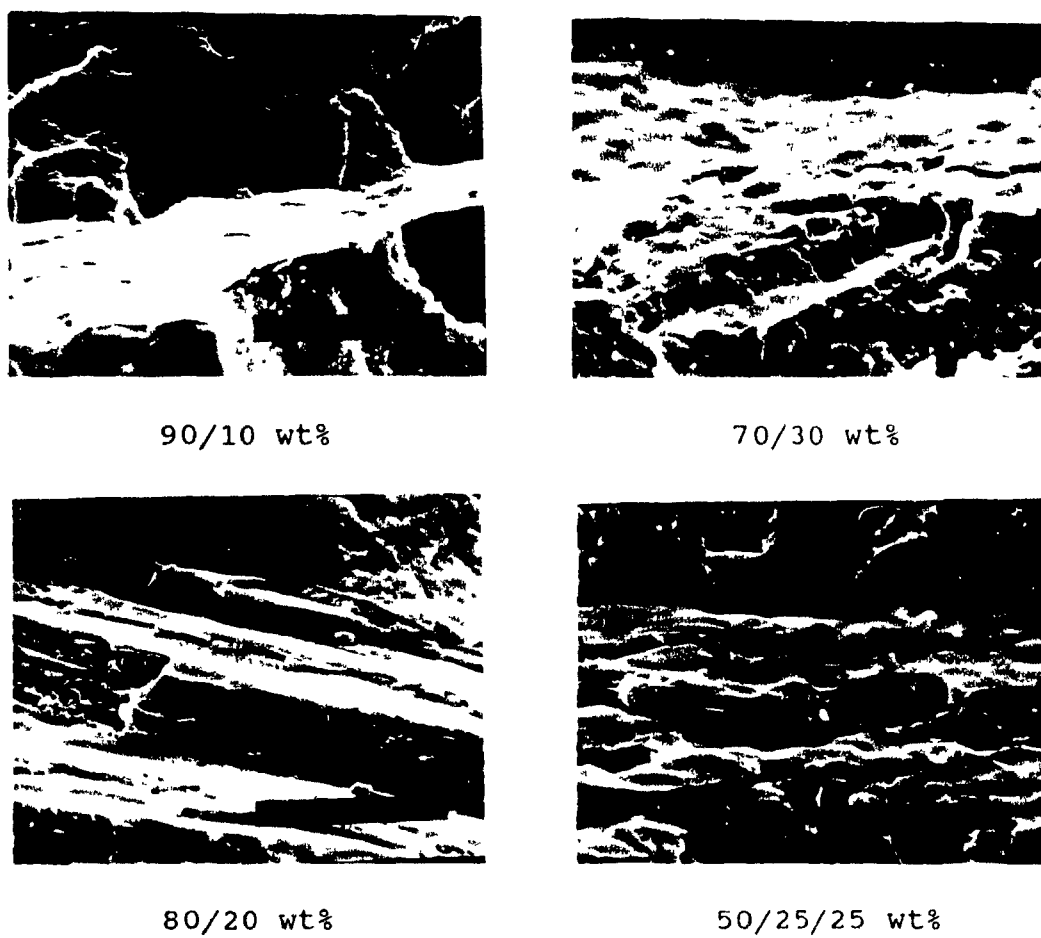


Figure 4.34 SEM micrographs for a MAPP2/EVOH blend system showing the Effect of Composition on Laminar Structure Development in the Core Region (Metering Screw, $T_{D_{1e}}=215^{\circ}\text{C}$, 60rpm, $h=0.5\text{mm}$).

higher speed (Figure 4.34) show laminar structure, even for a 90/10wt% composition ratio.

In Figures 4.35 and 4.36, micrographs are given for both processing conditions for the mixing screw. The differences between the mixing screw and metering screw, as presented in the SEM micrographs, are minor. Thus, the arguments presented above regarding the microstructure obtained with the metering screw also hold for the mixing screw.

The composition ratio 50wt% MAPP2, 25wt% PP, and 25wt% EVOH was employed to study the effect of pure PP on the compatibility behavior and overall structure.

All data suggest that the incorporation of PP has diminished the adhesion between the dispersed phase and the matrix, resulting in a well defined laminar structure in the core region of the extrudate. Also, higher screw speeds produce more and thinner layers which seem to be better incorporated into the overall structure, thus working against the design goal of this set of experiments.

(c) Adhesion

The replacement of pure PP with adhesive polymer MAPP2 resulted in improved adhesion between the dispersed EVOH phase and MAPP2 matrix phase. This improvement in adhesion is most noticeable in the intermediate region, where it is very difficult to distinguish between the dispersed and matrix phases.

The micrographs given in Figures 4.37 and 4.38 show the core and intermediate zones for two composition ratios and both screw types. The number of adhesion "spots" in the laminar oriented core has considerably increased, but fracture still occurs at the layer surface, indicating that the adhesion between individual layers is still not satisfactory.

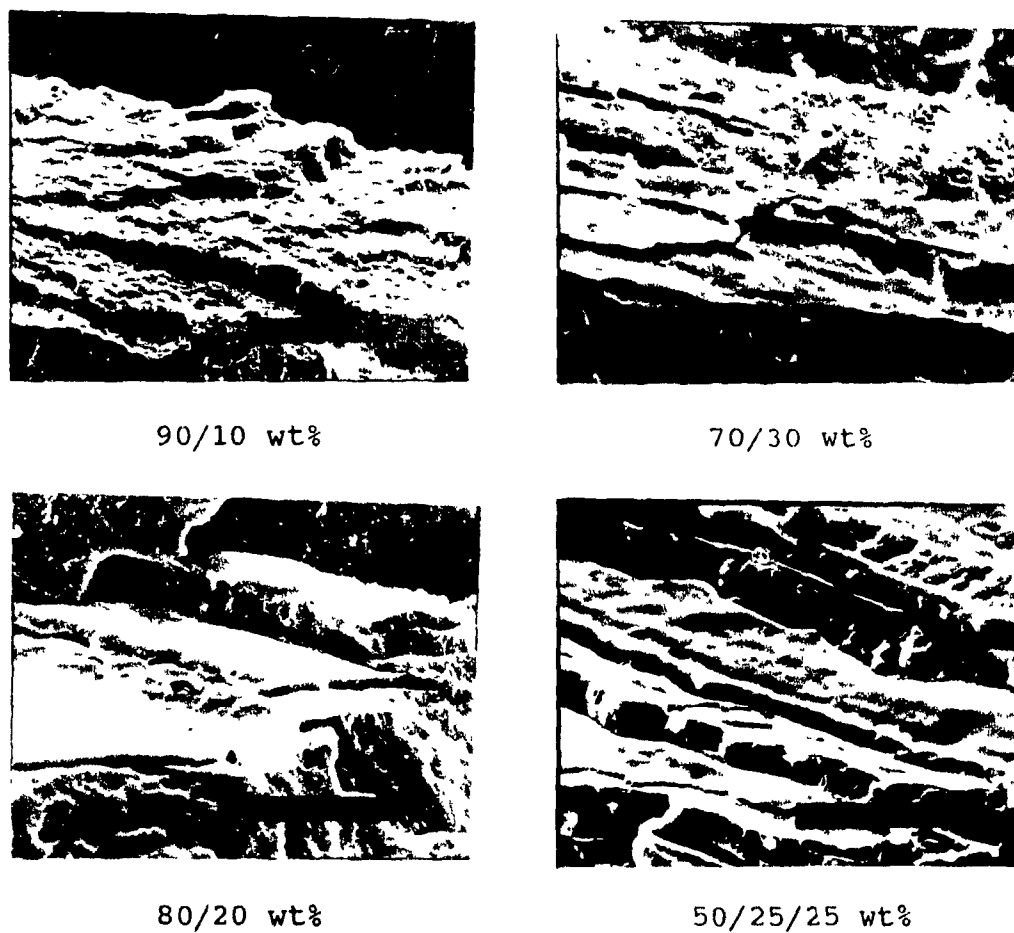
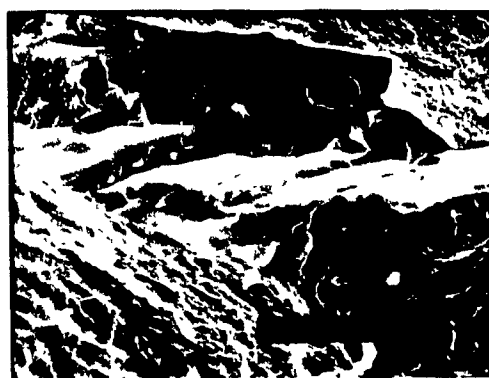
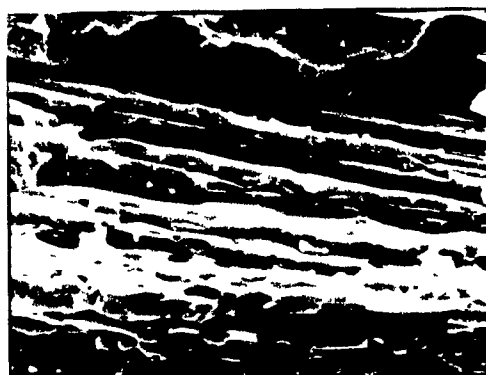


Figure 4.35 SEM micrographs for a MAPP2/EVOH blend system showing the Effect of Composition on Laminar Structure Development in the Core Region (Mixing Screw, $T_{D1e}=230^{\circ}\text{C}$, 30rpm, $h=0.5\text{mm}$).



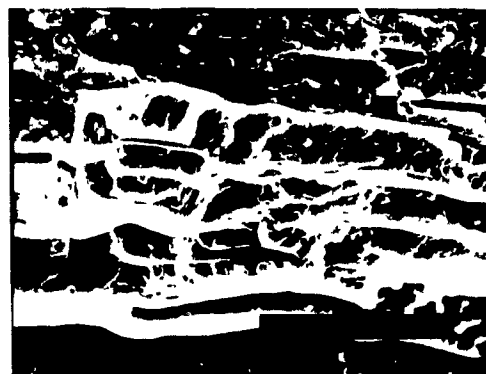
90/10 wt%



70/30 wt%



80/20 wt%



50/25/25 wt%

Figure 4.36 SEM micrographs for a MAPP2/EVOH blend system showing the Effect of Composition on Laminar Structure Development in the Core Region (Mixing Screw, $T_{D1.0}$ =215°C, 60rpm, $h=0.5$ mm).

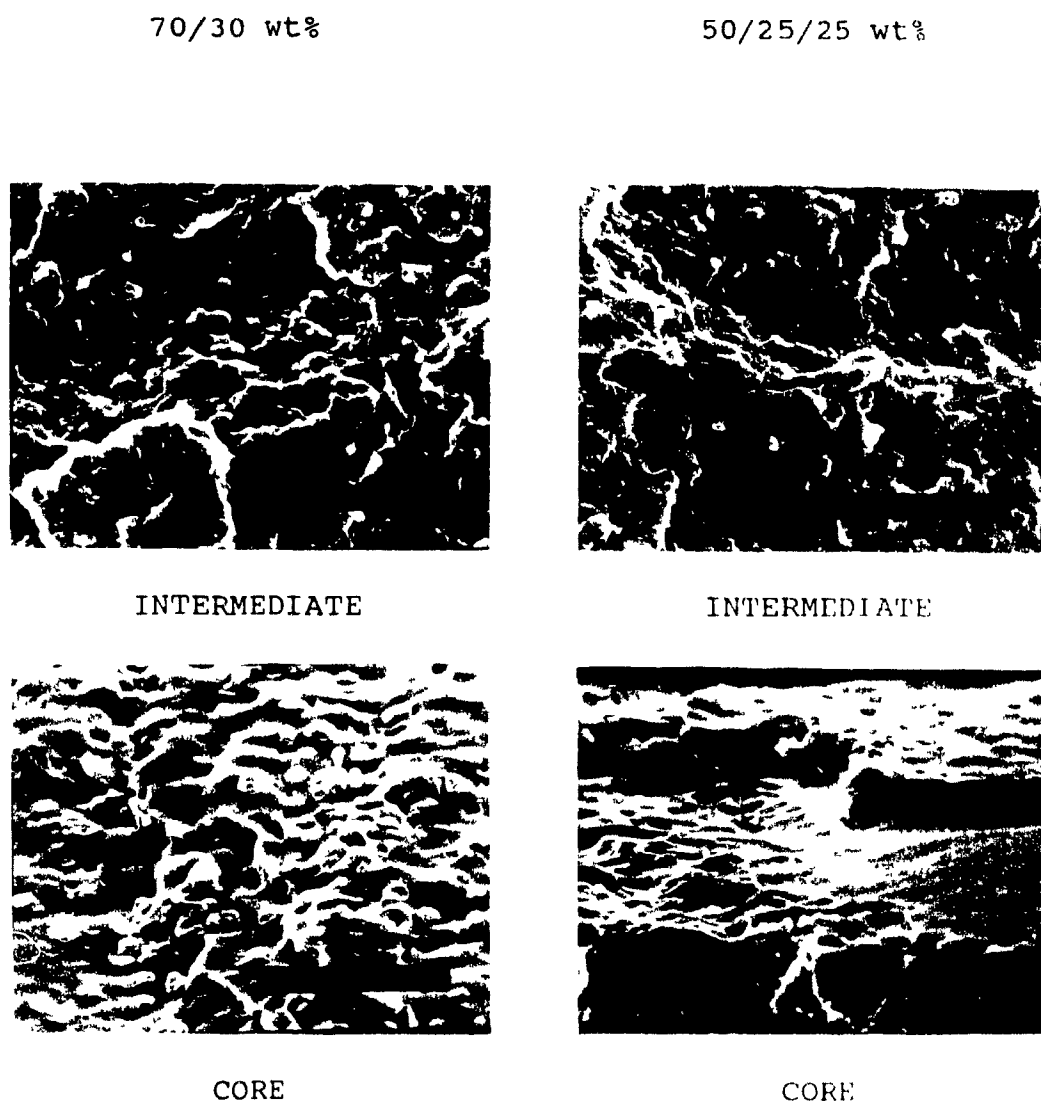
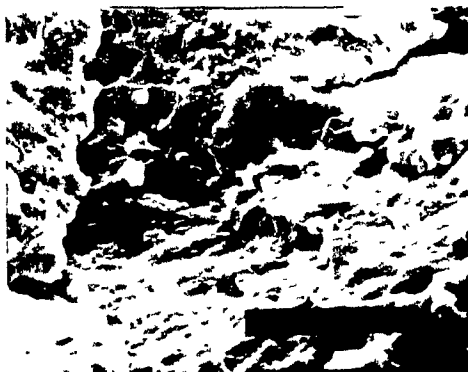


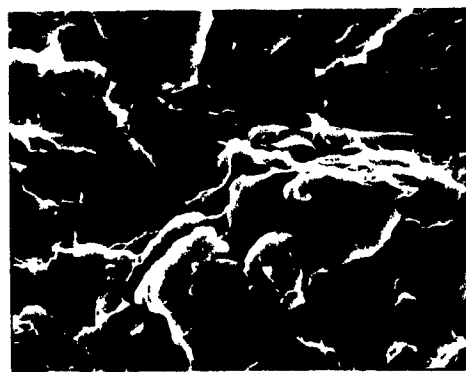
Figure 4.37 SEM micrographs for a MAPP2/EVOH blend system showing Adhesion for two Composition Ratios (Metering Screw, $T_{D_{10}}=230^{\circ}\text{C}$, 30rpm, $h=0.5\text{mm}$).

70/30 wt%

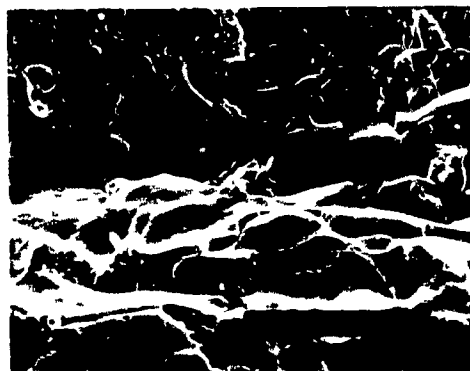


INTERMEDIATE

50/25/25 wt%



INTERMEDIATE



CORF



CORE

Figure 4.38 SEM micrographs for a MAPP2/EVOH blend system showing Adhesion for two Composition Ratios (Mixing Screw, T_{D10} =230°C, 30rpm, $h=0.5$ mm).

As pointed out above, the composition ratio 50/25/25wt% MAPP2/PP/EVOH has a laminar structure in the center region which is easily detectable, and has less adhesion due to the incorporation of pure PP. On the other hand, the intermediate region for this composition ratio shows the same features as a 70/30 wt% MAPP2/EVOH blend. The dispersed phase and matrix phase are well bonded to each other, and the fracture surface does not reveal sharp boundaries of the dispersed phase.

4.2.3 Summary of Morphological Observations

The studies into the morphology of extruded polymer blends have shown that the incorporation of a slit die produces a laminar orientation of the dispersed EVOH phase in the PP matrix phase. This laminar structure is located in the core of the extrudate and is replaced towards the surfaces by dispersed phase agglomerates of different sizes and shapes, which are oriented both parallel and perpendicular to flow.

The study of the effects of different processing conditions indicates that the laminar structure itself is a result of the die design, specifically the converging section of the adapter and the diverging section in the slit die. The processing conditions only affect the shape and dimensions of the laminar core region.

The composition ratio has a very strong influence on the laminar structure, showing that when EVOH content decreases, the layers are replaced by platelets. Different experiments indicate that the optimum EVOH content is approximately 25wt%, where a change from the platelet structure into the layered form occurs.

The SEM analysis did not provide conclusive information regarding the adhesion at the interface between the dispersed and matrix phases, when a compatibilizing agent was incorpo-

rated into the blend system. On the other hand, experiments with pure compatibilizer as the matrix phase showed that, in the core region, the adhesion between the different layers was weak. However, near the surfaces, the dispersed phase agglomerates were very well incorporated into the matrix phase and it was difficult to differentiate between the two phases. This observation suggests that the amount of functionalized groups present in the two compatibilizing agents employed is insufficient to provide strong bonding between the phases during flow through the die.

4.3 Impact Properties

4.3.1 Pure Resins

Tests conducted on sheets extruded from the pure homopolymers displayed different modes of failure. For the ethylene vinyl-alcohol copolymer, the impacted area shattered and broke away from the rest of the test specimen. On the other hand, the polypropylene showed a punch-like fractured surface. The punched out cap, even though highly drawn out by the impact ram head, was still attached to the test specimen on one side.

The load-deflection curve revealed, for both materials, very different impact traces, as shown in Figure 4.39. The EVOH load-deflection curve has a high slope and high ultimate force at short displacement, whereas the load-deflection curve for PP (the same holds for MAPP1 and MAPP2) showed a small slope and small ultimate force at considerably longer displacement. Sample load-deflection curves for PP and EVOH are given in Appendix D.

4.3.2 PP/EVOH and PP/MAPP/EVOH Blends

In general, the fractured specimens in this category showed EVOH-like behavior. The impacted area shattered and broke away from the rest of the specimen and the fractured pieces showed

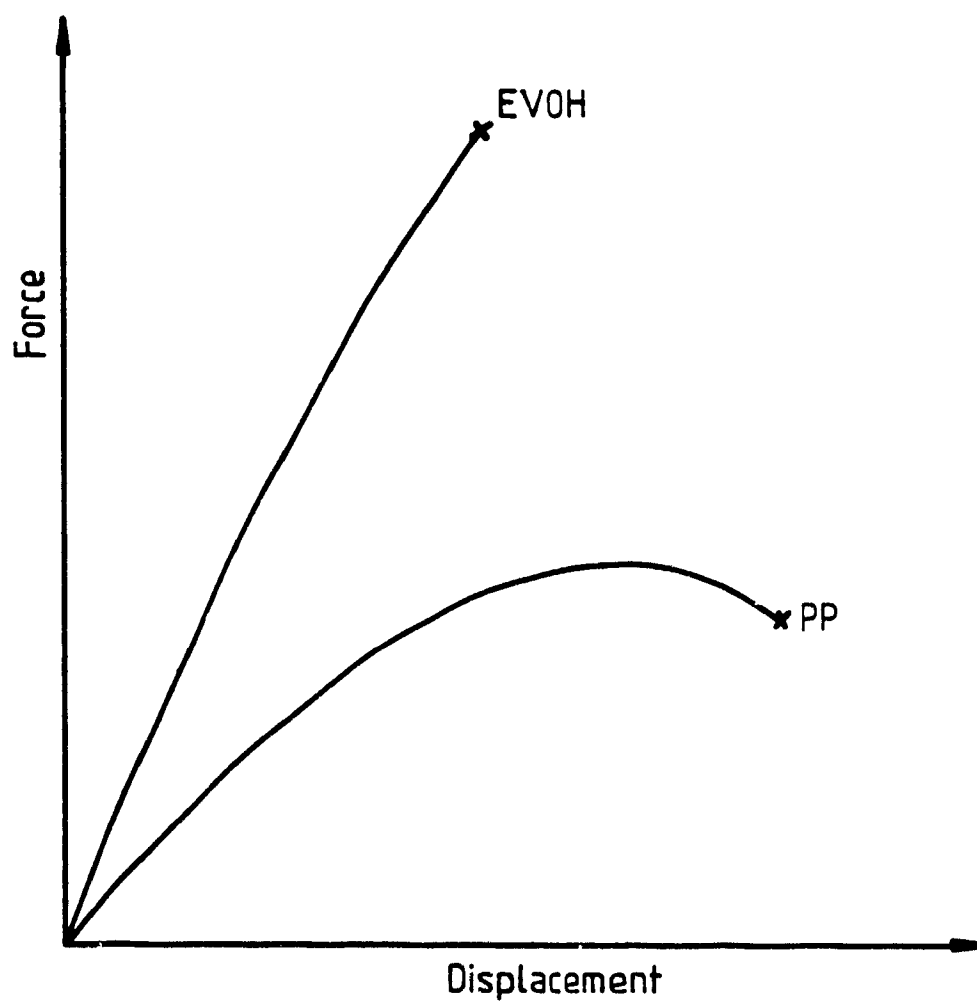


Figure 4.39 Schematic of typical Impact Traces for EVOH and PP.

extensive white crazes and cracks.

In Figure 4.40, the impact ultimate force is given as a function of composition and processing temperature. It can be seen that the impact ultimate force for these blends is inferior to that of pure PP. The decline in ultimate force for the blend of PP and EVOH was expected, due to the incompatible behavior of these two polymers. This graph shows that the incorporation of as little as 10wt% EVOH is sufficient to destabilize the PP matrix, and only a minor force is required to create cracking and tearing inside the specimen. A further increase in EVOH content leads to an additional reduction in ultimate force. At the higher EVOH content, the morphological analysis showed a well developed laminar structure. Impact tests suggest that these layers lie loosely on top of each other, enabling fast crack propagation throughout the sample.

The results for experiments with different levels of compatibilizing agent reveal that the conditions of incorporating the adhesive polymers into the systems are insufficient to produce strong bonding between the two phases. The results show, however, some improvement in impact behavior.

For the pure PP/EVOH blends, the effect of processing temperature is not detectable, whereas for the blends with compatibilizer, the higher temperature results consistently show slightly higher ultimate force. This suggests that the mobility and reactivity of the functionalized groups at the interface are important.

The impact slope values follow the same trend as the ultimate force values, as shown in Figure 4.41. The influence of the processing temperature can be seen for all composition ratios. Even for the pure PP/EVOH blends, the higher temperature gives lower slope values, confirming that the impact behavior of laminar blend systems depends on the amount and dimensions of

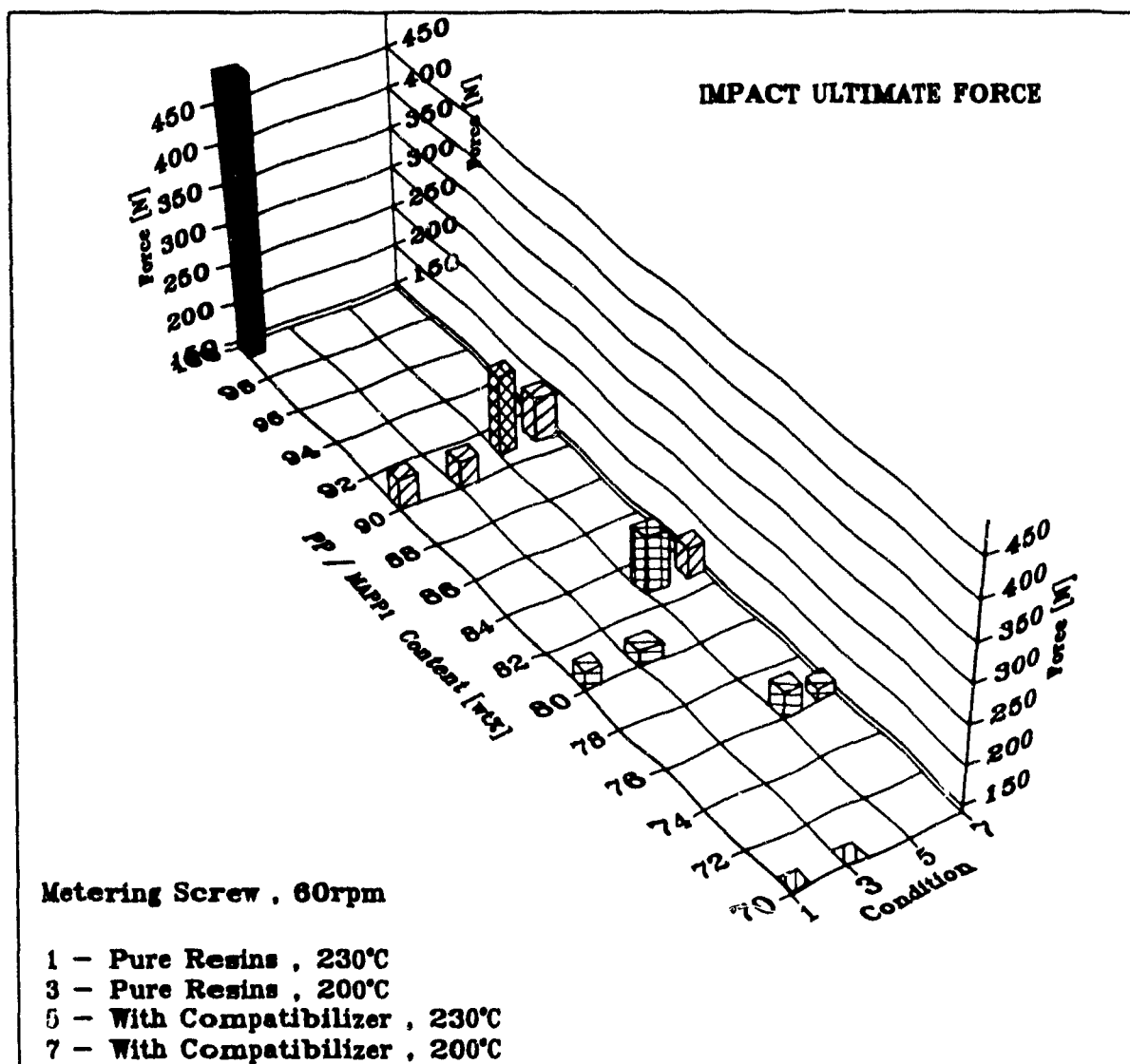


Figure 4.4G Impact Ultimate Force for PP/EVOH and PP/MAPP1/EVOH blend systems as a Function of Composition and Die Temperature.

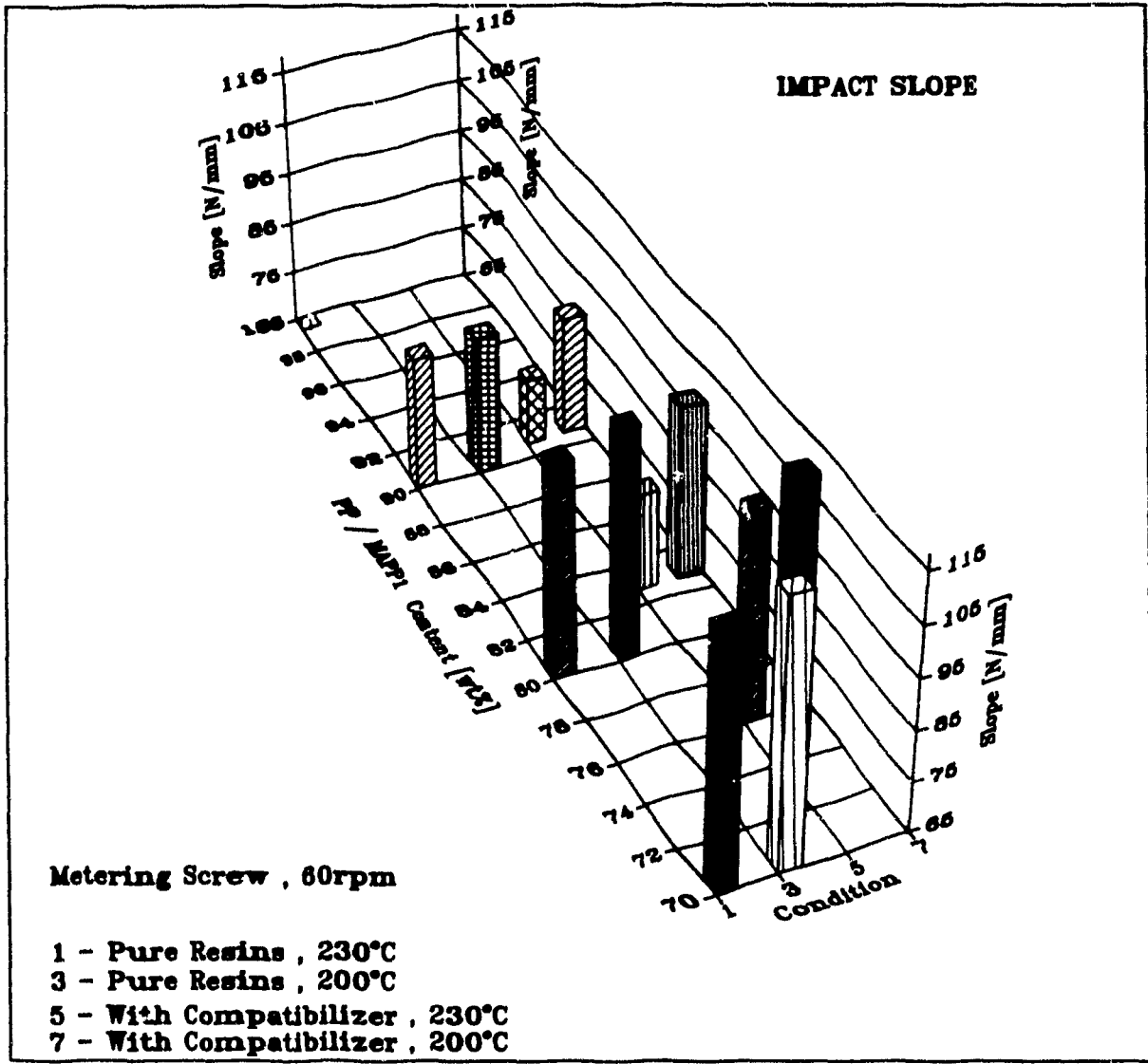


Figure 4.41 Impact Slope for PP/EVOH and PP/MAPP1/EVOH blend systems as a Function of Composition and Die Temperature.

layers. The strong influence of the processing temperature can be seen for the 80-20(90) and 90-10(90) PP-EVOH(MAPP1) composition ratios. In these cases, the slope is considerably lower compared to the other blends tested, indicating that at high processing temperatures, small amounts of EVOH (9.2 and 6.9 wt%, respectively) can be better incorporated into the overall structure with improved adhesion. This suggests that the addition of compatibilizing agents into the blend system changes the mechanical behavior towards the load-deflection curve of PP.

A comparison between impact ultimate force and slope indicates that the measurement of the slope is more sensitive than the ultimate force to minor improvements in adhesion in two-phase systems. The ultimate force is a measure of the overall impact strength, and minor additional amounts of adhesion do not contribute significantly to an increase in the impact resistance of the material.

Figure 4.42 presents a comparison of impact data for different screw designs and composition ratios. Both testing criteria show that, within the reproducibility of the measured values, an increase in concentration of compatibilizer by 5wt% does not result in a considerable increase in the ultimate force or decrease in the slope value. Also, no changes are noticeable between the materials obtained with metering and mixing screws, or when the compatibilizing agent is changed from MAPP1 to MAPP2.

Since the mixing screw seems to yield a product with similar impact behavior to that produced with the metering screw, it appears that the latter provides sufficient mixing to introduce the compatibilizing agent to the interface. Although improved properties are obtained when the compatibilizing agent is used, it appears that the amounts of functionalized groups used are insufficient to create a strong bond between

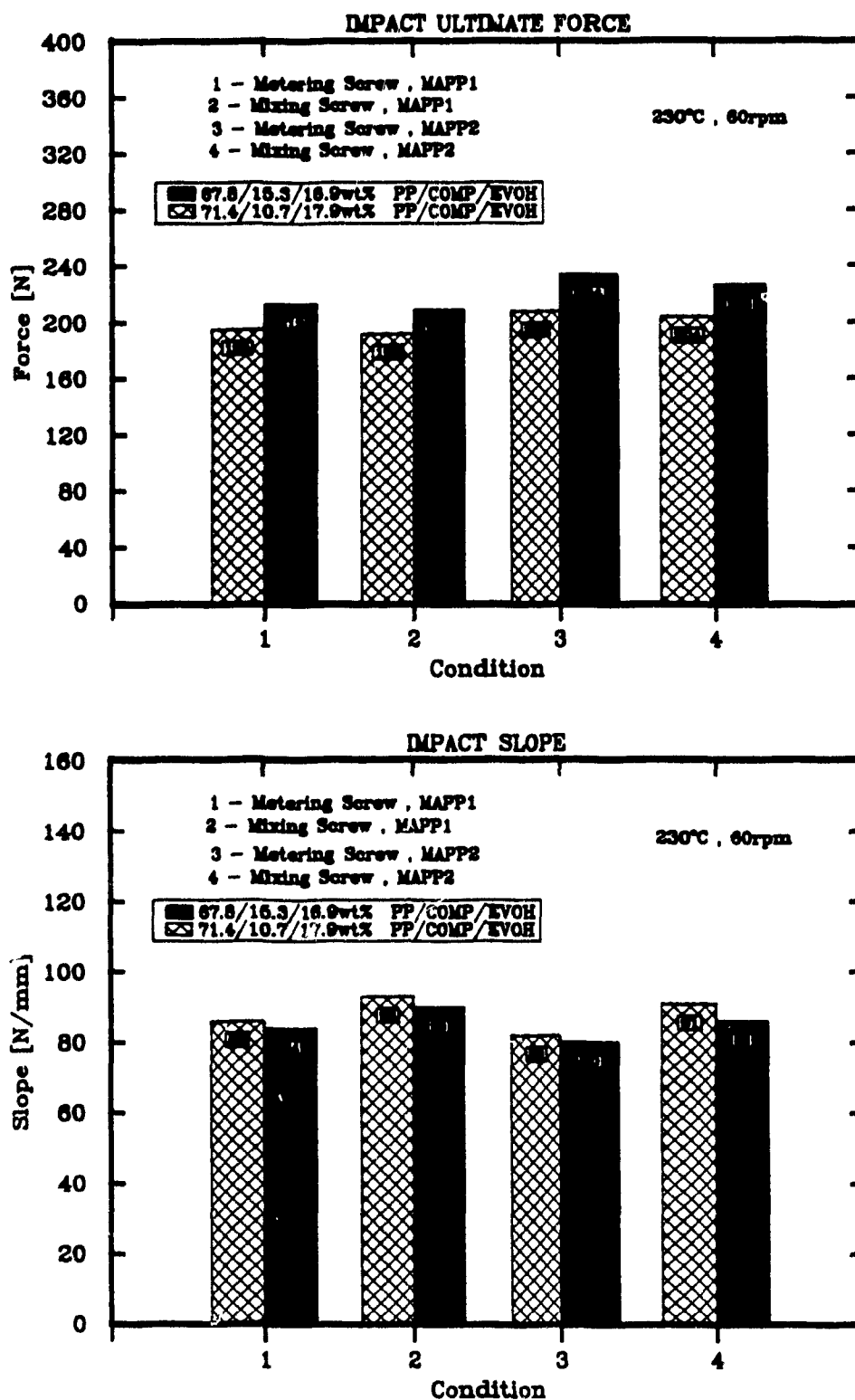


Figure 4.42 Impact Ultimate Force and Slope for a PP/MAPP/EVOH blend system as a Function of Composition and Screw Design.

the PP and EVOH phases, due to the deformation behavior and short residence time of the dispersed phase during flow through the metering zone, adapter, and slit die.

4.3.3 MAPP2/EVOH Blends

It was hoped that the substitution of MAPP2 for PP in the blend system would ensure constant availability of functionalized groups at the interface. The resulting blend system should show a totally different behavior under impact testing conditions.

In Figure 4.43, the impact ultimate force is presented for the four different composition ratios and four processing conditions employed in this group of experiments. The change in impact behavior from Figure 4.41 to 4.43 is clearly evident. It can be seen that the MAPP2 matrix can incorporate up to 20wt% EVOH without losing its stability. Above 20wt%, the matrix phase is strongly disturbed, due to the formation of a strong laminar structure in the core region of the extrudate and larger agglomerates near the surfaces. Thus, crazing and tearing of the overall structure occurs at lower force values and shorter displacements. The type of screw employed has no effect on the ultimate force values for EVOH contents below 20 wt%. Above 20wt%, the results for the mixing screw are inferior to those obtained with the metering screw. The morphological studies showed that, for the mixing screw, more EVOH was present in the surface regions. The impact ultimate force values seem to indicate that the impact behavior of the blend, especially for higher loadings of EVOH, does not only depend on the laminar structure in the core region, but also on the content of dispersed phase near the surfaces of the extrudate. Higher dispersed phase content near the surfaces increases the number of craze locations, thus increasing the amount of weak spots in the extrudate.

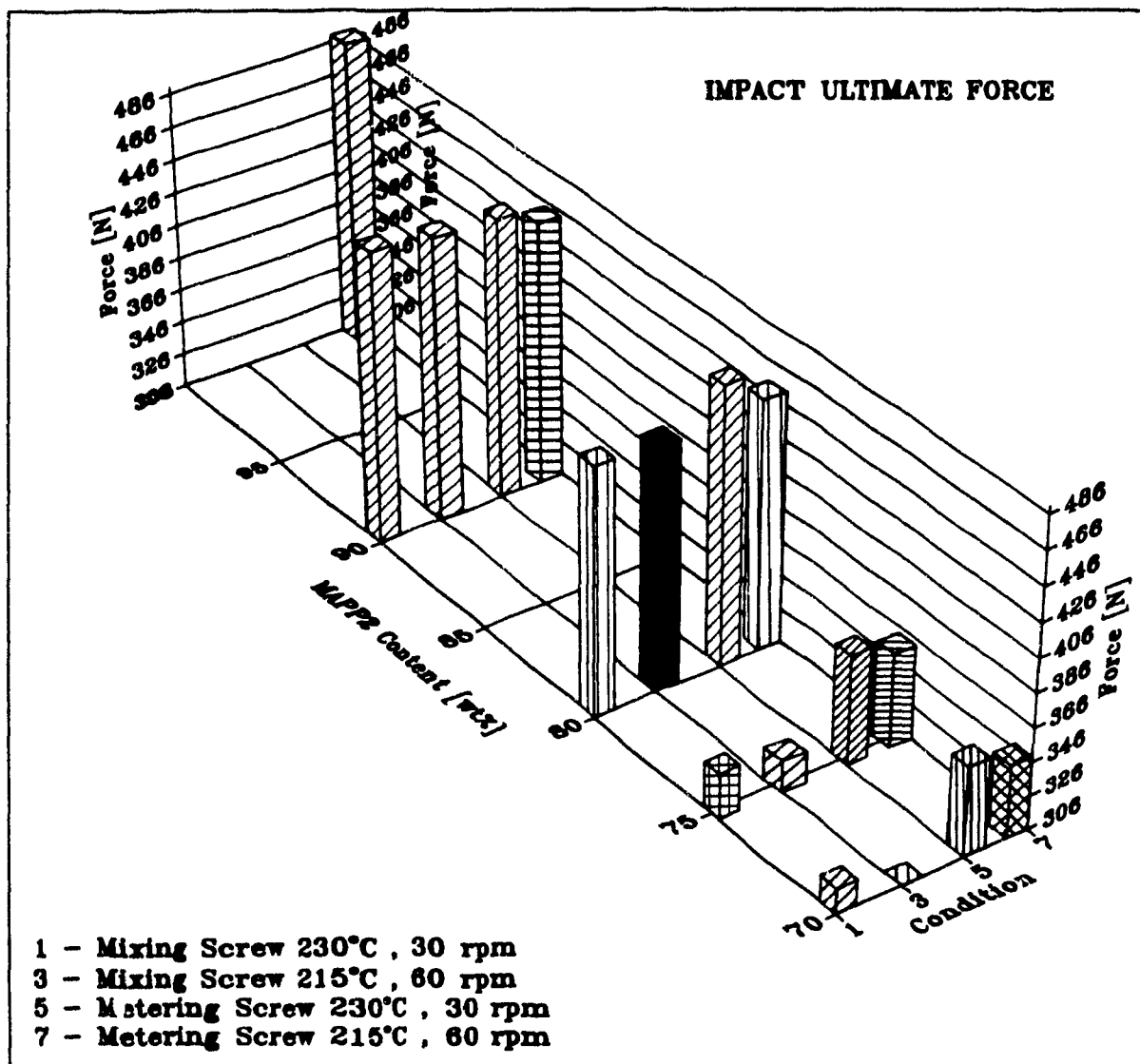


Figure 4.43 Impact Ultimate Force for a MAPP2/EVOH blend system as a Function of Composition and Processing Conditions.

The fracture behavior showed significant dependence on composition. Samples containing up to 20wt% EVOH showed impact fracture behavior similar to that of PP samples. On the other hand, samples with 25 and 30wt% EVOH showed white crazes and cracks everywhere, and the center portion of the specimen was shattered and broke away.

Figure 4.44 shows the impact slope for this group of experiments. Again, the impact slope provides a more sensitive means of distinguishing between the effects of different processing conditions. For both screw types, the processing conditions with high die temperature and long residence time, designed to improve adhesion between the two phases, result in slope values which are considerably lower than those measured for experiments with a lower die temperature and shorter residence time. For all four composition ratios and both processing conditions, the metering screw gives better results than the mixing screw, probably for the same reasons given above. For the metering screw at 230°C and 60rpm, the differences in the slope value for 10 and 20wt% of EVOH compared to pure PP are only minor, thus reinforcing the results obtained for the impact ultimate force.

The results for this group of experiments show that the amount of functionalized groups present at the interface, the amount of EVOH incorporated into the blend system, the screw type, the die temperature, and the residence time of the blend in the extruder and die system have a profound effect on the mechanical behavior of the final product. The impact data indicate that, for the system used in this study, up to 20wt% EVOH can be incorporated into the blend without considerable loss in impact strength. On the other hand, the impact data also show that the amount of functionalized groups present in the compatibilizing agent must be increased, or the type of compatibilizer changed, if higher amounts of EVOH are required. Otherwise, inferior mechanical properties would be obtained.

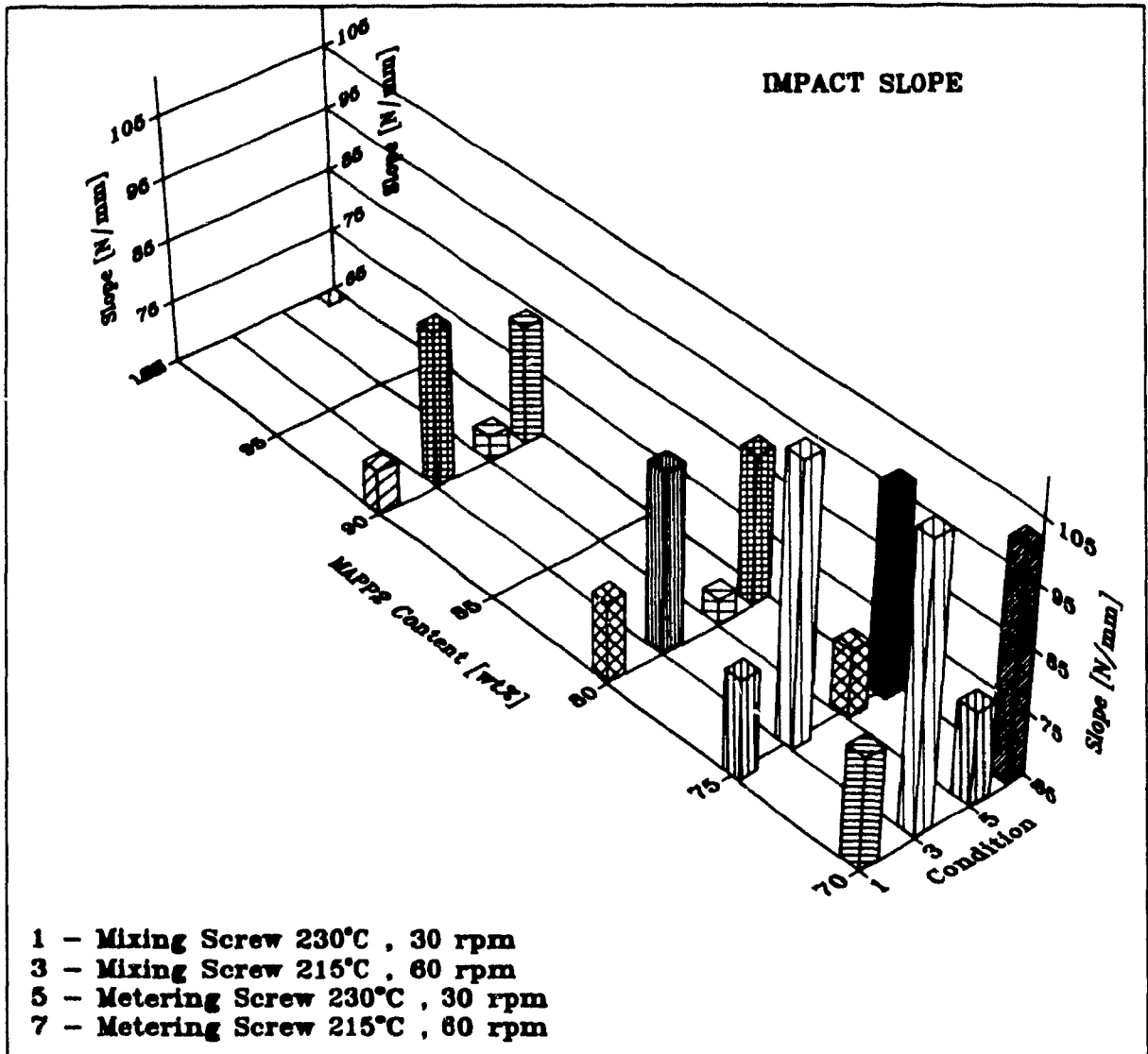


Figure 4.44 Impact Slope for a MAPP2/EVOH blend system as a Function of Composition and Processing Conditions.

4.4 Specific Extruder Energy

During extrusion, the power required by the motor is a function of screw speed, n , and the torque, M , acting on the screw. The specific energy input, \bar{e} , is defined as the power divided by the mass throughput rate, \dot{m} , thus leading to the following equation for the specific extruder energy [90]:

$$\bar{e} = \frac{P}{\dot{m}} = \frac{M \cdot \omega}{\dot{m}} = \frac{M \cdot 2\pi n}{\dot{m}} = \frac{Wh}{kg} \quad (33)$$

where ω is the angular speed of the screw. The specific extruder energy is a measure of the amount of work to melt, mix, and pump the resins fed to the extruder, and can be readily measured on commercial extrusion lines. This value has been suggested as a possible criterion for evaluating mixing quality [90].

It should be understood that the specific extruder energy is governed by a number of parameters. These include energy dissipation, effective melt viscosity, screw design, as in the case of including a mixing section, melt throughput rate, rotational speed of the screw, and pressure buildup in the extruder. Many of these variables are interdependent, and, furthermore, not all of them are directly or indirectly related to mixing quality. Therefore, the objective of the present set of experiments has been to measure the specific extruder energy, and to determine if any correlations between specific extruder energy and mixing quality, as indicated by microstructural analysis, exist. It was thought that if good correlations were obtained, the specific extruder energy could be employed as a useful tool for process and product quality control.

During the experiments, the extruder power was calculated from the armature current and voltage of the motor. The average

mass flow rate was calculated from the weight of extrudate, collected for 30 seconds, as an average over 20 samples.

4.4.1 PP/EVOH and PP/MAPP/EVOH Blends

In Figure 4.45 the specific extruder energy is given as a function of temperature and composition ratio for the metering screw at an extruder rpm of 60 1/min. The results show that the influence of the die temperature on the specific extruder energy is considerable. The change to a lower die temperature was achieved by reducing the overall temperature profile along the extruder barrel (Table 3.2). This colder temperature profile raises the viscosities of the melts of the two phases (Figure 3.1), thus requiring a higher energy input at otherwise constant processing conditions.

For the mixtures of the pure homopolymers, the effect of composition ratio on specific extruder energy is minor, but a decline with increasing amount of EVOH is noticeable, although the viscosity of EVOH is higher than that of PP. The result may be explained by the slippage between the layered, dispersed phase and the matrix phase, which is due to the poor interfacial interaction between the two phases. This slippage leads to decreasing power requirement, as more layers are incorporated into the system.

The specific extruder energy results are in agreement with viscosity measurements. The viscosities that Lepoutre [40] obtained for the PP/EVOH blend system were lower than the respective homopolymer viscosities, which led to designating the blends as negatively deviating. This deviation from the additivity rule has also been observed for other blend systems [27, 28, 29, 39].

The results for experiments with minor amounts of compatibilizing agent also show the strong influence of processing temperature on the specific extruder energy. The differences

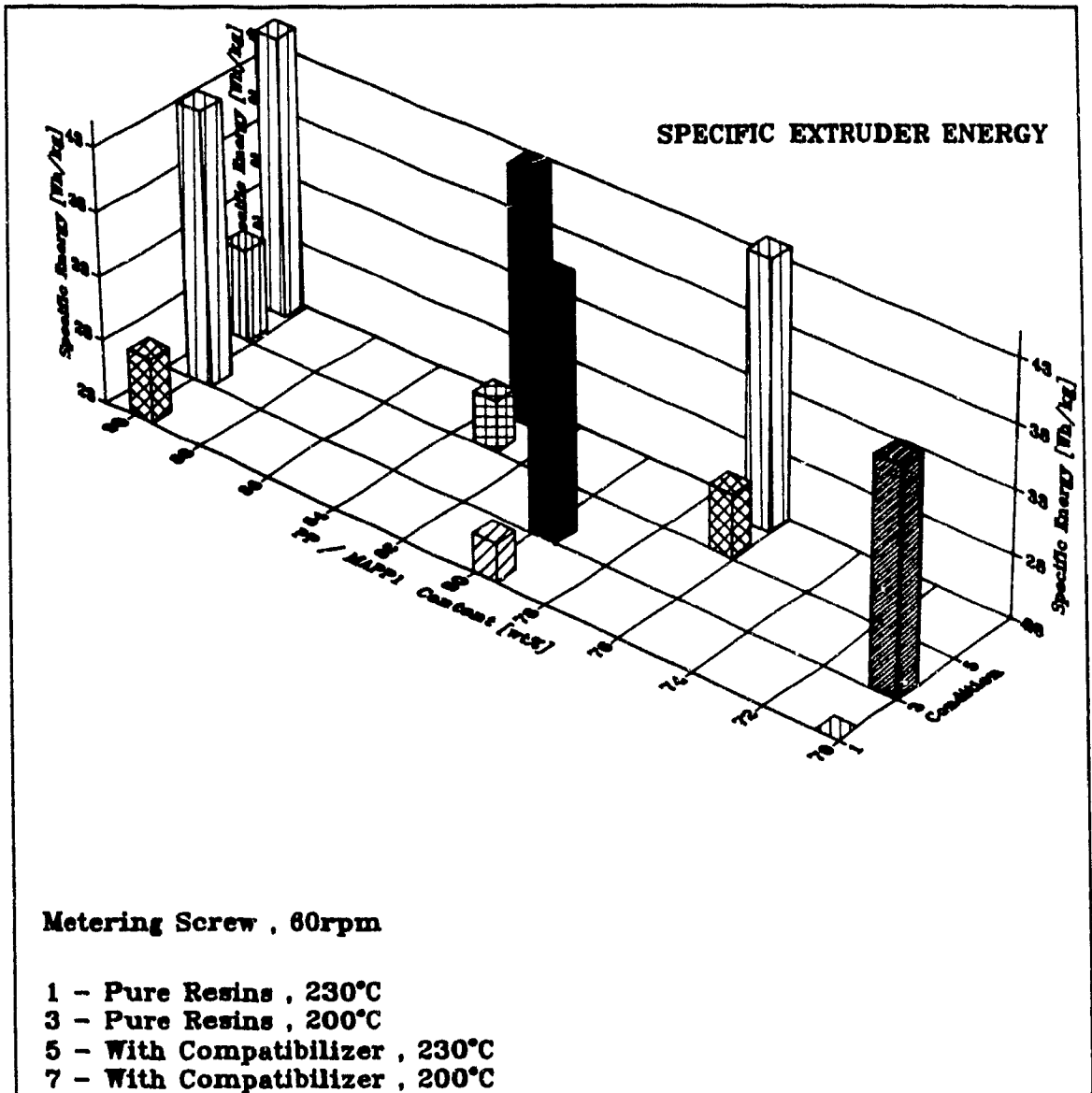


Figure 4.45 Specific Extruder Energy for PP/EVOH and PP/MAPP1/EVOH blend systems as a Function of Composition and Die Temperature ($h=1.0\text{mm}$).

between the experiments, with or without compatibilizer, for both temperatures are minor, and they fall within the range of experimental error for the measurements. The results for the specific extruder energy reinforce the results obtained with the impact tests, which indicate that the amount of available functionalized groups and the procedure of introducing the compatibilizer to the system are insufficient to promote interfacial activity between the dispersed and matrix phases.

A comparison of different adapter angles and two die exit gap thicknesses is given in Figure 4.46. The results show that although the use of a mixing screw increases energy consumption, temperature changes appear to have a stronger effect, about twice the value in the ranges shown. For both screw types, the specific extruder energy changes marginally for a change in exit gap thickness.

In Figure 4.47 the influence of extruder speed is given. Increasing extruder speed or employing a mixing screw results in higher energy consumption. The increase in extruder energy due to an increase in rpm is equal for an exit gap size of 0.5mm or 1.0mm, for both screw types.

4.4.2 MAPP2/EVOH Blends

Figure 4.48 gives a summary of the specific extruder energy for this group of experiments. The composition ratio 50/25/25wt% MAPP2/PP/EVOH will be discussed separately. In comparison to experiments without, or with minor amounts of, compatibilizer, the specific extruder energy values measured with the MAPP2/EVOH blends are approximately 30% higher for the metering screw, and 45% higher for the mixing screw. Note that the rheological data given in Figure 3.1 have shown that all three polypropylene based resins have very similar viscosities over the shear rate range tested.

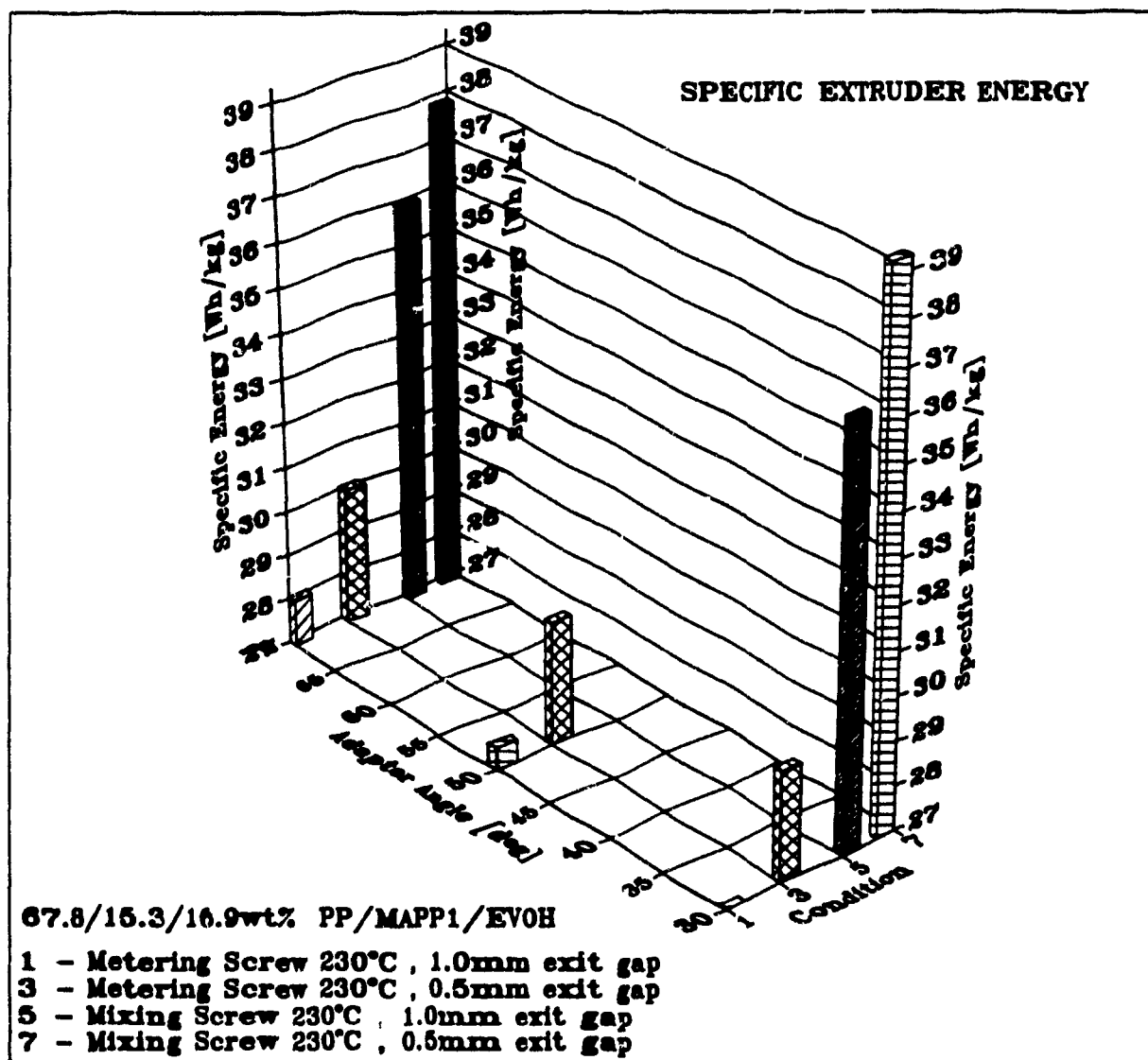


Figure 4.46 Specific Extruder Energy for a PP/MAPP1/EVOH blend system as a Function of Adapter Angle, Exit Gap Size and Screw Design (60 rpm).

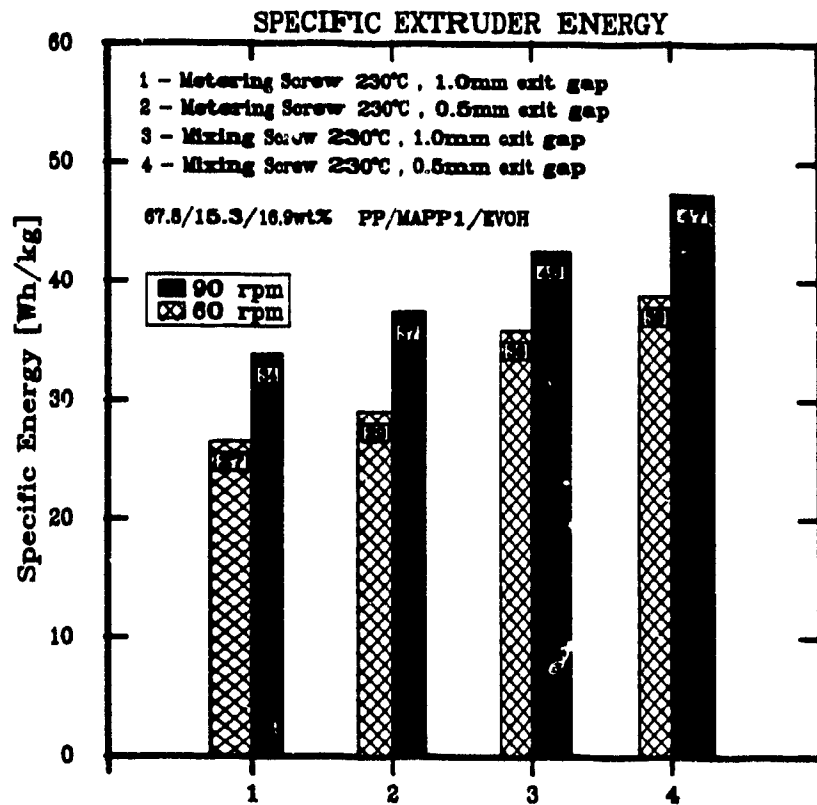


Figure 4.47 Specific Extruder Energy for a PP/MAPP1/EVOH blend system as a Function of Screw Speed and Exit Gap Size.

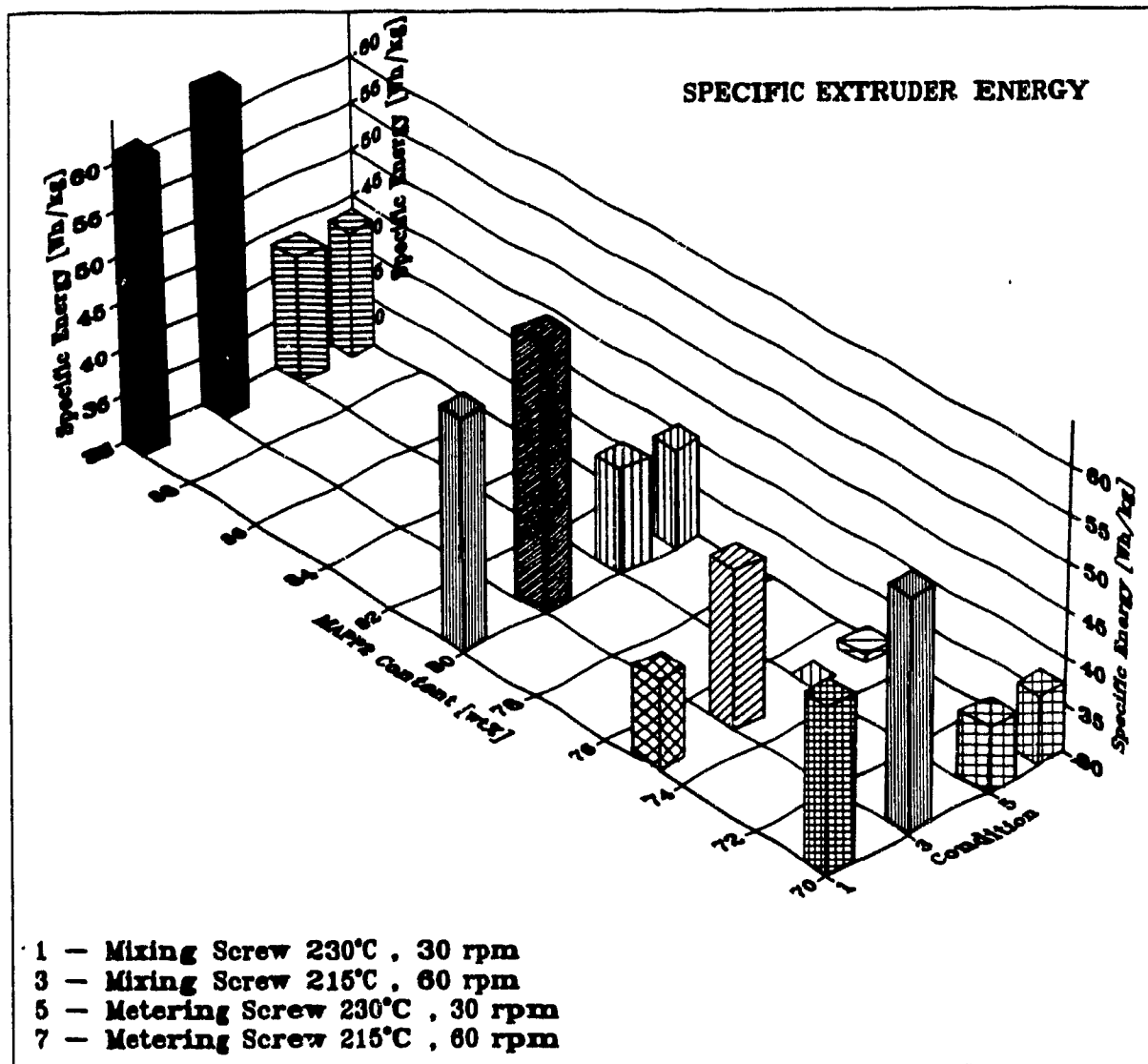


Figure 4.48 Specific Extruder Energy for a MAPP2/EVOH blend system as a Function of Composition and Processing Conditions ($h=0.5\text{mm}$).

The measured energy values suggest that, for the MAPP2/PP blend system, the specific extruder energy is strongly influenced by compositional and interfacial effects. Differences in energy consumption, between the metering and mixing screws, are believed to be due to the surface area of the dispersed phase which interacts with the matrix phase. The mixing screw produces a homogeneously distributed dispersed EVOH phase in a PP matrix phase (Figure 4.6). This homogeneous distribution of the dispersed phase involves larger overall surface area when compared to the distribution achievable with the metering screw. Therefore, the data shown in Figure 4.48 seem to imply that surface area and interfacial activities have a more pronounced effect on the energy consumption than a change in temperature or extruder speed. The decrease in specific extruder energy with increasing EVOH content might be attributed to the excess availability of dispersed EVOH and the resulting lack of interfacial interaction, due to the insufficient amounts of functionalized groups available in the compatibilizer.

The energy values for the mixing ratio 50/25/25wt% MAPP2/PP/EVOH, for all four processing conditions, support the idea that interfacial activity can be influenced by careful process design. In all cases, a smaller amount of energy is required to process the blend when 25wt% of MAPP2 is replaced by pure PP. This amount of pure PP is sufficient to reduce activity at the interface, thus acting during the extrusion process as a lubricant and lowering the required power consumption by the extruder.

The experimental data presented in Figures 4.45 to 4.48 show that the specific extruder energy could be a useful parameter for controlling the mixing and product quality in a polymer blend extrusion system, but the effects of composition and processing conditions have to be studied in more detail to evaluate the significance of this parameter.

4.5 Oxygen Permeability

The incorporation of different amounts of ethylene vinyl-alcohol copolymer into a polypropylene matrix resin was designed with the objective of forming the dispersed EVOH phase as a laminar structure within the PP matrix phase. The layers would act as a barrier, e.g. against oxygen permeation, thus lowering the very high oxygen permeation rate through virgin polypropylene. The same objectives also apply to the permeability of hydrocarbons or other organic solvents, which easily penetrate polyethylene or polypropylene materials. The utility of the laminar structure is based on the idea that these EVOH platelets/layers act as barriers to the permeant molecule by providing a long tortuous path. The barrier properties thus obtained should be comparable to those obtained with co-extruded multi-layer products incorporating PP and EVOH.

The results for oxygen permeability, PO_2 , are reported in Table 4.1 for the pure resins and in Figures 4.49 to 4.51 for the blends. Measurements on triplicate ribbons were reproducible to better than $\pm 7\%$. The result for EVOH is comparable to values reported in the literature [66,91], and differences can be attributed to sample preparation, processing conditions etc.

In Figure 4.49, the oxygen permeability for PP/EVOH blends is given as a function of processing temperature. The addition of only 10wt% EVOH already reduces the oxygen permeation by 40%. An EVOH amount of 30wt% results in a reduction of more than 60%. The lower processing temperature results in a reduction of the oxygen permeability, but it is not as effective as the higher temperature. These data indicate that the thickness of the layers/platelets is important, where thinner layers in larger numbers are more effective in reducing the permeation rate than thicker layers in smaller numbers.

Table 4.1 Oxygen Transmission Rates.

Polymer	PO_2 [cc.mm/m ² .24hr.atm]
PP	41.0
EVOH	0.7
MAPP1	43.1
MAPP2	64.1

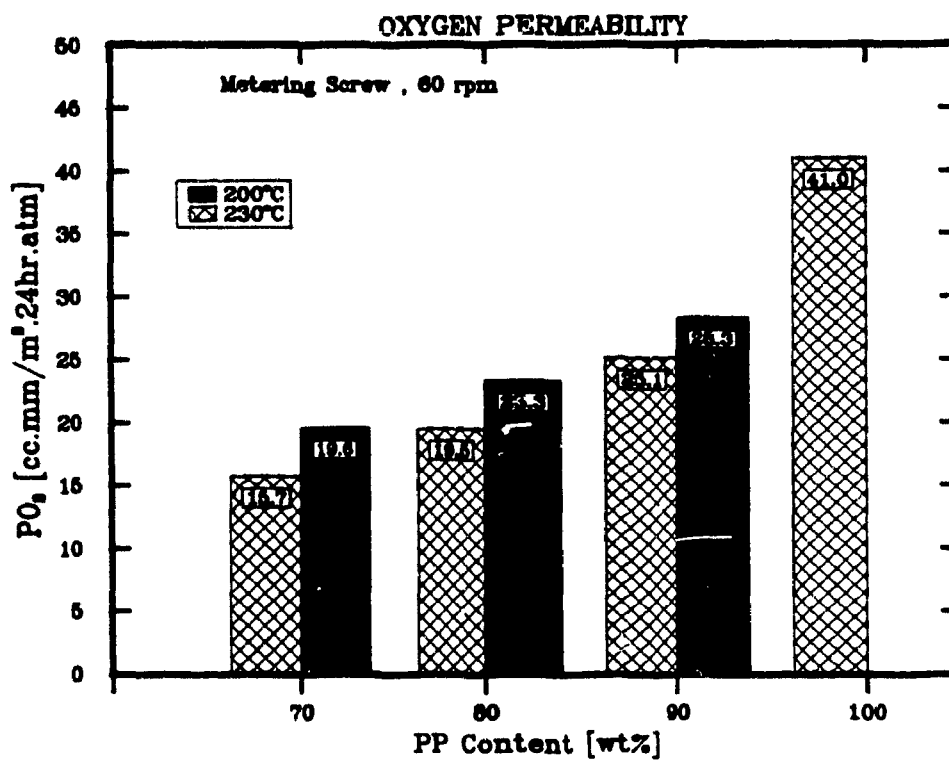


Figure 4.49 Oxygen Permeability for a PP/EVOH blend system as a Function of Composition and Die Temperature.

A comparison of two extruder speeds is given in Figure 4.50. An increase in rpm results, for both types of screws, in a decrease in the permeation rate. This is in accordance with the micrographs obtained for different extruder speeds, where an increase in rpm results in a larger number of thinner layers.

The oxygen permeation rates for the MAPP2/EVOH blend system are compared in Figure 4.51. Generally, an increase in the amount of EVOH causes a reduction in permeation rate for all four processing conditions, but different processing conditions have a varying effect on the permeation behavior of the extrudate. The use of a mixing screw results in higher permeation rates compared to the metering screw. For both screw types, the processing conditions designed to improve adhesion - high temperature, long residence time - show superior oxygen barrier properties than the conditions less favorable to adhesion. The data also show that the improvement in adhesion is more important in producing an effective barrier, through a well bonded internal structure, than process conditions designed to achieve a strong laminar structure through higher rpm, which produce thinner layers, but with inferior bonding.

4.5.1 Evaluation of Barrier Performance

Some theoretical approximations can be made with regard to the barrier properties of the above materials. The barrier properties of a homogeneous system, by analogy to Maxwell's [92] treatment of conductivity for a dispersion of non-conducting spherical particles in a conducting matrix, may be expressed as follows :

$$\tau = 1 + \frac{\phi_d}{2} \quad (34)$$

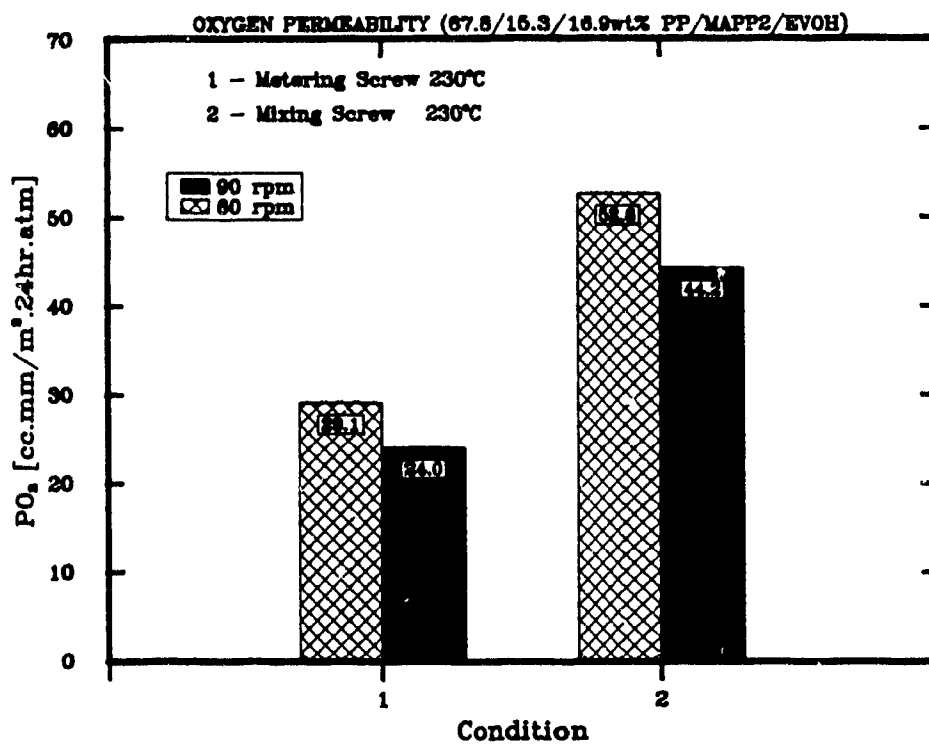


Figure 4.50 Oxygen Permeability for a PP/MAPP2/EVOH blend system as a Function of Screw Design and Speed.

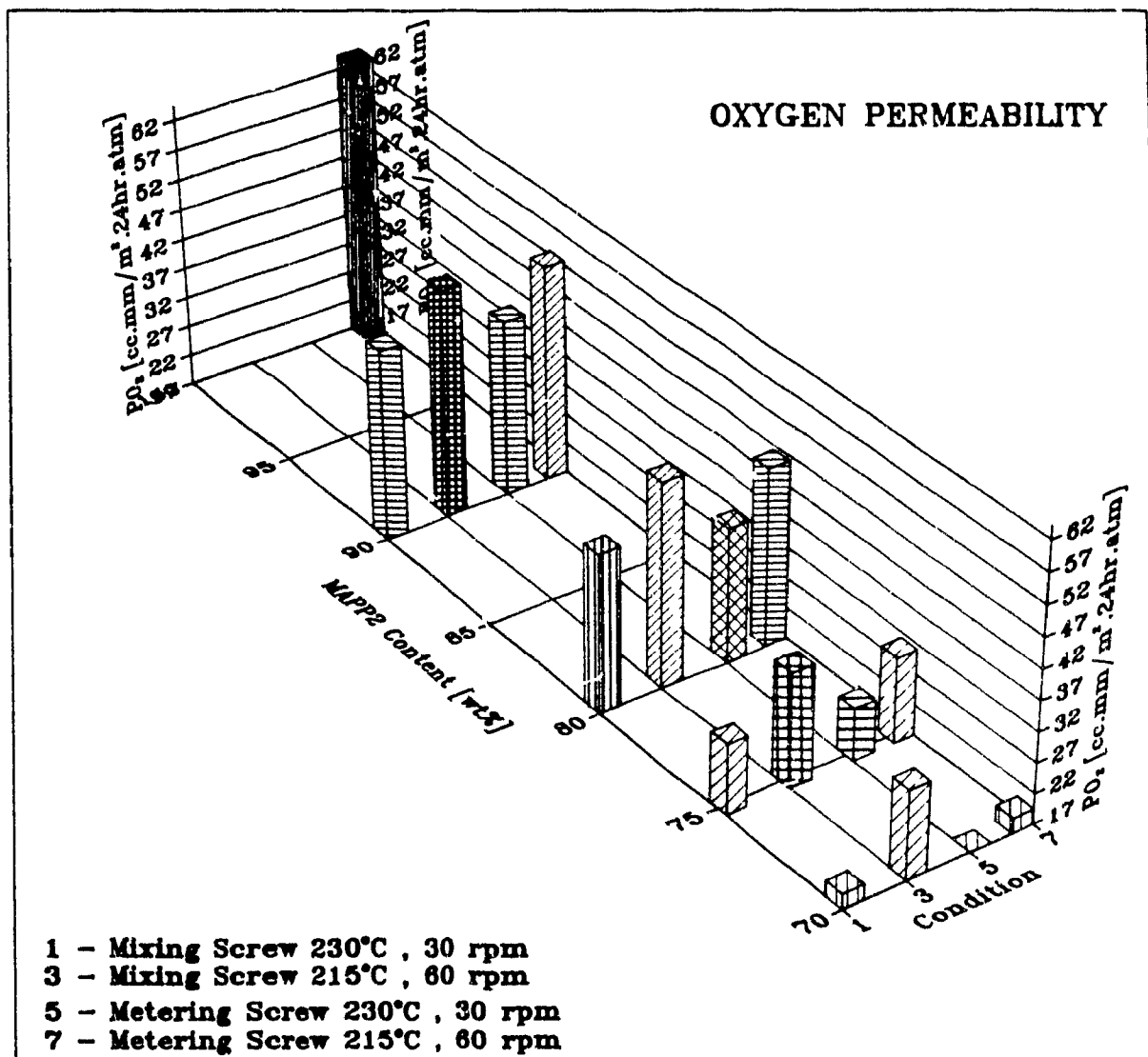


Figure 4.51 Oxygen Permeability for a MAPP2/EVOH blend system as a Function of Composition and Processing Conditions.

where τ is the tortuosity, and ϕ_d is the volume fraction of the dispersed phase.

A commonly used approximation for the ratio of the permeability of the conducting, continuous phase as a function of the tortuosity and the volume fraction of matrix polymer, ϕ_m , has been proposed by Michaels and Bixler [93] and Barrer et al. [94] :

$$\frac{P_c}{P_m} \approx \frac{\phi_m}{\tau} \quad (35)$$

where P_c is the permeability of the composite, and P_m is the permeability of the matrix.

To describe the effect of a conducting, spherical filler on the overall composite permeability, Robeson et al. [95] report Maxwell's result as :

$$P_c = P_m \cdot \left[\frac{P_d + 2P_m - 2\phi_d \cdot (P_m - P_d)}{P_d + 2P_m + \phi_d \cdot (P_m - P_d)} \right] \quad (36)$$

where P_d is the permeability of the dispersed phase.

The permeability through a composite of two layers can be approximated by [95] :

$$\frac{1}{P_c} = \frac{\phi_1}{P_1} + \frac{\phi_2}{P_2} \quad (37)$$

where P_1 and P_2 are the permeabilities of the respective phases, and ϕ_1 and ϕ_2 are their corresponding volume fractions.

In Figure 4.52, oxygen permeation data for condition 5 (Figure 4.51) are compared to the theoretical predictions for homogeneous and laminated systems. The calculations based on Equ-

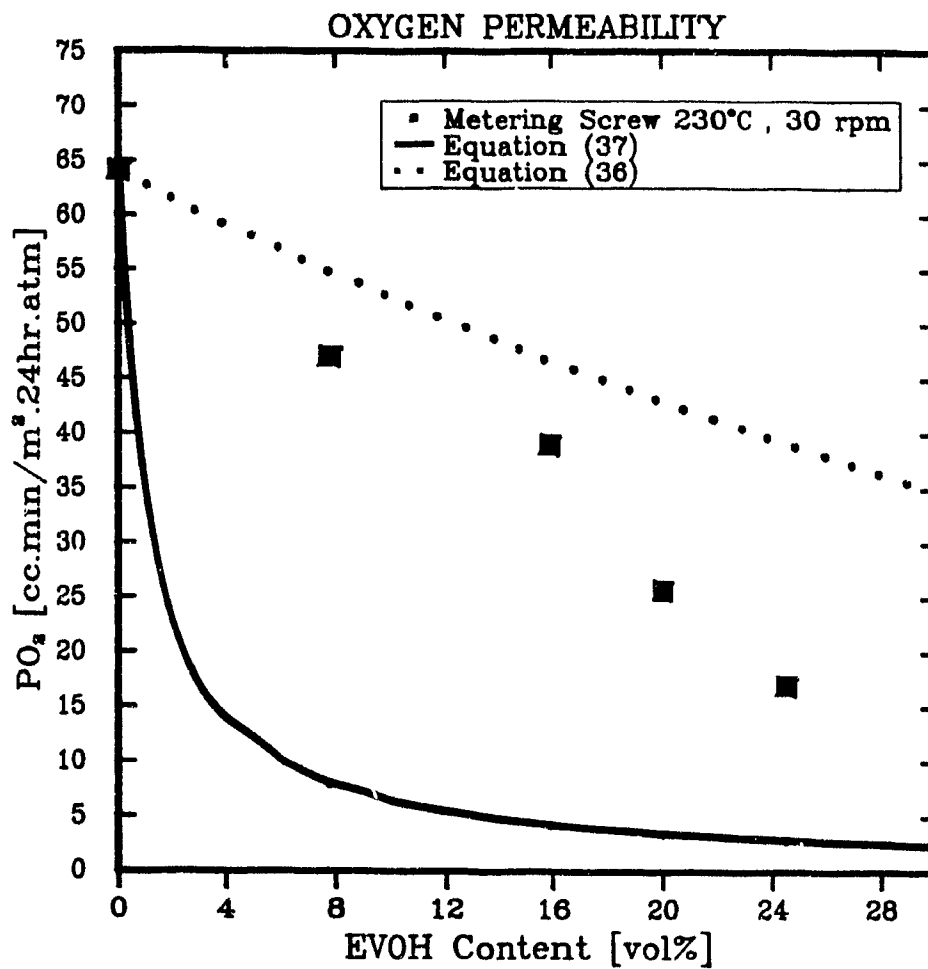


Figure 4.52 Comparison of Measured Oxygen Transmission Rates with Model Predictions for a MAPP2/EVOH blend system.

tion (36) are the upper bound and show a slow decrease in permeation rate as a function of EVOH content. Equation (37), on the other hand, is the lower bound, representing a case in which EVOH would exist as a continuous, undisturbed layer in PP. The experimental data for this study fall inside the range defined by the upper and lower bounds. Up to an EVOH content of 20wt% (15.9vol%), the improvement in oxygen permeability is only minor, and the measured data points are close to the curve calculated for a homogeneous blend. Above 20wt% EVOH, the oxygen permeation rate is considerably reduced, and the data show a clear trend towards the lower bound.

The behavior of blends with EVOH content below 20wt% is interesting because the SEM analysis has indicated (Figure 4.24) the absence of laminar structure. The platelet morphology observed in these systems is not effective in reducing the permeation rate considerably, since it appears to behave similarly to a homogeneous blend system.

Figure 4.52 presents evidence that the incorporation of minor amounts of a thermoplastic barrier material in a low cost matrix material is a suitable approach to efficiently reduce the gas permeability through polyolefin matrix materials, when the dispersed phase barrier material is obtained in laminar form in the matrix material during the manufacturing process.

CHAPTER 5

CONCLUSIONS AND RECOMMENDATIONS

5.1 Conclusions

The studies into the morphology of extruded polymer blend systems have shown that it is feasible to create a laminar structure of a dispersed EVOH phase in a matrix PP phase. The one-dimensional threadlike, or fiber, structure, obtained in the capillary extrusion process, is replaced by a two-dimensional structure of the dispersed phase, when a slit die is incorporated into the extrusion process.

The laminar structure forms in the core of the extrudate. However, near the surfaces, the dispersed phase forms agglomerates of different sizes and shapes, which are oriented parallel and perpendicular to flow.

Morphological studies, including a study of morphology development inside the die and studies of the effect of processing conditions on the morphology of the final product, revealed that the laminar structure is a result of die design. Processing conditions influence mainly the shape and dimensions of the laminar core region of the extrudate.

Die design plays a critical role in the development of the laminar structure. The entrance angle of the adapter controls the orientation and distribution of the dispersed phase in the matrix phase. In this zone, the dispersed phase is streamlined and forced into coalescence. The adjoining tubular section enhances migration of the dispersed phase towards the center axis. Even for a very fine and uniform distribution of the dispersed phase in melt leaving the extruder, a sharp and short conical section in the adapter is sufficient to orient

and coalesce the dispersed phase towards the center axis. Thus, even when a mixing screw is used, a laminar structure of the dispersed phase in the final extrudate is achievable.

The large dispersed phase agglomerates, located near the adapter axis, are transformed and oriented in the diverging section of the slit die into two-dimensional layer and platelet structures, which flow as stable microstructures through the remaining slit section. In the contraction zone, where the final exit gap thickness is adjusted, a highly extensional flow field stretches the two-dimensional layers and platelets in the flow direction. This produces very thin layers and platelets in the core region of the final extrudate.

The main features of the extrudate morphology are established in the short flow geometry of the adapter, where the dispersed phase is concentrated mainly near the adapter axis, and in thin circular laminar arrangements near the channel wall. The retention of this structure during transformation, from a circular laminar structure in the tubular adapter section into a rectangular laminar structure in the slit die, shows a remarkable flow stability, even for strong dimensional changes in the flow geometry.

The composition ratio has a very strong influence on the laminar structure, showing that, for a lower EVOH content, layers are replaced by a platelet structure. SEM analysis has shown that the optimum EVOH content is approximately 25wt%, where a change occurs from a predominant platelet structure into the layered structure.

The shape and dimensions of the laminar structure are influenced by processing conditions. Depending on the blend system chosen, a higher processing temperature results in a more dispersed phase concentration in the core region, due to improved coalescence and migration in the adapter. A higher flow rate

introduces higher extensional rates in the contraction section of the slit die, thus producing larger and thinner layers due to stretching in the flow direction. The same holds for smaller exit gap thicknesses, where a larger contraction ratio has the same effect on the orientation and extension of the laminar dispersed phase.

The specific extruder energy could provide a valuable tool for differentiating between different types of blend systems, and between the flow characteristics of various compositions. In addition, specific extruder energy may be used to evaluate the extent of interfacial activity in blend systems.

Impact ultimate force and slope measurements have shown independently that the PP matrix can incorporate, when good adhesion is achieved, up to 20wt% EVOH without significantly changing the desirable impact properties of PP. Above 20wt% EVOH, a sharp drop in ultimate force is observed, indicating a destabilization of the matrix phase.

Oxygen permeation tests have shown that the blend exhibits lower oxygen permeability than pure PP, when EVOH is incorporated as the dispersed phase into the system. Oxygen transmission rates obtained with a blend system can be as low as those obtained with a multi-layer coextrusion product, although only at high EVOH concentrations. Comparison of experimental data with theoretical permeation predictions shows that, up to 20wt% EVOH, the reduction in oxygen transmission rate is only minor, and follows the prediction for a homogeneous system. At 25wt%, a considerable decrease is noticeable, and the trend for higher EVOH contents is towards the behavior of a multi-layer system.

The results underline the difficulties associated with incorporating compatibilizing agents (adhesive polymers) into blend systems. The concentrations of functionalized groups in the

adhesive polymers employed in this work are sufficient to produce strong bonding between layers in a multi-layer coextrusion process. On the other hand, for a PP/EVOH blend system, the concentration of functionalized groups, the procedure of incorporating the compatibilizing agent into the blend system, and the processing conditions need to be manipulated, in order to provide sufficient contact time and appropriate conditions at the interface favorable for strong bonding.

For the processing conditions studied, the most favorable results were achieved with a metering screw, a die temperature of 230°C, and an extruder rpm of 30 1/min. These conditions increase residence time in the extruder and die, thus favoring improved adhesion at the interface between the dispersed EVOH phase and the functionalized PP matrix phase.

5.2 Recommendations for Future Work

The results of this work indicate the importance of the conditions at the interface between the dispersed EVOH phase and the matrix PP phase. The dispersed phase is deformed constantly during flow through the extruder and die units, which placing severe and delicate constraints on the optimal conditions for bonding and on the compatibilizing agent.

The influence of the concentration of functionalized groups, present in the graft copolymers, on interfacial adhesion should be studied carefully. The amount of maleic anhydride should be increased in steps to an amount of 2wt%, which is the limit set by FDA regulations for resins in contact with food. In addition, other commercially available or specifically synthesized copolymers, which are based on di- or tri-blocks, should be considered. Other studies have shown that these block copolymers are more effective in obtaining improved adhesion than graft copolymers.

Another area of improvement relates to the sequence of operations employed in the preparation of blends. The optimum sequence of combining the dispersed phase, matrix phase, and compatibilizing agent should be established, with the purpose of optimizing interfacial adhesion. The results of the present work indicate that the available amount of functionalized groups at the interface is the most important requirement in achieving good bonding. Based on this requirement, it is proposed to pre-blend EVOH with the compatibilizing agent in a batch mixing operation. The modified EVOH would then be fed with the PP matrix phase as a dry blend to the extruder. In this fashion, the objective of locating the functionalized groups at the interface is achieved in the pre-blending step.

Another problem of concern relates to the impact properties at higher loadings of EVOH, which are necessary to achieve the required permeation barrier properties in food packaging. The proposed future work on the improvement of interfacial adhesion should, in principle and if successful, also improve the impact properties of the extrudate. In addition, other researchers have shown that the incorporation of small amounts of a rubber phase into brittle polymers greatly enhances the impact behavior of these modified polymers. It is recommended to evaluate the feasibility of incorporating small amounts of a rubber phase into a EVOH/Compatibilizer-PP blend system.

With regard to processing conditions and equipment design, the following aspects should be considered :

(a) The morphology should be studied in conjunction with a coat-hanger slit die, in comparison to the fish-tail slit die used in this study. The coat-hanger die is more suitable for extruding thin and wide plastics plates, and the effect of these special design features on the extrudate morphology should be analyzed.

(b) The blend system should be evaluated in conjunction with a blow-molding machine. Both the parison extrusion and inflation stages should be analyzed, in relation to the influence of various design and operating variables on part morphology and properties.

(c) The manufacturing of thin plastic sheets usually involves a roller-die head, where a slit die extrudes the polymer system onto a combination of rollers which, by means of different roller nip clearances, form the extrudate into its final width and thickness. The effect of the flow behavior in the nip between the rollers on the morphology should be studied.

5.3 Original Contributions to Knowledge

i) Production, for the first time, of sheets based on laminar blends of a dispersed ethylene vinyl-alcohol copolymer phase in a polypropylene matrix phase, with good oxygen barrier properties.

ii) Detailed study, for the first time, of the interactions of morphology with processing, design, and compositional variables, during extrusion of a polymer blend in a slit die.

iii) Design of a die system where blend morphology control may be achieved, instead of controlling morphology in the screw zone, which presents more processing limitations.

iv) Analysis of morphological development inside the adapter and slit die units.

v) The EVOH/PP blend system was processed on conventional processing equipment. Morphological studies revealed that the laminar structure is a result of die design. Processing conditions influence mainly the shape and dimensions of the laminar core region of the extrudate.

vi) The incorporation of a mixing screw into the extrusion process did not inhibit the development of a laminar structure. A sharp and short conical section in the adapter is sufficient to orient and coalesce the dispersed phase towards the center axis, even for a very fine and uniform distribution of the dispersed phase in melt leaving the extruder.

vii) Comparison of experimental data with theoretical predictions shows that, up to 20wt% EVOH, the reduction in oxygen transmission rate is only minor, and follows the prediction for a homogeneous system. At 25wt%, a considerable decrease is noticeable, and the trend for higher EVOH contents is towards the behavior of a multi-layer system.

REFERENCES

1. G. I. Taylor, Proc. Roy. Soc., A138, 41 (1932)
2. G. I. Taylor, Proc. Roy. Soc., A146, 501 (1934)
3. H. Lamb, "Hydrodynamics", Chap. 11, 562, 6th ed. Cambridge (University Press), London (1932)
4. C. E. Chaffey and H. Brenner, J. Colloid Interf. Sci., 24, 258 (1967)
5. R. G. Cox, J. Fluid Mech., 37, 601 (1969)
6. N. A. Frankel and A. Acrivos, J. Fluid Mech., 44, 65 (1970)
7. B. M. Turner and C. E. Chaffey, Trans. Soc. Rheol., 13, 411 (1969)
8. H. B. Chin and C. D. Han, J. Rheology, 23, 557 (1979)
9. S. J. Choi and W. R. Schowalter, Physics Fluids, 18, 420 (1975)
10. W. Bartok and S. G. Mason, J. Colloid Sci., 13, 293 (1958)
11. W. Bartok and S. G. Mason, J. Colloid Sci., 14, 13 (1959)
12. F. D. Rumscheidt and S. G. Mason, J. Colloid Sci., 16, 238 (1961)
13. H. J. Karam and J. C. Bellinger, I&EC Fundamentals, 7, 576 (1968)
14. S. Torza, R. G. Cox and S. G. Mason, J. Colloid Interf. Sci., 38, 395 (1972)
15. F. Gauthier, H. L. Goldsmith and S. G. Mason, Rheol. Acta, 10, 344 (1971)
16. J. J. Elmendorp and R. J. Maalcke, Polym. Eng. Sci., 25, 1041 (1985)
17. H. L. Goldsmith and S. G. Mason, J. Colloid Sci., 17, 448 (1962)
18. F. Gauthier, H. L. Goldsmith and S. G. Mason, Trans. Soc. Rheol., 15, 297 (1971)

19. C. van der Reijden-Stolk and A. Sara, Polym. Eng. Sci., 26, 1229 (1986)
20. E. Bartram, H. L. Goldsmith and S. G. Mason, Rheol. Act., 14, 776 (1975)
21. C. D. Han and K. Funatsu, J. Rheology, 22, 113 (1978)
22. H. B. Chin and C. D. Han, J. Rheology, 24, 1 (1980)
23. H. VanOene, J. Colloid Interf. Sci., 40, 448 (1972)
24. J. M. Starita, Soc. Rheol. Trans., 16, 339 (1972)
25. H.-K. Chuang and C. D. Han, J. Appl. Polym. Sci., 29, 2205 (1984)
26. V. E. Dreval, G. V. Vinogradov, M. P. Zabugina, N. P. Krasnikova, E. V. Kotova, and Z. Pelzbauer, Rheol. Acta, 22, 102 (1983)
27. C. D. Han and T. C. Yu, J. Appl. Polym. Sci., 15, 1163 (1971)
28. C. D. Han and T. C. Yu, Polym. Eng. Sci., 12, 81 (1972)
29. C. D. Han, Y. W. Kim and S. J. Chen, J. Appl. Polym. Sci., 19, 2831 (1975)
30. S. Danesi and R. S. Porter, Polymer, 19, 448 (1978)
31. T. I. Ablazova, M. B. Tsebrenko, A. V. Yudin, G. V. Vinogradov and B. V. Yarlykov, J. Appl. Polym. Sci., 19, 1781 (1975)
32. M. V. Tsebrenko, A. V. Yudin, T. I. Ablazova and G. V. Vinogradov, Polymer, 17, 831 (1976)
33. M. V. Tsebrenko, Polym. Sci. USSR, 20, 108 (1978)
34. N. P. Krasnikova, E. V. Kotova, G. V. Vinogradov and Z. Pelzbauer, J. Appl. Polym. Sci., 22, 2081 (1978)
35. M. V. Tsebrenko, N. M. Rezanova and G. V. Vinogradov, Polym. Eng. Sci., 20, 1023 (1980)
36. N. Alle and J. Lyngaae-Jorgensen, Rheol. Acta, 19, 94 (1980)
37. N. Alle and J. Lyngaae-Jorgensen, Rheol. Acta, 19, 104 (1980)
38. N. Alle, F. E. Andersen and J. Lyngaae-Jorgensen, Rheol. Acta, 20, 222 (1981)

39. K. Min, J. L. White and J. F. Fellers, Polym. Eng. Sci., 24, 1327 (1984)
40. P. Lepoutre, M.Eng. Thesis, Dep. of Chemical Engineering, McGill University (1989)
41. P. M. Subramanian, Polym. Eng. Sci., 25, 483 (1985)
42. P. M. Subramanian and V. Mehra, Polym. Eng. Sci., 27, 663 (1987)
43. Personal Communication with P. M. Subramanian, E.I. du Pont de Nemours & Co.
44. B. D. Favis and J. P. Chalifoux, Polymer, 29, 1761 (1988)
45. B. D. Favis and J. P. Chalifoux, NRCC/IMRI "Polyblends-'87" Symposium, Montreal 4/1987
46. S. Wu, Polym. Eng. Sci., 27, 335 (1987)
47. F. Ide and A. Hasegawa, J. Appl. Polym. Sci., 18, 963 (1974)
48. Y. Minoura, M. Ueda, S. Mizunuma and M. Oba, J. Appl. Polym. Sci., 13, 1625 (1969)
49. W. M. Barentsen, D. Heikens and P. Piet, Polymer, 15, 119 (1974)
50. D. Heikens and W. M. Barentsen, Polymer, 18, 69 (1977)
51. H.-K. Chuang and C. D. Han, in: C. D. Han, ed. "Polymer Blends and Composites in Multiphase Systems", Adv. Chem. Ser. (206), Am. Chem. Soc. (1984)
52. H.-K. Chuang and C. D. Han, J. Appl. Polym. Sci., 30, 165 (1985)
53. C. D. Han and H.-K. Chuang, J. Appl. Polym. Sci., 30, 2431 (1985)
54. H.-K. Chuang and C. D. Han, J. Appl. Polym. Sci., 30, 2457 (1985)
55. R. Fayt, R. Jerome and Ph. Teyssie, J. Polym. Sci., Polym. Lett. Ed., 19, 79 (1981)
56. R. Fayt, R. Jerome and Ph. Teyssie, J. Polym. Sci., Polym. Phys. Ed., 19, 1269 (1981)
57. R. Fayt, R. Jerome and Ph. Teyssie, J. Polym. Sci., Polym. Phys. Ed., 20, 2209 (1982)

58. R. Fayt, R. Jerome and Ph. Teyssie, J. Polym. Sci., Polym. Lett. Ed., 24, 25 (1986)
59. R. Fayt, R. Jerome and Ph. Teyssie, Makromol. Chem., 187, 837 (1986)
60. T. Ouhadi, R. Fayt, R. Jerome and Ph. Teyssie, J. Appl. Polym. Sci., 32, 5647 (1986)
61. R. Fayt and Ph. Teyssie, Polym. Eng. Sci., 29, 538 (1989)
62. J. M. Willis and B. D. Favis, NRCC/IMRI "Polyblends-'88" Symposium, Montreal 4/1988
63. Technical Information of NPP7200-AF, Quantum Chemical Co.
64. Technical Information of MODIC, Mitsubishi Petrochemical Co., LTD.
65. Technical Information of ADMER, Mitsui Petrochemicals (America), LTD.
66. Technical Information on EVAL®EP-F Series, EVAL®Company of America
67. Personal Communication with R. H. Foster, Technical Development Manager, EVAL®Company of America
68. The Aldrich Library of FT-IR Spectra, 1st edn, Vol.1, 718 (1985)
69. S. Y. Hobbs, R. C. Bopp and V. H. Watkins, Polym. Eng. Sci., 23, 380 (1983)
70. B. C. Trivedi and B. M. Culbertson, eds "Maleic Anhydride", 1st edn, Plenum Press, New York (1982)
71. N. G. Gaylord, J. Polym. Sci., Polym. Lett. Ed., 21, 23 (1983)
72. S. Hozhabr-Ghelichi, M.Eng. Thesis, Dep. of Chemical Engineering, McGill University (to be submitted 1990)
73. L. Erwin, Polym. Eng. Sci., 18, 572 (1978)
74. L. Erwin, Polym. Eng. Sci., 18, 1044 (1978)
75. K. Y. Ng and L. Erwin, Polym. Eng. Sci., 21, 212 (1981)
76. D. W. Gailus and L. Erwin, SPE Techn. Papers, 27, 639 (1981) (39th ANTEC)

77. F. Mokhtarian and L. Erwin, SPE Techn. Papers, 28, 476 (1982) (40th ANTEC)
78. Technical Bulletin No.100, EVAL® Company of America
79. A. T. Mutel, "MORPHAN", Image Analysis System for Polymer Composite and Blend Morphologies, Dep. of Chem. Eng., McGill University (1989)
80. G. E. Owen, Polym. Eng. Sci., 21, 467 (1981)
81. R. P. Nimmer, Polym. Eng. Sci., 23, 155 (1983)
82. "High Speed Impact Tester : A Preliminary Manual", Rheometrics Inc., Union, NJ, 1978
83. S. L. Kessler, G. C. Adams, S. B. Driscoll and D. R. Ireland, eds "Instrumented Impact Testing of Plastics and Composite Materials", ASTM STP 936, American Society for Testing and Materials, Philadelphia, 1987
84. C. W. Knakal and D. R. Ireland in [83] pp. 44-57
85. T. F. Blahovici and G. R. Brown, Polym. Eng. Sci., 27, 1611 (1987)
86. Z. Tadmor and C. G. Gogos, eds "Principles of Polymer Processing", 1st edn, Wiley, New York (1979)
87. J. R. A. Pearson, ed. "Mechanics of Polymer Processing", 1st edn, Elsevier, New York (1985)
88. R. Diraddo, Ph.D. Thesis, Dep. of Chemical Engineering, McGill University (1989)
89. Personal Communication with Y. Machida, Manager, Mitsui Petrochemicals (America), LTD.
90. T. Bartilla, D. Kirch, J. Nordmeier, E. Promper, and Th. Strauch, Adv. Polym. Techn., 6, 339 (1986)
91. L. B. Ryder, Plastics Eng., 40, 41 (1984)
92. J. C. Maxwell, "Electricity and Magnetism", 3rd edn, Vol.1, Dover, New York (1904)
93. A. S. Michaels and H. J. Bixler, J. Polym. Sci., 50, 413 (1961)
94. R. M. Barrer, J. A. Barrie and M. G. Rogers, J. Polym. Sci. Part A, 1, 2565 (1963)
95. L. M. Robeson, A. Noshay, M. Matzner and C. N. Merriam, Die Angew. Makromol. Chem., 29/30, 47 (1973)

APPENDIX A

SCREW AND EXTRUDER DESIGN

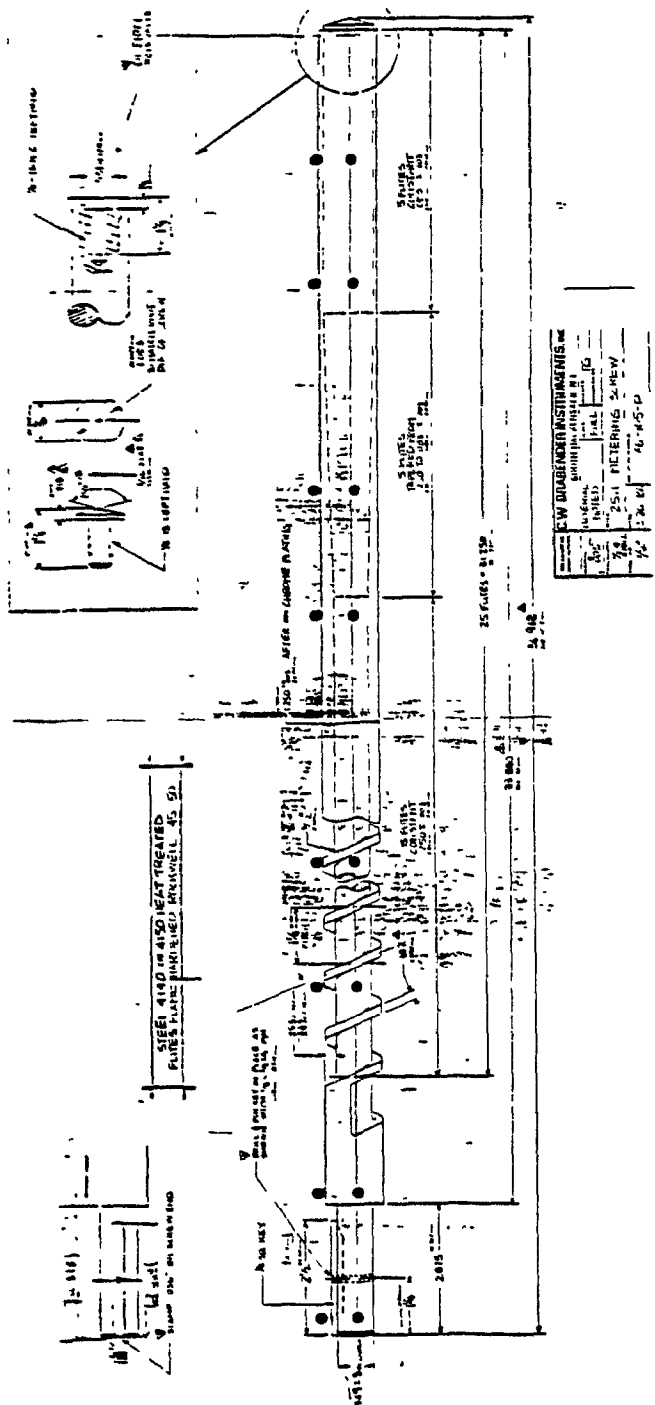


Figure A1 Metering Screw Design (C.W.Brabender Instruments, Inc.).

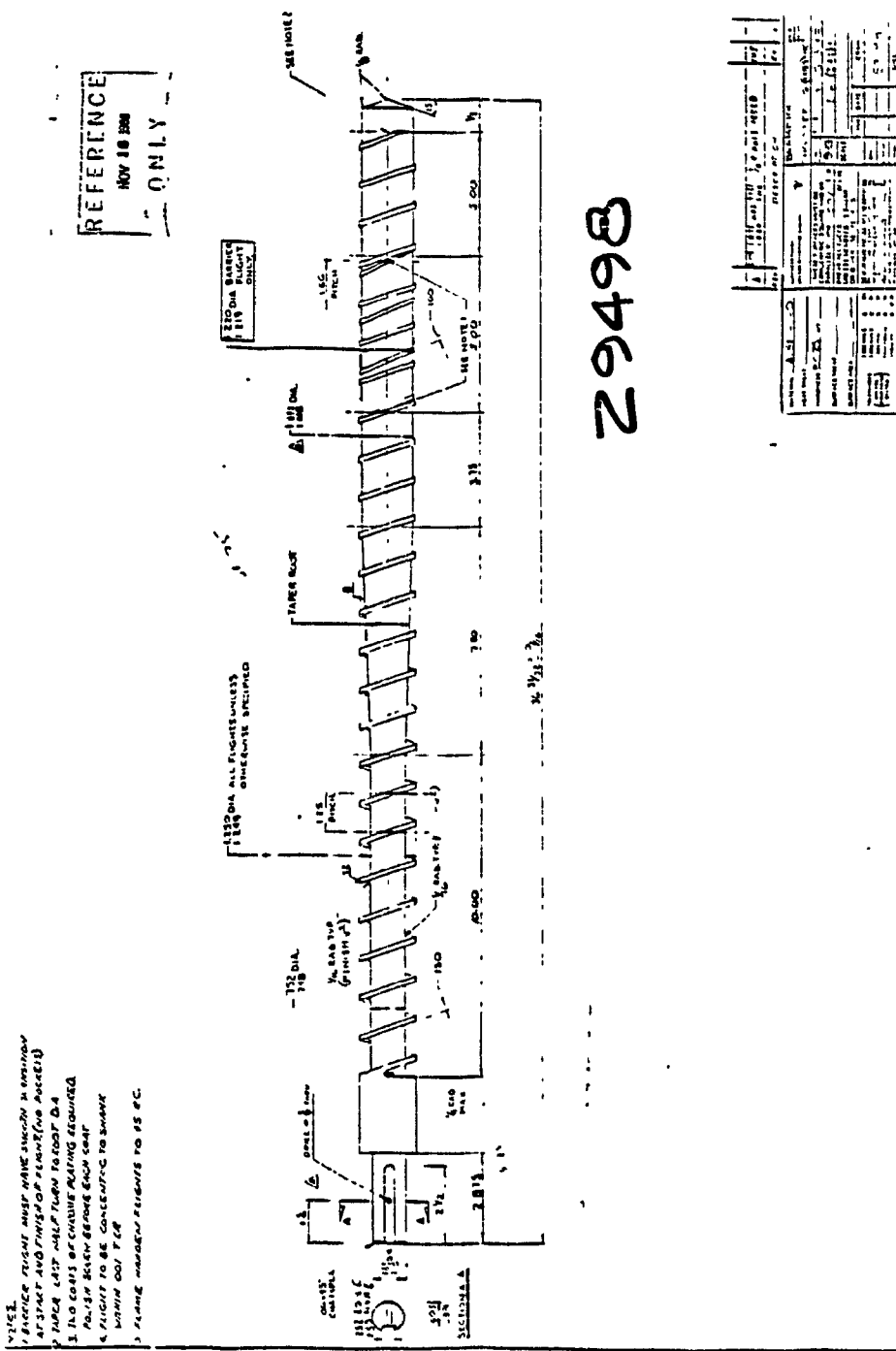


Figure A2 Mixing Screw Design (Brampton Engineering, Inc.).

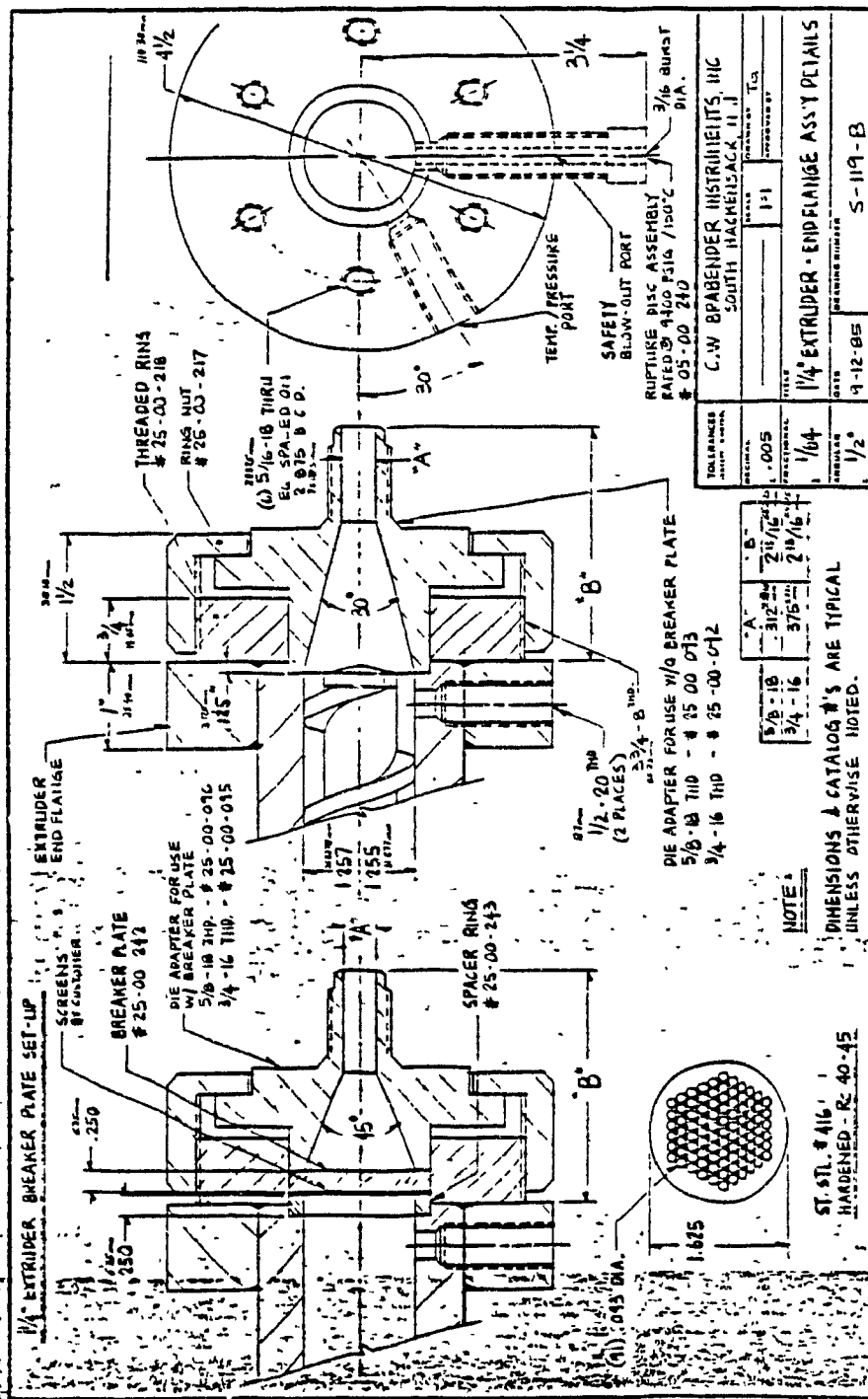


Figure A3 Extruder-Endflange Assembly Details (C.W.Brabender Instruments, Inc.).

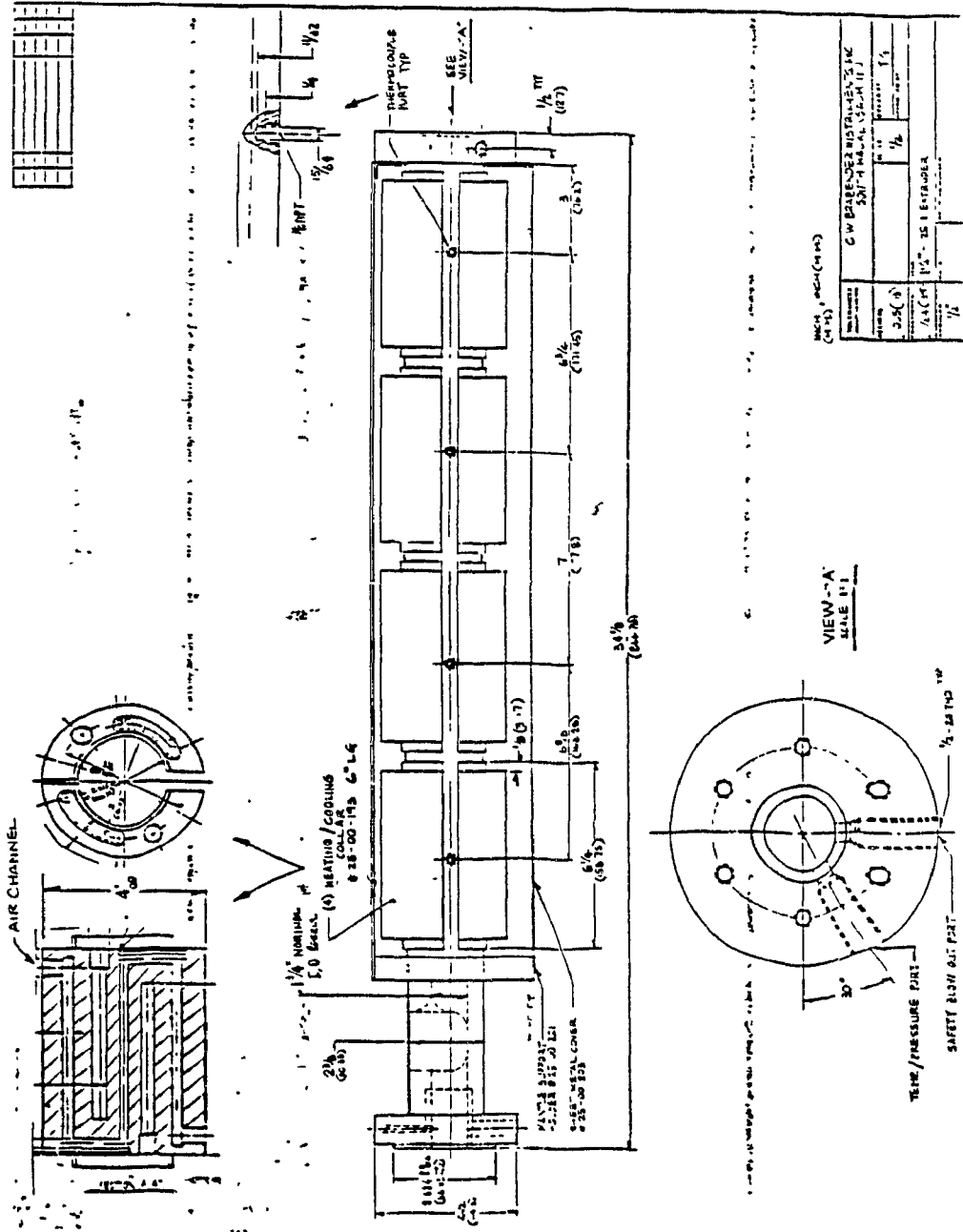
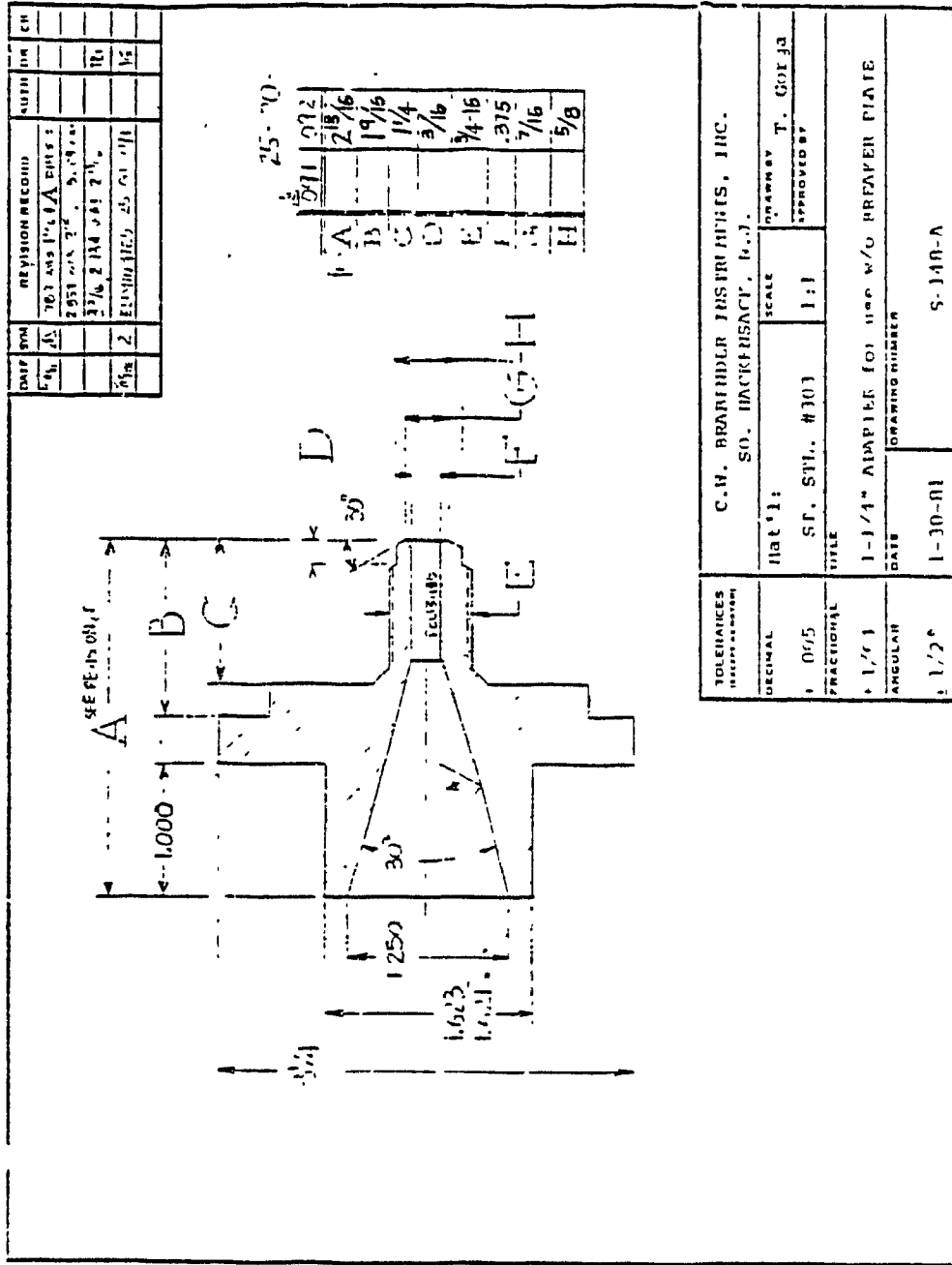


Figure A4 Heating/Cooling Collar Design Arrangements (C.W.Brabender Instruments, Inc.).

APPENDIX B

ADAPTER AND SLIT DIE DESIGN



C.W. BRABENDER INSTRUMENTS, INC.		SO. HACKENSACK, N.J.	
PLAT 1:1	SCALE	DESIGNED BY	T. GOEJZ
ST. STL. #303	1:1	APPROVED BY	
TITLE			
1-1/4" ADAPTER FOR USE W/O PREPARED PLATE			
DATE	DRAWING NUMBER		
1-30-50	S-148-A		

SALES SKETCH
MADE IN U.S.A.

C.W. BRABENDER INSTRUMENTS, INC.
ENGINEERS & SCIENTISTS

Figure B1 Adapter Design (C.W.Brabender Instruments, Inc.).

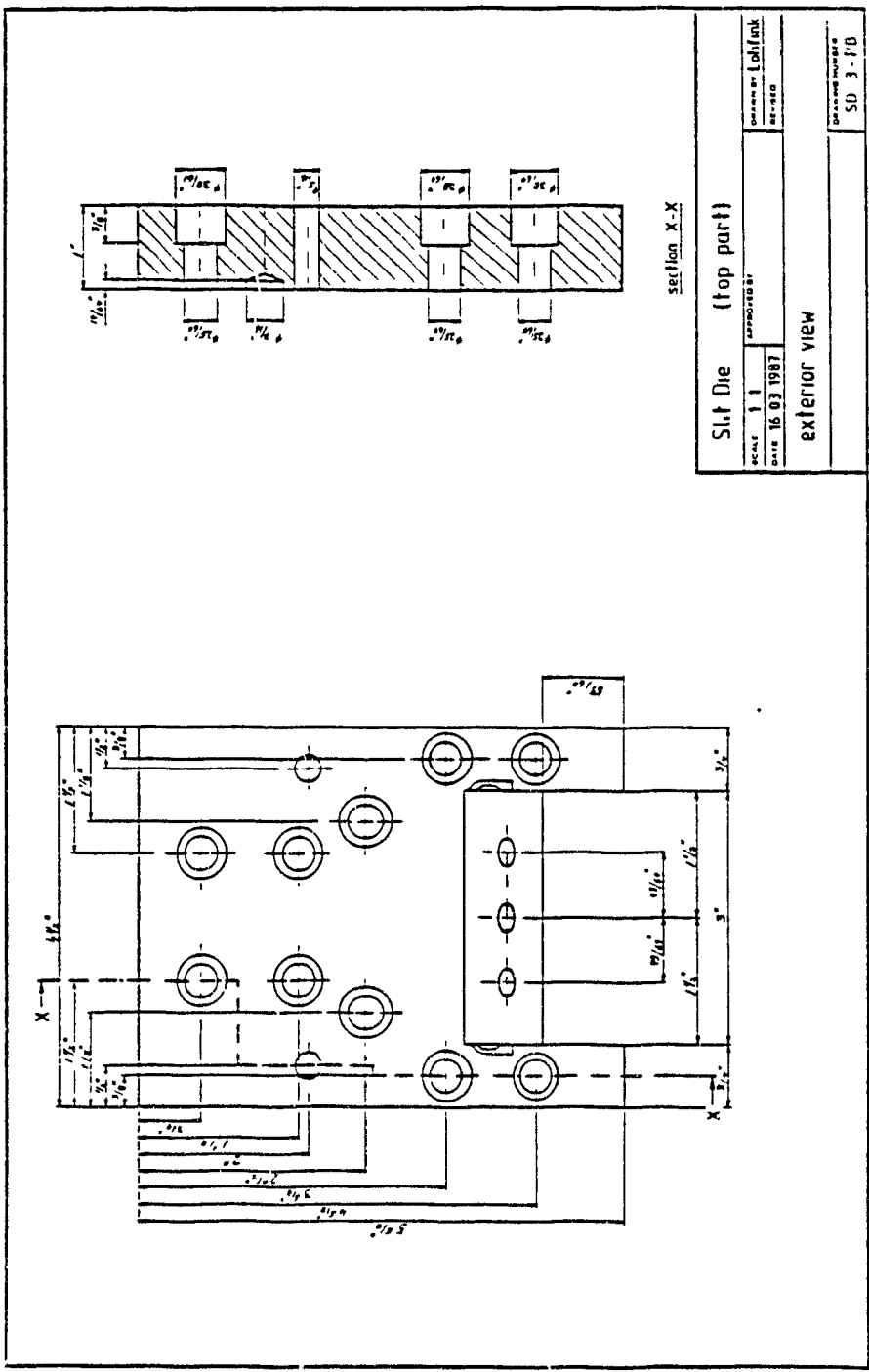


Figure B3 Slit Die - Top Part (Exterior View).

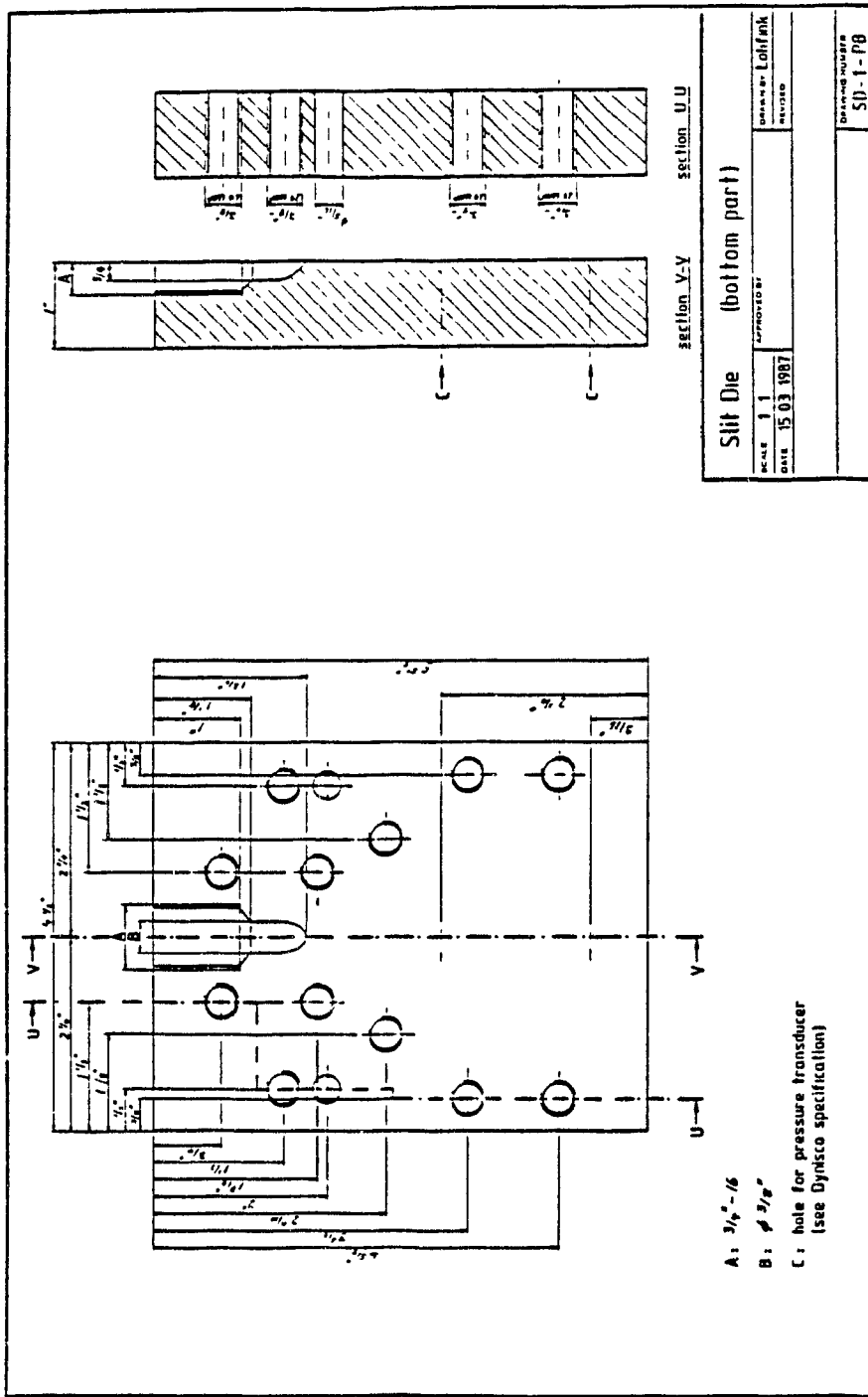


Figure B4 Slit Die - Bottom Part.

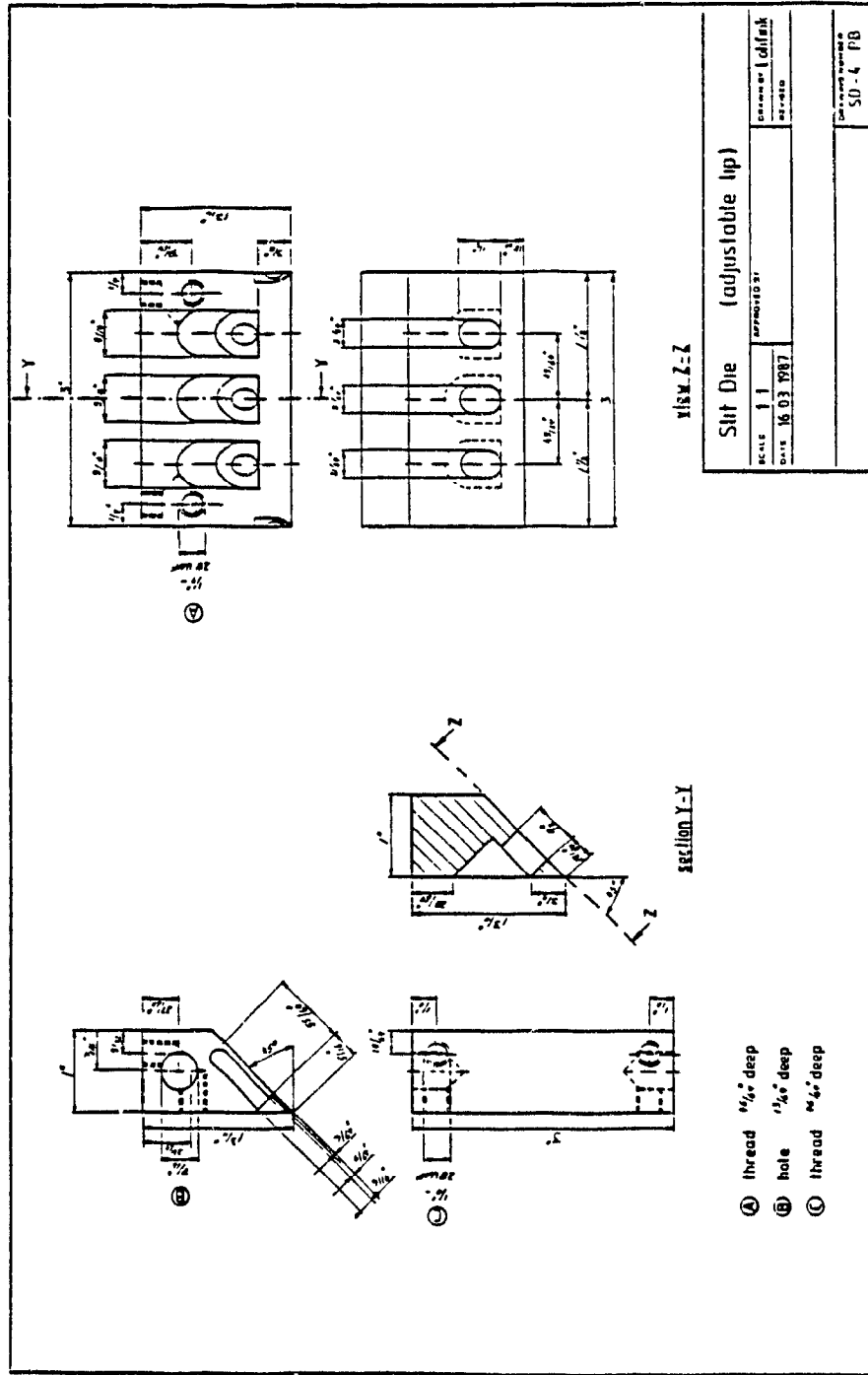


Figure B5 Slit Die - Adjustable Die Land.

APPENDIX C

SOFTWARE PACKAGE FOR SLIT DIE TEMPERATURE

CONTROL AND DATA ACQUISITION

The "ORIGINAL.GL5" program is used to control the slit die temperature and collect experimental data. The program is written in BASIC computer language and compiled with Quick-Basic 3.0. It consists of the following sections :

- i) a section for information of experiment specific data
 - Die Specification
 - Extruder / Screw Specification
 - Resin Specification
 - Die Control Characteristics
- ii) a section controlling the 'Heat-up Cycle' which outputs the time, the die temperature and control characteristics. The program gives a signal when die temperature has reached steady-state.

Throughout the next three sections, the program continues to control permanently the die temperature in addition to the following tasks :

- iii) a section which outputs the time, the die temperature and the die pressure. The program is in MANUAL control and operator decides when die pressure has reached steady-state.
- iv) a section performing DATA COLLECTION which outputs the time, extruder zone 4 temperature, die temperature, die pressure, rpm and torque.
- v) a section permitting a change in die temperature setpoint, change in extruder rpm, change in setup conditions and to stop the experiment.

The program is linked to the "PCLAB" program [Data Translation, Inc., 1985] which allows the collection of analog experimental data.

A personal computer with a 640k memory was used throughout the study. To achieve fast response times for the die temperature control, the 640k RAM was split, and a 256k virtual disk C: was installed.

```

250 DIM A1(2),A2(4),A3(8),ANALOG.ARRAY1%(200),ANALOG.ARRAY2%(400),ANALOG.ARRAY3%(400),AN.AR1%(10
),AN.AR2%(100),AN.AR4%(100),AN.AR5%(100)
260 KEY OFF
270 GOTO 1300
280 ' SUBROUTINE CONTROL
290 NU.OF.VAL%=00 DAC.SEL%=0 : FREQ%=50 : CLOCK.DIV%=8000 : TIME.SOURCE%=0
300 CALL SETUP_DAC(TIME.SOURCE%,DAC.SEL%)
310 CALL SET_CLOCK_DIVIDER(CLOCK.DIV%)
320 DT%='D'-SEPTD' ' deviation from setpoint
330 IF DT% > -25 THEN 400 ' full power to heater
340 CALL DAC.SERIES(NU.OF.VAL%,AN.AR1%(1))
350 RETURN
360 IF DT% > -2 THEN 430 ' 25%/40% power to heater
370 CALL DAC.SERIES(NU.OF.VAL%,AN.AR3%(1))
380 RETURN
390 IF DT% > 0 THEN 460 ' 17%/17% power to heater
400 CALL DAC.SERIES(NU.OF.VAL%,AN.AR4%(1))
410 RETURN
420 CALL DAC.SERIES(NU.OF.VAL%,AN.AR5%(1)) ' no power to heater
430 RETURN
440 ' SUBROUTINE DATA1
450 FREQ%=1000! CLOCK.DIVIDER%=(40000!/FREQ!)-.5 : TIMING.SOURCE%=0
460 START.CHAN%=0 : END.CHAN%=1 : GAIN%=500 : NUMBER.OF.VALUES%=200
470 SCALED.LSB%=LSB!/GAIN% : SCALED.LOW%=LOW.V!/GAIN% : SCAN.LENGTH%=(END.CHAN%+1)-START.CHAN% :
XSCAN%=NUMBER.OF.VALUES%/SCAN.LENGTH%
480 CALL SETUP_ADC(TIMING.SOURCE%,START.CHAN%,END.CHAN%,GAIN%)
490 CALL GET_ERROR.CODE(ERROR.VALUE%)
500 IF ERROR.VALUE%<>0 THEN PRINT"Error in SETUP.ADC (Subroutine Control1)",ERROR.VALUE%
510 CALL SET_CLOCK_DIVIDER(CLOCK.DIVIDER%)
520 CALL ADC.SERIES(NUMBER.OF.VALUES%,ANALOG.ARRAY1%(0))
530 CALL GET_ERROR.CODE(ERROR.VALUE%)
540 IF ERROR.VALUE%<>0 THEN PRINT"Error during acquisition (Subroutine Control1).",ERROR.VALUE%
550 FOR JJ2=0 TO SCAN.LENGTH%-1
560 CHAN%=JJ2+START.CHAN% : SUM!=0
570 KK1=JJ2 : KK2=NUMBER.OF.VALUES%-SCAN.LENGTH%+JJ2 : KK3=SCAN.LENGTH%
580 FOR II1=KK1 TO KK2 STEP KK3 : SUM!=SUM!+ANALOG.ARRAY1%(II1) : NEXT
590 A1(CHAN%)=SUM!/XSCAN%
600 NEXT
610 FOR JJ3=START.CHAN% TO END.CHAN%
620 VOLTAGE%=(A1(JJ3)*SCALED.LSB!)+SCALED.LOW!
630 IF JJ3=0 THEN TEMPT5%=(VOLTAGE!+.0002898)/5.536E-05
640 IF JJ3=1 THEN TEMPT6%=(VOLTAGE!+.0002898)/5.536E-05
650 NEXT
660 RETURN
670 ' SUBROUTINE DATA2
680 FREQ%=1000! CLOCK.DIVIDER%=(40000!/FREQ!)-.5 : TIMING.SOURCE%=0
690 START.CHAN%=0 : END.CHAN%=3 : GAIN%=500 : NUMBER.OF.VALUES%=400
700 SCALED.LSB%=LSB!/GAIN% : SCALED.LOW%=LOW.V!/GAIN% : SCAN.LENGTH%=(END.CHAN%+1)-START.CHAN% :
XSCAN%=NUMBER.OF.VALUES%/SCAN.LENGTH%
710 CALL SETUP_ADC(TIMING.SOURCE%,START.CHAN%,END.CHAN%,GAIN%)
720 CALL GET_ERROR.CODE(ERROR.VALUE%)
730 IF ERROR.VALUE%<>0 THEN PRINT"Error in SETUP.ADC (Subroutine Control2)",ERROR.VALUE%
740 CALL SET_CLOCK_DIVIDER(CLOCK.DIVIDER%)
750 CALL ADC.SERIES(NUMBER.OF.VALUES%,ANALOG.ARRAY2%(0))
760 CALL GET_ERROR.CODE(ERROR.VALUE%)
770 IF ERROR.VALUE%<>0 THEN PRINT"Error during acquisition (Subroutine Control2).",ERROR.VALUE%
780 FOR JJ4=0 TO SCAN.LENGTH%-1
790 CHAN%=JJ4+START.CHAN% : SUM!=0
800 KL1=JJ4 : KL2=NUMBER.OF.VALUES%-SCAN.LENGTH%+JJ4 : KL3=SCAN.LENGTH%
810 FOR II2=KL1 TO KL2 STEP KL3 : SUM!=SUM!+ANALOG.ARRAY2%(II2) : NEXT
820 A2(CHAN%)=SUM!/XSCAN%
830 NEXT
840 FOR JJ5=START.CHAN% TO END.CHAN%
850 VOLTAGE%=(A2(JJ5)*SCALED.LSB!)+SCALED.LOW!
860 IF JJ5=0 THEN TEMPT5%=(VOLTAGE!+.0002898)/5.536E-05

```



```

910     IF JJS=1 THEN TEMPT6!=(VOLTAGE!+.0002898)/5.536E-05
920     IF JJS=2 THEN PREN!=VOLTAGE!*150508.4013-7.4083
930     IF JJS=3 THEN PREX!=VOLTAGE!*149585.7846-37.4099           '0-2000 psi
940 NEXT
950 RETURN
960 'SUBROUTINE DATA COLLECTION
970 FREQ!=1000! * CLOCK.DIVIDER%=(400000!/FREQ!)- 5 : TIMING.SOURCE%=0
980 START.CHAN%=0 : END.CHAN%=3 GAIN%=500 : NUMBER.OF.VALUES%=400
990 SCALED.LSB'=LSB!/GAIN% : SCALED.LOW'=LOW V'/GAIN% : SCAN.LENGTH%=(END.CHAN%+1)-START.CHAN%
XSCAN%=NUMBER.OF.VALUES%/SCAN.LENGTH%
1000 CALL SETUP.ADC(TIMING.SOURCE%,START.CHAN%,END.CHAN%,GAIN%)
1010 CALL GET.ERROR.CODE(ERROR.VALUE%)
1020 IF ERROR.VALUE%<>0 THEN PRINT"Error in SETUP.ADC (Collection Subroutine).",ERROR.VALUE%
1030 CALL SET.CLOCK.DIVIDER(CLOCK.DIVIDER%)
1040 CALL ADC.SERIES(NUMBER.OF.VALUES%,ANALOG.ARRAY3%(0))
1050 CALL GET.ERROR.CODE(ERROR.VALUE%)
1060 IF ERROR.VALUE%<>0 THEN PRINT "Error during acquisition (Collection Subroutine).",ERROR.VALUE%
1070 FOR J1=0 TO SCAN.LENGTH%-1
1080     CHAN%=J1+START.CHAN% : SUM!=0
1090     K1=J1 : K2=NUMBER.OF.VALUES%-SCAN.LENGTH%+J1 : K3=SCAN.LENGTH%
1100     FOR I1=K1 TO K2 STEP K3 : SUM!=SUM!+ANALOG.ARRAY3%(I1) . NEXT
1110     A3(CHAN%)=SUM!/XSCAN%
1120 NEXT
1130 FOR J2=START.CHAN% TO END.CHAN%
1140     VOLTAGE!=(A3(J2)*SCALED.LSB')+SCALED.LOW!
1150 IF NOT J2=3 THEN 1190
1160 PREX!=VOLTAGE!*149585.7846-37.4099           '0-2000 psi
1170 START.CHAN%=4 * END.CHAN%=7 . GAIN%=1 * NUMBER.OF.VALUES%=400
1180 GOTO 990
1190     IF J2=0 THEN TEMPT5!=(VOLTAGE!+.0002898)/5.536E-05
1200     IF J2=1 THEN TEMPT6!=(VOLTAGE!+.0002898)/5.536E-05
1210     IF J2=2 THEN PREN!=VOLTAGE!*150508.4013-7.4083
1220     IF J2=4 THEN TEMPZ4!=130!*VOLTAGE!
1230     IF J2=5 THEN RPMIN!=-VOLTAGE!*17.168           '17.511
1240     IF J2=6 THEN CURR!=VOLTAGE!*6!
1250     IF J2=7 THEN VOLT!=VOLTAGE!*36!
1260 NEXT
1270 POWEX!=CURR!*VOLT!*.9
1280 TORQUE!=CURR!*VOLT!*8.594367/RPMIN!
1290 RETURN
1300 CLS
1310 LOCATE 5,1
1320 PRINT "      Extrusion Die Temperature Control and Experimental Data Collection      "
1330 PRINT
1340 PRINT "                                     by Guenter W. Lohfink                                     "
1350 FOR I%=1 TO 32000 : NEXT
1360 CLS : PRINT : PRINT
1370 PRINT " Connect as follows : Then press any key to continue      "
1380 PRINT : PRINT
1390 PRINT " Input Channels      "
1400 PRINT
1410 PRINT " Channel 0 - Die Thermocouple 1 (entrance) - T5 - 20mVdc"
1420 PRINT " Channel 1 - Die Thermocouple 2 (exit) - T6 - 20mVdc"
1430 PRINT " Channel 2 - Pressure Transducer (entrance) - PR EN - 20mVdc"
1440 PRINT " Channel 3 - Pressure Transducer (exit) - PR EX - 20mVdc"
1450 PRINT " Channel 4 - Extruder Zone 4 - 4 - 5.0 Vdc"
1460 PRINT " Channel 5 - Extruder rpm - RPMIN - 8.75 Vdc"
1470 PRINT " Channel 6 - Motor Current - CURRENT - 5.0 Vdc"
1480 PRINT " Channel 7 - Motor Voltage - VOLTAGE - 5.0 Vdc"
1490 PRINT : PRINT
1500 PRINT " Output Channels      "
1510 PRINT
1520 PRINT " DAC 0 - SSR1 and/or SSR2      "
1530 PRINT " DAC 1 - RPM OUT      "
1540 PRINT

```



```

2190 INPUT " Name : ",INITS
2200 INPUT " Date (day.month.year) : ",DAT$
2210 INPUT " Time (hour:minute) : ",ZEITS
2220 PRINT
2230 INPUT " Are corrections to the general information necessary ? (Y/N) . ",COR1$
2240 IF COR1$="y" OR COR1$="Y" THEN 2140
2250 PRINT#1,INITS;" ";DAT$;" ";ZEITS
2260 CLS : PRINT
2270 PRINT "*****"
2280 PRINT "**                      DIE SPECIFICATION                      **"
2290 PRINT "*****"
2300 PRINT
2310 INPUT " Die Specif.cation (capillary or slit) : ",DIES
2320 IF DIES="SLIT" OR DIES="slit" THEN 2430
2330 INPUT " Capillary Die (tubular, converging or diverging) : ",TYP$
2340 INPUT " Diameter (mm) : ",D
2350 INPUT " L/D ratio : ",R
2360 INPUT " Setpoint for Die Temperature [C] . ",SP!
2370 INPUT " Pressure Transducer Positions -choose two- (entrance, middle or exit) : ",P1$,P2$
2380 PRINT
2390 INPUT " Are corrections to the capillary die specification necessary ? (Y/N) : ",COR2$
2400 IF COR2$="y" OR COR2$="Y" THEN 2260
2410 PRINT#1,DIES;" ";TYP$;" ";D;" ";R;" ";SP!;" ";P1$;" ";P2$
2420 GOTO 2490
2430 INPUT " Gap Size (mm) : ",G
2440 INPUT " Setpoint for Die Temperature [C] : ",SP!
2450 PRINT
2460 INPUT " Are corrections to the slit die specification necessary ? (Y/N) : ",COR3$
2470 IF COR3$="y" OR COR3$="Y" THEN 2260
2480 PRINT#1,DIES;" ";G;" ";SP!
2490 CLS : PRINT
2500 PRINT "*****"
2510 PRINT "**                      EXTRUDER / SCREW SPECIFICATION                      **"
2520 PRINT "*****"
2530 PRINT
2540 INPUT " Extruder Diameter (mm) . ",EXD
2550 INPUT " Extruder L/D ratio : ",EXR
2560 INPUT " Setpoint for Extruder Zone Temperatures (Zone1 to Zone4) [C] : ",SPTEX1,SPTEX2,SPTEX3,SPTEX4
2565 INPUT " Adapter Entrance Angle (deg) : ",AEA
2570 INPUT " Screw Speed (l/min) : ",RPM!
2580 INPUT " Mass Flowrate (g/min) : ",MFR!
2590 INPUT " Volumetric Flowrate (cm^3/min) : ",VFR!
2600 INPUT " Screw Design (metering, single-stage-mixing or two-stage-mixing) . ",SCRDS
2610 PRINT
2620 INPUT " Are corrections to the extruder/screw specification necessary ? (Y/N) : ",COR4$
2630 IF COR4$="y" OR COR4$="Y" THEN 2490
2640 PRINT#1,EXD;" ";EXR;" ";SPTEX1;" ";SPTEX2;" ";SPTEX3;" ";SPTEX4;" ";RPM!;" ";MFR!;" ";VFR!;" ";SCRDS
2650 CLS : PRINT
2660 PRINT "*****"
2670 PRINT "**                      RESIN SPECIFICATION                      **"
2680 PRINT "*****"
2690 PRINT
2700 INPUT " Blend Specification (example: A-B or A-B-C) . ",BLSP$
2710 INPUT " Mixing Ratio by WEIGHT (example: 25-75 or 15-80-5) . ",MR1$
2715 INPUT " Mixing Ratio by VOLUME (example: 20-80 or 10-85-5) . ",MR2$
2720 INPUT " Viscosity Ratio (dispersed phase / matrix phase) . ",VR
2730 PRINT
2740 INPUT " Are corrections to the resin specification necessary ? (Y/N) : ",COR5$
2750 IF COR5$="y" OR COR5$="Y" THEN 2650
2760 PRINT#1,BLSP$;" ";MR1$;" ";MR2$;" ";VR
2770 CLS : PRINT
2780 PRINT "*****"
2790 PRINT "**                      DIE CONTROL CHARACTERISTICS                      **"
2800 PRINT "*****"

```

```

2810 PRINT
2820 PRINT " Setpoint for Die Temperature (C) has been choosen to : ";SP!
2830 INPUT " Maximum Temperature Deviation from Setpoint (C) : ",TR!
2840 INPUT " Number of Consecutive Readings for Determining Steady State : ",NRSS%
2850 PRINT
2860 INPUT " Are corrections to the die control characteristics necessary ? (Y/N) : ",COR6S
2870 IF COR6S="y" OR COR6S="Y" THEN 2770
2880 PRINT#1,SP!,"";TR!,"";NRSS%
2890 CLS . PRINT
2900 INPUT " Would you like to have a hardcopy ? (Y/N) : ",HCS
2910 IF HCS="n" OR HCS="N" THEN 3320
2920 LPRINT
2930 LPRINT " Name ..... : ";INITS
2940 LPRINT " Date ..... : ";DATS
2950 LPRINT " Time ..... : ";LEITS
2960 LPRINT : LPRINT
2970 LPRINT " Filename for Data File ..... : ";FILES
2980 LPRINT . LPRINT
2990 LPRINT " Die Specification ..... : ";DIES
3000 IF DIES="SLIT" OR DIES="slit" THEN 3070
3010 LPRINT " Capillary Die Type ..... : ";TYP5
3020 LPRINT USING " Diameter .....D = ###.## mm ";D
3030 LPRINT USING " L/D Ratio .....R = ### ";R
3040 LPRINT USING " Setpoint for Die Temperature .....SPTD = ### C ";SP!
3050 LPRINT " Pressure Transducer Positions ..... : ";P1S,P2S
3060 GOTO 3090
3070 LPRINT USING " Gap Size .....G = ###.## mm ";G
3080 LPRINT USING " Setpoint for Die Temperature .....SPTD = ### C ";SP!
3090 LPRINT
3100 LPRINT " Extruder / Screw Specification "
3110 LPRINT USING " Extruder Diameter .....EXD = ###.## mm ";EXD
3120 LPRINT USING " Extruder L/D Ratio ..... EXR = ### ";EXR
3130 LPRINT USING " Setpoint for Extruder Temperature - Zone1 = ### C ";SPTEX1
3140 LPRINT USING " - Zone2 = ### C ";SPTEX2
3150 LPRINT USING " - Zone3 = ### C ";SPTEX3
3160 LPRINT USING " - Zone4 = ### C ";SPTEX4
3165 LPRINT USING " Adapter Entrance Angle .....AEA = ### deg ";AEA
3170 LPRINT USING " Screw Speed .....RPM = ### 1/min ";RPM!
3180 LPRINT USING " Mass Flowrate .....MFR = ###.## g/min ";MFR!
3190 LPRINT USING " Volumetric Flowrate .....VFR = ###.## cm^3/min ";VFR!
3200 LPRINT " Screw Design ..... : ";SCRDS
3210 LPRINT
3220 LPRINT " Resin Specification "
3230 LPRINT " Blend Specification ..... : ";BLSPS
3240 LPRINT " Mixing Ratio by WEIGHT .. : ";MR1S
3245 LPRINT " Mixing Ratio by VOLUME ..... : ";MR2S
3250 LPRINT USING " Viscosity Ratio (dispersed/matrix phase) VR = ###.## ";VR
3260 LPRINT
3270 LPRINT " Die Control Characteristics "
3280 LPRINT USING " Setpoint for Die Temperature .....SPTD = ### C";SP!
3290 LPRINT USING " Max. Temperature Deviation from Setpoint TR = ### C";TR!
3300 LPRINT " Number of Consecutive Readings for Determining "
3310 LPRINT USING " Steady State .....NRSS = ### ";NRSS%
3320 CLOSE #1
3330 CLS
3340 LOCATE 5,15 . PRINT " Collection of SETUP Information has been completed. "
3350 LOCATE 10,15 : PRINT " During experiment press 'F9' to change any SETUP "
3360 LOCATE 11,15 : PRINT " condition. Program will close data files currently "
3370 LOCATE 12,15 : PRINT " used and will ask user for a new data file name. "
3380 LOCATE 15,10 . PRINT " Press 'F5' to change Die Temperature Setpoint at any time. "
3390 LOCATE 17,15 : PRINT " Press 'F10' to STOP the experiment at any time. "
3400 LOCATE 22,15 . PRINT " Press any key to start the experiment."
3410 AS=INKEYS . IF AS="" THEN 3410
3420 CLS . LOCATE 10,33 PRINT " HEATUP CYCLE "
3430 PRINT
3440 TAILIBS=".hup" . FILE1BS=NOSES+FILES+TAILIBS

```

```

3450 KL%=1
3460 OPEN FILE1BS FOR OUTPUT AS #1
3470 SPTD!=SP!+.1
3480 TIMES="00:00:00"
3490 NTIME%=0 : NCOUNT%=0 : NSEL%=0 : XTIME!=0 : M%=20
3500 RD!=0
3510 PVRD!=RD!
3520 IF NOT FL%=0 THEN 4630
3530 GOSUB 480 'Subroutine Data1
3540 RD!=TEMPT6!
3550 GOSUB 320 'Subroutine Control
3560 MNS%=VAL(MIDS(TIMES,4,2))+(VAL(LEFTS(TIMES,2))*60) : SEC%=VAL(RIGHTS(TIMES,2))
3570 IF MNS%=NTIME% THEN 3600
3580 IF SEC%>=30 AND NSEL%=1 THEN 3610
3590 GOTO 3510
3600 NSEL%=1 : NTIME%=NTIME%+1 : GOTO 3620
3610 NSEL%=0
3620 PRINT#1,USING " ###.##";XTIME!,TEMPT5!,TEMPT6!,RD!,PVRD!
3630 IF NOT M%=20 THEN 3680
3640 M%=0 : CLS
3650 LOCATE 1,1 : PRINT " Time TEMPT5 TEMPT6 RD PVRD "
3660 LOCATE 2,1 : PRINT " (min) (C) (C) (C) (C) "
3670 LOCATE 4,1
3680 PRINT USING " ###.## ";XTIME!,TEMPT5!,TEMPT6!,RD!,PVRD!
3690 M%=M%+1
3700 XTIME!=XTIME!+.5
3710 IF RD!>(SP!+TR!) OR RD!<(SP!-TR!) THEN 3510 'steady state ?
3720 IF PVRD!>(SP!+TR!) OR PVRD!<(SP!-TR!) THEN 3510 'steady state '
3730 NCOUNT%=NCOUNT%+1
3740 IF NCOUNT%<NRS3% THEN 3510
3750 CLS
3760 LOCATE 5,19 : PRINT " HEATUP CYCLE FOR DIE TEMPERATURE COMPLETED "
3770 LOCATE 8,19 : PRINT " Die Temperature has reached Steady-State. "
3780 LOCATE 15,17 : PRINT " Turn Extruder Motor ON and set to selected RPM."
3790 LOCATE 18,17 : PRINT " Press 'F8' to change Extruder RPM at any time."
3800 LOCATE 22,17 : PRINT " Press 'F6' for Start-Up Procedure of Extruder "
3810 LOCATE 24,4 : PRINT " and switch RPM CONTROL on motor control box in COMPUTER control box.
on."
3820 GOTO 3510
3830 CLS
3840 LOCATE 5,26 : PRINT " Program is in MANUAL control."
3850 LOCATE 10,10 : PRINT " Operator decides when DIE-PRESSURE has reached Steady-State "
3860 LOCATE 20,3 : PRINT " When Die-Pressure at Steady-State , press 'F7' to start DATA ACQUISITION."
3870 PRINT : PRINT
3880 FOR IN7=1 TO 100 : AN.AR3%(IN7)=2049 AN.AR4%(IN7)=2049 : NEXT 'no power
3890 FOR ID=1 TO 100 STEP 10
3900 AN.AR3%(ID)=3687 : AN.AR3%(ID+1)=3687 : AN.AR3%(ID+2)=3687
3910 AN.AR3%(ID+3)=3687
3930 NEXT '40% power
3940 FOR ID=1 TO 96 STEP 6
3950 AN.AR4%(ID)=3687
3970 NEXT '17% power
3975 SPTD!=SP!
3980 TIMES="00:00:00"
3990 NTIME%=0 : NSEL%=0 : XTIME!=0 : M%=20
4000 IF NOT FL%=0 THEN 4630
4010 GOSUB 710 'Subroutine Data2
4020 RD!=TEMPT6!
4030 GOSUB 320 'Subroutine Control
4040 PVRD!=RD!
4050 MNS%=VAL(MIDS(TIMES,4,2))+(VAL(LEFTS(TIMES,2))*60) : SEC%=VAL(RIGHTS(TIMES,2))
4060 IF MNS%=NTIME% THEN 4090
4070 IF SEC%>=30 AND NSEL%=1 THEN 4100
4080 GOTO 4000
4090 NSEL%=1 : NTIME%=NTIME%+1 : GOTO 4110

```

```

4100 NSEL%=0
4110 PRINT#, USING " ####.#", XTIME!, TEMPT5!, TEMPT6!, PREN!, PREX!
4120 IF NOT M%=20 THEN 4170
4130 M%=0 . CLS
4140 LOCATE 1,1 : PRINT "   Time   TEMPT5   TEMPT6   PREN   PREX   "
4150 LOCATE 2,1 . PRINT "   (min)   (C)       (C)       (psi)   (psi)  "
4160 LOCATE 4,1
4170 PRINT USING " ####.# "; XTIME!, TEMPT5!, TEMPT6!, PREN!, PREX!
4180 M%=M%+1
4190 XTIME!=XTIME!+.5
4200 GOTO 4000
4210 CLOSE #2 . CLS
4220 FL%=0
4230 TAILCS=" Dat" . FILECS=NOSES+FILES+TAILCS
4240 (L%=0)
4250 OPEN FILECS FOR OUTPUT AS #3
4260 LOCATE 10,32 . PRINT " DATA COLLECTION "
4270 PRINT : PRINT
4275 SPTD!:=3P'-1
4280 TIMES="00.00:00"
4290 NTIME%=1 XTIME!=0 : NSEL%=1 : M%=20
4300 IF NOT FL%=0 THEN 4630
4310 GOSUB 960
4320 PRINT#, USING " ####.#"; XTIME!, TEMPZ4!, TEMPT5!, TEMPT6!, PREN!, PREX!, RPMIN!, TORQUE!, POWEX!
4330 IF NOT M%=20 THEN 4380
4340 M%=0 . CLS
4350 LOCATE 1,1 : PRINT "   Time   TEMPZ4   TEMPT5   TEMPT6   PREN   PREX   RPM
TORQUE   "
4360 LOCATE 2,1 : PRINT "   (min)   (C)       (C)       (C)       (psi)   (psi)   (1/min)
: Nm)   "
4370 LOCATE 4,1
4380 PRINT USING " ####.# "; XTIME!, TEMPZ4!, TEMPT5!, TEMPT6!, PREN!, PREX!, RPMIN!, TORQUE!
4385 M%=M%+1
4390 XTIME!=XTIME!+.5
4400 IF NOT FL%=0 THEN 4630
4410 GOSUB 480
4420 RD!=TEMPT6!
4430 GOSUB 320
4440 PVRD!=RD!
4450 MNS%=VAL(MID$(TIMES,4,2))+VAL(LEFT$(TIMES,2))*60 : SEC%=VAL(RIGHT$(TIMES,2))
4460 IF MNS%=NTIME% THEN 4490
4470 IF SEC%>=30 AND NSEL%=1 THEN 4500
4480 GOTO 4400
4490 NSEL%=1 : NTIME%=NTIME%+1 : GOTO 4300
4500 NSEL%=0 . GOTO 4300
4510 FL%=5
4520 RETURN
4530 FL%=6
4540 RETURN
4550 FL%=7
4560 RETURN
4570 FL%=8
4580 RETURN
4590 FL%=9
4600 RETURN
4610 FL%=10
4620 RETURN
4630 IF FL%=5 THEN 4690
4640 IF FL%=6 THEN 4910
4650 IF FL%=7 THEN 4210
4660 IF FL%=8 THEN 5010
4670 IF FL%=9 THEN 5130
4680 IF FL%=10 THEN 5210
4690 ' Change in Setpoint for Die Temperature - F5
4700 CLS . PRINT
4710 PRINT " Setpoint for Die Temperature (C) is : "; SP!

```

```

4720 PRINT
4730 PRINT " Maximum Temp. Deviation from Setpoint (C) is : ";TR!
4740 PRINT : PRINT
4750 INPUT " New Setpoint for Die Temperature (C) : ",SP!
4760 PRINT
4770 INPUT " New Maximum Temp. Deviation from Setpoint (C) : ",TR!
4780 PRINT
4800 IF NOT <L%=1 THEN 4840
4810 PRINT#1,USING" ####.#",<TIME!,SP!,TR!
4815 SPTD!:=SP!+.1
4820 FL%=0
4830 GOTO 3510
4840 IF NOT <KL%=2 THEN 4880
4850 PRINT#2,USING" ####.#",<XTIME!,SP!,TR!
4855 SPTD!:=SP!
4860 FL%=0
4870 GOTO 4000
4880 PRINT#3,USING" ####.#",<XTIME!,SP!,TR!
4885 SPTD!:=SP!-1
4890 FL%=0
4900 GOTO 4300
4910 ' Start-Up procedure of Extruder - F6
4920 CLOSE
4930 TAIL2S=" ext" : FILE2S=40SES+FILES+TAIL2S
4940 KL%=2
4950 OPEN FILE2S FOR OUTPUT AS #2
4960 VALUE'=RPM!*15.7462 'RPM computer controlled
4970 ANALOG.DATA.VALUE%=VALUE!+2048
4980 DAC.SELECT%=1 : CALL DAC.VALUE(DAC.SELECT%,ANALOG.DATA.VALUE%)
4990 FL%=0
5000 GOTO 3830
5010 ' Change in Extruder RPM - F8
5020 CLOSE
5030 CLS . PRINT
5040 PRINT " Current Extruder RPM (1/min) is : ";RPM!
5050 PRINT
5060 INPUT " New Extruder RPM (0-130) (1/min) : ",RPM!
5070 PRINT
5080 PRINT " Last Filename used : ";FILES
5090 PRINT
5100 INPUT " New Filename for Data File (for new RPM) : ",FILES
5110 FL%=0
5120 GOTO 4930
5130 ' Change in SETUP conditions - F9
5140 CLOSE
5150 ANALOG.DATA.VALUE%=2049 'Heater Off (5mVdc)
5160 DAC.SELECT%=0 : CALL DAC.VALUE(DAC.SELECT%,ANALOG.DATA.VALUE%)
5170 ANALOG.DATA.VALUE%=2048 'RPM set to zero
5180 DAC.SELECT%=1 : CALL DAC.VALUE(DAC.SELECT%,ANALOG.DATA.VALUE%)
5190 FL%=0
5200 GOTO 1900
5210 ' STOP of experiment - F10
5220 CLOSE
5230 ANALOG.DATA.VALUE%=2049 'Heater Off (5mVdc)
5240 DAC.SELECT%=0 : CALL DAC.VALUE(DAC.SELECT%,ANALOG.DATA.VALUE%)
5250 ANALOG.DATA.VALUE%=2048 'RPM set to zero
5260 DAC.SELECT%=1 : CALL DAC.VALUE(DAC.SELECT%,ANALOG.DATA.VALUE%)
5270 CLS . PRINT
5280 LOCATE 10,20 : PRINT " Experiment has been STOPPED "
5290 LOCATE 12,20 : PRINT " Die Heater(s) have been switched off."
5300 LOCATE 20,10 : INPUT " Would you like to start a new experiment ? (Y/N) . ",N$TC
5310 L=1
5320 FL%=0
5330 GOTO 1370
5340 CLS
5350 COLOR 23,0

```

```
5360 LOCATE 5,24 · PRINT "DO NOT FORGET TO COPY CONTENTS OF"  
5370 LOCATE 9,36 : PRINT "DRIVE C."  
5380 LOCATE 13,26 : PRINT "BEFORE SHUTTING OFF POWER !!!"  
5390 LOCATE 22,1  
5400 COLOR 7,0  
5410 STOP  
5420 END
```


APPENDIX D

HIGH SPEED IMPACT TESTER LOAD-DEFLECTION CURVES

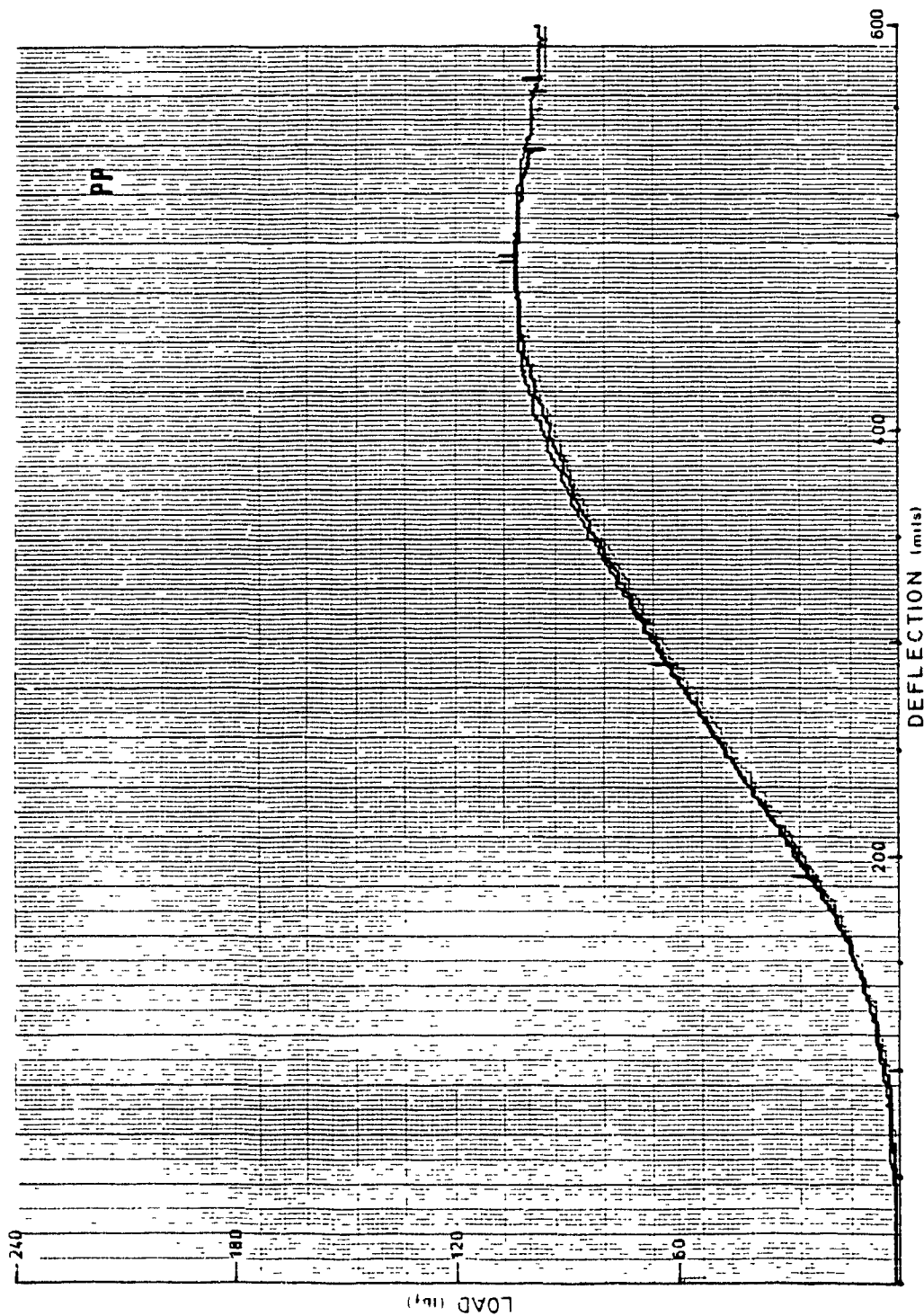


Figure D1 RVIST Load-Deflection Curves for PP.

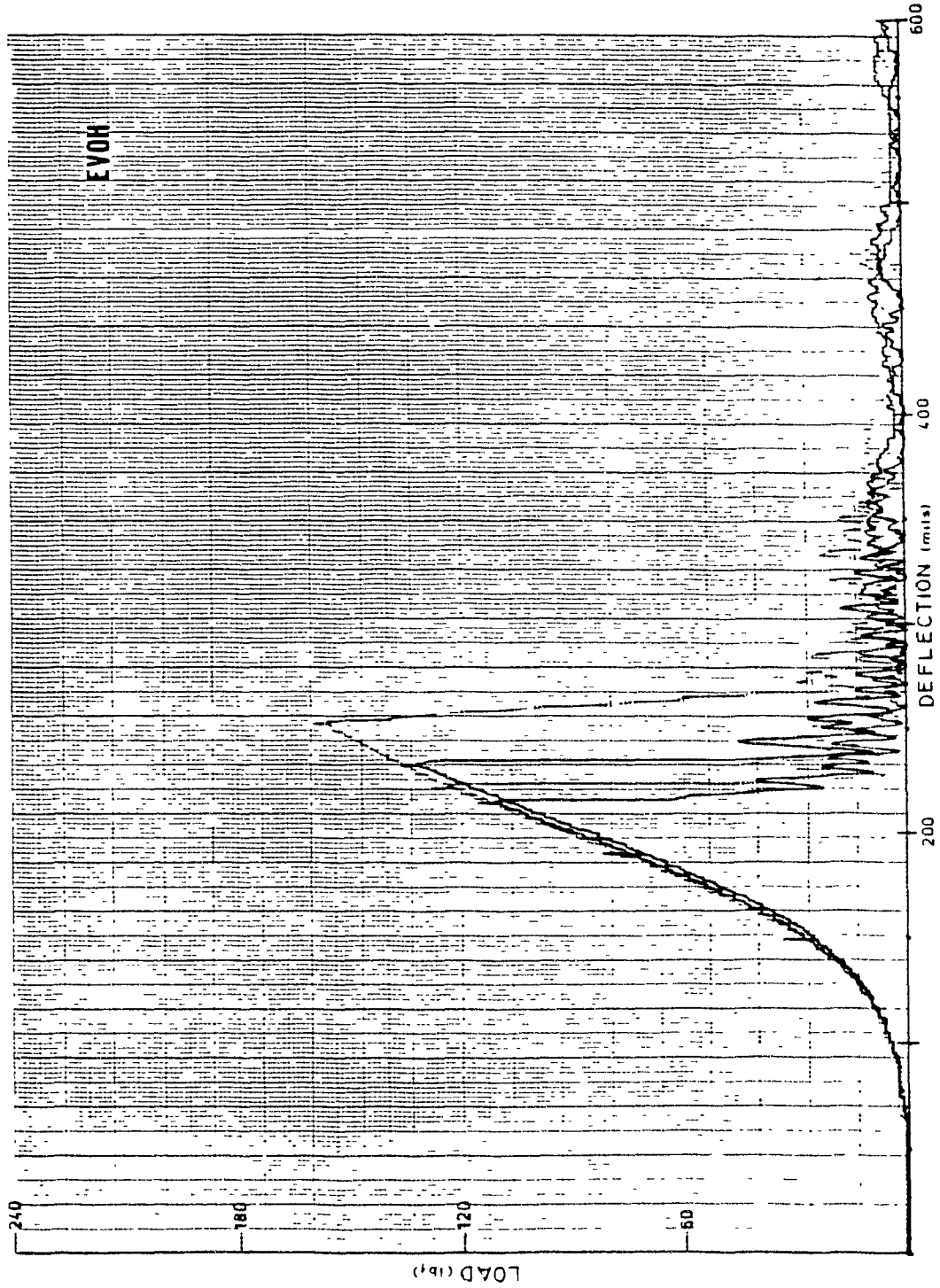


Figure D2 RVIST Load-Deflection Curves for EVOH.